Attachment Mechanisms of a Novel, Targeted, Lipid-Based, Ultrasound Contrast Agent

Adele Edgeworth

PhD – The University of Edinburgh – 2010

Declaration

The work within this thesis has been carried out and written by myself. Where work has been carried out with others they have been clearly acknowledged. The following work has not been submitted for any other professional degree or qualification and where work may have been published elsewhere it has been identified as such.

Adele L. Edgeworth
December 2009

Contents

Table of Figures

Table of Tables

Table of Symbols

The following symbols have been used consistently throughout this thesis.

f_0	Resonant frequency	λ	Wavelength
r	Microbubble radius	ϑ	Angle between incident laser beams
γ	Adiabatic ideal gas constant	Re	Reynolds number
P_0	Ambient fluid pressure	ρ	Density
ρ_0	Ambient fluid density	μ	Dynamic viscosity
σ_{st}	Surface tension of microbubble	υ	Kinematic viscosity
MI	Mechanical index	v_s	Mean fluid velocity
$p-$	Peak negative pressure	h	Characteristic length
f_c	Central frequency	D_h	Hydraulic diameter
σ	Scattering cross-section	A	Cross-sectional area
k	Microbubble radius	U	Wetted perimeter
κ	Adiabatic compressibility of a medium	Le	Entrance length
κ_s	Adiabatic compressibility of a scatterer	τ	Wall shear stress
ρ	Density of medium	du/dx	Shear rate
ρ_s	Density of scatterer	Q	Flow volume
v	Fluid velocity	w	Width of flow channel
d_f	Fringe spacing	$V-$	Peak negative voltage
f_d	Scattered frequency	η	Hydrophone sensitivity

Preface

The following thesis describes the development of a novel, targeted, lipid-based ultrasound contrast agent (UCA) for the assessment of coronary heart disease (CHD). The agent is currently being developed at the University of Edinburgh.

The general aim of the research presented throughout this thesis was to further the development of the UCA described above and to demonstrate active targeting of the agent to a cellular surface under flow. This was achieved through the specific objectives outlined below:

- To optimise the agent for use with 40MHz intravascular ultrasound (IVUS).
- To develop a flow chamber for the assessment of targeted microbubble attachment under high wall shear stress (WSS).
- To develop a method of assessing microbubble attachment to cells under flow.
- To demonstrate attachment of the in-house UCA to a cellular surface under flow conditions.

The cardiovascular system and coronary heart disease are described in Chapter 1. This chapter explains the motivation for developing the UCA, in addition to providing some background information on the causes and current and developing diagnostic techniques for CHD.

Ultrasound imaging techniques and UCAs are described in Chapter 2. The use of UCAs is described and the interactions of UCAs with ultrasound explained through a review of the available literature. Different methods used to produce microbubbles have been described and past, current and developing contrast agents identified. In addition, a brief review of the literature and current understanding of ultrasound and UCA safety has been provided.

Chapter 3 outlines the methods and techniques used to optimise the novel UCA for use with high-frequency intravascular ultrasound (IVUS). A variety of techniques has been tried and investigated to produce the most echogenic microbubble sample.

Echogenicity has been assessed using visual and radio-frequency (RF) analysis of IVUS images.

A novel flow chamber designed for the assessment of microbubble attachment under known, high WSS has been described in Chapter 4. The flow chamber design and purpose has been explained and calibration of the flow chamber using laser Doppler anemometry (LDA) has been detailed.

The UCA has been developed for use with IVUS. The scanner and transducer used for the optimisation and detachment investigations, detailed in this thesis, has been characterised and described in Chapter 5.

Targeting of the UCA has been achieved through the attachment of antibodies to the microbubble shell. Attachment of antibodies was via a streptavidin-biotin bridge. Chapter 6 identifies the techniques used to optimise antibody attachment to the microbubbles.

The strength of the streptavidin-biotin bond has been tested up to 50Pa WSS as described in Chapter 7. The novel flow chamber calibrated in Chapter 4 has been used to assess the WSS under which microbubbles remain attached to a streptavidin coated surface. Attachment was assessed using the IVUS scanner described and characterised in Chapter 5.

Cellular adhesion within the flow chamber and within micro flow slides has been investigated in order to determine the optimum technique for assessment of microbubble attachment to cells under WSS. This work is detailed in Chapter 8.

The final experimental chapter details the targeting of the UCA to a cellular surface in static conditions and under very low WSS. Chapter 9 describes the development of methods leading to successful targeting of the UCA.

Conclusions and evaluation of the techniques and methods used throughout this thesis can be found in Chapter 10. This chapter outlines the advances made during this PhD in the development of the microbubble UCA and the further investigations required.

Acknowledgements

The first big ‘thank you’ goes to my supervisors; Carmel Moran, Jim Ross and Tom Anderson for all the support they have given me over the past three years and for reading and re-reading my chapters, reports and papers without complaint (in my earshot). In particular I would like to thank Carmel for somehow knowing when to apply pressure and when to back off; this thesis wouldn’t be here without you!

Linda Norrie, thank you for the countless cells you grew for me. Ian Ansell and Kathryn Sangster, thank you for helping me find my way around your lab. Bill Easson, thank you for your expertise and patience with me during the laser Doppler anemometry phase of my research.

Thank you to Medical Physics and the broom-cupboard for the tea, cakes and entertainment! Mairead Butler and Dave Hardman, you have been both fantastic friends and amazing sources of help throughout the last three years. Irene Craig, an amazing secretary, person and baker! Lauren Thomas, thank you for bringing a splash of brilliance to my days in the office!

Sarah Wilkinson, Karen Wainwright, Pippa Meekings and Keely Phillips, you have always been there for me with a bottle of wine when things were not going well and another bottle of wine when things were going well, thank you for being my friends.

Louise and Dave Cromie, Michael and Jessica Jefferson, Keith Duncan and Xanthe Holmes, Jamie Henderson and the rest of 142 Squadron, thank you for believing in me from the start and helping to distract me when needed. To my former flatmate Deborah Wiseman, for all the good times we had – thank you!

Dad and Pauline, thanks for proof reading and graciously accepting that I would be a broke student for a further three years.

Thanks to Millie Mooo, my sister for believing in me and inspiring me.

Mum and Rob there is no way I would fit all the things I want to thank you for within the word limit, so instead, I dedicate this thesis to you both.

Abstract

This thesis presents the development of a novel, targeted, lipid-based, microbubble ultrasound contrast agent (UCA) for assessment of coronary heart disease (CHD) with high frequency intravascular ultrasound (IVUS). The targeting mechanisms assessed for microbubble attachment include a streptavidin-biotin mechanism, electrostatic mechanism and antibody targeting.

The microbubble has been optimized for use with 40MHz IVUS through an investigation into the effect of various production methods on the echogenicity of the agent. Echogenicity has been assessed from quantification of the RF data and determination of the mean ultrasound backscatter. Agitation was found to be the optimal method of production resulting in a 3.94(±1.14)dB increase in the mean backscatter. The stability of the agent has also been assessed over time and optimal storage of the agent determined.

A novel flow chamber has been developed for assessment of microbubble detachment under very high WSS. The flow chamber has been calibrated to 50Pa wall shear stress (WSS) using laser Doppler anemometry (LDA). Higher WSS was achieved through the use of higher viscosity fluids. The streptavidin-biotin bond has been assessed within the flow chamber and was found to be 75 times stronger than an electrostatic control.

Antibody attachment to the microbubbles via a streptavidin-biotin bridge has been optimised with 91.20(±0.02)% of the microbubbles having antibodies attached. A flow system has also been developed for assessment of microbubble attachment to cells under very low WSS.

Microbubbles have been successfully targeted to SK-Hep-1 cells using acoustic radiation force. In addition attachment of the microbubbles to SK-Hep-1 cells has been observed under 0.03Pa WSS in the Ibidi μ-slides.

Chapter 1 The Cardiovascular System and Coronary Heart Disease

Coronary Heart Disease (CHD), also known as coronary artery disease, ischemic heart disease or atherosclerotic heart disease, is a type of cardiovascular disease (CVD) which affects the heart and blood vessels of the cardiovascular system. It is the result of a build up of atheromatous plaque within the arteries of the heart. With CHD causing over 100,000 deaths each year, it is the most common cause of mortality in the UK (BHF 2007).

1.1. The Cardiovascular System

The Cardiovascular system is the body's transport system and has the following functions (Levick 2003):

- To distribute nutrients and oxygen and remove waste from around the body according to requirements.
- To facilitate temperature regulation.
- To distribute hormones as required.
- To produce penile erection during reproduction.

The cardiovascular system achieves this by means of a network of arteries, veins and capillaries. These vessels transport blood to the various organs of the body whereby the oxygen or nutrients required are able to diffuse into the cells of the organ.

A schematic of the cardiovascular circulation can be seen in Figure 1-1. Blood is pumped from the right ventricle (RV) to the lungs via the pulmonary artery where it is oxygenated and is returned to the left atrium (LA) by the pulmonary veins, completing the short pulmonary circulation. The LA then contracts and forces blood into the left ventricle (LV), followed by a ventricular contraction increasing pressure in the LV from 0 to 120mmHg (Arronson et al. 2004), and the blood is forced into the aorta travelling down the pressure gradient.

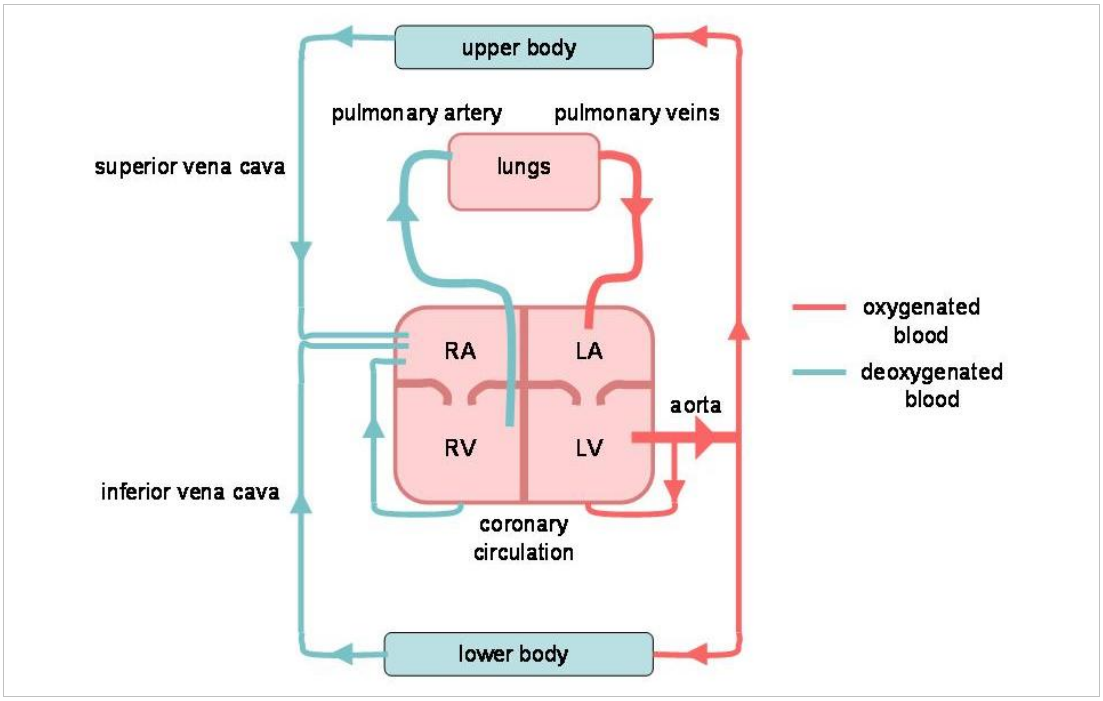

Figure 1-1: Cardiovascular Circulation.

The first arterial branch provides the coronary circulation with oxygenated blood, the aorta then splits into two, the first branch transports blood to the upper body, brain and lungs and the second transports blood to the lower body, abdominal cavity and

digestive tract where nutrients are collected. Blood from the upper body is then returned to the right atrium (RA) of the heart via the superior vena cava and blood from the lower body returned by the inferior vena cava. The RA then contracts forcing blood into the RV where it returns to the pulmonary circulation.

1.1.1. The Heart and Blood Vessels

The heart is a muscular pump which drives blood around the body by way of blood vessels. The blood vessels are made up of arteries, which transport blood away from the heart and veins which transport blood back to the heart, these vessels are linked by smaller arteries called arterioles, capillaries and venules (small veins) as illustrated in Figure 1-2. The structure of both veins and arteries can be seen in Figure 1-3 and consists of the following layers:

Tunica Intima

Sheet of flattened endothelial cells connected to the media by a thin layer of connective tissue and elastin. A smooth layer to aid blood flow and act as a barrier to blood plasma.

Tunica Media

Smooth muscle cells containing collagen and elastin. This layer is thicker in the arteries to enable the vessels to withstand higher pressures.

Elastin

A thin layer of elastin marks the boundary of the media and externa layers.

Tunica Externa

A sheath of connective tissue which tethers the vessel to surrounding tissue.

Valve (Veins only)

The valve is present to prevent blood at low pressures from flowing in the wrong direction along the vessel. It is not required in the arteries due to the high pressure at

which the blood is propelled along by the heart, however, by the time the blood reaches the veins this pressure has dropped to approximately 15mmHg.

Vessel	Wall thickness	Lumen diameter
Aorta	2 mm	25 mm
Muscular Conduit Artery	1 mm	4 mm
Arteriole	30 µm	30 µm
Capillary	0.5 µm	6 µm
Venule	3 µm	30 µm
Vein	0.5 mm	5 mm
Vena Cava	1.5 mm	30 mm

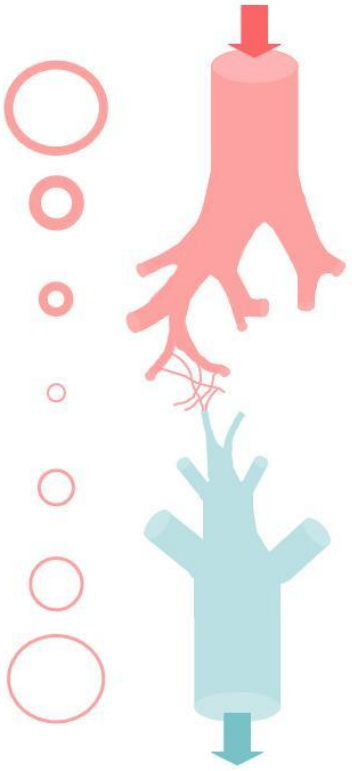

Figure 1-2: Blood vessels, wall thickness and lumen diameter, data provided by Arronson et al. (2004) and Levick (2003).

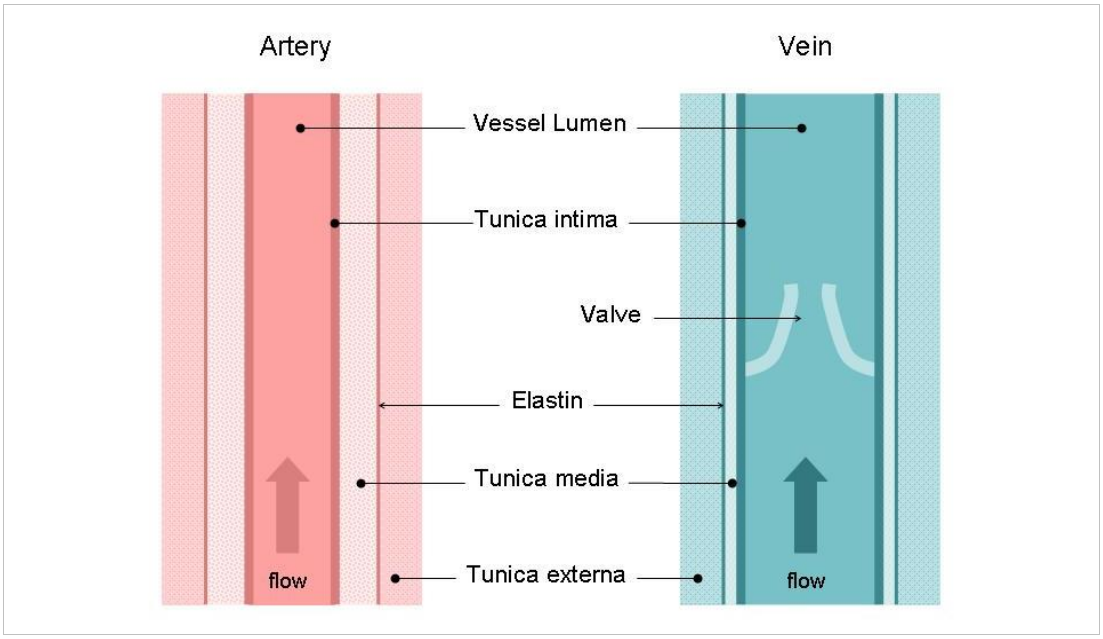

Figure 1-3: Structure of arteries and veins

1.1.2. Coronary Circulation

Due to the muscular nature of the heart it requires a continuous blood supply, carrying the necessary oxygen and nutrients, to enable it to propel blood around the body. The coronary circulation is a network of arteries which fulfils this requirement; the coronary circulation can be seen in Figure 1-4. The left and right coronary arteries originate from the aortic sinus at the base of the aorta. The right coronary artery is 120-140mm in length and supplies the ventricles and right atrium in addition to the sinoatrial node via the posterior descending and right marginal branches. The left coronary artery supplies the ventricles and left atrium via the circumflex (60-80mm in length), left marginal and anterior descending arteries (100-130mm in length). The right and left coronary and marginal arteries are linked by anastomoses; however, these are not wide enough to maintain the necessary blood flow to the heart if one side of the coronary circulation is blocked. In order for the heart to function correctly it is therefore vital that this supply is not occluded.

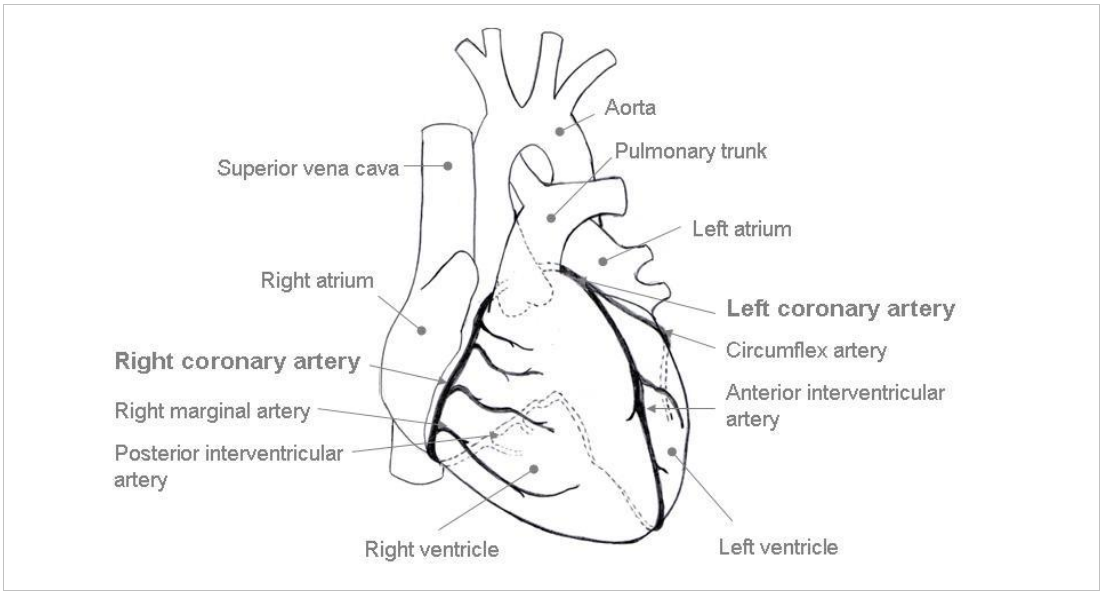

Figure 1-4: The coronary circulation

1.2. Cardiovascular Disease

A cardiovascular disease is any type of disease which affects either the heart, or blood vessels. There are a large number of such diseases as listed in Table 1-1 below, these diseases are not independent and often occur simultaneously and as a result of one another. However, the most common cardiovascular disease is coronary heart disease and so often the description is used to describe atheromatous plaque build-up in the arteries.

Type of disease	Brief description
Aneurysms	Dilation of blood vessels.
Angina	Chest pain, often as a result of other disease.
Arrhythmia	Abnormal electrical activity in the heart resulting in irregular or distorted heart beat.
Atherosclerosis	Build up of atheromatous plaque in arterial blood vessels.
Cardiomyopathy	Disease of the myocardium (heart muscle).
Cerebrovascular Accident (Stroke)	Brain injury resulting from blood supply to brain being cut off.
Cerebrovascular Disease	Disease of blood vessels supplying the brain.
Congenital Heart Disease	Structural heart defects in infants.
Congestive Heart Failure	Structural or functional disorder impairing ability of heart to maintain normal function.
Myocarditis	Inflammation of myocardium.
Valve Disease	Failure of coronary or venous valves.
Coronary Artery Disease	Build up of atheromatous plaque in coronary arteries.
Dilated Cardiomyopathy	Weakened and enlarged heart.
Diastolic Dysfunction	Impaired heart relaxation.
Endocarditis	Inflammation of inner layer of the heart.
Hypertension	High blood pressure.
Hypertrophic Cardiomyopathy	Thickening of the myocardium.
Mitral Valve Prolapse	Abnormally thick mitral valve.
Myocardial Infarction	Heart attack.
Venous Thromboembolism	An embolism caused by segregation of a thrombus.

Table 1-1: Cardiovascular Diseases, highlighted sections are those of interest in this study.

1.2.1. Atherosclerosis

As explained previously, CHD involves the build up of atheromatous plaque within the arteries of the coronary circulation. This is a disease known as atherosclerosis. Atherosclerosis can affect any arterial blood vessels and is caused by the formation of plaques within the arterial walls, resulting in hardening of the arteries. Plaque formation is the result of a chronic inflammatory response(Blasi 2008; Maseri and Fuster 2003).

Atherogenesis

Development of an atherosclerotic plaque begins during childhood as lipids accumulate in the tunica intima. Cholesterol and other lipids are transported around the body by lipoproteins. The genesis of an atheroma is believed to be due to the oxidation of low density lipoproteins (LDLs) (Arronson et al. 2004; Kunitomo 2007). The presence of LDLs increases with the intake of cholesterol.

As the presence of LDL in the blood stream is increased some of the LDL is able to pass through the endothelial monolayer of the arterial wall, here it reacts with oxygen free radicals to form oxidized-LDL. Arronson (Arronson et al. 2004) suggests that the oxidized-LDL then goes on to cause or exacerbate endothelial cell damage and also enhance expression of adhesion molecules on the endothelial surface, prompting the inflammatory response (Figure 1-5a). Circulating monocytes within the blood stream are attracted to the adhesion molecules and taken into the tunica intima, where they mature into macrophages. Although uptake of LDL is usually highly regulated, in the presence of oxidized LDL the macrophages are unable to control uptake and become foam cells which form fatty streaks along the arterial wall, as illustrated in Figure 1-5b.

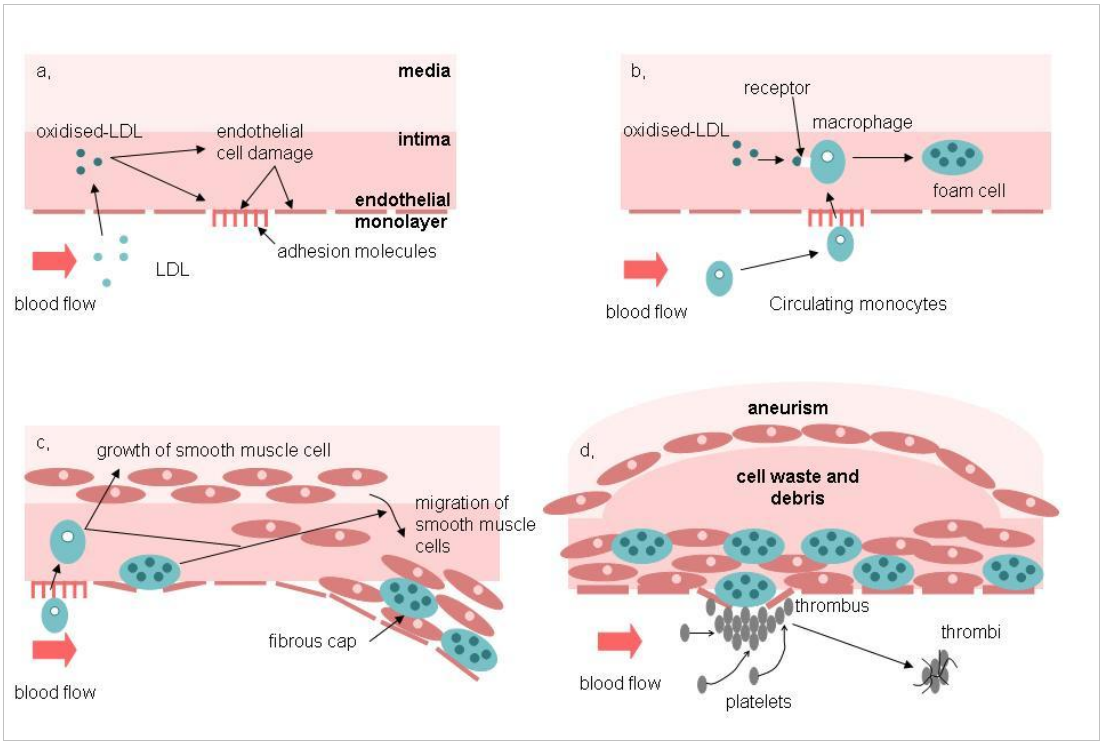

Figure 1-5: Diagram illustrating atherogenesis: a, absorption of LDL by cell wall; b, uptake of LDL by macrophages and formation of foam cells; c, growth and migration of smooth muscle cells; d, plaque forming an aneurism and rupture of plaque wall resulting in thrombus formation.

The collective effect of the damaged endothelial layer and uptake of oxidized-LDL by macrophages contribute to growth of the smooth muscle cells within the tunica media which then migrate into the tunica intima forming a fibrous cap (Figure 1-5c and d). As the foam cells are produced and die, the area beneath the fibrous cap fills with cellular debris and lipids causing the cell wall to distort (see Figure 1-5d). In some cases the plaque will partially occlude the vessel lumen, creating a stenosis; alternatively the wall will distort outwards causing a bulge in the vessel at this point. This is known as outward remodelling. Ultimately this can lead to the formation of an aneurism.

Stable and Unstable plaque

Two types of plaque can be formed as a result of atherogenesis; stable plaque or vulnerable (unstable) plaque. Stable plaque is characterised by regular and

predictable angina pectoris (severe chest pain), particularly when the victim is undergoing strenuous exercise, this is due to a permanent narrowing of the lumen resulting from a build up of plaque. When at rest the artery is able to provide the heart with all the blood it requires, however, when undergoing intense exercise the heart requires a greater amount of blood which, if slightly occluded, the artery is unable to provide, resulting in angina pectoris (pain). With time, stable plaque can build up and eventually block off an artery leading to myocardial infarction, however this only accounts for about 30% of heart attacks (Cooley 1996).

Vulnerable plaque is thought to be the leading cause of acute coronary syndromes (ACS) (Maseri and Fuster 2003), as a result a vast amount of research is being carried out into the causes and identifying factors of vulnerable plaque in the fight against CHD (DeMaria et al. 2006; Dickson and Gotlieb 2003; Fichtlscherer et al. 2004; Galonska et al. 2008; Kips et al. 2008; Leber et al. 2008; Lind 2003; Maseri and Fuster 2003). Maseri et al. (Maseri and Fuster 2003) specifies the identifying markers of vulnerable plaque as follows:

- Complex coronary stenoses
- Coronary plaque fissures
- Fresh thrombi
- Plaque inflammation

It is believed that plaque instability is a consequence of a lipid-rich plaque with a thin fibrous cap, whilst a stable plaque will have a thick fibrous cap. Dickson et al. (Dickson and Gotlieb 2003) suggests that there are three steps to the formation of a vulnerable plaque:

- Transformation of a stable plaque into a vulnerable plaque, whereby there is a decrease in the smooth muscle cells of the fibrous cap resulting in thinning.
- Destabilization of the vulnerable plaque, caused by fissures in the fibrous cap, further thinning and inflammation.
- Complications following destabilization of the plaque resulting in plaque rupture.

When a vulnerable plaque ruptures platelets within the blood begin to clot around the 'wound', a typical immune response. If the blood clot (thrombus) continues to increase in size this can result in occlusion of the vessel, causing myocardial ischemia or infarction. In some instances the thrombus may not occlude the vessel but under the pressure of the blood flow a small section may break off and travel along the vessel to a narrower part where it can occlude the artery causing an embolism, this can also result in myocardial infarction and sudden death.

1.2.2. Symptoms and Diagnosis

Atherosclerosis is asymptotic during the early phases and is therefore not detected until symptoms occur later in the disease or signs of atherosclerosis are found during routine examinations. The disease is often not picked up until a more serious condition is observed, such as angina or a myocardial infarction. In the latter case this can sometimes result in death. Kips (Kips et al. 2008) has described a variety of non-invasive and invasive methods of assessing the presence of vulnerable plaque.

Many of the imaging modalities are designed to assess the degree of stenosis within an artery, however there is extensive research confirming that most acute myocardial infarctions are a result of non-stenotic plaques (Falk et al. 1995; Schroeder and Falk 1995; Virmani et al. 2000). As the plaque builds up the vessel responds by increasing the cross-sectional area retaining a large lumen and the sufferer therefore will not suffer from angina pectoris, meaning that vulnerable coronary plaques are largely asymptotic (Crouse et al. 1994; Glagov et al. 1987).

Intravascular ultrasound (IVUS) and angiography, two invasive techniques which are in current clinical practice, are used to monitor the disease. Some techniques derived from these imaging modalities are currently being researched and are described below. In addition ongoing research is being done into non-invasive techniques.

Invasive techniques

Angiography is a contrast x-ray technique in which a radio-opaque iodine dye is injected into the blood vessels and thereby highlights the vessels in an x-ray image.

This technique has been used for more than fifty years (Rudd et al. 2005) in the assessment of CHD and is a high resolution technique. It is an effective method of identifying stenosis within the arteries. With over 300,000 angiography procedures performed annually in the UK (Hart and Wall 2002) it is currently the 'gold standard' in CHD assessment. However the limitations of angiography include the inability to identify non-stenotic plaques, and determining stability of identified plaques. In addition the technique utilises ionising radiation.

Intravascular ultrasound with frequencies of 20-50MHz is another popular imaging modality used to detect arteriosclerosis (DeMaria et al. 2006). It involves an ultrasound transducer mounted onto a coronary catheter which is inserted into the coronary arteries and forms a cross-sectional image of the artery. The higher the emitted ultrasound frequency the higher the axial resolution of the image, axial resolutions range from 200-100μm. IVUS is discussed in more detail in Chapter 5. IVUS provides a real-time imaging technique capable of identifying calcified from fibrous plaques, however soft plaques and plaques with a thick fibrous cap produce a similar backscatter and therefore it is not possible to distinguish between the two. There are currently many new techniques emerging which utilise the benefits of IVUS in identifying soft plaques.

Palpography and elastography are similar techniques utilising IVUS. The techniques involve measuring the stress and strain of the arterial wall resulting in a strain diagram such as the one that can be seen in Figure 1-6. This is achieved by studying and processing the ultrasound signals from the vessel under varying pressures. Because different materials deform differently under mechanical pressure they will have different strain values and will therefore be identifiable on a strain diagram. Recent studies have shown that soft plaques are associated with higher strain values than fibrous plaques and these techniques would therefore be able to distinguish between stable and unstable plaques (Schaar et al. 2006). Palpography produces a strain diagram of the superficial wall, whilst elastography produces an image of the whole wall thickness. This technique is currently under investigation (Schaar et al. 2006). The quality and value of these techniques are dependent upon the quality of

the ultrasound used and arrythmias and motion artefacts are both limitations of the modality.

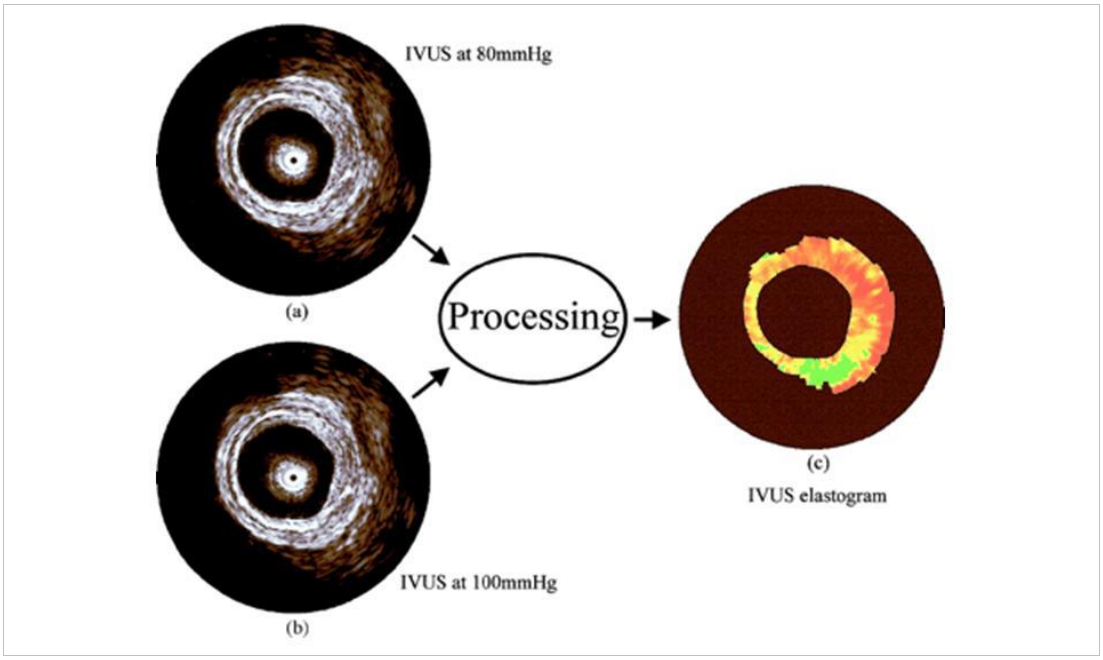

Figure 1-6: An elastography strain diagram (permission granted for reproduction (Biondi-Zoccai 2006)).

IVUS radio-frequency (RF) assessment involves the capture and fast Fourier transform (FFT) of the RF data from an IVUS examination. This provides more detailed information than the IVUS image alone and the potential application of this technique to the determination of plaque stability is currently under investigation (DeMaria et al. 2006).

Contrast IVUS is another IVUS technique which is currently being developed as a method to identify vulnerable plaques at the University of Edinburgh (Moran et al. 2003b; Moran et al. 2006). This technique will involve the injection into the blood stream of a high-frequency, microbubble, ultrasound contrast agent targeted to inflammation receptors associated with vulnerable plaques, once attached to the plaques the contrast agent is highly echogenic and will therefore enable identification of the extent of vulnerable plaques within the coronary arteries. This technique is the focus of this thesis and the benefits of contrast IVUS would include the ease of

identifying vulnerable plaques, real-time imaging and cost effectiveness of ultrasound imaging. The technique however is invasive and therefore carries the associated risks, in addition adverse reactions to ultrasound contrast agents have been documented (Dijkmans et al. 2005).

In addition a variety of optical techniques including angioscopy (Thieme et al. 1996), optical coherence tomography (OCT) (Yabushita et al. 2002; Zimarino et al. 2007) and spectroscopy (Pedro R. Moreno 2003; Wang et al. 2002) are currently undergoing clinical trials. Angioscopy uses a mini-camera which is inserted into the coronary arteries by way of a catheter, when imaged; a lipid-rich artery will glisten yellow whilst a healthy artery will glisten white (Kips et al. 2008; Ueda et al. 2003), the ability to distinguish between stable and vulnerable plaque is however limited. OCT uses infrared light to obtain images at the microscopic level, it is an incredibly high resolution technique (4-20μm) and is capable of determining the thickness of the fibrous cap, however the technique is high-risk as the blood must be rapidly flushed through the vessels which can result in endothelial damage and induced ischemia. Spectroscopy depends upon the Raman-effect in which the wavelength of backscatter light is dependent upon the molecule reflecting the light, it is therefore possible to determine the chemical composition of the plaque. However spectroscopy has a penetration depth less than 1.5mm and must also be used in conjunction with another imaging technique such as IVUS in order to obtain structural information about the plaque.

Non-invasive techniques

Non-invasive ultrasound of frequencies between 3.5-10MHz can be used in the assessment of plaque and is commonly used in studies of the carotid arteries, however coronary arterial imaging still poses many problems (DeMaria et al. 2006).

Single photon emission tomography (SPECT) and Positron emission tomography (PET) are nuclear imaging techniques which involve the introduction of a radioisotope to the body, if the radioisotope can be conjugated to a compound involved in the atherosclerotic process then it will become possible to identify the areas of high plaque density. PET involves the introduction of a positron emitting

radioactive tracer compound to the body, the emitted positrons annihilate with electrons within the body producing two γ-photons at 180° to each other. A surrounding scintillator detector will be set to coincidence detection such that when two γ-photons are detected at the same time a line between the two detectors will identify where the annihilation occurred and therefore the location of uptake of the tracer. SPECT involves an isotope emitting gamma radiation which is identified by a scanner in a similar manner to PET. SPECT and PET are both low resolution techniques (Lodge et al. 2005) relative to ultrasound and angiography as identified in Table 1-2, in addition these techniques involve the use of highly ionising radiation and therefore continue to remain in the research domain.

Multi-slice computed tomography (CT) is a rotational X-ray technique in which the source and detector rotate around the patient to build up a 2 dimensional cross-sectional image. It is 17% faster than single slice CT (Pawelski 2005) and therefore reduces the amount of motion artefacts; however it also entails higher radiation doses. Multi-slice CT might be able to distinguish between fibrous and lipid-rich plaques (Galonska et al. 2008; Leber et al. 2008).

Magnetic resonance imaging (MRI) has previously been investigated as a method to assess myocardial ischemia and viability using intracellular sodium MRI (Jansen et al. 2006). In addition MRI is a technique which shows significant promise in the detection of atherosclerotic plaque. Magnetic resonance angiography is useful in assessing the arterial lumen and high-resolution MRI can help to identify plaque components (Chun Yuan 2004; Hyafil and Fayad 2007). The disadvantage of MRI is the cost and examination time, the spatial resolution of MRI is improved with longer examination times. There is also research being done into the use of MRI contrast agents (Frías et al. 2008).

The advantages and disadvantages and stages of research for each imaging technique described above have been summarised in Table 1-2.

Imaging modality	Resolution (µm)		Penetration	Advantages	Disadvantages	Status
	Spectral	Axial				
IVUS	250	100-200	Total	Low cost Portable Good resolution	Invasive Unable to identify vulnerable plaques	Clinical use
IVUS RF data analysis	40	100	Total	Low cost Portable Good resolution	Invasive	Preclinical
Elastography/ palpography	100	200	Total	Low cost Portable	Invasive	Preclinical
Contrast IVUS	100	100	Total	Low cost Portable Good resolution	Invasive	Preclinical
Angiography	10	n/a	Poor	High resolution Able to image large areas	Invasive, Ionising radiation Cannot observe non-stenotic plaques.	Clinical use
OCT	4-20	4-20	1-2mm	High resolution	High-risk	Clinical studies
Spectroscopy	n/a	n/a	1.5mm	Identification of lipid rich areas	Invasive High risk	Preclinical
Ultrasound	600	400	n/a	Non-invasive	Low-resolution	Clinical use
Multi-slice CT	400	400	n/a	Non-invasive High accuracy	Low-resolution Ionising radiation	Clinical studies
MRI	40-400	3000	n/a	Non-invasive	Low-resolution	Clinical studies
SPECT	10,000-14,000	n/a	n/a	Identification of vulnerable plaques possible	Low-resolution Ionising radiation	Preclinical
PET	5000-7000	n/a	n/a	Superior resolution to SPECT	Low-resolution Ionising raditation	Preclinical

Table 1-2: Imaging modalities for assessment of atherosclerotic plaque (Kips et al. 2008)

1.2.3. Treatment

Treatment of atherosclerosis is either via lifestyle changes or pharmaceuticals, in the more advanced cases surgical intervention is required. There are a variety of drugs which are currently in use globally aimed at thinning the blood or interrupting the plaque formation. Surgical intervention can be either an angioplasty procedure, which expands narrowed vessels, or bypass surgery to create an increased blood supply to affected areas.

Asymptotic patients are often treated using aspirin or other drugs which prevent plaque rupture (Wald and Law 2003). However treatment of such patients is controversial and currently much emphasis is on lifestyle changes to prevent development or worsening of the disease.

1.2.4. Causes

There are many causes of atherosclerosis, the most well known are illustrated in Figure 1-7. These include smoking, diabetes and high blood pressure. Some aspects are within a person's control, such as the level of exercise, smoking and diet choices. However, some of the factors are independent of personal choice such as gender, age, or a genetic predisposition to the disease.

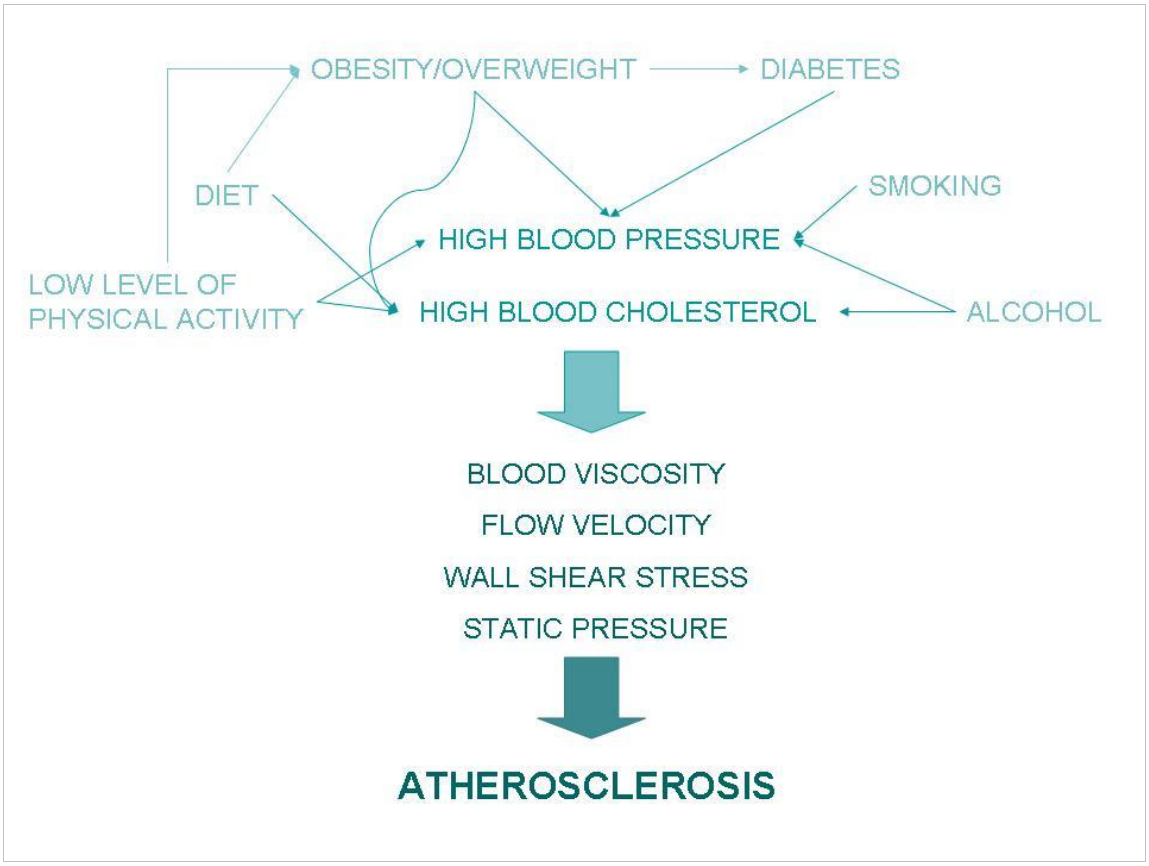

Figure 1-7: Flow diagram describing direct and indirect causes of atherosclerosis and relations between them.

As mentioned, age is a determining factor in the development of atherosclerosis as the fatty deposits build up over time, eventually forming atherosclerotic plaque. However, by being aware of the environmental factors which exacerbate and speed up the development of plaque there is control over development and progression of the disease.

Blood viscosity is increased by a number of the known causes of atherosclerosis; age, smoking and obesity. It is also known that the viscosity of blood is directly related to the hematocrit of the blood see Figure 1-8. Hematocrit is a measure of the percentage of red blood cells within a sample of blood. A study by De Backer et al. (De Backer et al.

2002) suggested that blood viscosity has no direct correlation to CAD however, as blood viscosity is a measure of the shear stress between layers of a fluid it can therefore be surmised that blood viscosity will have a direct effect on the shear stress which is related to causes of atherosclerosis.

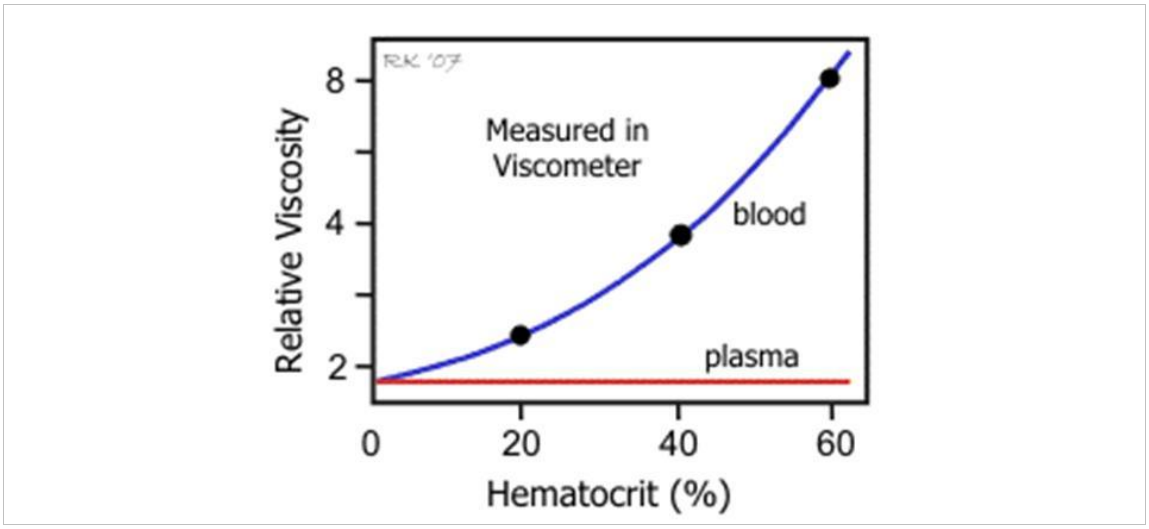

Figure 1-8: Relationship of hematocrit and blood viscosity (permission given for reproduction (Klabunde 2005))

It has been documented that a laminar, constant shear stress is in fact atheroprotective and therefore a constant high shear stress is beneficial in the prevention of atheromas. However, when low or oscillatory shear stress occur this can lead to the development of atherosclerotic plaques (Cunningham and Gotlieb 2004). The development of atherosclerotic plaques at areas of low or non-linear shear stress is due to damage to the endothelial cell wall, resulting in the arrival of inflammatory markers which instigate the development of plaque.

Similarly, flow velocity, which is directly proportional to the wall shear stress can also cause an increase in atherogenesis if the flow is non-linear.

The main factors relating to the formation of atherosclerotic plaques are the endothelial damage caused by smoking, high blood pressure and low or oscillatory wall shear stress and the quantity of cholesterol and LDLs in the diet.

1.3. Summary

Coronary heart disease is one of the major causes of mortality in the western world and despite a greater understanding of the disease morphology CHD is still the number one killer in the UK. Prevention and treatment of the disease is possible however, due to its asymptotic nature, prediction of myocardial events is not always possible. A number of researchers are investigating different methods of identifying the extent of the disease in individuals. IVUS is already in routine use for the assessment of CHD although it is not yet able to distinguish between stable and vulnerable plaques.

It is evident that a method of identifying vulnerable plaque in the coronary arteries is required in order to assess the risk of a patient with CHD suffering a myocardial infarction. Targeted UCAs are a promising solution to this problem. Edinburgh University is currently developing a targeted microbubble UCA for use with high-frequency IVUS. Although the development is still in its infancy the UCA will be targeted to inflammation markers exhibited by vulnerable plaques within the coronary arteries.

Chapter 2 Ultrasound Contrast Agents

Ultrasound has become increasingly popular as an imaging modality in the past few decades with over 20% of medical imaging in the UK being ultrasound examinations (Department_of_Health 2008) as illustrated in Figure 2-1. Ultrasound is widely used in cardiology, obstetrics, gynaecology and abdominal imaging. Another clinical use of ultrasound includes Doppler ultrasound which provides a measure of blood flow using the Doppler shift. More recent developments in ultrasound have enabled 3-D or 4-D ultrasound scans which are popular in obstetrics fields.

Superior transducer materials and enhanced signal processing techniques (Ali et al. 2008) have resulted in improved image resolution, signal to noise ratio and sensitivity of ultrasound scanners.

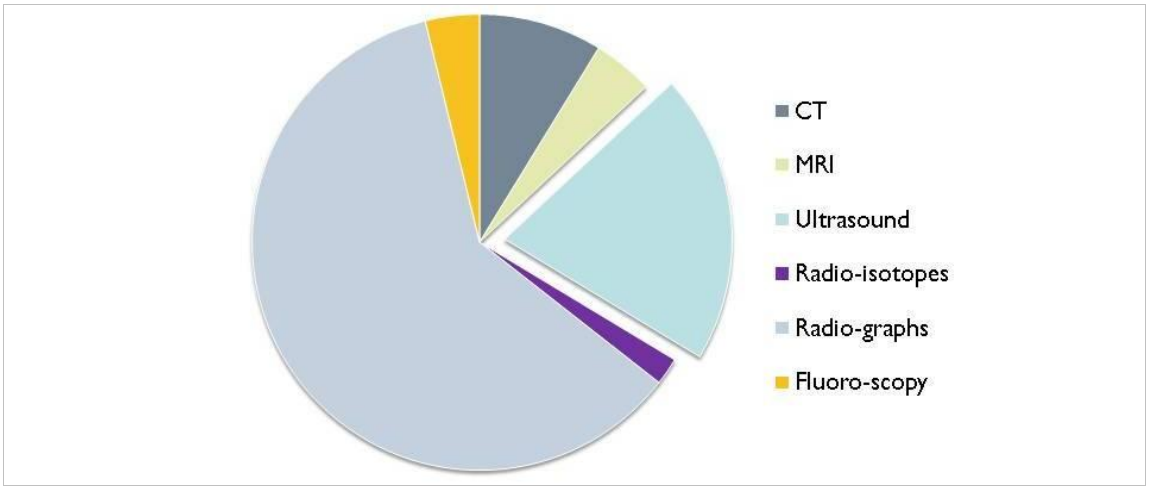

Figure 2-1: Number of diagnostic imaging examinations by modality.

The introduction of Ultrasound Contrast Agents (UCAs) has also improved ultrasound both diagnostically and therapeutically. The advantages of ultrasound over its competitors are that it is the most cost-effective modality to run (Bierig and Jones 2009; Picano 2005); ultrasound scanners are also compact and can therefore be used at a patient's bedside. In addition it is a real-time method of producing images and does not utilize ionizing radiation. The more recent development of UCAs has extended the capability of ultrasound, allowing for assessment of perfusion, in addition to furthering its use both diagnostically and therapeutically, as described throughout this chapter. The predominant clinical use of UCAs is in echocardiography and UCAs are licensed for both ventricular opacification and endocardial border delineation (Harvey et al. 2000) which can help to identify abnormalities in the heart wall. In addition UCAs are used as tracers in the study of cirrohsis of the liver (Cosgrove 2006).

The use of contrast agents in ultrasound was first approached in the 1960s when cardiologist Charles Joyner noticed transient echoes occurring after injections of indocyanine green through a catheter in the left ventricle (Gramiak and Shah 1968; Harvey et al. 2000). Joyner put the source of these echoes down to small air bubbles formed on the catheter tip. Although initially after their discovery there was no further

investigation or development of UCAs, in the past three decades the field has evolved dramatically.

2.1. Ultrasound Contrast Agents

An ultrasound contrast agent has been described as;

"…an exogenous substance that can be administered either in the blood pool or in a cavity to enhance ultrasonic signals…"

(Correas et al. 2001).

Ideally a UCA should be non-toxic and capable of producing an enhancement to the ultrasound signal. Additionally it should be capable of crossing the pulmonary capillary bed and stable for the duration of the investigation, it must also be safe for intravenous injection and introduction into other body cavities.

Ophir and Parker (Ophir and Parker 1989) described the five different classes of ultrasound contrast agents as; colloidal suspensions, emulsions, aqueous solutions and free and encapsulated gas bubbles. It is the latter two which form the majority of commercial contrast agents and are the focus of most research today, they also provide the best enhancement with current imaging methods which utilize distinct properties of the microbubbles and are described in Section 2.2. The evolution of microbubble contrast agents can be found in Table 2-1, and is described below.

Agent	Produced by	Gas	Shell/stabilizing agent	Uses	Microbubble Diameter	Concentration	Imaging modality	Availability/ Production
First Generation Contrast Agents: (non transpulmonary)								
Agitated Saline		air	no shell					
Echovist®	Schering, Berlin	air	Galactose	Tubal Patency	99% < 12µm; mean 3µm	200, 300 or 400mg/ml	Doppler echocardiography	EU and USA approved
Second Generation Contrast Agents: (transpulmonary blood pool agents)								
Levovist®	Schering, Berlin	air	palmitic acid	Blood pool enhancer	99% < 10µm; mean 3µm	200, 300 or 400mg/ml	Colour/power doppler	EU approved
Albunex®	Mallinkrodt	air	sonicated albumin	Ventricular opacification	95% < 10µm; mean 3.8µm	3-5 microsperes/ml	B-mode/ colour doppler	No longer available
Third Generation Contrast Agents: (transpulmonary, blood pool/organ specific agents)								
Optison™ (FS069)	GE Healthcare	octafluoropropane	sonicated albumin	Cardiac wall motion	93% < 10µm			EU and USA approved
Echogen®	Sonus/Abbott	dodecafluoropentane	liquid droplet surfactant	left ventricle opacification		Various		
Sonovue™ (BR1)	Bracco Diagnostics Inc	sulphur hexafluoride	phospholipids	Heart chambers	99% < 11µm; mean 2-3µm	2-10µl/ml	Microbubble specific methods	EU approved
Definity®/Luminity	Lantheus Medical Inc	octafluoropropane	phospholipids	Left ventricle opacification	98% < 10µm			EU and USA approved
PESDA	University of Nebraska	perfluorobutane	sonicated albumin	Blood pool agent	4.7µm			Self-made
Quantison™	Andaris Ltd	air	dried albumin	CAD	mean 3.2µm			
Imavist®/Imagent® (AF0150)	Imcor Pharmeceuticals Inc	perfluorohexane/ nitrogen	lipids	Cardiology, prostate and liver	99% < 10µm; mean 6µm	5x10^8 microbubbles/ml.	B-mode/ colour doppler/harmonic	USA approved
Sonavist®	Schering	air	cyanoacrylate shell	Liver studies	mean 1µm		Microbubble specific methods	
Sonazoid™ (NC100100)	GE Healthcare	perfluorobutane	phospholipids	Liver-specific	2.6µm 99.9% < 7µm			Japan approved
BR14	Bracco	perfluorobutane	phospholipids	Liver-specific	mean 3µm 95% < 10µm		Non-linear imaging methods	In development
biShpere™	POINT Biomedical	air	biodegradeable polymers	Renal studies				In development
CARDIOsphere™ (PB127)	POINT Biomedical	nitrogen	Polyactide/ albumin	Myocardial perfusion	3µm		Gated harmonic power doppler	In development
Imagify™ (AI700)	Acusphere Inc	Decafluorobutane	Poly-l-lactide-co-glycolide		Mean 2µm			Awaiting approval

Table 2-1:Current and past commercially available and developing microbubble contrast agents 2008 (Harvey et al. 2000)

Ultrasound contrast agents are generally classified into first generation, second generation and third generation contrast agents, dependent upon the gas contained and their stability in the blood flow. However not all authors use the same classifications (Harvey et al. 2000; Harvey et al. 2002; Miller and Nanda 2004). Agitated saline, the first widely used microbubble contrast agent is generally considered to be the earliest first generation agent. The first commercial microbubble contrast agent was Echovist (Schering, Berlin), a galactose based first generation agent. The air filled microbubbles originate from the water soluble galactose particles and are then released in suspension. Echovist was first marketed in 1991 and mostly used to assess fallopian tubal patency during infertility investigations (Calliada et al. 1998; Harvey et al. 2000). Echovist, due to the advent of more stable agents, is no longer manufactured (NHS 2007).

The variation in microbubble classification begins with the definition of a second generation agent. Whilst Miller et al. (Miller and Nanda 2004) describe second generation agents as containing low solubility gases, Harvey et al. (Harvey et al. 2000; Harvey et al. 2002) consider second generation agents to be air filled microbubbles with a stabilising shell. For the purpose of this thesis the author will follow the latter convention.

By the latter convention, Levovist, Echovist's successor, is a second generation agent. This agent is also a galactose based contrast agent but with the addition of palmitic acid which acted as a shell stabilizer making the agent more stable. Due to its improved stability, Levovist is widely used as a blood pool enhancer as it is able to withstand the higher pressures of the blood pool.

Another second generation agent is Albunex (Mallinckrodt), these microbubbles are formed by sonication of albumin, and are air filled bubbles with a thin albumin shell, they have a mean diameter of 4µm (Cosgrove 1997). Albunex was the first approved

UCA in the US for cardiac applications. The bubbles have a short half-life of less that one minute and are very sensitive to pressure changes (Correas et al. 2001). Albunex microbubbles are however no longer in production due to the introduction of more stable third generation contrast agents (Miller and Nanda 2004).

Third generation contrast agents involve the use of low solubility gases, such as perfluorocarbons encapsulated inside either lipid or protein shells (although some agents defined as third generation contain air encapsulated by lipid or protein shells). The low solubility gas takes longer to diffuse out of the shell than air and therefore increases the stability of the microbubble. There are two main materials used to provide a stabilizing shell to these microbubbles, these are phospholipids and sonicated albumin. Some of these third generation agents are detailed in Table 2-1.

2.1.1. Producing microbubbles

Methods of producing microbubble contrast agents include rapid agitation, stirring, sonication and mechanical techniques. Sonication involves the application of sound waves in order to produce microbubbles; two contrast agents produced by sonication of human albumin include Albunex and PESDA (Perfluorocarbon-exposed sonicated dextrose albumin). The latter is a third generation research agent and is formed by the sonication of albumin in the presence of a perfluorocarbon.

Edinburgh University in-house microbubbles are a lipid-shelled contrast agent. These microbubbles are produced by stirring the lipids during and after heating. Due to the hydrophobic nature of the lipid tails (as illustrated in Figure 2-2a), when in the presence of a water solution, the tails will gather together to form small bubbles of air (micelles illustrated in Figure 2-2c) with the hydrophilic head sections of the lipids on the outer side. Alternatively the hydrophobic tail sections may gather together in a lipid bi-layer as illustrated in Figure 2-2b. The lipid bi-layer will then form a liposome (Figure 2-2d). The in-house microbubbles have been shown to form multilamellar liposomes in which there are many lipid bi-layers within the liposome, a multilamellar liposome can be seen

in Figure 2-2e and an image of the in-house multilamellar liposomal microbubble in Figure 2-3. Stirring of the lipid suspension during the heating and cooling phases prevents larger bubbles from forming, thereby producing a suspension of microbubbles. Different methods have been investigated to increase the echogenicity of this agent and are discussed in depth in Chapter 3.

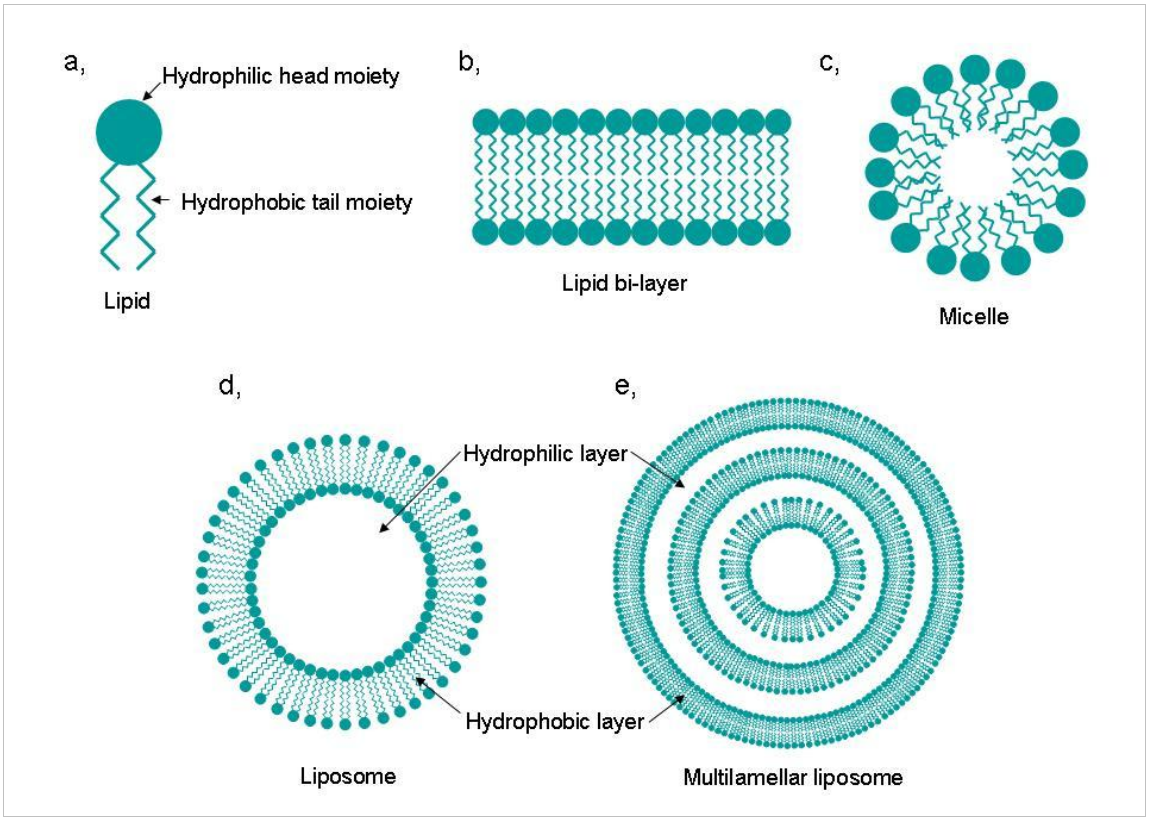

Figure 2-2: Illustrating the: a, lipid molecule and the respective hydrophobic and hydrophilic moieties; b, a planar lipid bi-layer; c, a micelle with all the hydrophobic tails gathered in the centre; d, a liposome formed with a lipid bi-layer; e, a multilamellar liposome.

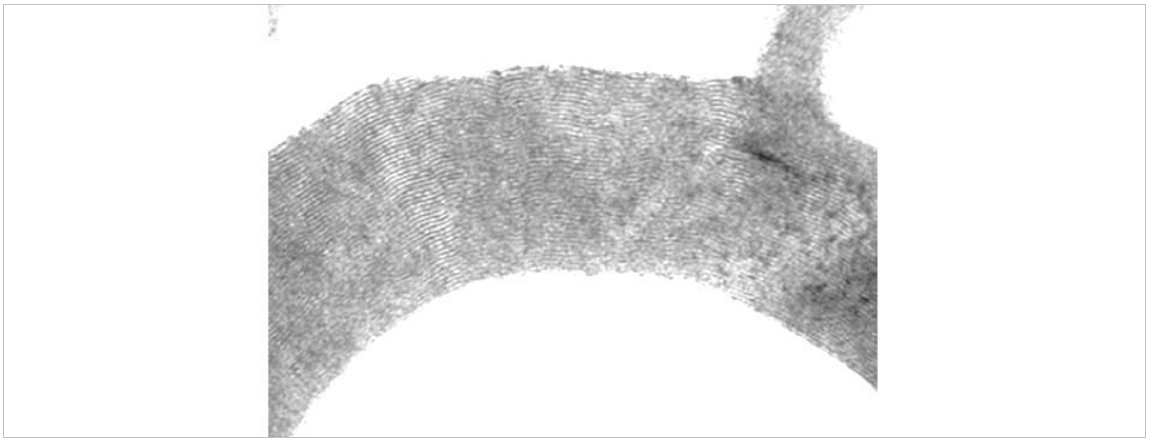

Figure 2-3: Electron micrograph image of the multilamellar in-house microbubble (courtesy of Professor J Ross).

The commercial agent Definity/Luminity™ is formed by rapid shaking of the agent in the presence of perfluoropropane (Harvey et al. 2000). This is achieved by use of the CapMix™ device which rapidly agitates small vials and is illustrated in Chapter 3. These microbubbles form in a similar manner to the in-house microbubble contrast agent.

Less common means of contrast microbubble manufacture includes mechanical formation of microbubbles through gas injection, or through a mechanical high shear valve (double syringe needle) (Klibanov et al. 2004; Schneider et al. 2006). Other methods proposed include micro-fluidization and milling (Cantrell 2000; Klibanov et al. 2004). However, the literature on these methods is limited.

2.1.2. Interactions of Microbubbles with Ultrasound

When an ultrasound field is incident on a microbubble, a range of interactions may occur including; reflection, refraction, scatter, absorption, oscillation or a combination of the five.

Reflection

Reflection occurs when an acoustic wave is incident upon a boundary between two mediums of different acoustic impedances. Acoustic impedance is characterised by the density and speed of sound through a medium as shown by Equation 2-1:

$$Z = \rho \times c$$

Equation 2-1: Acoustic impedance (Brown et al. 1999)

Where Z = acoustic impedance, ρ = density and c = speed of sound.

Since the acoustic pressures and velocities on either side of the boundary must be equal, yet must still satisfy the relationship in Equation 2-2 below, this gives rise to formation of a second sound wave in the first medium, this wave is known as the reflected wave which is illustrated in Figure 2-4.

$$Z = p \diagup u$$

Equation 2-2: Pressure-velocity relationship of acoustic impedance.

Where p is the acoustic pressure and u the velocity of sound through the medium.

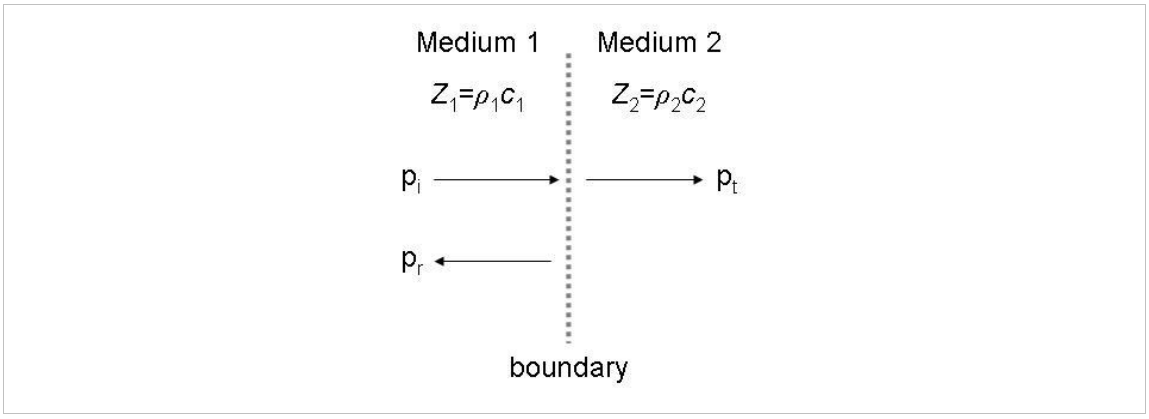

Figure 2-4: Reflection at a large boundary.

The greater the difference in acoustic impedance at a boundary, the greater the reflection observed. Gases have an acoustic impedance of approximately 1×10^{2}Pa·s·m-1 which is of an order of 10^{3} less than fluids (Baun 2009). The acoustic impedance of soft tissue is 1.63×10^{5}Pa·s·m^{-1} (Fields and Dunn 1973) (where 1Pa·s·m^{-1} is equal to 1rayl). The reflection coefficient (R) is a function of the acoustic impendence of the different mediums (Z_1 and Z_2) and gives the percentage reflection at a boundary. This is shown in Equation 2-3 (Larson et al. 2010).

$$R = \left(\frac{Z_2 - Z_1}{Z_2 + Z_1} \right)^2$$

Equation 2-3: Reflection Coefficient.

Refraction

Refraction occurs when a wave meets a boundary of two different refractive indexes. The degree of refraction is dependent upon the incident angle of the wave. Refraction in ultrasound imaging is a source of artefacts and is avoided and controlled where possible.

Scatter

Reflection, as described above occurs when the sound wave is incident on a boundary which is large relative to the acoustic wavelength. When the sound wave is incident upon a boundary that is about the same size as the wavelength diffuse reflection is observed, where the sound waves are reflected at a range of angles. If the boundary is very small relative to the wavelength Rayleigh scattering will take place (Brown et al. 1999; Hoskins et al. 2002) this results in the reflection of the sound waves uniformly in all directions. Red blood cells are 8-9μm (Brown et al. 1999) in diameter and therefore act as Rayleigh scatterers. In addition, mediums which are non-uniform in density and stiffness will also cause scattering. It is scatter that is predominantly observed in an ultrasound image. Since microbubbles are of a size similar to red blood cells (5-10 μm) they also result in Rayleigh scattering.

Absorption

When sound energy passes through a medium it can be absorbed by the molecules in that medium. This happens when an energy transfer occurs and the sound energy is transferred to thermal energy or kinetic energy when the molecule vibrates. Absorption of sound energy is dependent upon the frequency of the incident wave in addition to the properties of the material. Attenuation of the ultrasound beam is largely caused by absorption.

Oscillation

If the radius of the bubble is significantly smaller than the wavelength of the incident ultrasound wave the bubble will begin to oscillate (Frinking et al. 2000). The degree of this oscillation is dependent upon the microbubble characteristics, such as the shell properties, gas contained and size, and also on the frequency of the ultrasound and the incident acoustic pressure. It is a fortunate coincidence that microbubbles happen to resonate at the frequencies (1-40MHz) and pressures (0.45-3.80MPa (Barnett and Kossoff 1997)) utilized in diagnostic ultrasound (Cosgrove 2006; Harvey et al. 2000).

Oscillations occur because the gas inside the microbubble is more compressible than the surrounding tissues and fluid, as a result the microbubble is able to expand and contract on insonation, in sympathy with the ultrasound wave. The resonant frequency of the microbubble is inversely proportional to the radius and can be found in its simplified version using Equation 2-4 (Harvey et al. 2000; Ophir and Parker 1989):

$$f_0 = \frac{1}{2\pi r}\sqrt{\frac{3\gamma P_0}{\rho_0}}$$

Equation 2-4: free bubble resonance

Where the resonant frequency is given by f_0, the bubble radius by r and the ambient fluid pressure and density are given by P_0 and ρ_0 respectively. The symbol γ is the

adiabatic ideal gas constant. This equation is determined for a free gas bubble, more complex factors are involved when the microbubbles have a stiff stabilized shell and in this situation the equation must be modified to incorporate the surface tension of the shell, σ_{st} as in Equation 2-5 (Goldberg et al. 1994):

$$f_0 = \frac{1}{2\pi r}\sqrt{\frac{3\gamma}{\rho_0}\left(P_0 + \frac{2\sigma_{st}}{r}\right)}$$

Equation 2-5: Encapsulated microbubble resonance

McDonald et al (2004) has also derived an equation for the microbubble resonant frequency which takes into account additional shell properties, the shell elasticity parameter (χ). This is presented in Equation 2-6.

$$f_0 = \frac{1}{2\pi}\sqrt{\frac{3\gamma}{\rho_0 r}\left(P_0 + \frac{2\sigma_{st}}{r} + \frac{2\chi}{r}\right) - \frac{2\sigma_{st}}{\rho_0 r^3} - \frac{6\chi}{\rho_0 r^3}}$$

Equation 2-6: MacDonald equation for encapsulated microbubble resonance frequency.

This resonance response increases the backscatter from the microbubbles. Backscatter is the most important factor in conventional fundamental imaging as this imaging mode relies upon backscatter echoes to generate images (Ophir and Parker 1989). However, with new imaging modes now available the more complex microbubble behaviours are of greater interest.

2.1.3. Mechanical Index

The magnitude of the local acoustic pressure is a significant parameter when examining microbubble behaviour. This factor is determined by the output pressure and attenuation of the ultrasound beam. In order to characterize this pressure the mechanical index (MI) is a parameter used to estimate the output pressure of the transducer, it is commonly

used as a safety index (Duck 2008) as a threshold for potential of mechanical effects. The MI is the ratio of peak negative pressure (p-) (MPa) to the square root of the central frequency (fc) (MHz) as in Equation 2-7 (Frinking et al. 2000) it is a derated parameter and as such the parameter is deliberately stated as lower than its true value to take into account attenuation of the ultrasound beam.

$$MI = \frac{p_-}{\sqrt{f_c}}$$

Equation 2-7: Mechanical Index

Depending upon the MI, the microbubble response can be divided into four different regimes, which are described as follows:

MI < 0.1

At this low acoustic power, the microbubbles oscillate linearly at the same frequency as the incident ultrasound beam. Due to the impedance mismatch between the gas in the bubble and the surrounding medium, the microbubble acts as an extremely efficient scatterer, as mentioned above this is vital when using conventional imaging modes. The scattering cross-section of a free non-encapsulated microbubble is given by Equation 2-8 (Deng and Lizzi 2002; Goldberg et al. 1994):

$$\sigma = \frac{4\pi}{9} k^4 r^6 \left[\left(\frac{\kappa_s - \kappa}{\kappa} \right) + \frac{1}{3} \left(\frac{3(\rho_s - \rho)}{2\rho_s + \rho} \right)^2 \right]$$

Equation 2-8: Scattering cross-section

Where σ is the scattering cross section, k is the wave number of the acoustic field, r is the radius of the bubbles, κ_s and κ are the adiabatic compressibility of the scatterer and surrounding medium respectively and, ρ_s and ρ, the densities of the scatterer and

medium respectively. In order to take into account the backscatter from a collection of scatterers, a factor of N, where N is the concentration of scatterers per unit volume should be included (Goldberg et al. 1994). Additional considerations include the effect of a stabilized bubble where the boundary conditions of the microbubble become more complex this has been described by (Church 1995).

Due to the low pressures applied to the microbubbles at this MI, there is little disruption, meaning that most of the microbubbles remain intact during the scan. Therefore low MI imaging has applications in Doppler and fundamental imaging techniques if the agent produces an observable echo (Correas et al. 2001).

MI: 0.1-0.5

At higher insonating powers the microbubble interactions become more complex. Due to the increase in pressure the contractions and expansions of the bubble begin to get larger, because the contractions of the bubbles are limited the expansions get bigger, leading to non-linear behaviour. This non-linear behaviour gives rise to harmonic signals at multiples or fractions of the insonating signal frequency, this phenomena is discussed by (Correas et al. 2001; Cosgrove 2006). These harmonic signals are unique to each type of microbubble and also enable the signal to be distinguished from that arising from soft tissue. This is utilized very effectively with the harmonic imaging mode and pulse inversion imaging.

MI ≥ 0.5

When the MI reaches 0.5 or more, the incident pressure can be sufficiently high to cause microbubble disruption (Smith et al. 2007), dependent upon the microbubble shell properties. This gives rise to a phenomenon known as stimulated acoustic emission (SAE) and many other factors which have in recent years been exploited through different imaging techniques (Fatemi and Greenleaf 1999). Stimulated acoustic emission is used to describe the acoustic emissions observed when subjected to a localized oscillating force, such as an ultrasound field. Microbubble disruption is also

being researched as a therapeutic tool both in thrombolysis therapy (Unger et al. 2001b) and also to enable drug or gene delivery to specific sites (Bekeredjian et al. 2005a; Liu et al. 2006; Tachibana and Tachibana 1999; Unger et al. 2001a).

2.1.4. Microbubble phenomena

Translation

High-speed cameras (>10Mfps) provide a means of directly observing microbubble behaviour. It has been observed that translations of microbubbles occurs both in the direction of the sound field and towards each other (de Jong et al. 2000a; Postema et al. 2004b). It is believed that microbubble translation in the direction of the sound field is caused by a primary radiation force which is the result of a pressure gradient occurring across the microbubble surface. The primary radiation force has been investigated further in Chapter 9.

Whilst primary radiation forces are attributed to the translation of microbubbles in the direction of the sound field, secondary radiation forces, caused by the varying pressure fields resulting from microbubble oscillation, can be attributed to the translation towards each other. If the two microbubbles in question are both either above or below the resonant size, they will be attracted towards each other, however, if they oscillate out of phase, they will recede (Postema et al. 2004b). Translation of microbubbles towards each other can lead to coalescence.

Coalescence

On occasions, during the expansion phase of the microbubbles oscillation, when two microbubbles lie next to each other, the pressure on the film between them increases to a point where it flattens and thins. When the film reaches a critical thickness, usually about 0.1µm, the film between the bubbles ruptures and the bubbles coalesce. Microbubble coalescence has been observed by Yonemoto (2008) and Postema et al. (2004a). This coalescence of microbubbles can pose a health issue; if it were to happen

in a small artery, of a size relative to the microbubble diameter, this could cause a blockage which, depending on the artery, could cause serious damage. However the phenomena also has therapeutic potentials in drug and gene delivery (Postema et al. 2004a; Postema et al. 2004b).

Fragmentation

The fission of microbubbles into smaller bubbles is known as fragmentation. This was first observed with high-speed cameras in 2001 and Postema et al.(2002; 2004b) also captured images of this phenomenon using a fast framing camera and a high speed camera respectively. Often the acoustical observations for fragmentation are coupled with microbubble destruction.

Sonic Cracking

Ultrasound incident upon a microbubble can cause defects in the microbubble shell causing gas to escape from the microbubble, this phenomena is known as sonic cracking. The exact mechanism behind this phenomenon is as yet unknown; it is thought to be due to tiny flaws in the microbubble shell which may cause some shells to crack whilst others remain intact. (Postema et al. 2004b).

Jetting

Jetting is the phenomena observed when a microbubble undergoes a rapid contraction near to a boundary. Due to the boundary the collapse of the microbubble will be asymmetrical, which may lead to a high speed jet forming which projects through the bubble towards the boundary. (Postema et al. 2004b).

2.2. Ultrasound Imaging Techniques

Initially, when the enhanced scattering properties from microbubbles were discovered it was thought that they would be used solely to increase the backscatter for fundamental (B-mode) and increase the sensitivity of Doppler techniques. However, it was soon

determined that in order to get the optimum signal from contrast microbubbles other imaging techniques which capitalised on the non-linear properties of the microbubbles would give better contrast to tissue ratios in which the backscatter from the contrast agent is observably brighter than the observed scatter from surrounding tissue. Three techniques; harmonic imaging, pulse-inversion imaging and power modulation, were developed to image the contrast agents at low acoustic pressures thus reducing the disruption of the contrast microbubbles and thus allowing them to be imaged over a longer period of time.

2.2.1. Fundamental Imaging

This mode of imaging was commonly used in cardiology, in addition to imaging other parts of the body. In fundamental imaging UCAs provided left ventricle opacification resulting in improved imaging of the endocardial border which enhanced detection of abnormalities in the wall motion (de Jong et al. 2000b; Frinking et al. 2000; Gramiak and Shah 1968). Fundamental imaging is a low MI technique but is rarely used today due to the advent of improved imaging techniques. In narrow vessels or areas of the body where the microbubble concentration is lower, this imaging mode is limited by tissue backscatter masking the grey-scale increase, this is known as a low contrast-to-tissue ratio. Therefore it is evident that other methods would be required to optimize the use of microbubbles in the presence of soft tissue. These imaging techniques are based on specific microbubble properties.

2.2.2. Harmonic Imaging

Harmonic imaging employs the harmonic properties of tissue and microbubble contrast agents when in the presence of an ultrasound field. As explained previously, when the microbubbles are in the presence of an ultrasonic field with MI greater than 0.1, they begin to undergo non-linear oscillations and produce harmonics at multiples or fractions of the incident frequency, most significantly the second harmonic (Correas et al. 2001; de Jong et al. 2000b; Frinking et al. 2000). Similarly due to the non-linear elasticity of

tissue, it also demonstrates non-linear expansions and contractions which result in propagation of a second harmonic signal. Browne et al. (2004) has shown that tissue harmonic imaging significantly improves the lateral resolution of ultrasound.

Tissue harmonic signals increase with increasing acoustic pressure, so at low acoustic pressures (low MIs) the harmonic signal from the microbubbles will tend to be larger than that from the tissue, hence the harmonic signals received by the ultrasound can be used to distinguish the presence of microbubbles from tissue. However, a narrow bandwidth is required in order to remove the contribution from the tissue signal which causes a loss of resolution, this results in a trade-off between the ability to detect contrast and the image resolution (de Jong et al. 2000b) as illustrated in Figure 2-5.

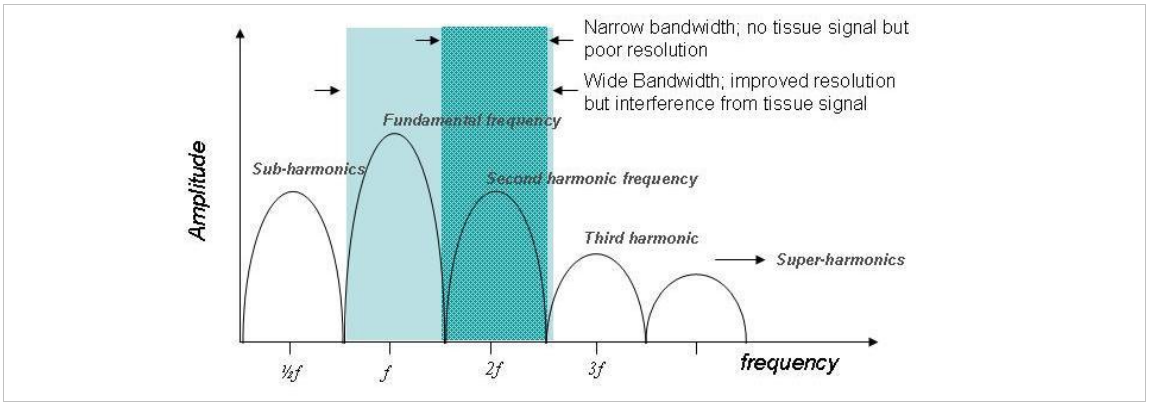

Figure 2-5: Contrast harmonic imaging and transducer bandwidth.

2.2.3. Pulse Inversion Imaging

This imaging technique was developed to overcome the trade-off between the ability to detect contrast and image resolution. In this mode a sequence of two pulses are transmitted, the second pulse being the same as the first but 180° out of phase. If these pulses are both reflected from a linear reflector, when they are received the sum of the two reflected pulses is zero. If there is a degree of non-linearity the sum of the two responses will not be zero and the remainder is related to the degree of non-linearity. A

schematic of this imaging mode is shown in Figure 2-6. Pulse inversion imaging is advantageous because it can operate over a wide bandwidth and therefore can be used without loss of resolution. (Correas et al. 2001; de Jong et al. 2000b; Frinking et al. 2000).

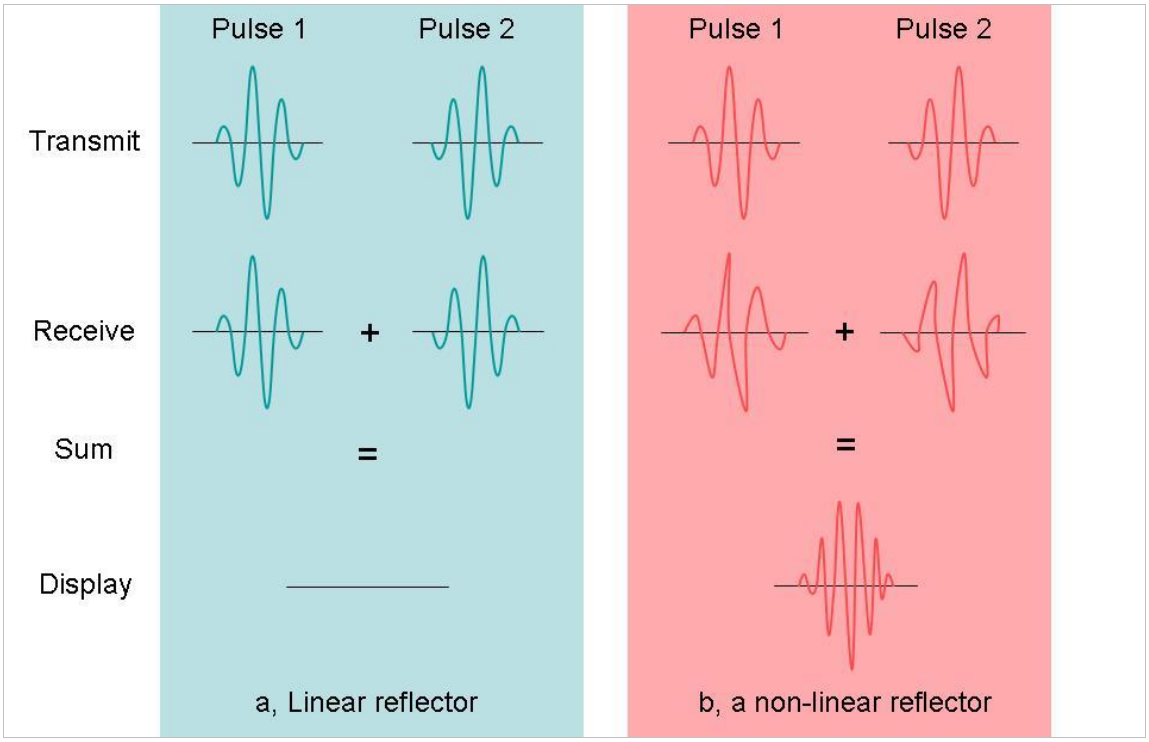

Figure 2-6: A schematic showing pulse inversion imaging; a, the sum of received pulses from a linear reflector and b, the sum of received pulses from a non-linear reflector such as microbubbles or tissue.

Coded excitation has been used to improve the contrast to tissue ratio in ultrasound imaging and has been found to increase microbubble response by 10-13dB (Borsboom et al. 2003). This technique involves excitation of the ultrasound using chirp sequences and results in enhanced axial resolution and bandwidth without the need for higher acoustic pressures (Oelze 2007). However, despite some promise of improving non-linear microbubble imaging Shen (2007)and Cheng (2007b) suggest that contrast to tissue ratio is consistently lower after excitation with pulse-inversion imaging.

In addition amplitude modulation has been shown to improve the contrast to signal ratio for pulse-inversion imaging (Eckersley et al. 2005). In amplitude modulated pulse-inversion imaging the second pulse is both phase and amplitude modulated. This increases the sensitivity of the imaging technique to non-linear scatterers and was shown to improve the signal by 4dB on combination of the two techniques (Eckersley et al. 2005).

2.2.4. Subharmonic Imaging

The second harmonic nature of microbubbles is exploited in harmonic imaging, however, as well as producing a second harmonic when undergoing non-linear oscillations the microbubbles also emit a subharmonic component (Forsberg et al. 2000); these are at half of the transmitted frequency. The advantages of subharmonic imaging are described by Dollet et al. (2008) and Shi et al. (1999) and these are given below:

- Subharmonic imaging displays a better contrast-tissue ratio as tissues do not generate sub-harmonic signals.
- It gives a stronger signal than higher harmonics for high frequency ultrasound.
- It is less sensitive to attenuation and non-linear propagation.

Since subharmonics produces a stronger signal with high frequency ultrasound it is commonly used in conjunction with intravascular ultrasound (IVUS) (Shi et al. 1999). Goertz et al. have demonstrated potential use of subharmonics for vasa vasorum imaging with IVUS (Goertz et al. 2007). However subharmonic imaging has lower spatial resolution.

2.3. Microbubble Targeting

There have been many advances in the field of ultrasound contrast agents in recent years. The concepts of targeting microbubbles to specific tissues within the body and the delivery of drugs or genes to specific sites show great promise in both diagnostic

(DeMaria et al. 2006; Klibanov 1999; Klibanov et al. 1999) and therapeutic domains (Liu et al. 2006; Tsutsui et al. 2004).

The requirements for a targeted microbubble were outlined by Klibanov (1999) as follows:

- The microbubbles should be able to arrive at, and flow through the target site.
- They should remain stable long enough to circulate and accumulate at the target site and also remain stable for the duration of the ultrasound examination.
- The microbubble – target binding should be firm enough to withstand shear stresses from the blood flow.
- They should provide a high target to background ratio in a short space of time.
- The total amount of contrast agent required should be small.

The shear stresses applied to the microbubbles whilst attached to the target are an important factor to consider when developing attachment mechanisms. A study of these shear stresses and the affect of relatively low shear stresses (3.4Pa) on targeted microbubbles has been carried out by Butler et al. (2005) who showed that a streptavidin-biotin bond can withstand physiological WSS in normal humans.

2.3.1. Targeting methods

Different targeting mechanisms are illustrated in Figure 2-7. Targeting can be achieved through either electrostatic (Figure 2-7a) or chemical (Figure 2-7b) attachment properties of the microbubble itself, for example, albumin and certain lipid shelled microbubbles are retained within the microcirculation of damaged and inflamed tissue (Lindner 2002a; Lindner et al. 1998). Another method of attachment can be through incorporating either ligands or antibodies in the surface of the microbubble (Figure 2-7c, d and e) which will attach to specific biological markers on the surface of cells. There are a variety of ways to achieve this but two of the most commonly employed are ligand-binding and antibody-antigen binding.

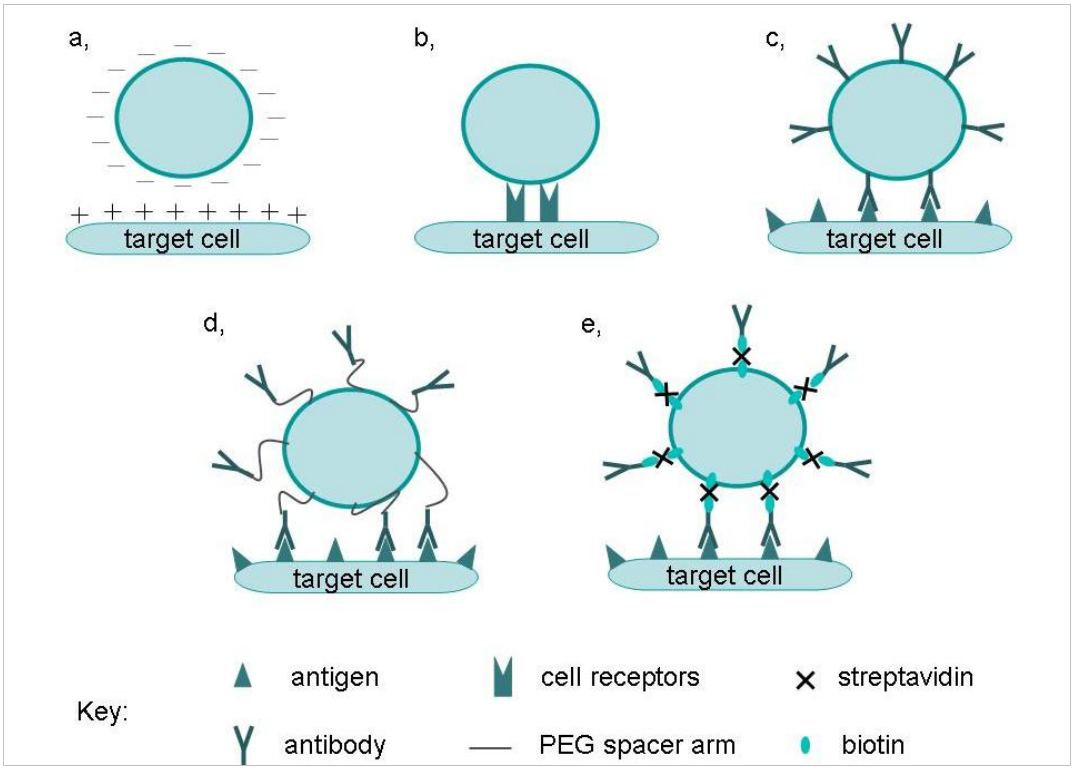

Figure 2-7: Targeting of microbubbles to a receptor coated surface, a, via electrostatic forces, b, via chemical interactions with microbubble shell, c, attachment of antibodies or ligands directly to microbubble shell, d, attachment of antibodies or ligands via a PEG spacer arm and e, attachment of antibodies or ligands via a streptavidin-biotin bridge (Lindner 2002b).

Ligands and Antibodies

A ligand is a molecule which binds specifically to cell receptor sites, in biological applications this allows for cell to cell recognition. Ligands have been used for targeting of microbubbles by Unger (2004) and Lindner (2002a). An antibody consists of a Y-shaped protein produced by the body to neutralize bacteria and viruses (4-Antibody 2009), each different type of virus and bacteria has an individual antigen and each antigen has a corresponding antibody. Antibody targeting of UCAs has been demonstrated by Korosoglou et al (2006) and Della Martina (2007). Occasionally however antibodies can lead to an unwanted immune response (Parham 2004). Ligands have the advantage because they are less bulky than antibodies making them easier to

attach to the microbubbles. Finally antibodies are not stable during storage and the processes (Klibanov 1999) involved in producing microbubbles can cause them to become inactive. However, antibodies do hold some advantages, there are a variety of them available against a range of antigens, and the affinity of the antibody-antigen interaction is high (Klibanov 1999).

2.3.2. Targeted Microbubble Preparation

The targeting ligands or antibodies to be attached can be added to the microbubbles before or after they have formed, the time-point at which they are added depends on the stability of the ligand or antibody during the microbubble production.

A range of attachment methods as described by Klibanov (Klibanov 1999) and Linder (Lindner 2002b) are illustrated in Figure 2-7 and described below:

- Proteins incorporated into the microbubble shell can covalently bind to the ligands.
- An 'anchor protein' can be incorporated into the microbubbles shell which the ligand can be attached to later.
- An avidin-biotin arm can be introduced to facilitate non-covalent bonding of the ligand.

It is important to purify the microbubble preparation at various stages during production to remove all constituents which are not incorporated in the shell as otherwise they can provide ligand binding sites and when the contrast agent is in use these 'loose' ligands can block the binding site. Other factors to take into account regarding binding ability of the microbubbles are their ability to come into direct contact with the target surface, the shear stress applied to the vessel wall by the flowing blood, and also the number of ligand-receptor pairs formed and the affinity (strength) of the interaction. It is thought that the incorporation of a spacer arm, for example in the avidin-biotin formation can facilitate attachment of the ligands to the target site as the ligands have some flexibility and therefore more ligands will be able to attach to the site (Klibanov 1999).

Uses of microbubble targeting already under study include the attachment of microbubbles to thrombi, for which the ligands involved are targeted to platelet glycoprotein 11b/111a Integrin which accumulates at sites of thrombi, this particular application also has a therapeutic advantage as the attachment of microbubbles to the thrombus can cause clot lysis (Lindner 2002a). In addition to targeting thrombi, it has also been shown that inflammation can be targeted as albumin and certain lipid shelled microbubbles are retained within the microcirculation of injured and inflamed tissue as there are interactions between these microbubbles and activated leukocytes. Targeting of dysfunctional endothelium has also been demonstrated by (Weller et al. 2002). Other potential applications of targeted microbubbles include assessment of malignant tumours and diseased tissues (Dai et al. 2006; Kaufmann and Lindner 2007; Lathia et al. 2004; Migaleddu et al. 2009).

2.3.3. Therapeutic Ultrasound

There are many potential therapeutic applications of ultrasound (ter Haar 2007). Thrombolytic therapy (Tachibana 2004), which is already a well established treatment, and tissue repair (Jackson et al. 1991) are just two of the more commonly explored areas. These methods have been studied and improved over many decades. However, in more recent times, therapeutic ultrasound has become a more complex field due to the discovery and advancement of microbubbles as a contrast agent.

Ultrasound has been thought to increase cell permeability (known as sonoporation) (Dijkmans et al. 2004) which can help drugs and genes injected into the body pass the cell membrane barrier. It is also believed that ultrasound can aid thrombolysis, the break up of thrombolytic clots, and therefore has an application in treating Deep Vein Thrombosis among other conditions which cause or are caused by thrombi (Dijkmans et al. 2004). Ultrasound has also been shown to encourage transdermal drug delivery (delivery of drugs through the skin such as nicotine or oestrogen patches) (Tachibana and Tachibana 1999).

The presence of contrast microbubbles can improve the therapeutic effects of ultrasound (Tachibana and Tachibana 1999). The key mechanism believed to produce this enhancement is microbubble destruction (Bekeredjian et al. 2005b; Stride and Saffari 2003b), although it has been suggested that simply the presence of microbubbles provides some enhancement. Microbubbles can also be used as vehicles to carry drugs or genes through the body and if targeted, to specific sites (Lanza and Wickline 2001; Liu et al. 2006; Unger et al. 2004).

Ultrasound targeted microbubble destruction (UTMD)

The mechanisms involved in microbubble destruction (Bekeredjian et al. 2005a; Tachibana and Tachibana 1999; Unger et al. 2001a) which may enhance the delivery of drugs incorporated into the microbubbles include:

- Pore formation which occurs after microbubble destruction
- Inertial cavitation in which micro-jets can be formed which can help to penetrate cell membranes
- Secondary shock waves as a result of inertial cavitation can cause high local temperatures and high shear stresses which may aid drug or gene delivery to cells.

The advantages of delivering drugs or genes via UTMD are threefold; firstly the drug or gene vectors can be delivered directly to the target region and can result in a higher concentration in the focal area, secondly by transporting the drugs and gene vectors encased in the encapsulated bubbles the effect on healthy tissues are limited and therefore more powerful drugs can be used, finally destruction of the microbubbles can enhance the delivery of the drug or gene into the target cells.

UTMD has also been shown to produce therapeutic effects without any transported substances. This is through heating effects produced by inertial cavitation, microjetting and other microbubble phenomena described earlier. The use of UTMD in thrombolysis

has been shown in dogs (Culp et al. 2003). It has also been suggested that UTMD in skeletal muscle can induce arteriogenesis (Bekeredjian et al. 2005b).

Production of drug or gene loaded microbubbles

Unger (2001a; 2001b), Dijkmans (2004) and Liu (2006) have all described the variety of ways in which drugs or genes can be attached to microbubbles. These are illustrated in Figure 2-8 below.

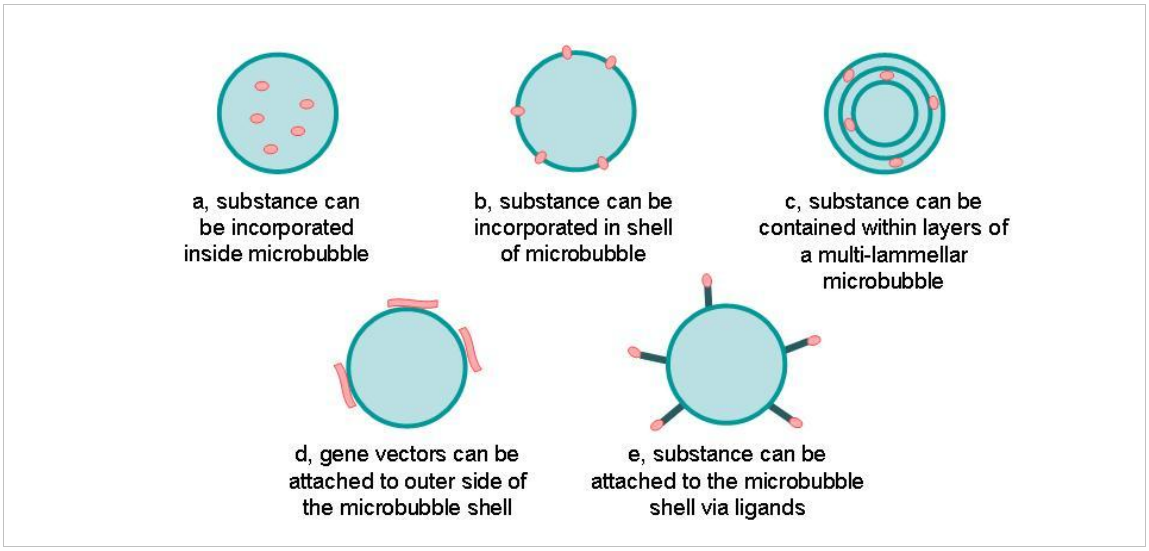

Figure 2-8: Ways of incorporating drugs or genes into microbubbles.

2.4. Safety

2.4.1. Ultrasound

Ultrasound is one of the safest imaging procedures due to the fact that an ultrasound examination does not involve the use of ionising radiation. However, despite this, ultrasound, especially when contrast agents are used, can pose some degree of risk to the patient and this must be assessed carefully.

As the output power of the ultrasound is increased the theoretical risk to the patient is increased. An increase in output power will result in an increase in the local acoustic pressure which can cause cavitation effects or cellular damage (Clinical Safety Statement for Diagnostic Ultrasound 2006; Church 2002; Duck 2008; Singh 2007). The MI, as described in Section 2.1.2, is used to provide a safety reference number for the acoustic output of the ultrasound system and guidelines as to the use of MI in routine ultrasound examinations are provided by the British Medical Ultrasound Society (BMUS) and displayed in Table 2-2 (BMUS 2006).

MI> 0.3	There is a possibility of minor damage to neonatal lung or intestine. If such exposure is necessary, try to reduce the exposure time as much as possible.
MI> 0.7	There is a risk of cavitation if an ultrasound contrast agent containing gas micro-spheres is being used. There is a theoretical risk of cavitation without the presence of ultrasound contrast agents. The risk increases with MI values above this threshold.
TI> 0.7	The overall exposure time (including pauses) of an embryo or foetus should be restricted in accordance with maximum recommended exposure times for a foetus.
TI> 1.0	Eye scanning is not recommended, other than as part of a foetal scan.
TI> 3.0	Scanning of an embryo or foetus is not recommended, however briefly.

Table 2-2: BMUS ultrasound safety parameters.

The heating effects of ultrasound must also be considered in relation to the safety of an ultrasound examination. As an ultrasound beam is attenuated by soft tissue this will cause an increase in local temperature which could lead to cellular damage. A thermal index (TI) is used to quantify the degree of heating and BMUS guidelines for TIs are outlined in Table 2-2 above.

Provided the acoustic outputs and MI and TI are considered carefully and the 'as low as reasonably acheivable' (ALARA) principle is adhered to when an ultrasound examination is being planned the use of ultrasound as a non-invasive imaging technique is considered safe (BMUS 2006; ECMUS 2008).

2.4.2. UCAs

The safety effects of UCAs must also be carefully considered. These issues have been discussed by various authors (Bekeredjian et al. 2005b; Correas et al. 2001; Duck 2008; ECMUS 2008; Harvey et al. 2000; Stride and Saffari 2003a). UCAs have to date had a good safety profile when used with recommended clinical parameters for acoustical energy and microbubble concentration (Alvarez Sanchez et al. 2009; Dolan et al. 2009), although minor reactions include warm facial sensations, alteration of taste and general flush in about 1-5% of examinations (Correas et al. 2001), adverse reactions which can involve allergic reactions, chest pain, headache and nausea are very rare although they have been documented (Dijkmans et al. 2005).

Prior to being approved, a UCA must undergo extensive clinical trials as outlined by the Food and Drug Administration (FDA) in the US (Federal Food, Drug, and Cosmetic Act (FD&C Act) 2005) and by the Medicines and Healthcare Products Regulatory Agency (MHRA) in the UK (MHRA 2008) to ensure that there are no serious toxicological effects related to their use, the beneficial affects of their application must outweigh any deleterious effects.

Despite the excellent safety profile of UCAs with regards to toxicological effects there are significant bioeffects related to the use of microbubbles in ultrasound examinations. These bioeffects can be due either to thermal effects of UCAs or non-thermal effects. Although previously the localized heating due to UCAs was thought to be acceptable and non-damaging for low power US (Hilgenfeldt et al. 2000), these investigations were only carried out for free microbubbles. Stride et al (2004) has considered the effect of

an encapsulating shell on thermal effects of contrast agents and shown that the encapsulated microbubbles may pose a greater risk of thermal damage.

One significant bioeffect from both thermal and non-thermal effects, is cellular membrane damage which can be caused by sonoporation, this has been observed by Miller et al. (2004). Williams et al (2007) has similarly observed nephron damage in rat kidneys with the use of microbubble UCAs. Damage to cellular membranes can result in cell lysis (cell death) (Samuel et al. 2006).

Dalecki et al (2007) has described other bioeffects which have been observed with the use of UCAs. These include hemolysis (Dalecki et al. 1997), damage to the microvasculature (Miller and Gies 1998) and effects on cardiac rhythm (Dalecki et al. 2005), all of which could be potentially harmful to a patient.

Due to the potential harm of UCA bioeffects they continue to be studied in depth. However, to date there have been minimal deaths associated with the use of UCAs (Main et al. 2009) and the benefits of using UCAs is still believed to significantly out-weigh the risks (Dolan et al. 2009).

2.5. Summary

UCAs are a useful tool in both the diagnostic and therapeutic fields of ultrasound. Diagnostically contrast agents can enhance conventional ultrasound scans and also provide scope for the development of new and improved imaging modes such as harmonic and sub/super harmonic imaging. In addition, targeting of the microbubbles can enable imaging of specific conditions such as endothelial inflammation or the presence of thrombi in blood vessels. Therapeutically, UCAs can provide a vehicle for the transport of drugs and genes and be delivered to specific sites through targeting, and microbubble phenomena such as jetting and inertial cavitation can encourage the uptake of these substances. Unloaded microbubbles can also be used to promote thrombolysis and angiogenesis.

Through researching the various microbubble phenomena scientists have been able to improve ultrasound as both a diagnostic and therapeutic tool. Because of the rarity of adverse reactions to the agents, ultrasound contrast imaging has proved to be a safe option for improving diagnostic imaging techniques and the therapeutic effects may in time be developed to deal with many diseases and conditions.

Future possibilities for the use of ultrasound contrast agents include diagnosis and treatment of inflammatory conditions such as irritable bowel syndrome or Crohn's disease, and also for the detection and treatment of malignant tumours among the already used techniques such as thrombolysis and angiogenesis. In addition specific targeting of UCAs may help to determine the extent of vulnerable plaque formation in coronary heart disease which is the focus of this thesis.

Chapter 3 Optimization of a Novel, Lipid-Based, Microbubble Ultrasound Contrast Agent for High Frequency Ultrasound

The in-house microbubble contrast agent has been developed by the University of Edinburgh (Butler 2005; Moran et al. 2006). The microbubble has been developed to be targeted to atherosclerotic plaque within the coronary arteries as a method of identifying vulnerable plaques in coronary heart disease as described in Chapter 1. Attachment of the in-house microbubble to vulnerable plaque will be achieved by incorporating antibodies or peptides which target inflammatory sites such as those exhibited in vulnerable atherosclerotic plaques (Lindner 2001, 2002a). A variety of methods have been employed to maximize the echogenicity of the agent with high-frequency IVUS imaging:

- Sonication
- High shear mixing
- Agitation
- Heating
- Diffusion
- Varying the chemical composition of the shell

3.1. Production of In-house UCA

Previously the in-house UCA has been produced using a solvent method (Moran et al. 2006), this has since been adapted for production of the agent without the use of solvents. The current standard procedure for producing the in-house microbubble involves combining a selection of lipids in the quantities outlined in Table 3-1, hydrating the lipids for a period of two hours, whilst stirring, and then heating the lipids to 78°C for one hour. The suspension is then allowed to cool overnight with continued stirring (Ross and Moran 2006). The lipids used in the production of the in-house contrast agent include phosphatidylcholine (PC), cholesterol (CHOL), phosphatidylethanolamine (PE), phosphatidlyglycerol (PG) and a biotinylated phospholipid (BIOTIN) the latter is incorporated for targeting purposes.

Bubble type	**Quantity of constituent (mg) per 4ml saline**				
	PC	**CHOL**	**PE**	**PG**	**BIOTIN**
70% PE/1% Bio	18	10	70	1	1
45% PE/5% Bio	30	18	45	2	5
1% Biotin	55	30	11	3	1
3% Biotin	53	30	11	3	3
5% Biotin	56	30	6	3	5
15% Biotin	52	30	-	3	15
20% Biotin	47	30	-	3	20
70% PE	19	10	70	1	-
*30% CHOL**	56	30	11	3	-
60% PC	60	30	8	2	-

Table 3-1: Various in-house microbubble compositions (* standard composition)

3.2. Assessment of In-house UCA

Assessment of the in-house UCA was carried out through qualitative and quantitative analysis of the backscatter (echogenicity) produced by a sample of microbubbles, visualization under a high power microscope and measurement of the size distribution of each sample of microbubbles.

3.2.1. Echogenicity

The echogenicity of a sample was assessed using a 40MHz Atlantis™ SR Pro coronary imaging catheter in combination with a Clearview IVUS scanner (Boston Scientific, US) as described in Chapter 5. In order to assess the echogenicity of a sample IVUS images were captured and the mean backscatter from a ROI in each sample was calculated.

IVUS images were captured by a PC linked to the scanner via a video out cable. Images on the screen were then captured using a Matrox Intellicam (Matrox Imaging, Canada) program and saved.

In order to quantify the echogenicity of the microbubble samples it was necessary to eliminate the effects of transducer and scanner set up, as each transducer and scanner combination is unique. Radio frequency (RF) data was collected in order to avoid the effects of signal processing by the scanner and compared to the RF data from a perfect reflector in order to eliminate unavoidable variations in the scanner and transducer set-up.

The RF data was captured by a digitizing card (Gage Applied CS8500, Gage Applied Technologies, Lachine, Canada) added to the PC linked to the RF-Out socket on the IVUS scanner. RF line data was captured, 8 bits at 250Msamples per second, for each microbubble sample. The optimum sampling frequency (f_s) can be found with Equation 3-1, where B is the maximum signal frequency (60MHz). Optimal smapling frequency must therefore be greater than 120Msamples per second.

$$f_s \rangle 2B$$

Equation 3-1: Sampling frequency

The data was then analysed using a program previously written for this purpose by Dr. Robin Watson (Medical Physics, University of Edinburgh) in IDL (ITT Visual Information Solutions, USA). Analysis was performed by comparing the echo in a region of interest (ROI) (2mm from the image centre) to the echo received from a perfect reflector at the same distance; the software pathway is described in Appendix B. For the purpose of this investigation the perfect reflector was an air-water interface, the signal from which was collected after each contrast agent measurement session and is described more fully in Appendix C. The perfect reflector does not demonstrate the observed increase in backscatter relative to a clinical scenario, however the perfect reflector is easily reproducible and enables a comparison of the variation in mean backscatter from different microbubble samples. Tissue mimicking material (TMM) has been produced and compared to the mean backscatter from the microbubbles in the stability trials and can be seen in Figure 3-14.

Three ROIs were analysed for each microbubble sample so that an average backscatter power for the whole image could be calculated. All errors presented throughout this chapter are one standard deviation of three different microbubble samples unless otherwise stated. Figure 3-1 illustrates a region of interest at line 100. Features of the IVUS image and scan converted images are described in Chapter 5 and Appendix B respectively.

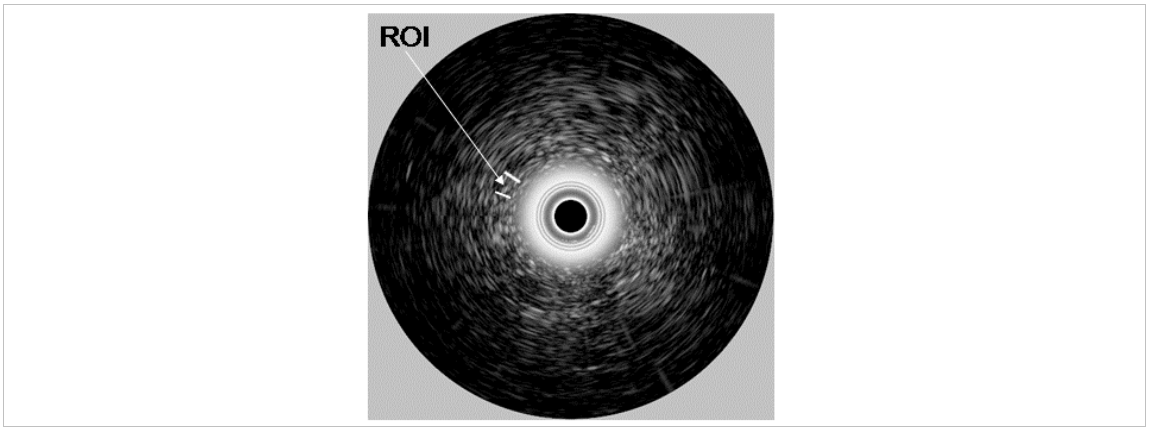

Figure 3-1: ROI at line 100, distance 660 (approx 2mm from transducer) on a scan converted IVUS image reconstructed from RF data.

The mean backscatter, in addition to other parameters, was then printed to a text file which could be opened in Microsoft Excel (Microsoft Corporation, USA) to compare the numerical backscatter for each sample.

3.2.2. Optical imaging of microbubbles

The microbubbles were optically imaged using bright-field microscopy with a Leica DMIRB fluorescence microscope (Leica Microsystems, UK). Objective lenses used include; 10x with a numerical aperture of 0.25 and 40x with a numerical aperture of 0.55, the eyepiece of the microscope had 10x magnification and a numerical aperture of 0.22. Microscopic images were captured in Openlab (Improvision, UK) using a Hamamatsu C4742-95 digital camera (Hamamatsu Photonics UK) connected to a Macintosh computer (Apple Inc, USA).

3.2.3. Sizing of microbubbles

A Malvern Mastersizer (Malvern Instruments, UK) was used to acquire the size distributions. This is achieved through measuring the diffraction pattern of a beam of laser light as it passes through a sample. In addition to the size distribution, this technique provides a value for the median microbubble size. The Malvern Mastersizer

can be seen in Figure 3-2. Predicted optimal microbubble size can be found in Appendix A.

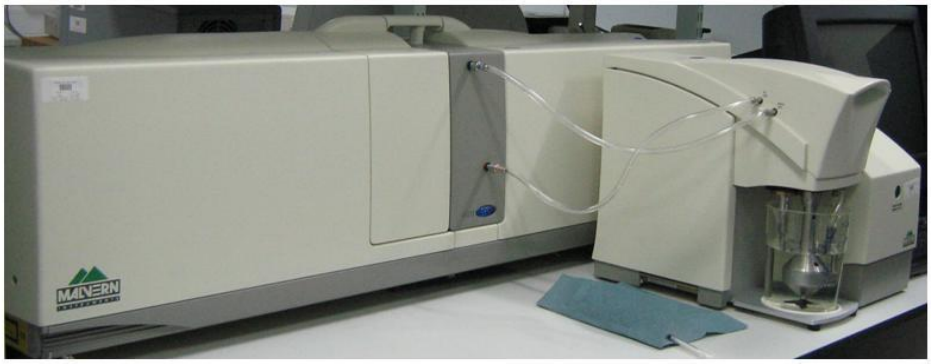

Figure 3-2: Malvern Mastersizer

3.3. Optimization Techniques

A variety of techniques have been investigated in order to determine the optimal production method of the microbubble UCA:

- Varying the chemical composition of the microbubble shell.
- Agitation
- Sonication
- Diffusion
- Addition of mannitol or trehelose
- High temperature production
- High shear mixing

The echogenicity of the microbubbles was also investigated over initially a 24 hour period and then a 3 month period to observe variations with time. Microbubble samples were characterized within one week of production and all trials were carried out with a minimum of three samples being assessed, with the exception of the three month time trial (section 3.3.2) for which only one of each sample was assessed due to time limitations and the large quantity of microbubbles required.

In addition to the effect of agitation on the size and echogenicity of the microbubble samples the length of agitation was investigated.

3.3.1. Composition comparison

Three of the different compositions as outlined in Table 3-1 were compared for echogenicity; this included the 70% PE, 30% cholesterol and 60% PC compositions. These compositions were chosen as they make the basis of all the other compositions, except for the biotinylated agents. The effect of biotin on the echogenicity of the agent has previously been investigated by Butler et al. (Butler 2005) and found to have no effect.

3.3.2. Stability Trials

In order to determine if the agent could be produced in advance of studies and stored until required, an investigation into deterioration of the agent was carried out. The initial investigation involved measuring the echogenicity and size of samples of standard and agitated 30% cholesterol microbubbles at intervals over a 24 hour period. A suspension was produced the day before investigation and left to cool and stirred overnight. The echogenicity was then investigated at fifteen minute intervals for the first hour and then hourly intervals for eight hours. The following day a measurement was collected at 24 hours after the agent had been removed from the hotplate.

The second stability trial involved a study of the agent's echogenicity over a three month period to assess the shelf life and optimum storage of the agent. A 32ml suspension of microbubbles was produced and split into four vials of 8ml. One of the samples was produced in the manner outlined above, one sample was agitated (see section 3.3.3) and one sample was sonicated, these samples were refrigerated. The final sample was agitated and stored at room temperature for the period of investigation.

All four samples were measured once a week and the size distribution of the samples were measured every four weeks.

3.3.3. Agitation

Agitation of the agent was achieved through use of the CapMix (3M ESPE AG, Germany) device illustrated in Figure 3-3. The agent to be agitated was transferred to a suitable vessel and agitated, initially, for 45s. Preliminary investigations assessed the difference in echogenicity and size distribution of a control and agitated sample of microbubbles. Further studies encompassed a comparison of agitation of the microbubbles directly after the heating stage of production and agitation after the cooling stage. A final investigation was carried out into how the length of agitation effects the microbubble population.

Figure 3-3: CapMix device

3.3.4. Sonication

A MSE Soniprep 150 bench mounted ultrasonic disintegrator (Sanyo, Japan) was used to sonicate microbubble samples using the exponential microprobe. The tip of the microprobe was placed centrally within the sample using markings on the probe and the suspension was sonicated for 45s. An initial comparison between sonicated, agitated and control samples was carried out followed by an investigation into the effect of sonication directly after the heating stage. The Soniprep 150 device can be seen in Figure 3-4.

Figure 3-4: MSE Soniprep 150 (Sanyo, Japan)

3.3.5. Diffusion

Diffusion was investigated as a method to increase the gas content of the microbubbles. To achieve this nitrogen gas was bubbled through the microbubble suspension via a small diffusion stone for two hours after the suspension had been heated as illustrated in Figure 3-5. Half of the sample was then agitated and then compared to a control sample.

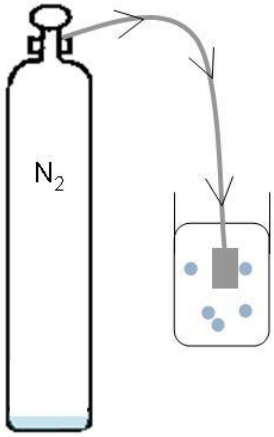

Figure 3-5: Diffusion of nitrogen gas through a microbubble suspension.

3.3.6. Addition of Mannitol or Trehelose Sugars

Mannitol and Trehelose had previously been incorporated into the solvent production method of producing the in-house microbubble contrast agent (Moran et al. 2007). Mannitol and Trehelose are sugars which are known to stiffen the microbubble shell when incorporated into the mixture (Ross and Moran 2007). Initial trials involved adding 5%, by weight, of mannitol or trehelose to the dry lipid mixture. Further studies involved adding 10, 15 and 20% of mannitol or trehelose to the dry lipids and comparing this to a control sample.

3.3.7. High Temperature Production

In some of the previous samples which were produced crystalline structures were observed under the microscope within the microbubble samples. The author and colleagues believed the formation of the crystals to be due to the production temperature being below the transition temperature for one of the lipids. As a result of this consideration it was decided that an investigation into different production temperatures should be carried out. Microbubbles were produced at the following temperature ranges:

- 70-80°C
- 80-90°C
- 90-100°C

Temperature ranges were maintained by continuous observation of the water bath temperature during the one hour heating period.

3.3.8. High Shear Mixing

Mechanical mixing has previously been used to produce microbubble suspensions by a number of researchers (Klibanov et al. 2004; Schneider et al. 2004; Schneider et al. 2006). An IKA® Ultra-Turrax® (IKA®, Germany) hand-held high shear homogenizer was used to provide high shear mixing to the microbubble suspensions, Figure 3-6 shows the homogenizer dipped into a microbubble suspension. The homogenizer was

used to combine the lipids in the saline during the hydration phase at a low speed setting for 60s to disperse the lipids evenly prior to heating. In addition the homogenizer was used on three different samples after the heating stage to encourage formation of smaller microbubbles. The results from both investigations were then compared to a control sample.

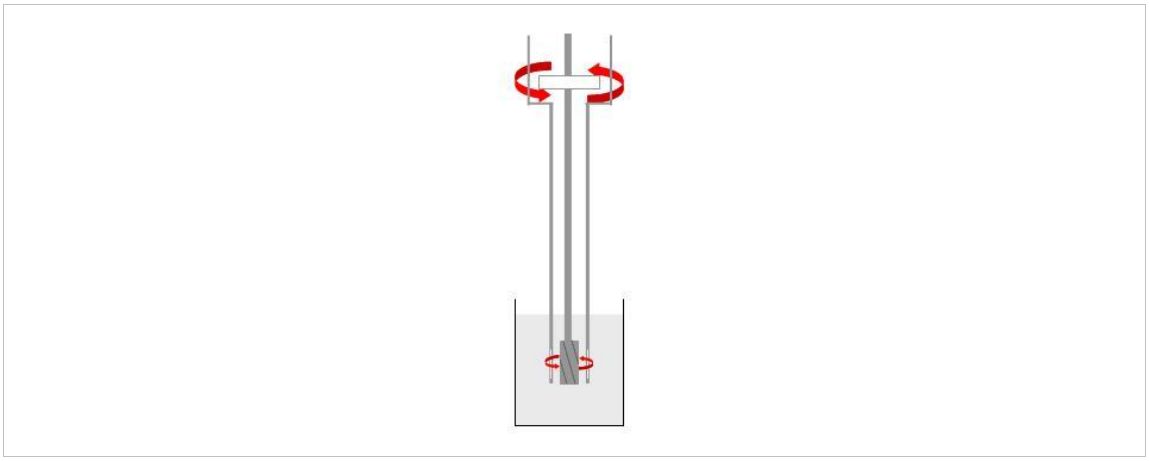

Figure 3-6: High shear mixing of a microbubble suspension using a homogenizer.

3.4. Results

3.4.1. Composition Comparison

Figure 3-7, shows the IVUS images of the three different microbubble compositions investigated. From these images it is evident that the 70% PE composition produces the least echogenic sample and that the 30% cholesterol sample is the most echogenic. This is verified in the quantified data shown graphically in Figure 3-8 where 0dB represents the bright echo received from an air-water interface.

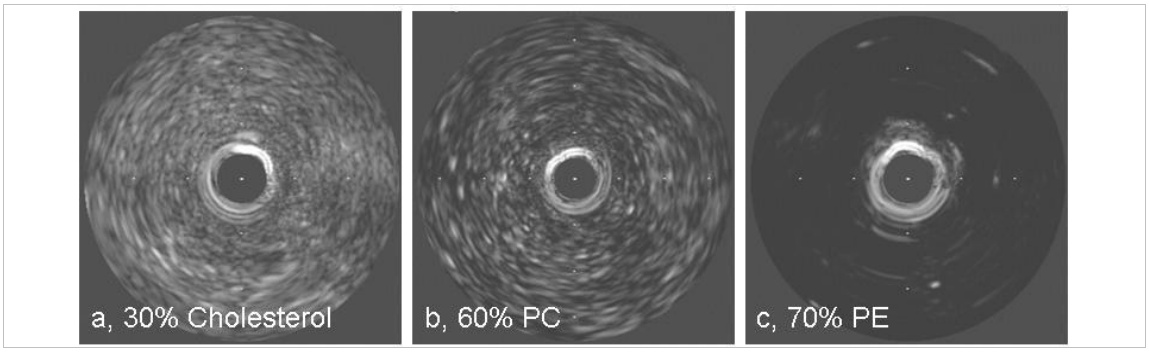

Figure 3-7: IVUS images of a, 30% cholesterol composition; b, 60% PC composition and; c, 70% PE composition of microbubbles.

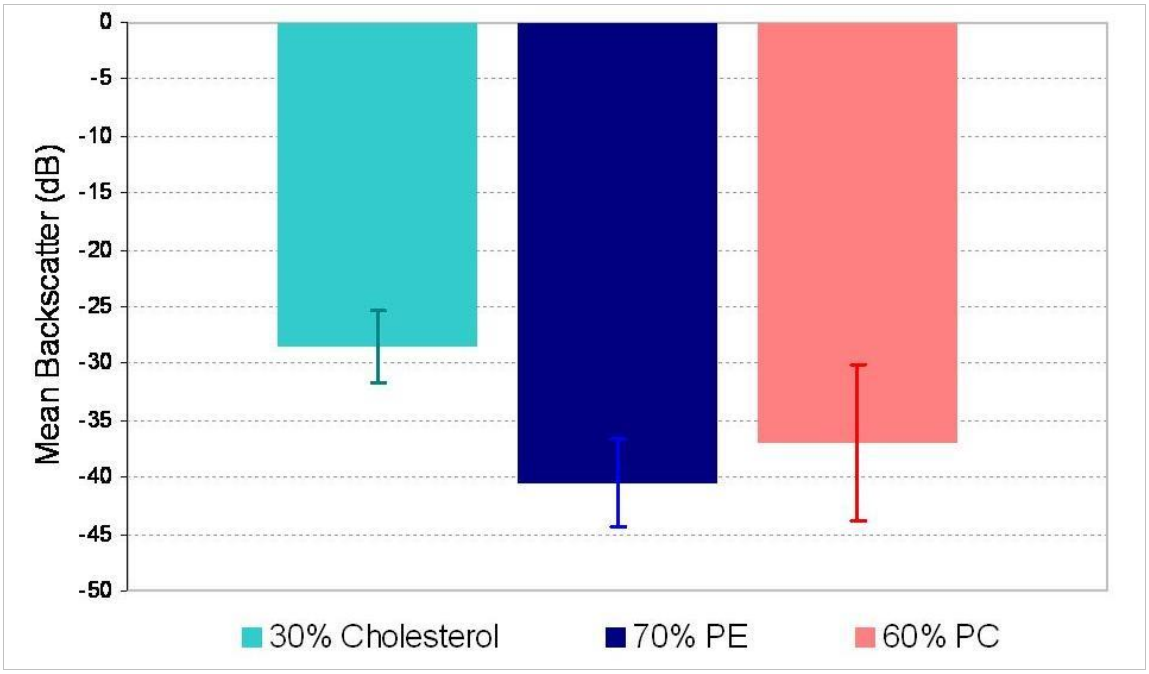

Figure 3-8: Bar chart illustrating the average, mean backscatter of the different microbubble compositions.

The size distributions of each different composition of microbubble are illustrated in Figure 3-9, where it can be seen that the 60%PC sample produces a narrow size distribution with the lowest median microbubble diameter, this is verified by the microscopic images seen in Figure 3-10 which show the variation in microbubble sizes

for each sample. Mean microbubble sizes for the 30% cholesterol, 60% PC and 70% PE composition microbubbles were 11.9(±3.4)µm, 7.4(±3.0)µm and 28.2(±14.3)µm respectively.

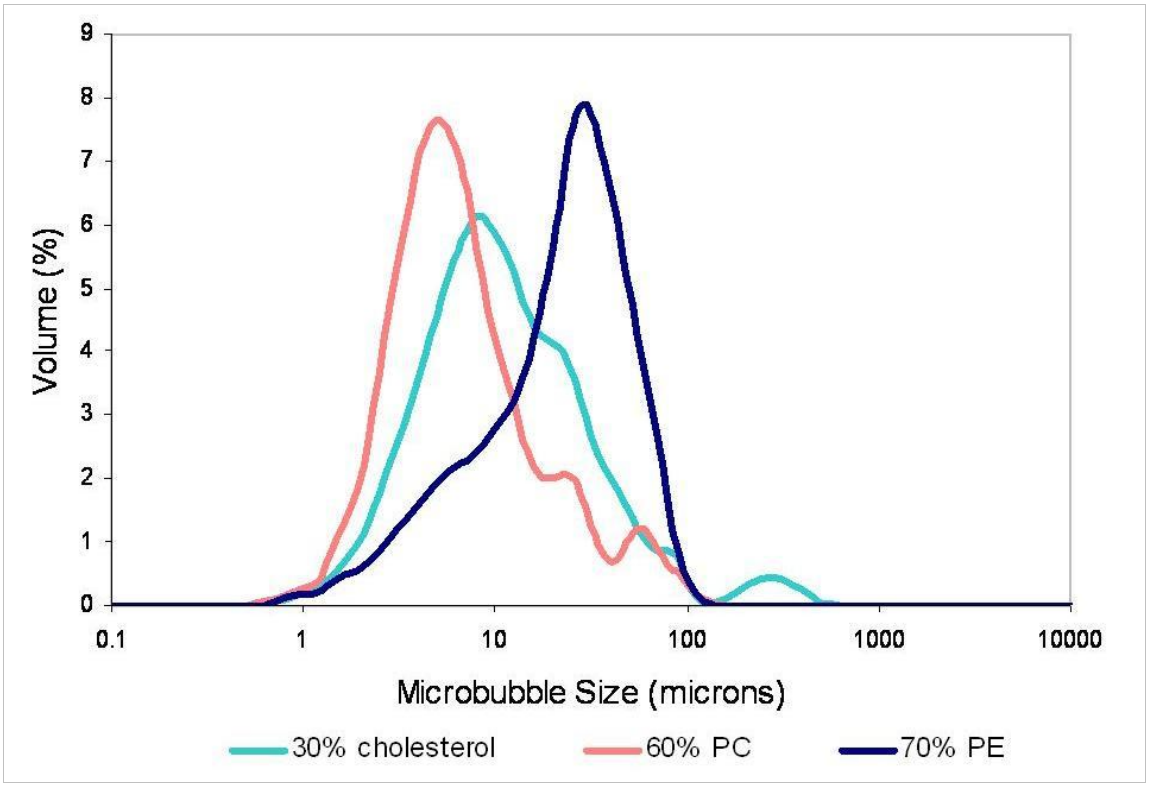

Figure 3-9: Average size distributions produced by different microbubble compositions.

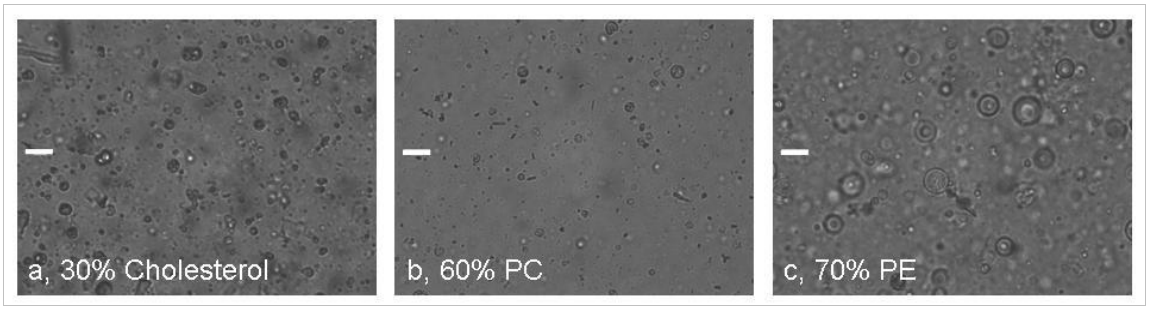

Figure 3-10: Microscopic images of different microbubble compositions (x40 magnification; scale bars equal to 25µm).

Due to the more echogenic nature of the 30% cholesterol microbubble composition it was used in further optimization trials despite having a slightly larger microbubble diameter and wider size distribution.

3.4.2. Stability trials

Initial time trials were carried out over a 24 hour period to assess any variations in echogenicity over this time. Figure 3-11 and Figure 3-12 illustrate the echogenicity and median microbubble sizes respectively within the first 24 hours after production.

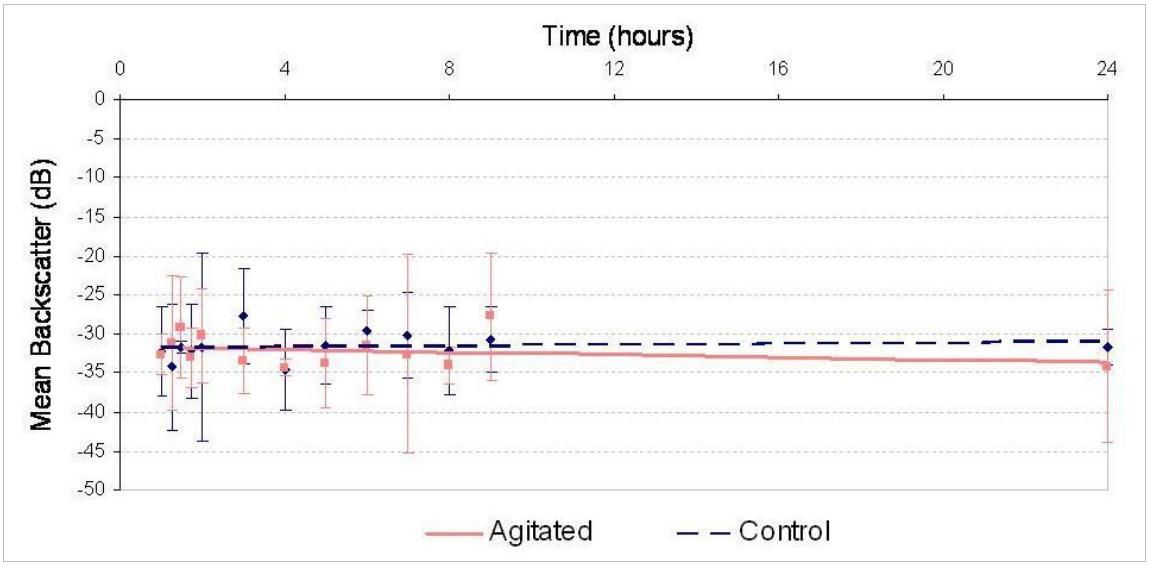

Figure 3-11: Mean backscatter produced by standard and agitated microbubble samples over 24 hours.

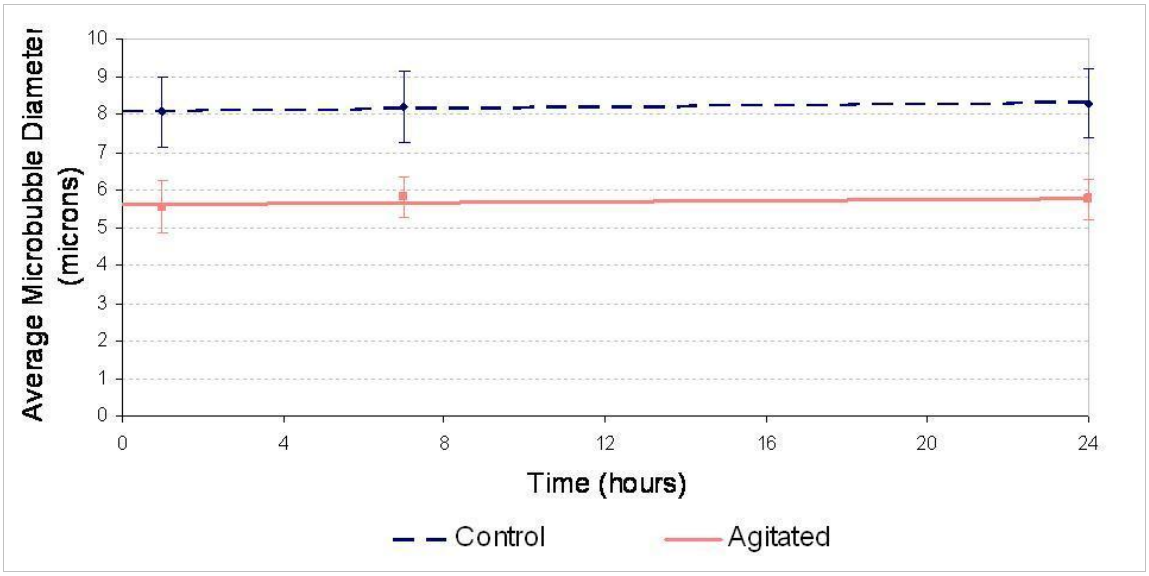

Figure 3-12: Mean microbubble size at 1, 7 and 24 hours after production of a standard and agitated microbubble sample.

Over the initial 24 hour time period the microbubbles showed a 2% variation in echogenicity and 1.5% variation in size, it was therefore decided that an investigation

over a longer time period was necessary in order to determine the shelf life of the in-house microbubble UCA. Figure 3-13 illustrates the size distributions at 1, 7 and 24 hours after production also suggesting very little variation.

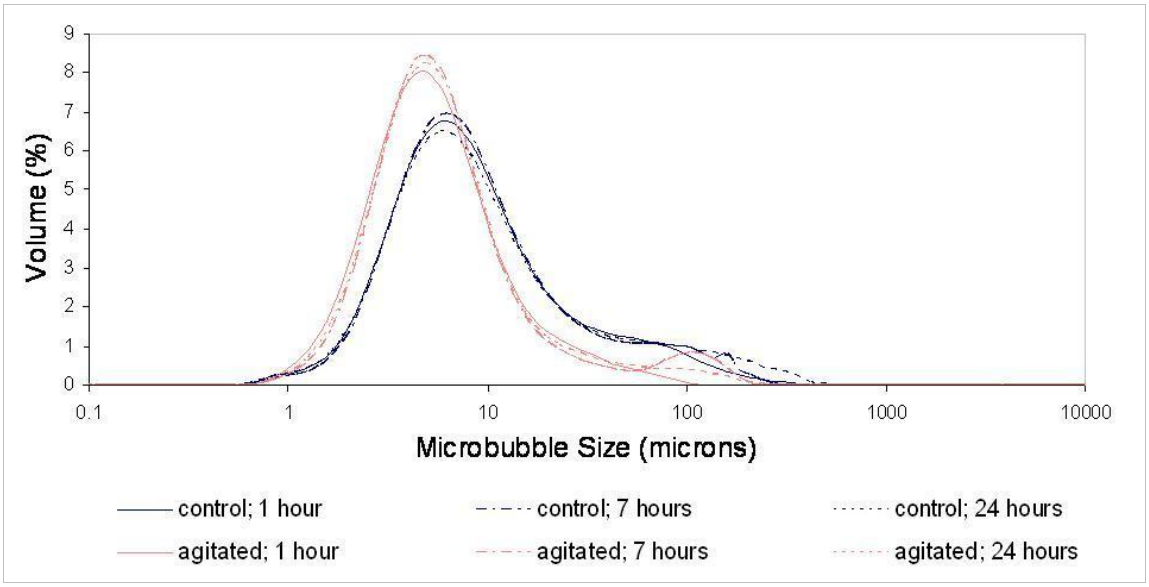

Figure 3-13: Microbubble size distributions at 1, 7 and 24 hours after production for agitated and control microbubble samples.

Figure 3-14 and Figure 3-15 show the variation in echogenicity and median microbubble size over a three month period for four different microbubble samples. This data suggests that with the exception of the control sample stored at room temperature the echogenicity shows a slight increase over fourteen weeks. Similarly, the average microbubble diameter over the fourteen weeks shows less than 1μm variation for the control and agitated refrigerated samples but increases by 15.7μm over the 14 weeks for the microbubble sample stored at room temperature. The increased microbubble diameter is thought to be due to coalescence of the microbubbles at room temperature.

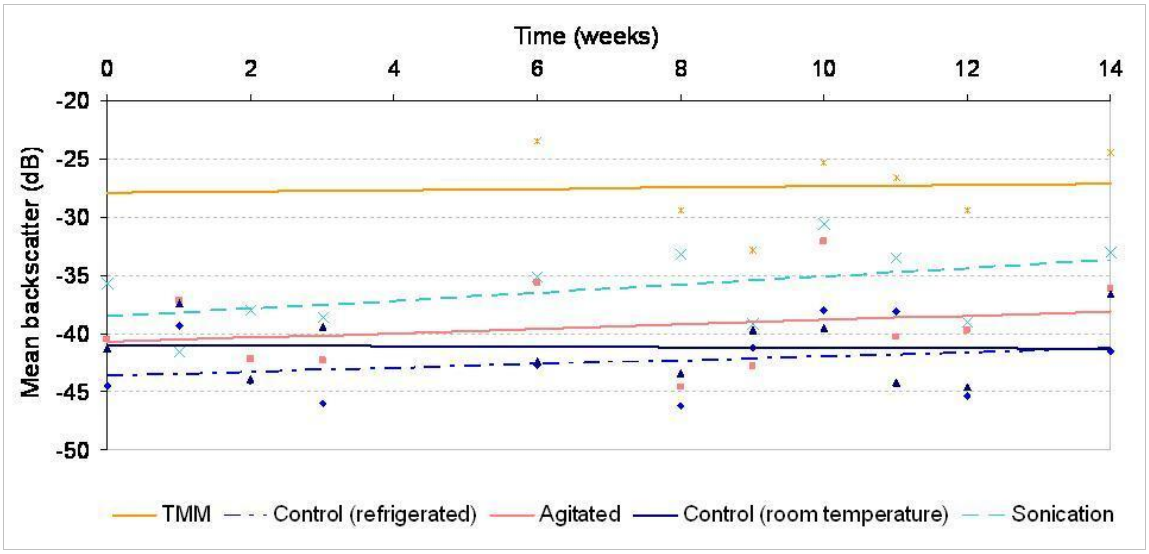

Figure 3-14: Echogenicity of the in-house UCA over a three month period (no error bars present as only one investigation was possible due to time and material constraints), TMM - tissue mimicking material.

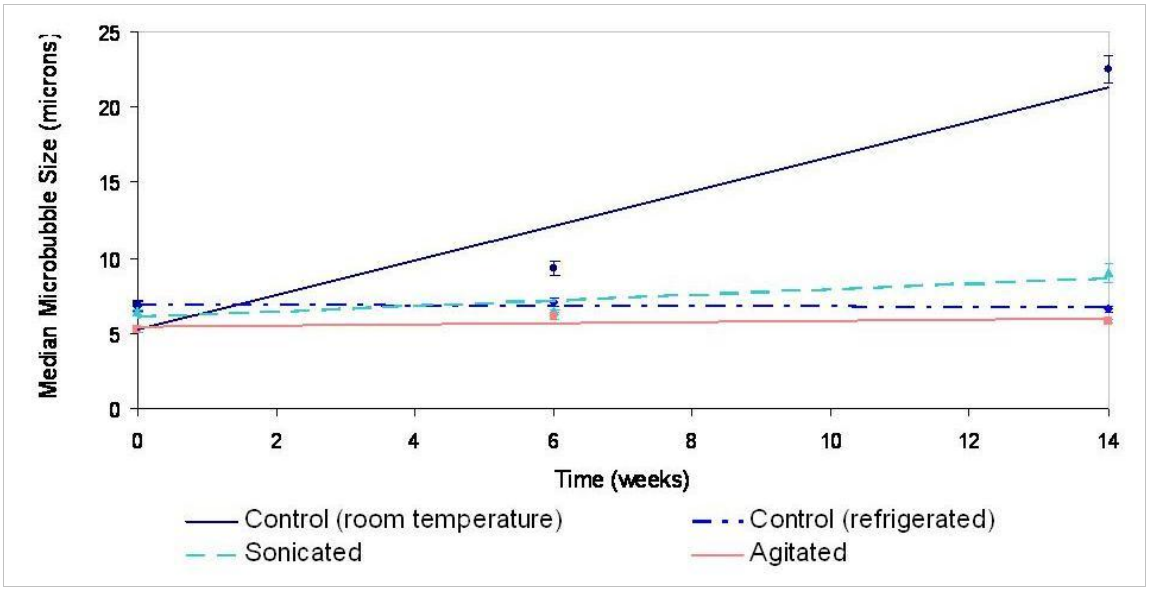

Figure 3-15: Average microbubble diameter over a three month period.

In light of the results collected and illustrated above the microbubbles should be stored in the refrigerator and can be used for up to three months after production provided no

other signs of deterioration are visibly evident on use. Some samples presented mould or coagulation after long periods of un-use and were therefore discarded.

3.4.3. Agitation and Sonication

The mean backscatter produced by the agitation or sonication of the in-house UCA is compared to a control sample in Figure 3-17 below. This data shows that there is a slight increase in echogenicity of the samples on agitation and sonication with agitation producing the largest increase of 3.9(±1.0)dB. This is supported by the IVUS images seen in Figure 3-16.

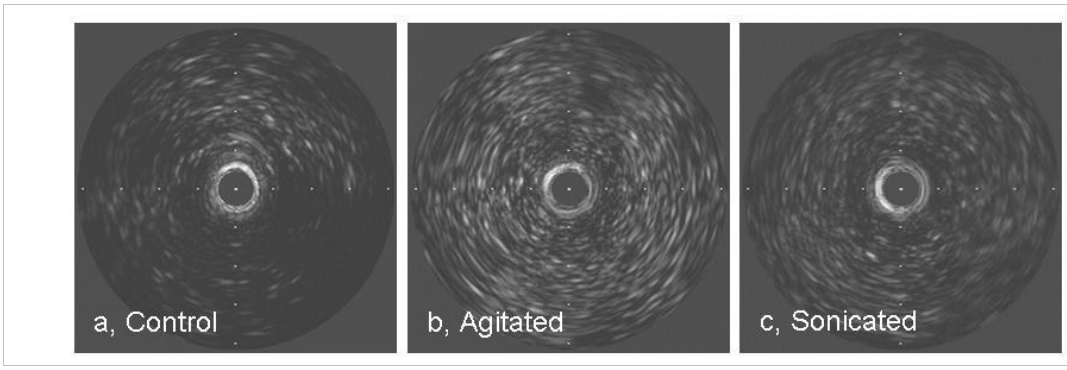

Figure 3-16: IVUS image comparison of; a, control; b, agitated and c, sonicated samples.

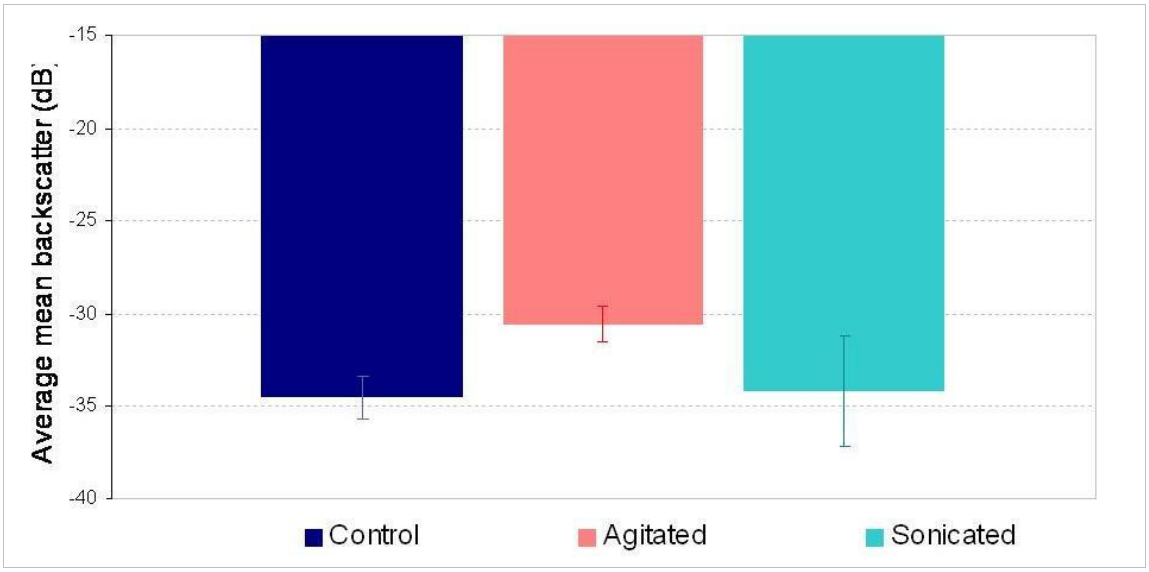

Figure 3-17: Echogenicity comparison of agitated, sonicated and control microbubble samples.

The microbubble size distributions are shown in Figure 3-18 below. Agitation and sonication of the samples produces very similar size distributions which are narrower than the control sample. Due to the narrower size distribution and 3.9(±1.0)dB increase in echogenicity, agitation will be used in production of future microbubble samples. Figure 3-19 shows the microscopic images of the three samples. Optically measured microbubble sizes are comparable with the size distributions produced by the Malvern Mastersizer.

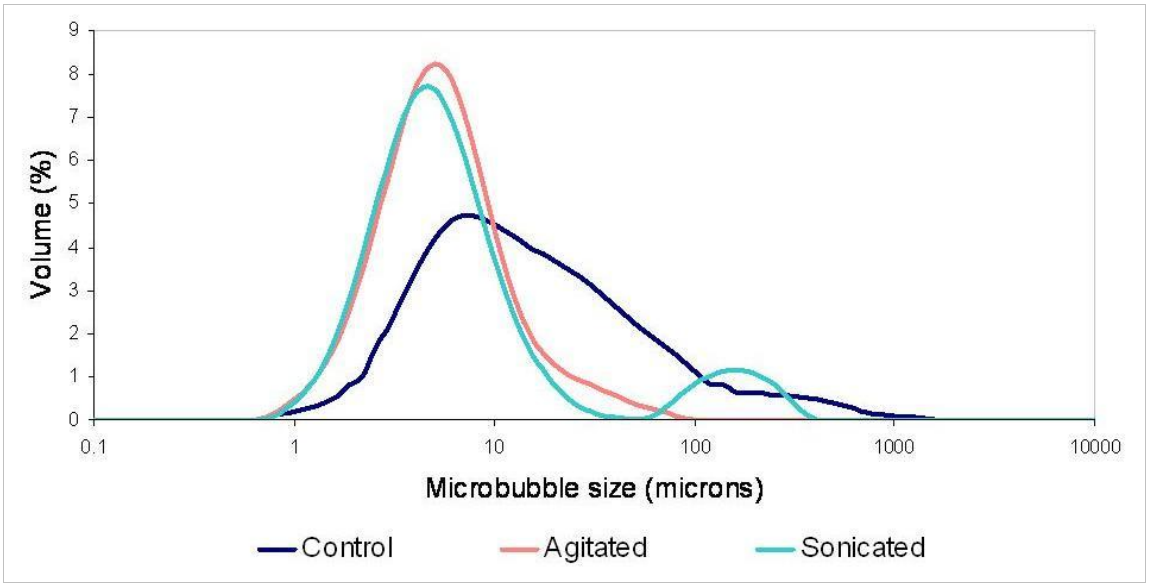

Figure 3-18: Microbubble size distributions, agitation and sonication comparison.

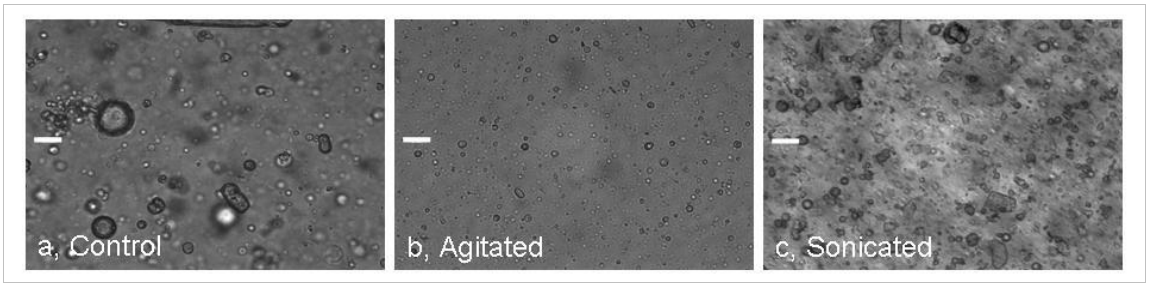

Figure 3-19: Microscopic images of control, agitated and sonicated microbubble samples.

If agitation is to be used to optimize future microbubble samples it is important to know the optimum agitation time. Figure 3-20 shows the mean backscatter produced by varying the time that a sample is agitated from 15s agitation to 240s. It is important to note that although there is an initial increase in the echogenicity from agitating the sample there is also a steep decline in the echogenicity if the agitation time exceeds 60s. The microbubble size distributions, as seen in Figure 3-21, show that the average microbubble size decreases with agitation time.

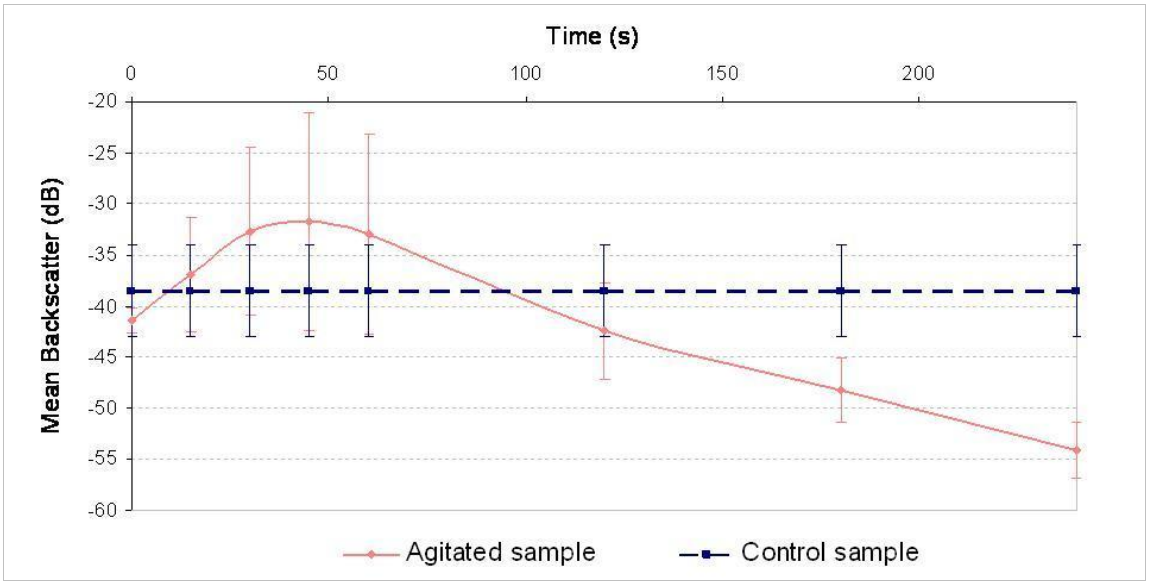

Figure 3-20: Mean backscatter produced by varying agitation time.

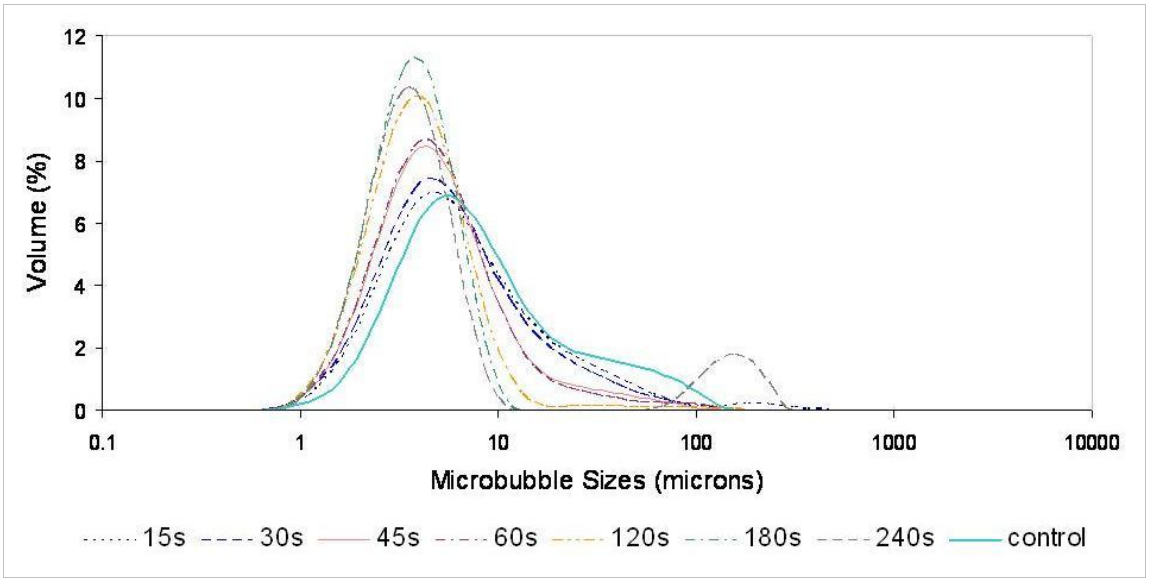

Figure 3-21: Size distributions produced by different agitation times.

The above data suggests that the optimum agitation time for the in-house microbubble UCA is 45s.

3.4.4. Diffusion

The microbubble samples were diffused with nitrogen gas directly after the heating stage. It was found that this diffusion technique did slightly increase the echogenicity of the microbubble suspension by 1.6(±1.2)dB, and agitation of the diffused sample produced an increase in the mean backscatter of 3.0(±1.5)dB. This data can be seen in Figure 3-22 below. However the size distribution data in Figure 3-23 shows that diffusion of the microbubbles alone produces a wide size distribution with two peaks, suggesting that up to 50% of the microbubble suspension has a diameter greater than 20µm. For this reason if diffusion was to be used as a method to optimize the microbubble suspension it would be important to agitate the sample after diffusing to maintain a narrow size distribution with a small average microbubble diameter in order for the UCA to be used in vivo.

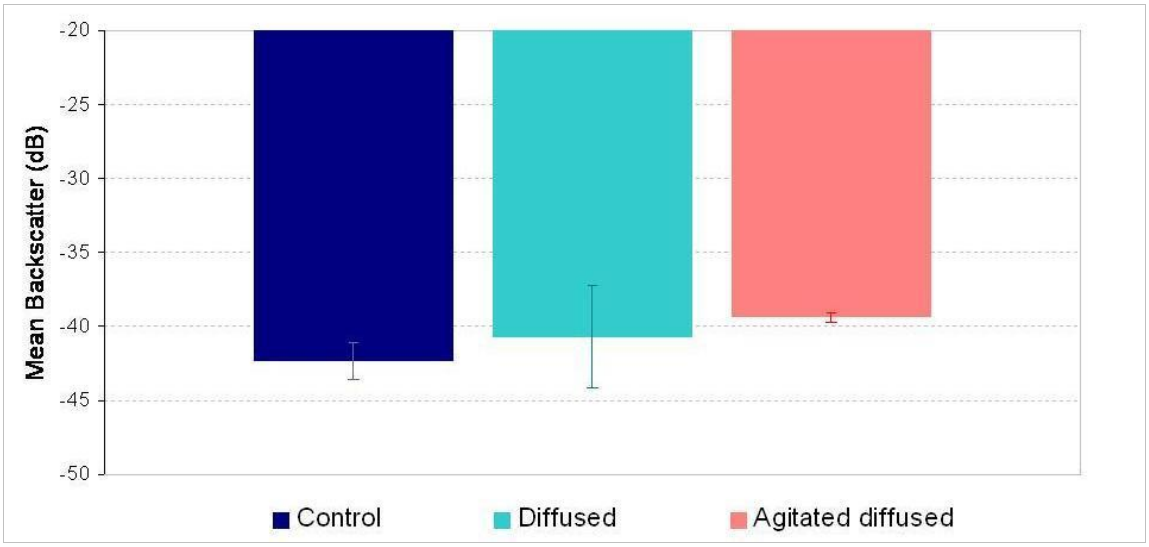

Figure 3-22: Mean backscatter produced by diffusing microbubble suspension with nitrogen, compared with a control sample.

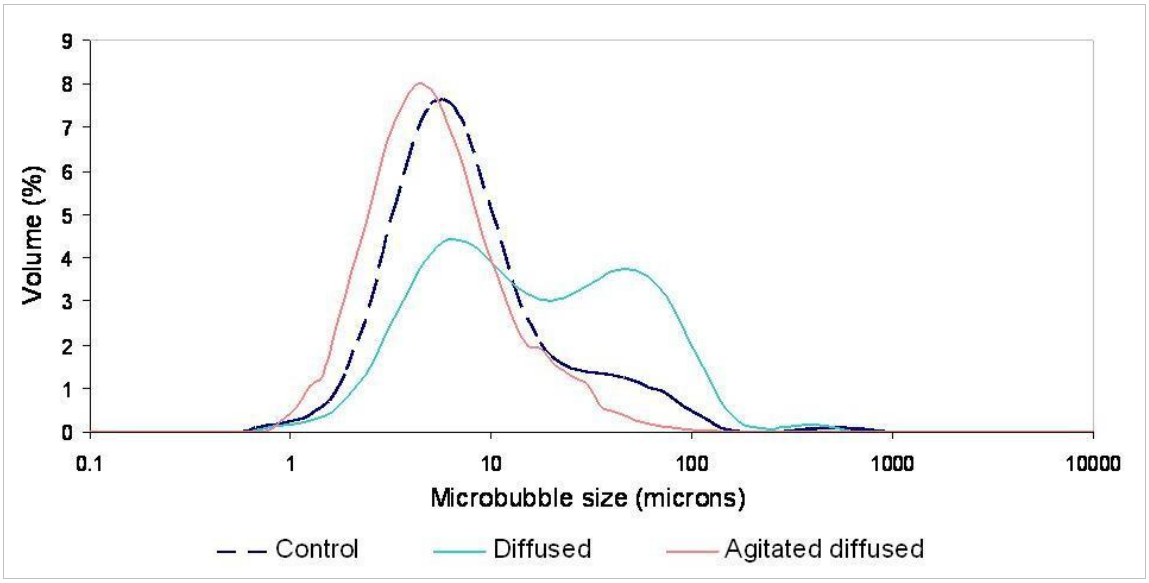

Figure 3-23: Microbubble size distributions for control, diffused and agitated samples.

3.4.5. Addition of Mannitol or Trehelose Sugars

With the exception of some anomalies the addition of mannitol and trehelose to the microbubble composition did not appear to significantly improve the echogenicity of the microbubbles. An increase in the amount of mannitol added appeared to cause a slight decrease in the echogenicity as illustrated by the linear trend line in Figure 3-24. The size distributions produced by different quantities of mannitol and trehelose are shown in Figure 3-25; these suggest that the addition of mannitol causes an increase in the average microbubble size which may account for the decrease in echogenicity of these samples.

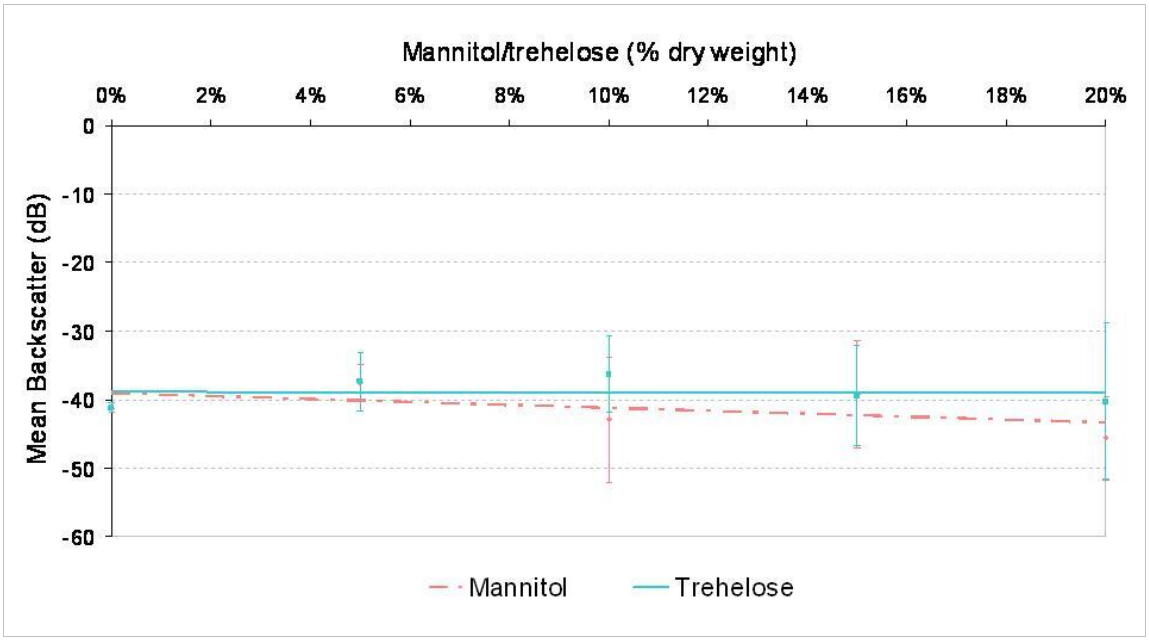

Figure 3-24: Mean backscatter at varying percentages of mannitol and trehelose.

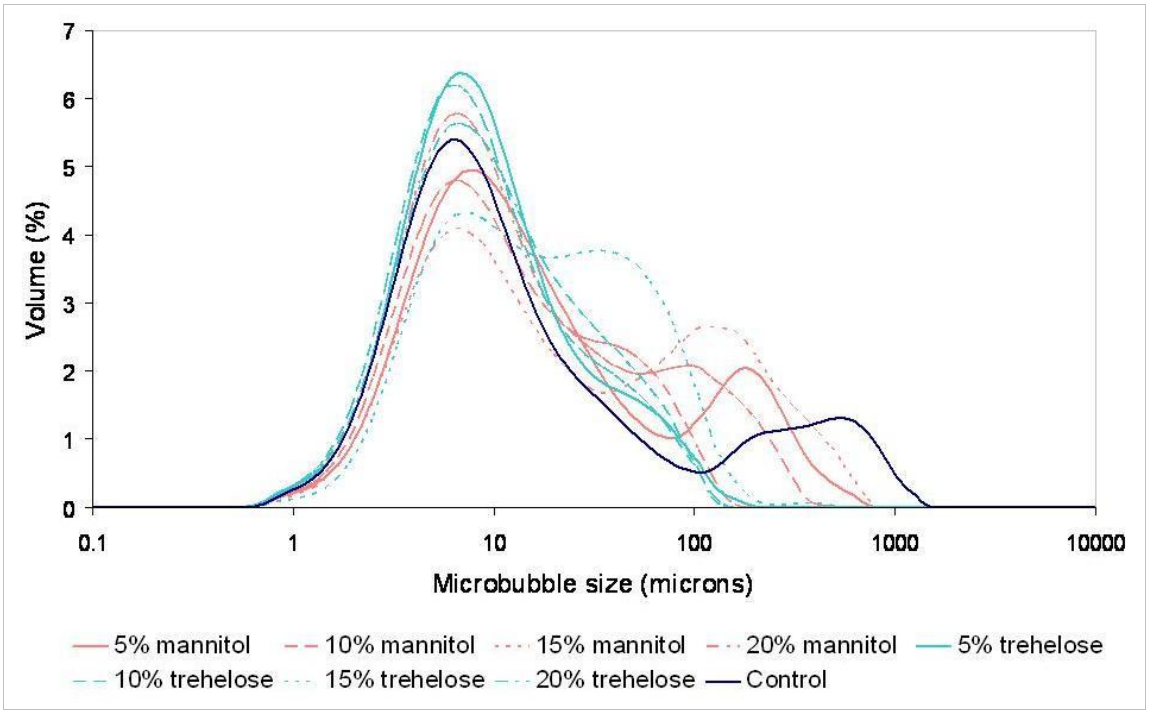

Figure 3-25: Size distributions produced by different percentages of mannitol and trehelose.

3.4.6. High Temperature Production

Figure 3-26 below shows the decrease in echogenicity observed for increasing production temperatures during the heating phase of the microbubble production. This data suggests that the optimum temperature range is between 70 and 80°C. However the transition temperature of the lipids lies between 60 and 77°C ('Avanti Catalogue 2008' 2008) so for all experiments the temperature was maintained above 77°C to ensure incorporation of all lipids into microbubble shell.

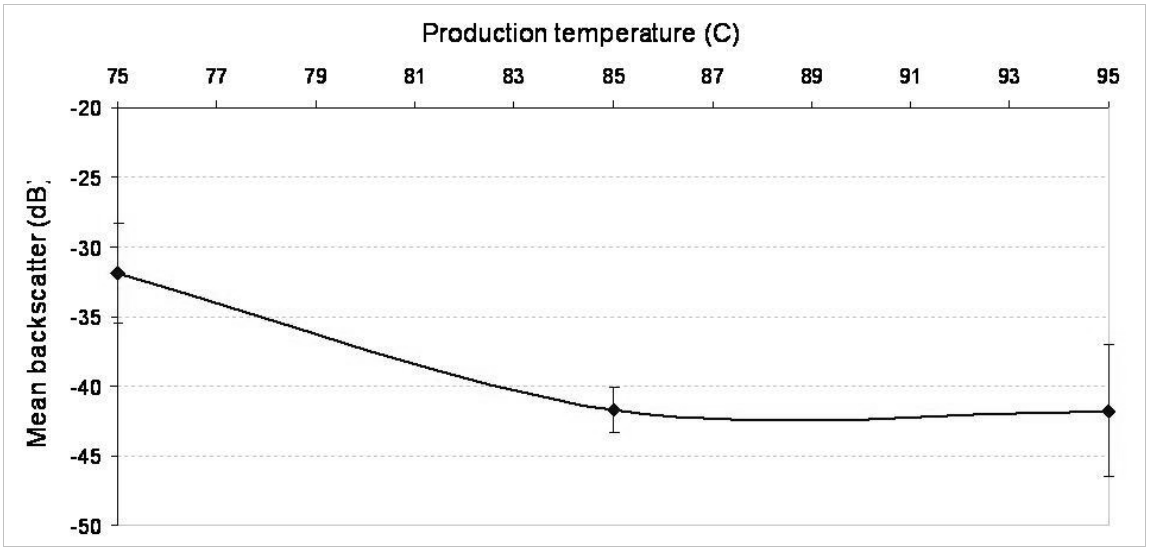

Figure 3-26: Mean backscatter produced by increasing production temperatures.

Figure 3-27 shows the size distributions produced by different production temperatures, all illustrate narrow size distributions with similar modal sizes suggesting that production temperature does not affect the sizes of the microbubbles; the author believes that the decrease in echogenicity could be due to degradation of the lipids at high temperatures.

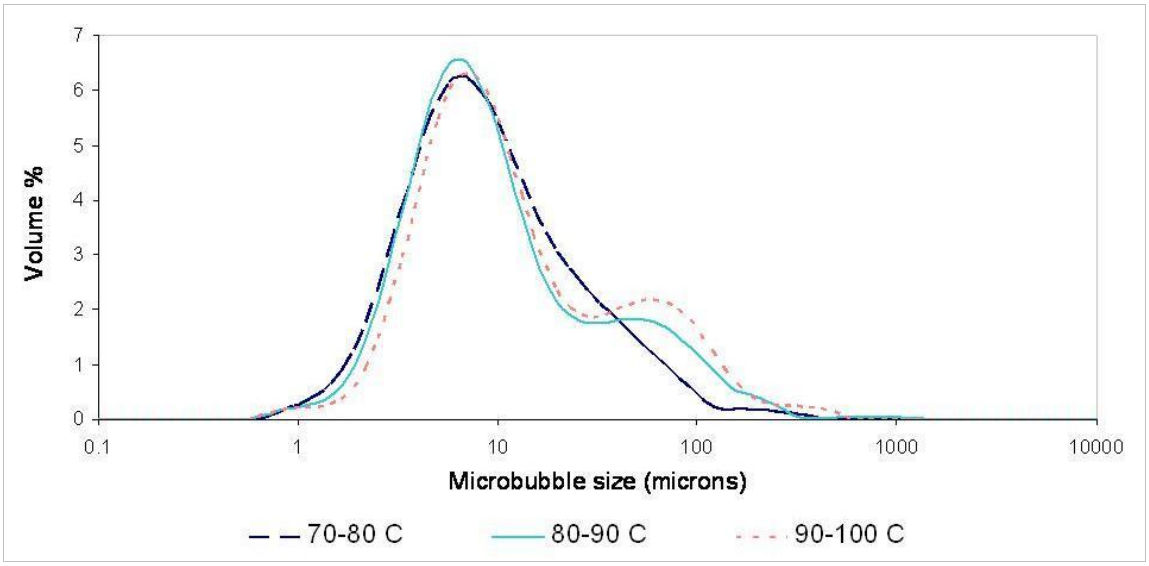

Figure 3-27: Size distributions observed at different production temperatures.

3.4.7. High Shear Mixing

The effect on the microbubble samples of mixing the lipids under high shear stress was assessed before and after the heating phase of production. It was found that both methods produced an increase in the echogenicity of the microbubble samples as shown in Figure 3-28 below. A smaller increase in echogenicity of the microbubbles was seen when combining the lipids with the high shear mixer before heating, but this difference was still >4dB. A significant increase of 8.4dB was seen when the microbubble sample was mixed after the heating phase.

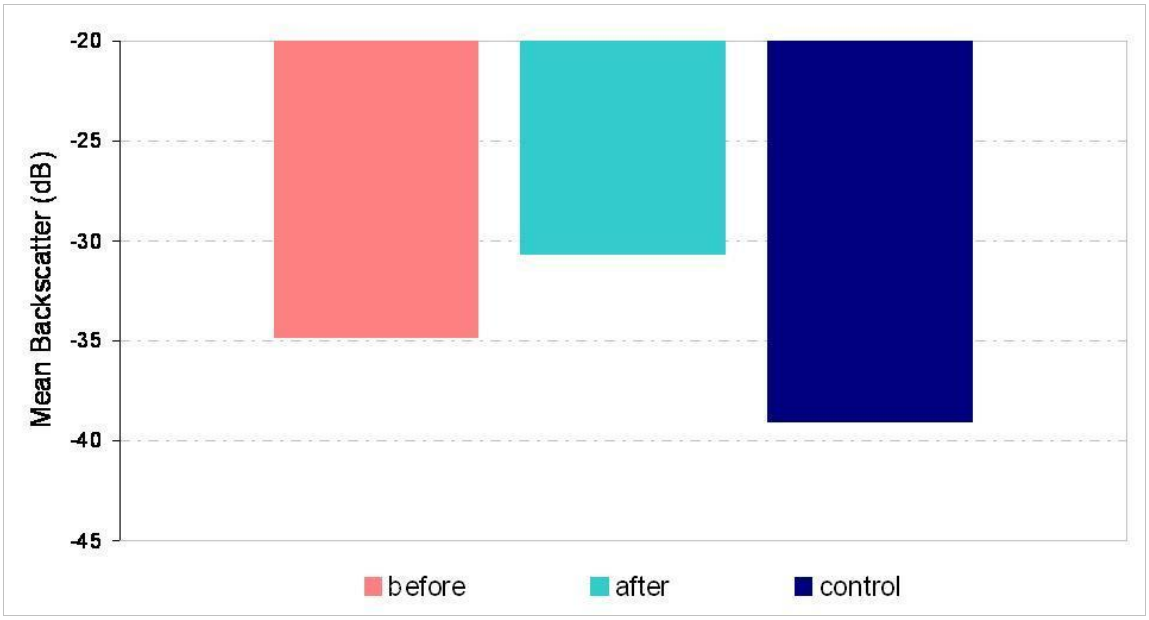

Figure 3-28: Mean backscatter produced by the high shear mixing device.

Although mixing after the heating phase produced the most significant increase in echogenicity it can be seen in Figure 3-29 below that this method produces a much wider size distribution with a greater average microbubble size. The greater microbubble size is not ideal for future in-vivo use and therefore high shear mixing before heating would be the optimum method to adopt.

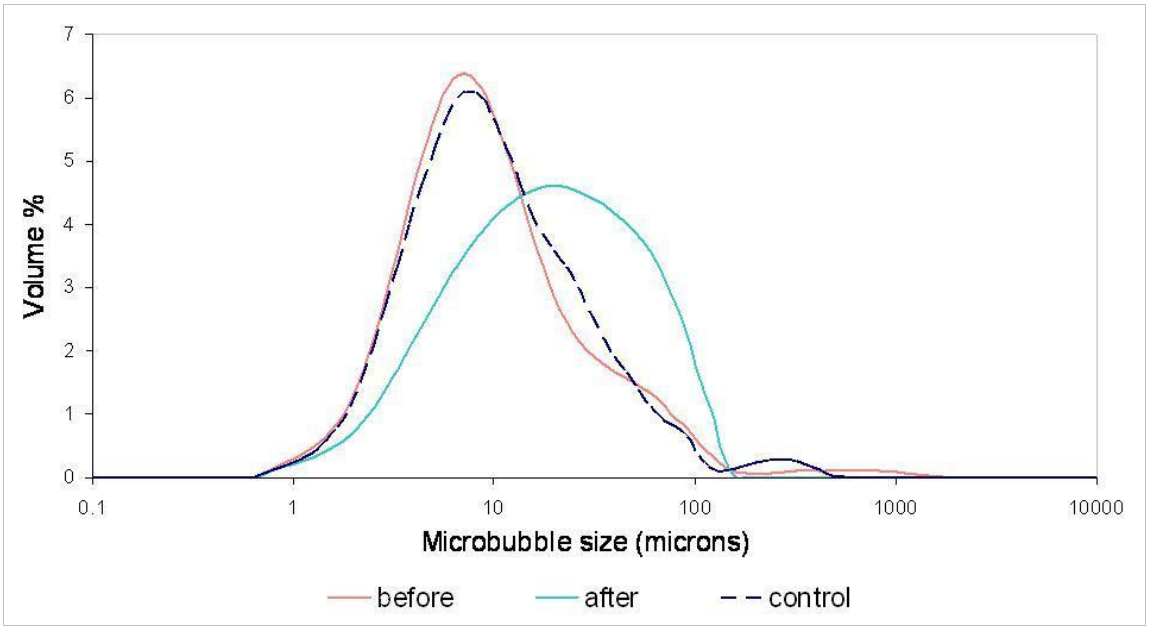

Figure 3-29: Average size distributions produced by high shear mixing of microbubble samples.

3.4.8. Summary

The chart in Figure 3-30 shows the relative echogenicity of each optimization technique investigated. This data shows that the three techniques which improve the echogenicity of the in-house microbubbles are agitation, sonication and high shear mixing. The control illustrated in Figure 3-30 was taken as an average of a variety of control samples, reproducibility of the in-house microbubble is varied, all results illustrated are taken as an average of at least three samples and any extreme variants were discarded and results collected again. There is a statistically significant difference in the mean backscatter from microbubbles produced using the different techniques ($p<0.001$).

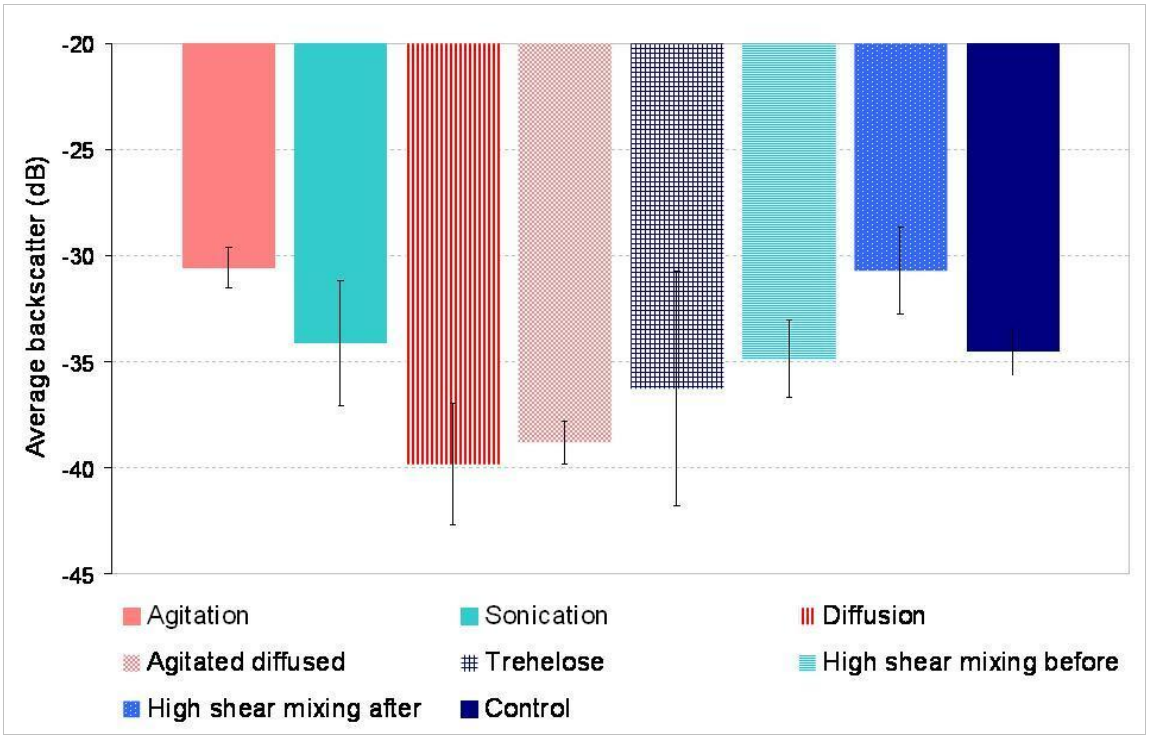

Figure 3-30: Comparison of different optimization techniques and their effect on the mean backscatter of the microbubble sample.

3.5. Discussion

Different chemical compositions and production techniques have been compared. This was in order to optimize the echogenicity of the in-house UCA for use with 40MHz IVUS. The echogenicity of the in-house agent has been assessed through the analysis of the RF data for each sample of microbubbles produced. In addition the agents have been observed under a microscope and their size distributions assessed.

An investigation into the chemical composition and its effect on the mean backscatter of the microbubbles has shown that the 30% cholesterol composition was the most echogenic sample. The 30% cholesterol microbubbles were also the most reproducible composition with the smallest standard deviation in the results. Since reproducibility is

an important factor in production of the in-house agent this was also a deciding factor in the selection of a composition for further optimization.

A variety of different techniques have been investigated in the optimization of the in-house agent. These have been compared in Section 3.4.8. From the comparison of results it was found that agitation and high shear mixing produced the most echogenic samples; this is inline with techniques used by other authors (Klibanov et al. 2004; Schneider et al. 2004; Schneider et al. 2006). Diffusion of the in-house agent was found to increase the microbubble size and as a result of this the mean backscatter of the samples was reduced.

Agitation was selected as the optimum production method for the in-house microbubble and an investigation carried out into the length of agitation and its effect on the mean backscatter of the microbubbles. This suggested that microbubble size decreases as the agitation time increases. In addition the mean backscatter results suggest that echogenicity increases with agitation time up to 45s and then decreases sharply as agitation time is increased beyond 60s. The author believes that agitating the microbubble samples for longer than one minute causes the microbubble sizes to drop below their resonance radius for 40MHz ultrasound, therefore making the samples less echogenic.

The stability of the in-house agent over time has also been assessed. There was found to be little significant variation in the mean backscatter of the agent over a 24 hour period. In addition it was discovered that the agent, if stored in a glass vessel at 2-5°C, can be stored for up to three months with minimal variation in the mean backscatter. However, it is advised that the agent is observed carefully after long storage periods as some samples have shown signs of fungal growth. This was likely to be due to contamination of the storage vessels.

The optimum microbubble size for resonance at 40MHz was 1.4µm diameter as presented in Appendix A. This is smaller than the size of microbubbles produced

throughout this investigation as, using the techniques demonstrated throughout this Chapter, it wasn't possible to reduce the microbubble diameter further. However this result was calculated using approximate values for the shell properties, fluid density and pressure. The results presented in Section 3.4.3 show that the echogenicity of the microbubbles dropped off with decreasing microbubble diameter suggesting that the larger 5-6µm microbubbles are resonating at 40MHz. Further investigations into micorbubble size, shell properties and resonance frequencies would need to be carried out in order to confirm this.

3.6. Summary

The data collected and illustrated in this chapter suggest that, of all the optimization techniques applied, agitation and high shear mixing produced the optimum microbubble suspension in terms of echogenicity and mean backscatter. However it is also important for an optimum microbubble sample to have a narrow size distribution with a small average microbubble diameter such that when reaching in-vivo studies the microbubbles will be small enough to pass through the vascular system. In conclusion, the production techniques which were employed for continued production of the microbubbles include high shear mixing prior to the heating phase of production and agitation post heating phase. In addition to improving the echogenicity and size distribution of the microbubble samples this also reduces production times. The final method of production can be seen in Appendix D.

Chapter 4 Laser Doppler Anemometry Measurements and Wall Shear Stress Estimations

4.1. Introduction

In order to assess the strength of attachment of a targeted microbubble ultrasound contrast agent under shear stress it was necessary to design a flow chamber in which the wall shear stress (WSS) on the cell surface could be accurately measured. Laser Doppler anemometry (LDA) has previously been used to acquire velocity profiles of low flow volumes within a novel chamber from which WSS has been calculated (Butler et al. 2005). In this chapter the development of a novel, high flow volume, flow chamber and the methods used to ascertain the WSS within the flow channel at different flow volumes and with different viscosity fluids is described.

Human physiological flow volumes in the coronary arteries lie between 80 and 120ml/min (Arronson et al. 2004). The flow chamber for this investigation has been designed to be used up to flow volumes of 350ml/min to enable assessment of very high

WSS. This was in order for attachment of the agent to be assessed under expected physiological wall shear stress in mice of 40Pa (Cheng et al. 2007a) for future small animal studies.

Different viscosity fluids have been observed in order to take into account viscosity variations due to hematocrit as described in Chapter 1 and to increase the maximum WSS attainable within the flow chamber. Glycerol solutions have been used to produce different viscosity fluids, varying from a 40% glycerol solution (by mass) to 80% glycerol with a range of viscosities from 0.0045Pa·s to 0.0599Pa·s.

4.2. Measuring flow velocity

There are several different methods currently used to measure flow velocity in different situations including, Doppler flow wire, particle image velocimetry (PIV) and laser Doppler anemometry (LDA).

A Doppler flow wire consists of a piezoelectric crystal mounted on the tip of a guide wire, about 0.014 inches (0.356mm) in diameter. Also known as a Doppler guide wire, it is predominantly used in cardiology to measure the velocity of blood in the coronary vessels (Gorski and Watson 2005; Millar 1988). This is an invasive technique and the physical presence of the guide wire within the flow can effect the measurements made, it is therefore not suitable for this application.

PIV is an optical method of acquiring flow velocities and is commonly used to assess aerodynamics around vehicles and aircraft. The set-up requires a laser focused into a light sheet, a camera, and seeding particles suitable for the flow to be studied. As the seeding particles are carried through the light sheet by the flow they scatter light. At least two exposures are needed from the camera in order to measure the velocity, when two frames have been collected the frames are divided into interrogation areas (IAs) and the displacement vector of the scattered light in each IA is calculated. The velocity of flow in the IA can then be calculated if the time between the frames is known. The

advantages of PIV are that no invasive probes are required and with high speed data analysis data can be collected in real time. However, due to the light sheet it would not be an effective or efficient technique for measuring the flow through a small channel in the parallel plate flow chamber described in Section 4.3.

LDA is a high resolution optical technique which uses laser light scattered from seeding particles within the flow to calculate the fluid velocity components from the Doppler Effect. LDA is an accurate method of determining flow profiles within small channels and as a result it the method of choice in determining the flow profiles within the flow chamber developed.

4.2.1. Laser Doppler Anemometry

LDA has been used to assess the velocity profiles within the flow chamber. The first reported use of LDA was in 1964, when the first velocity measurements using a reference beam system were made (Yea and Cummins 1964). This reference beam system can be seen in Figure 4-1. The laser beam is split and one beam focused through a flow tube containing scattering particles, the scattered laser light from this beam is then collected through a port in the flow tube and focused onto the detector. The other beam is focused directly onto the detector acting as a reference beam, with zero velocity value. The frequency of the scattered light can then be used to calculate the flow velocity, when compared to the reference beam.

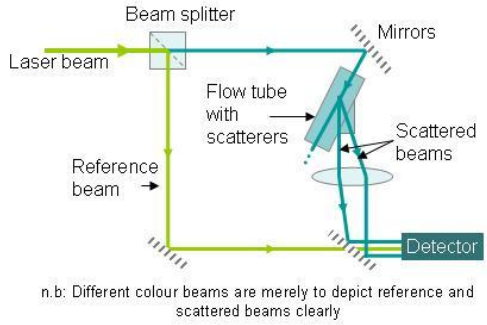

Figure 4-1: Reference beam system used by Yea and Cummins in 1964 adapted from image by Butler (2005).

This reference beam system has evolved into a dual beam system, the type of system which has been used for the investigations outlined in this chapter. The dual beam system is composed of a single beam, split into two. One beam is then passed through a Bragg cell and frequency shifted and both beams pass through a beam expander before bisecting to form a measurement volume, as illustrated in Figure 4-2a. The purpose of the frequency shift in the second laser beam is to enable identification of the direction of flow; the beam expander is designed to reduce the measurement volume and therefore improve the resolution of the system. Figure 4-2b shows how the backscattered light is collected by the photodiode for processing.

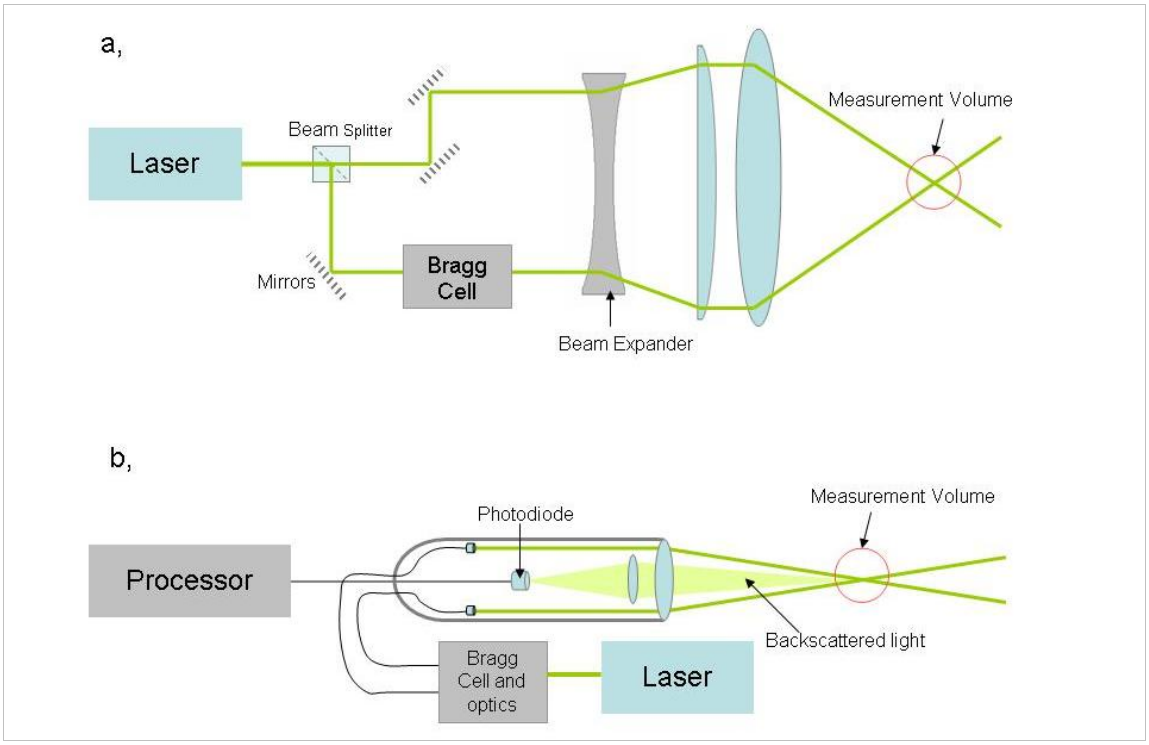

Figure 4-2: Dual beam LDA system: a, beam splitter, Bragg cell and beam expander; b, backscattered light from measurement volume (adapted from Dantec Dynamics reference material (DantecDynamics 2007)).

The LDA Fringe Model

The fringe model is often used to describe how velocity measurements can be acquired through the use of LDA (Durst et al. 1976; Watrasiewicz and Rudd 1976). As the coherent laser beams cross they create a fringe pattern as illustrated in Figure 4-3. When the seeding particle is introduced to the flow and passes through this fringe pattern it scatters light back to the sensor at a frequency which is proportional to the velocity of the particle. If it is assumed that the particle is travelling at the same velocity of the fluid the fluid velocity at that discreet point can be calculated using Equation 4-1.

$$v = f_d d_f$$

Equation 4-1: Fluid velocity

Where f_d is the scattered frequency and d_f is the fringe spacing calculated from Equation 4-2 in which λ is the wavelength of the laser light and θ the angle between the two incident beams:

$$d_f = \frac{\lambda}{2\sin\left(\theta/2\right)}$$

Equation 4-2: Fringe Spacing

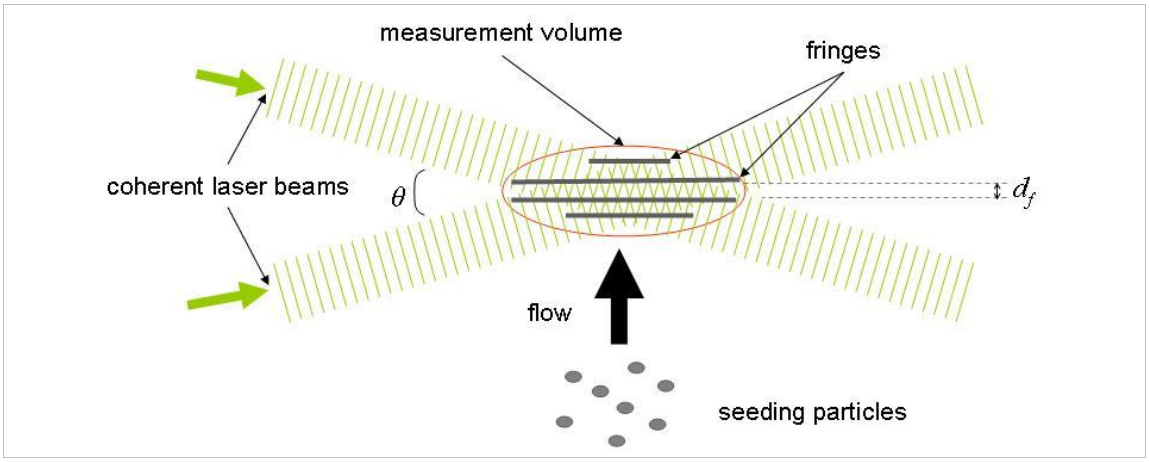

Figure 4-3: Fringe model

4.3. Flow Chamber Development

Butler et al (2005) initially developed a novel parallel plate flow chamber in order to measure the wall shear stress which would act upon a surface to which microbubbles could be attached. The flow chamber was calibrated to 3.4Pa. This flow chamber exhibits the following features:

- Glass slide at front of chamber making it suitable for use with LDA system.
- 6×2mm flow channel, 120mm in length.
- Two sample wells for attachment of microbubbles onto agar.
- Inlet and outlet reservoirs in order to stabilise the flow entering the flow channel.

In order to more accurately assess the wall shear stresses upon surfaces within coronary blood vessels at higher WSS, a new flow chamber has been designed as illustrated in Figure 4-4. The new flow chamber has been produced with a 3×3mm flow channel to more accurately resemble the cross section of a 3mm coronary artery, and the flow channel has been increased to 300mm in order to ensure that a fully developed flow profile is formed. The new flow chamber also exhibits a 140mm agar channel for attachment of microbubbles to a cellular surface. A glass microscope slide has been incorporated in the observation region for compatibility with the LDA system and two holes with 2mm diameter have been drilled behind the agar sample for IVUS investigations. Inlet and outlet reservoirs are also present with wider inlet and outlet to enable higher flow volumes.

Large bore Luer style connectors were used to attach tubing to the inlet and outlet of the flow chamber. The fluid travels through the tubing, propelled by the pump, and through the inlet identified on the left of Figure 4-4c. The inlet reservoir is then filled and the fluid travels along the flow channel of the central panel in Figure 4-4b and across the agar surface which is embedded in the rear panel such that it is flush with the back surface of the flow channel. The front panel in Figure 4-4a encases the front of the flow channel. The outlet reservoir then prevents turbulence occurring as the fluid passes out of the flow chamber and back through the pump.

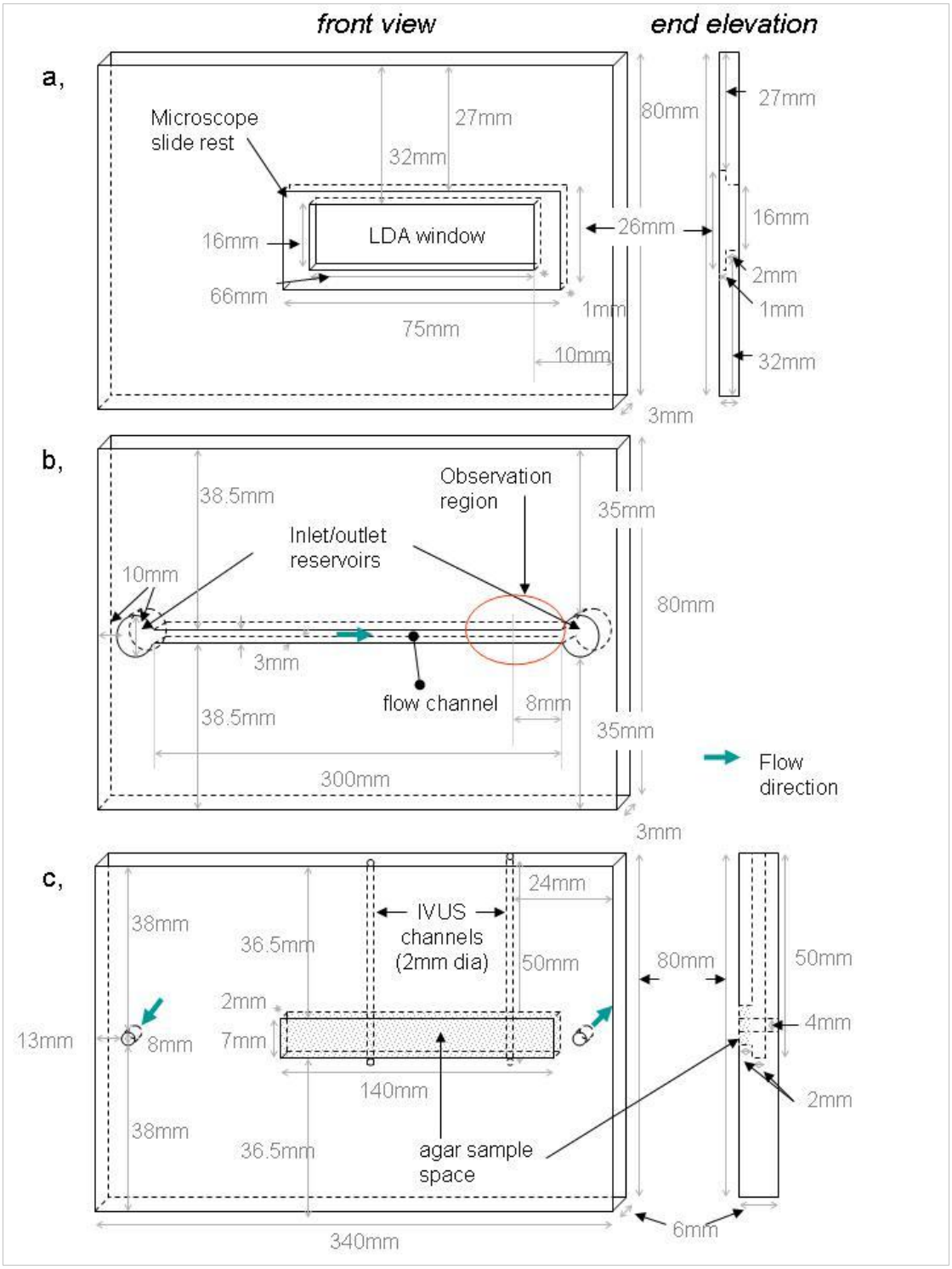

Figure 4-4; Schematic of parallel plate flow chamber showing features of a, front panel, b, central panel and c, rear panel (not to scale).

A photograph of the assembled flow chamber can be seen in Figure 4-5 identifying the various features.

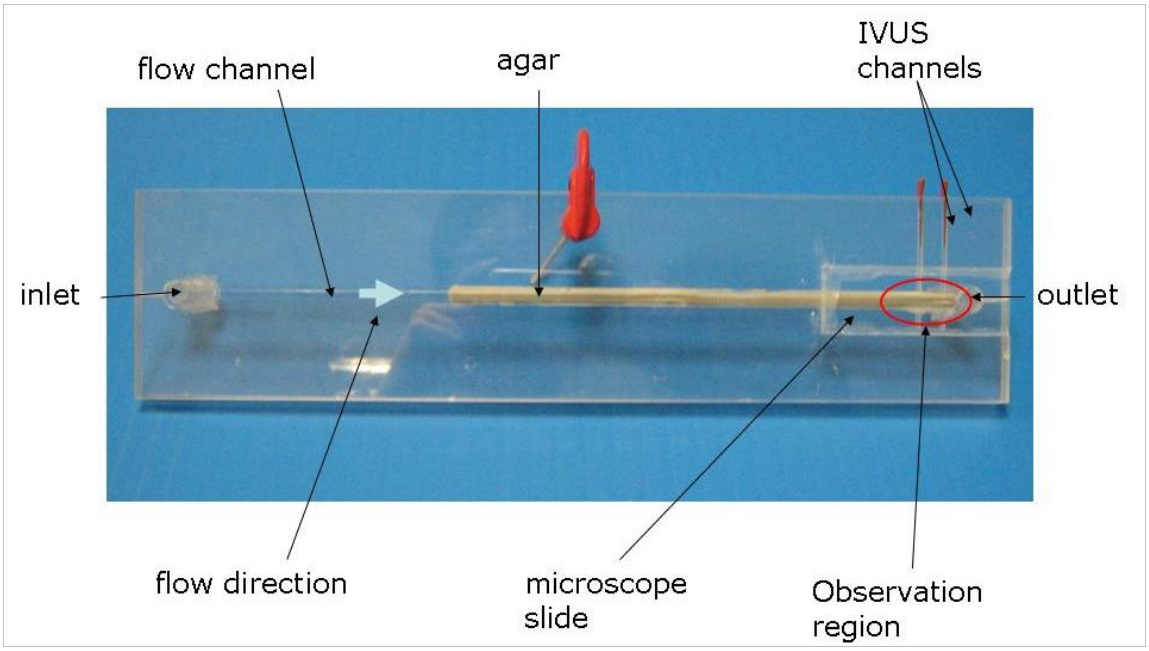

Figure 4-5: Photograph of assembled flow chamber.

4.3.1. Reynolds Number and Entrance Length

In order to accurately assess the wall shear stress (WSS) to which microbubbles will be subjected, it is important to understand the flow regime within the flow chamber. Laminar flow occurs when a fluid flows in parallel layers as illustrated in Figure 4-6, whilst turbulent flow is characterised by chaotic fluid motion. In blood vessels flow is often turbulent due to the many bifurcations and the surface variations. However, for the purpose of these investigations the flow chamber has been developed such that laminar flow can be maintained to enable an accurate assessment of the WSS. In true laminar flow a parabolic flow profile will be developed due to the drag between each layer of fluid, this is illustrated in Figure 4-6. A fully developed flow profile is achieved when the profile is parabolic and unchanging.

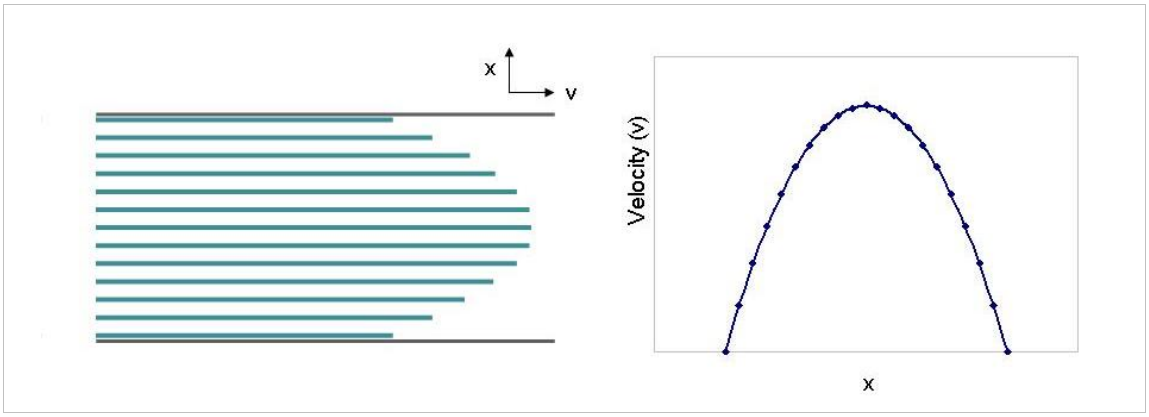

Figure 4-6: Laminar parabolic flow

Initially derived in 1883 (Reynolds 1883; Rott 1990), the Reynolds number is the ratio of viscous to inertial forces within a fluid and is used to predict flow regimes. Low Reynolds numbers suggest laminar flow whilst much higher Reynolds numbers indicate turbulent flow. The Reynolds number is used in fluid dynamics to determine whether turbulent flow can be expected and is also valuable in modelling aerodynamic shapes (Streeter 1962). The Reynolds number is defined in Equation 4-3 below (McDonald 1960; Nichols and O'Rourke 1990).

$$\mathrm{Re} = \frac{dynamic \cdot pressure}{shearing \cdot stress} = \frac{\rho \bar{v}_s^2 / h}{\mu \bar{v}_s / h^2} = \frac{\rho \bar{v}_s h}{\mu} = \frac{\bar{v}_s h}{\upsilon}$$

Equation 4-3: Reynolds number

Where Re is Reynolds number, ρ is density of the fluid, μ is the dynamic viscosity, υ the kinematic viscosity, h and $\bar{v}_s$ the characteristic length or hydraulic diameter and mean fluid velocity respectively (all SI units).

The hydraulic diameter is the equivalent diameter for a non-circular channel and can be found in Equation 4-4 (Nichols and O'Rourke 1990), where A is the cross-sectional area

and *U* is the perimeter of the channel in contact with the fluid. The dynamic viscosity is the absolute viscosity of a fluid whilst the kinematic viscosity is the dynamic viscosity divided by the density of the fluid.

$$D_h = \frac{4A}{U}$$

Equation 4-4: Hydraulic diameter

Reynolds numbers for the newly designed and developed chamber lie between 332 and 1935 for flow volumes of 60 to 350ml/min. The critical Reynolds number, at which laminar flow becomes turbulent lies in the region of 2000 to 3000 which suggests that laminar flow can be assumed in the flow chamber.

The entrance lengths (*Le*) within the flow chamber can be determined from Equation 4-5 (Richards 1989). This gives the distance at which a fully developed flow profile can be assumed.

$$Le = 0.06 \operatorname{Re} h$$

Equation 4-5: Entrance length

For water at flow volumes of 60-350ml/min in the flow chamber the entrance length lies between 59.7mm to 348mm. The chamber is only 300mm in length and as such at 350ml/min the flow profile may not be fully developed. At all other flow volumes studied and for all glycerol concentrations a fully developed flow profile can be assumed within the observation region. Reynolds numbers and entrance lengths derived from Equation 4-3 and Equation 4-5 respectively, at all glycerol solutions for the flow volumes investigated are given in Table 4-1.

Flow Volume (ml/min)	Water		40% glycerol		60% glycerol		80% glycerol	
	Re	Le (mm)	Re	Le (mm)	Re	Le (mm)	Re	Le (mm)
60	332	59.7	81.5	14.7	16.0	2.89	6.72	1.21
80	442	79.6	109	19.6	21.4	3.85	8.96	1.61
100	553	99.5	136	24.5	26.7	4.81	11.2	2.02
120	663	119	163	29.3	32.1	5.77	13.4	2.42
140	774	139	190	34.2	37.4	6.73	15.7	2.82
160	884	159	217	39.1	42.7	7.69	17.9	3.23
180	995	179	245	44.0	48.1	8.66	20.2	3.63
350	1935	348	475	85.6	93.5	16.8	39.2	7.06

Table 4-1; Reynolds numbers and entrance lengths for different viscosity fluids, at various flow volumes.

4.4. Method

The apparatus was set up as illustrated in Figure 4-7 below. The LDA probe volume was focused on the observation region, through the microscope slide, during measurements in order to avoid scattering from surface inconsistencies in the Perspex. This was achieved by moving the laser on its traverse until the point where the beams converge sat over the observation region of the flow channel.

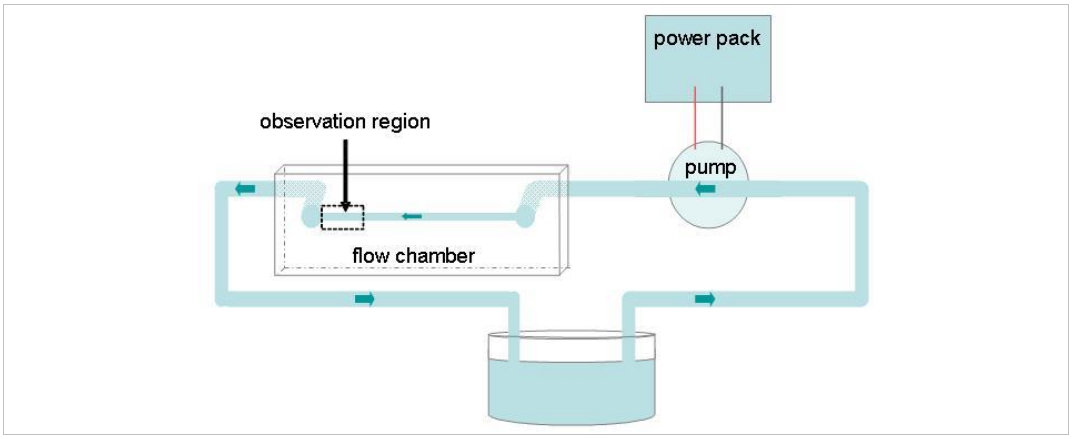

Figure 4-7; Experimental set-up for LDA investigations (arrows signify direction of flow)

The fluid under investigation was propelled through the chamber by a Micropump (IDEX corporation, Vancouver, WA USA), which was powered by a 30V power pack.

The fluid was seeded with Timiron® Super Silk (Merck, NJ USA), a fine powder with particle size range of 3-10μm.

4.4.1. Flow chamber

The parallel plate flow chamber was sealed with silicone grease and the different panels were firmly clamped together. Water or glycerol solution was then passed through the system at the maximum pump voltage for five minutes in order to remove bubbles from the system, this was verified visually.

The pump voltages were then calibrated in order to produce the flow volumes listed in Table 4-1. Calibration details can be found in Appendix E. The chamber was visually checked for leaks, bubbles and any blockages in the flow channel. Flow volumes were measured daily and whenever the flow chamber was taken part for cleaning to ensure reliable results, this was achieved in the manner described in Appendix E.

4.4.2. LDA

The position of the measurement volume was controlled by a traverse system with three dimensional translations. Prior to beginning measurements it was necessary to determine a (0,0,0) co-ordinate so that the location of the flow profile could be ascertained in relation to a central position, and to ensure that flow profiles were collected at the same position along the flow channel. For the purpose of these investigations the (0,0,0) co-ordinate was established as the centre of the flow channel as illustrated in Figure 4-8.

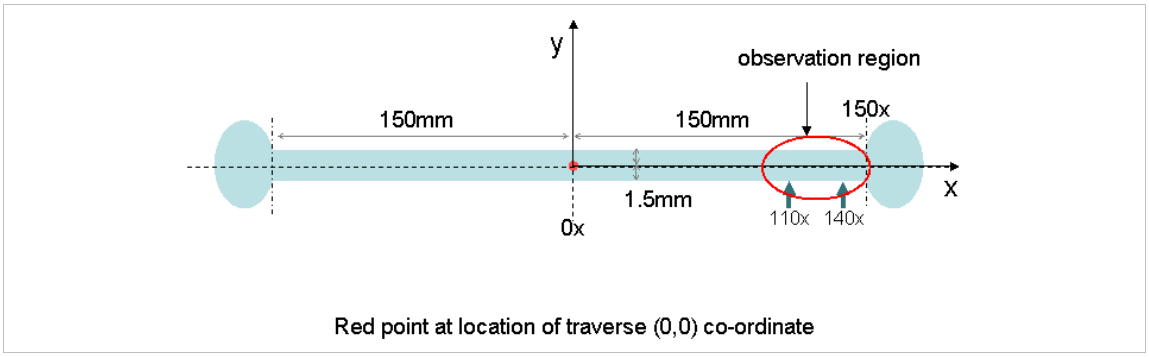

Figure 4-8; Location of traverse (0,0) co-ordinate, relative to flow channel; (110x and 140x locations identified)

4.4.3. Preliminary investigations

In order to find the location of $z = 0$, the centre of the flow channel in the z-plane, a selection of flow profiles from front to back of the channel were acquired at the (110, 0)mm co-ordinate, $y = 0$ was located visually and measurements were taken at 110mm along the flow channel, in the observation region. It was assumed that the location of the peak velocity would indicate the centre of the flow channel in the z-plane if a parabolic velocity profile was produced. Once this position was determined the probe volume was moved to the centre of the channel and the system was re-set at this location. Flow profiles produced through the z-plane can be seen in Appendix F. This procedure was repeated each time the chamber was set-up.

When the (0,0,0) co-ordinate was established measurement sets were collected between $-4 \leq y(mm) \geq +4$, at two different locations along the flow channel, $x = 110\,\text{mm}$ and $x = 140\,\text{mm}$, as illustrated in Figure 4-8. To ensure that a fully developed flow profile had been established, these flow profiles were then compared to a parabolic, quadratic trend-line, to confirm that parabolic flow was achieved. These results can be seen in Figure 4-9. The flow profiles in Figure 4-9 suggest that a fully developed flow profile is produced at $x = 110$ as the trend-lines illustrate a close correlation between the two profiles and the fit of the trend-line, as indicated by the R-squared value is >89%

(p<0.0001). However the results also suggest that there is more variance in the flow profile located 110mm along the flow channel than at 140mm, it is believed that this is due to the discontinuity between the Perspex and the glass slide on the front panel of the flow chamber. In light of this observation measurements were made at the $x = 140\,\text{mm}$ location.

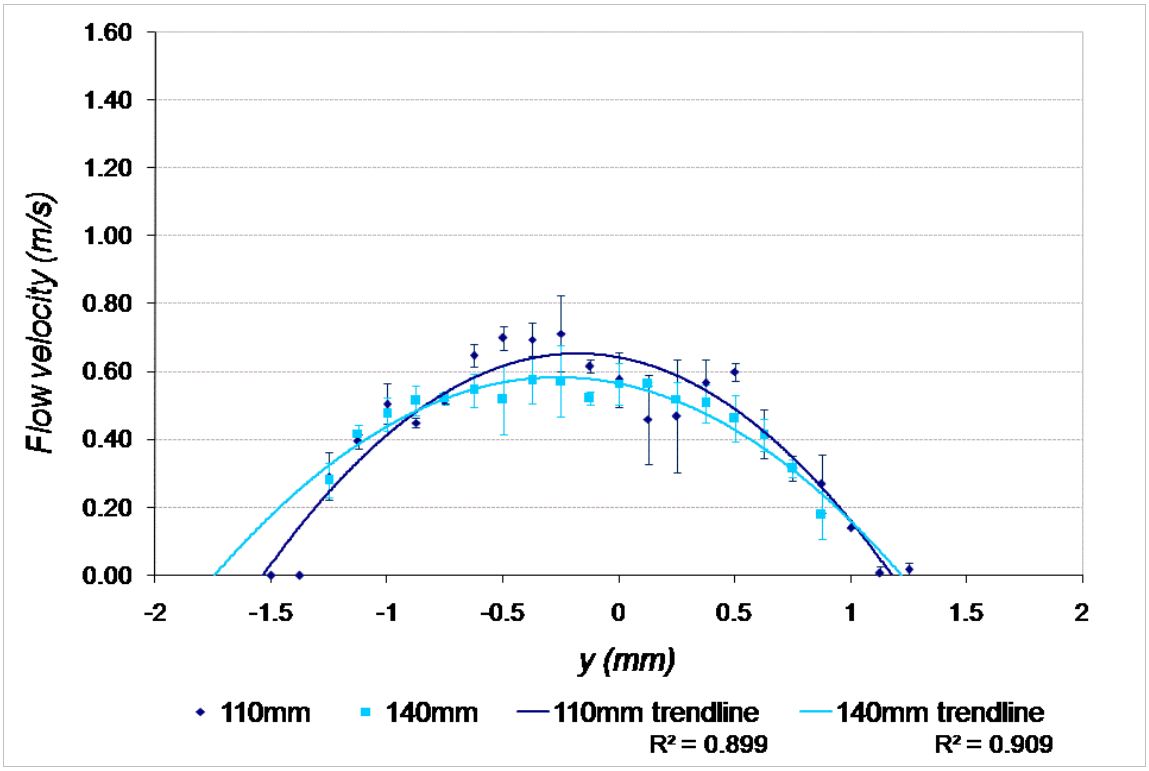

Figure 4-9; Graph illustrating fully developed flow profiles in observation region (160ml/min flow volume; error bars represent one standard deviation).

The following graph in Figure 4-10 illustrates the flow profiles achieved at $x = 110\,\text{mm}$ and $x = 140\,\text{mm}$, for a flow volume of 350ml/min. The quadratic trend-line at the $x = 110\,\text{mm}$ location has a fit <0.8 (p<0.0001), suggesting that fully developed flow has not been achieved here, however at $x = 140\,\text{mm}$ the trend-line has an R-squared value >0.95 (p<0.0001) and as a result despite numerical calculations, as presented in Table 4-1, suggesting that fully developed flow will not be reached at this flow volume, it will

be assumed that fully developed flow has been achieved, confirming the x=140mm location as a suitable co-ordinate for collecting the final results.

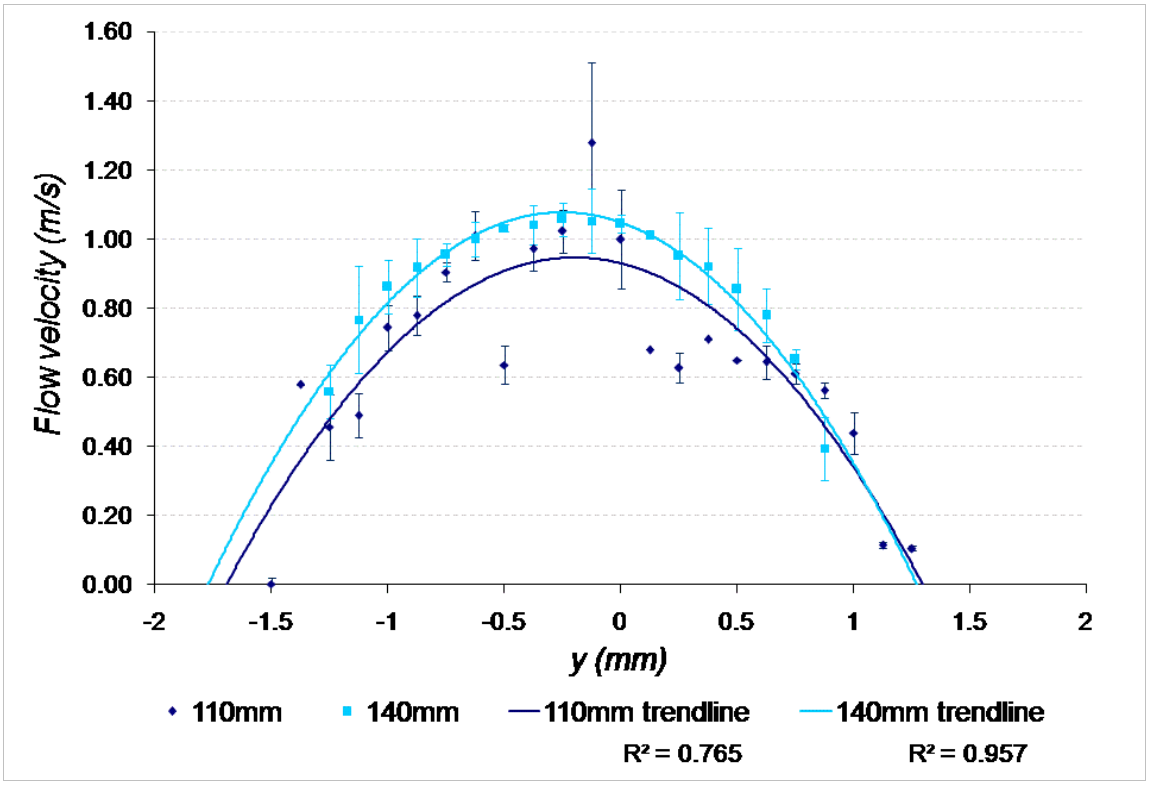

Figure 4-10; Flow profiles collected at 110mm and 140mm along the x-axis for a flow volume of 350ml/min.

Before commencing the final investigations it was important to assess the reproducibility of the results and flow profiles collected. The graph in Figure 4-11 shows four flow profiles collected at 350ml/min flow volume over two days. Run 1 and 2 were collected approximately 30 minutes apart and runs 3 and 4 were collected 24 hours later approximately 30 minutes apart. Before measurements 3 and 4 were collected the flow chamber was taken apart and reassembled to ensure that this did not affect the flow profiles collected. The results illustrated in Figure 4-11 show that the flow profiles are highly reproducible.

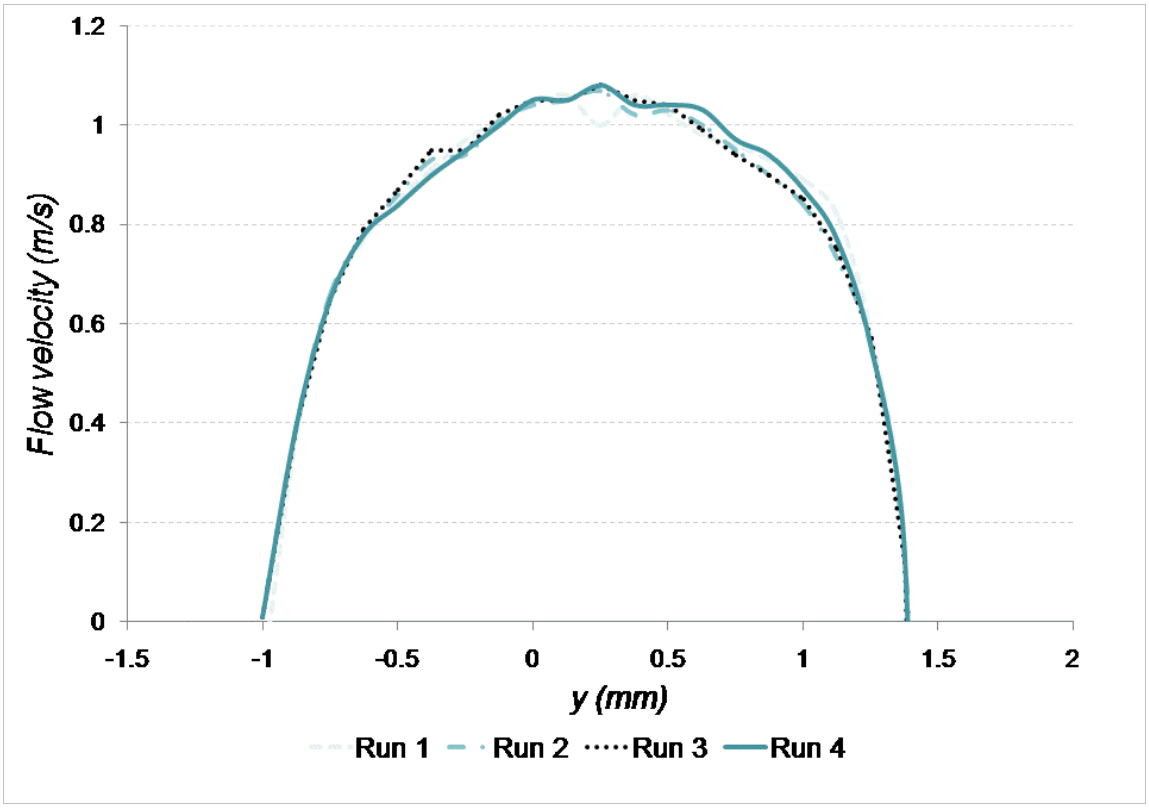

Figure 4-11; Four flow profiles collected over two days for 350ml/min flow volume.

The final preliminary investigation involved changing the direction of the flow within the flow chamber. The purpose of this investigation was to assess the effect of discontinuities in the flow chamber, in addition the potential for reflections or scatter from the agar well and IVUS channels could be eliminated. To achieve this, the flow inlet and outlet were reversed and the front panel of the flow chamber was rotated 180° in order to carry out measurements in the flow chamber close to the outlet as illustrated in Figure 4-12.

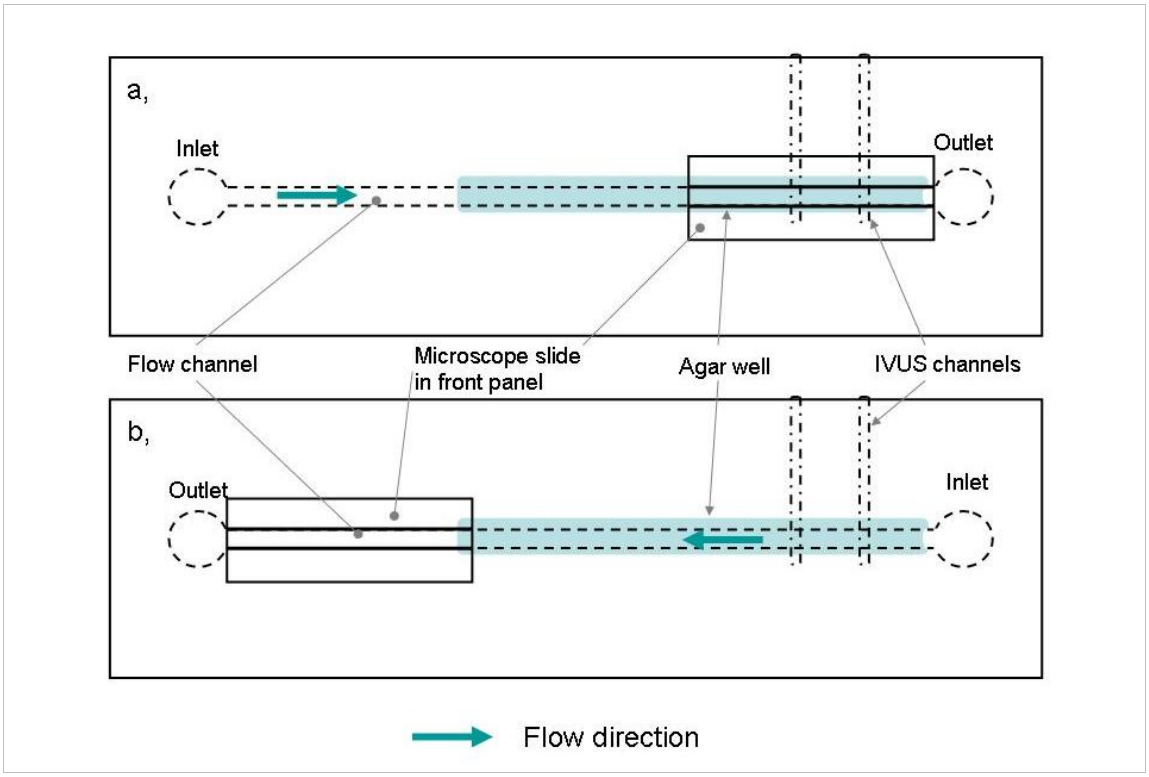

Figure 4-12: Schematic showing how reverse flow was acheived and measured; a, showing forward flow direction and b, showing reverse flow direction.

The graph in Figure 4-13 illustrates two average flow profiles collected for forward flow and reverse flow respectively at 140ml/min. The correlation of both data sets is above 85% ($p<0.0001$). In addition there is little variation in the two flow profiles indicating that there is good continuity with results from both directions and therefore, the flow channel is free of artefacts which may cause significant errors in the flow profiles collected. In light of this data the flow profiles were collected in the forward direction

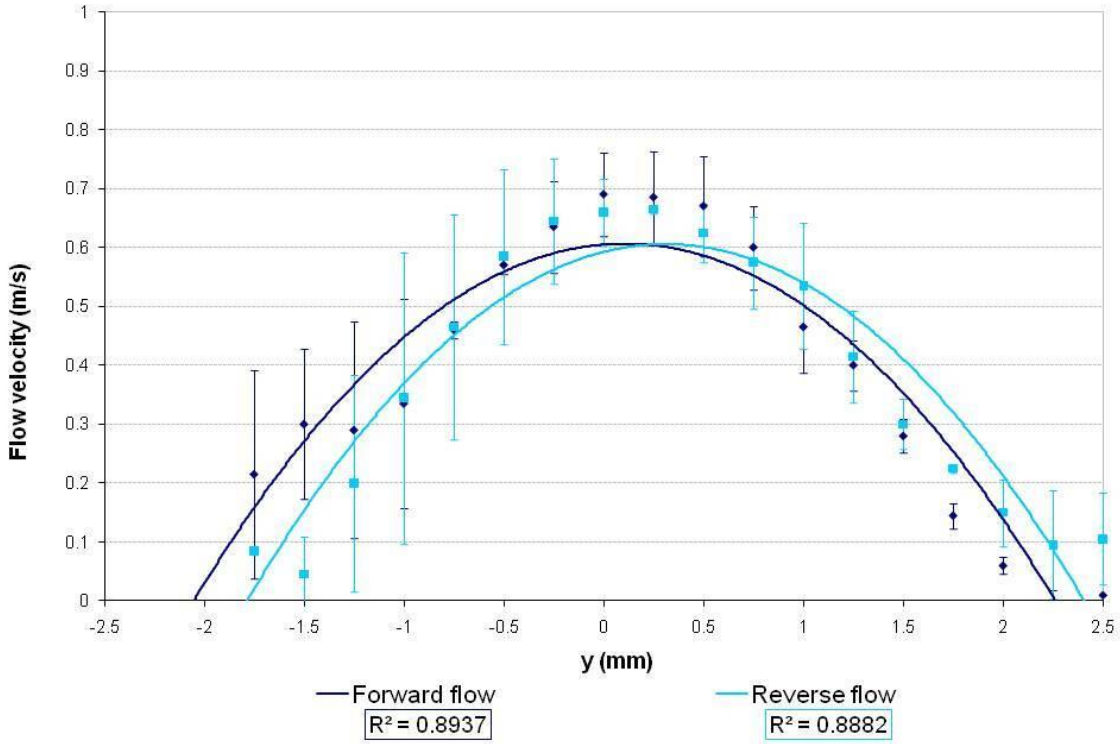

Figure 4-13; Flow profiles achieved from two opposite orientations with a flow volume of 140ml/min

4.4.4. Final Investigations

Once all controllable sources of error had been eliminated flow profiles were collected at $x = 140\,\text{mm}$ for flow volumes of 60, 80, 100, 120, 140, 160 and 180ml/min at glycerol and water solutions of 0 (water), 40, 60 and 80% glycerol by mass. Additional flow volumes of 350ml/min were studied for water, 40% and 60% glycerol solutions, however higher flow volumes were not attainable with an 80% glycerol solution, due to equipment limitations, so the maximum flow volume studied in this case was 250ml/min.

The results were then analysed and the wall shear stresses produced by different glycerol concentrations and the above flow volumes were calculated.

4.5. Final Results and Discussion

The following graphs show the flow profiles collected for water and 40%, 60% and 80% glycerol solutions at the flow volumes investigated. The data represented in these graphs has been corrected, where necessary, to show positive flow profiles, this has been achieved by multiplying the raw data by (-1). In addition the data below has been averaged over four investigations unless stated, and the errors illustrated represent one standard deviation of the data sets.

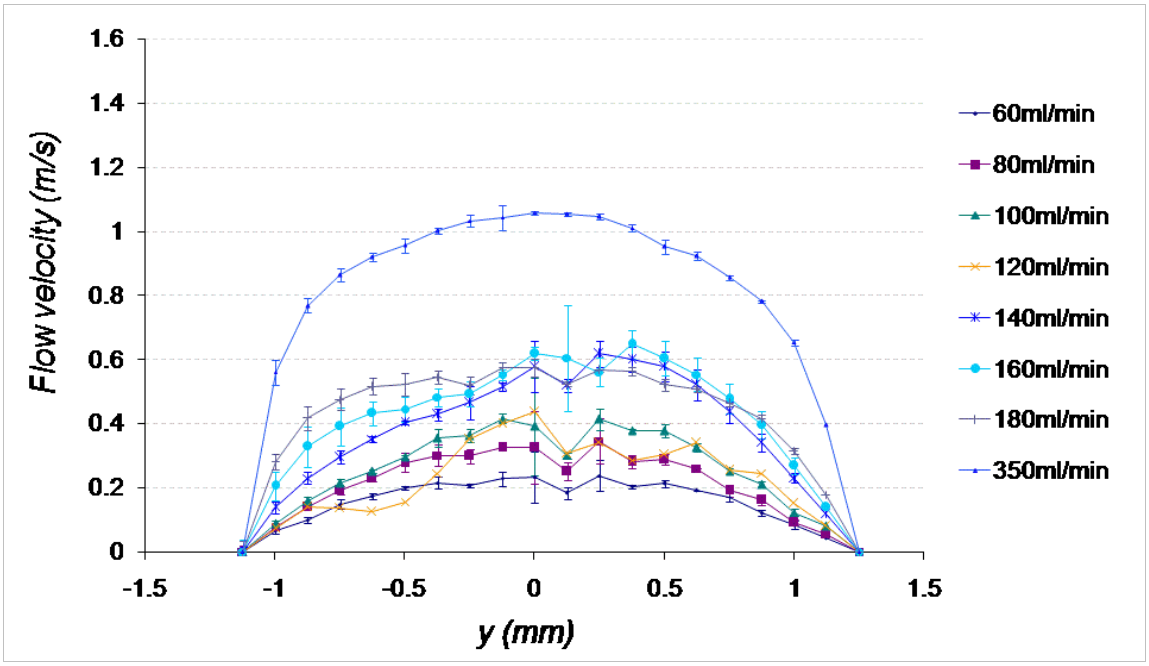

Figure 4-14; Average flow profiles for water; flow volumes between 60ml/min and 350ml/min.

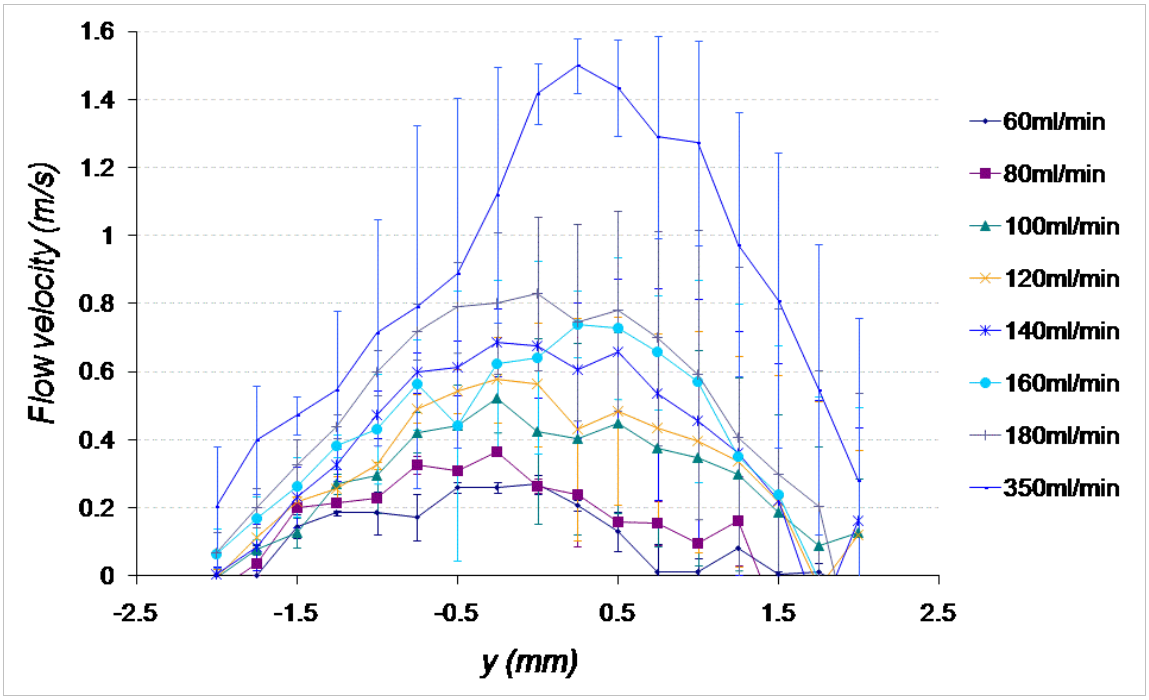

Figure 4-15; Average flow profiles for 40% glycerol solution; flow volumes between 60ml/min and 350ml/min.

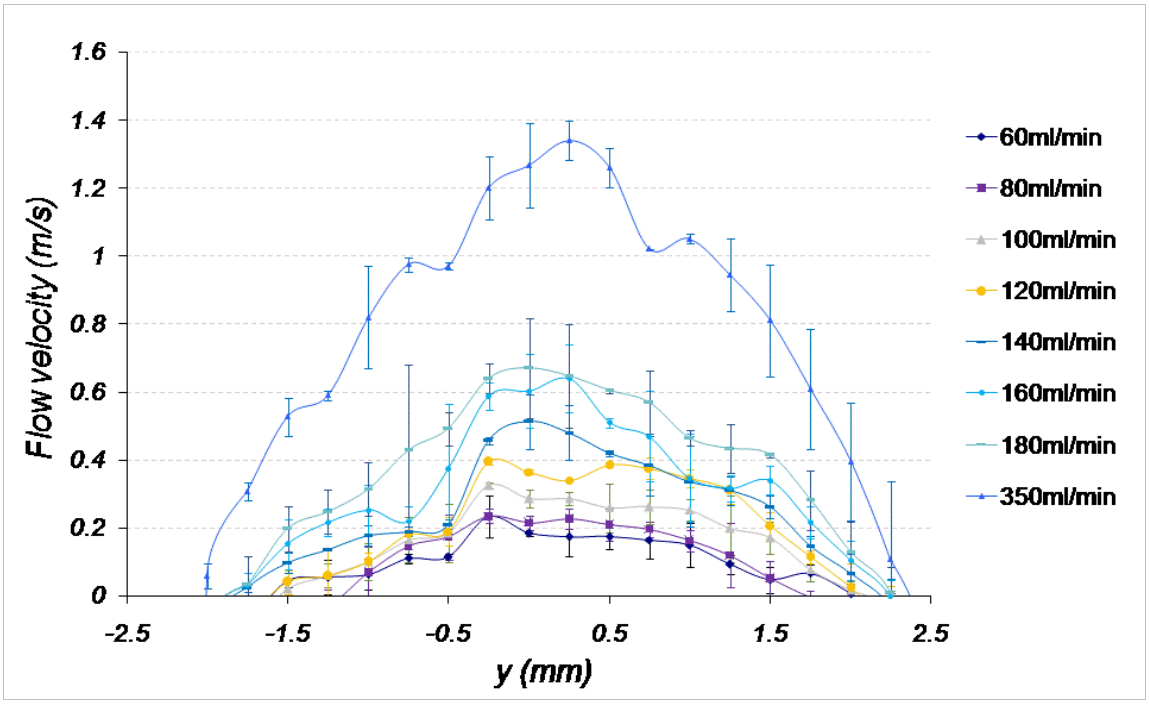

Figure 4-16; Average flow profiles for 60% glycerol solution; flow volumes between 60ml/min and 350ml/min.

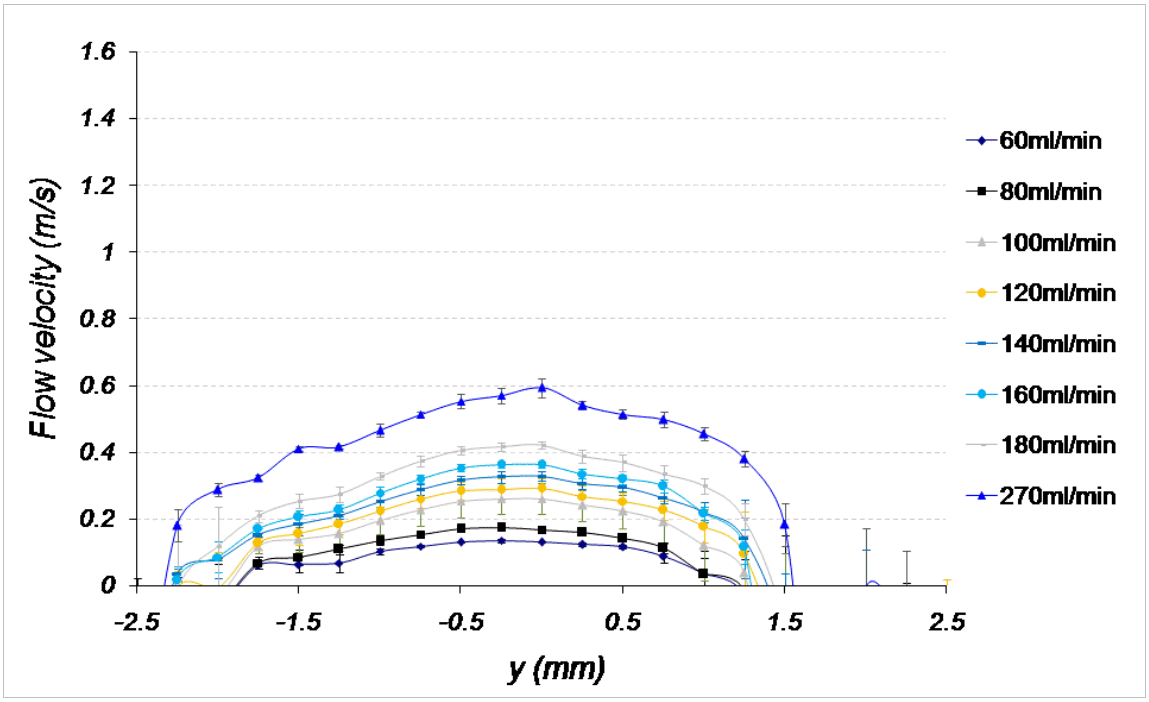

Figure 4-17; Average flow profiles for 80% glycerol Solution; flow volumes between 60ml/min and 270ml/min.

The flow profiles seen above were collected over a period of one month. Each flow profile was compared to a quadratic trend-line (Microsoft Excel) determined from the least squares principle. All average flow profiles had a fit, as measured by the R-squared value of at least 80%, with the exception of the lowest flow volume for 40% glycerol solution which had a fit of approximately 25%. However, the first two flow profiles collected both had a trend-line fit greater than 80% and it is therefore believed that the second two flow profiles collected illustrated anomalous results which could have been caused by grease acquiring in the flow channel or scattering of the laser light. The majority of results showed a fit of over 90% to a parabola suggesting that the flow profiles were fully developed.

The flow profiles in Figure 4-15 and Figure 4-16 are not as parabolic as those observed in Figure 4-14 and Figure 4-17, this is believed to be due to either the presence of an

obstruction in the flow, such as a bubble or grease smear, or light being scattered from the glass slide at the front of the chamber or agar sample at the back.

The following graph which can be seen in Figure 4-18 shows the relationship between the peak velocities acquired for the different viscosity fluids at a flow volume of 80ml/min. This data shows a small initial increase in the peak velocity of the flow at 40% glycerol solution followed a decrease in the peak velocity as the viscosity of the solution increases. The initial increase in peak velocity is due to the improved lubrication of the pump with the glycerol in solution, and the decrease is due to the increased viscosity requiring a greater force to propel the fluid through the channel.

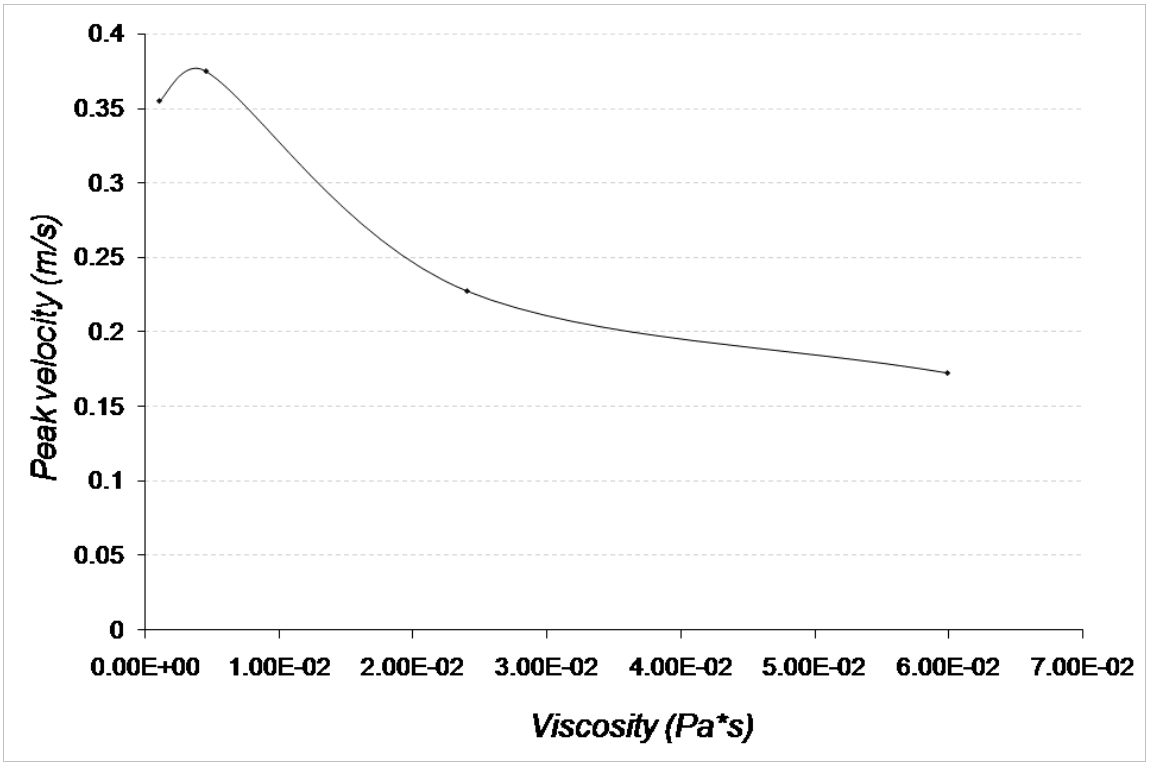

Figure 4-18: Peak velocities acquired with different viscosity fluids at a flow volume of 80ml/min.

4.5.1. Wall Shear Stresses

The wall shear stress (τ) was determined from the following Equation 4-6:

$$\tau = \mu \frac{du}{dx}$$

Equation 4-6; Wall shear stress

Where $\frac{du}{dx}$ is the shear rate and can be found as the gradient of the flow profile adjacent to the wall. The shear rate was attained by plotting the first three points of the flow profile in Microsoft Excel and adding a linear trend-line from the least squares principle, as seen in Figure 4-19. The gradient of the linear trend line can be treated as an estimate of the wall shear rate which can in turn be used to calculate the WSS. Three points were used instead of two in order to reduce the chance of anomalous results occurring. Four points were not used as the flow profiles are parabolic and the slope, and therefore the shear rate, may decrease as more points are used giving an inaccurate result.

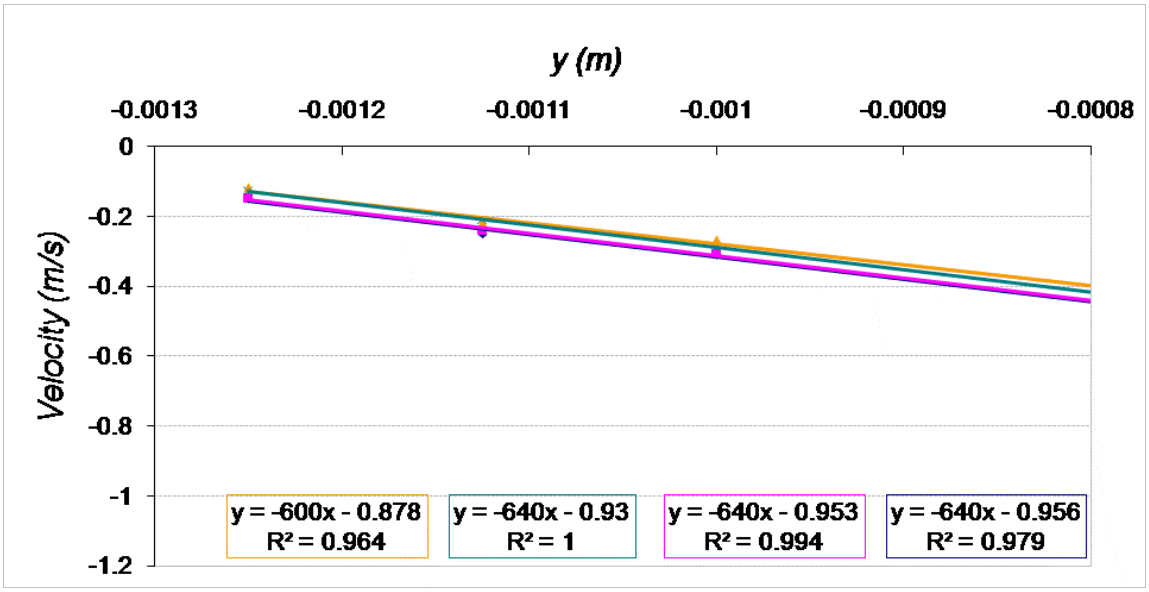

Figure 4-19; Wall shear rate estimation for 140ml/min flow volume, showing four measurements.

The wall shear stresses calculated can be seen in Table 4-2 below and are illustrated in Figure 4-20. The errors are given as standard deviations in results.

Flow volume (ml/min)	Wall Shear Stress (Pa)			
	Water	**40% glycerol**	**60% glycerol**	**80% glycerol**
60	0.31 ± 0.02	1.62 ± 0.44	4.74 ± 1.61	5.99 ± 1.02
80	0.48 ± 0.05	2.36 ± 0.11	5.95 ± 2.08	11.40 ± 1.90
100	0.53 ± 0.04	3.50 ± 0.09	8.02 ± 1.96	17.97 ± 4.91
120	0.65 ± 0.09	2.94 ± 0.58	10.80 ± 0.80	19.07 ± 6.00
140	0.88 ± 0.04	4.01 ± 0.20	17.20 ± 2.37	19.70 ± 4.12
160	0.98 ± 0.13	3.96 ± 0.31	20.00 ± 1.83	25.04 ± 4.98
180	1.24 ± 0.08	4.68 ± 0.18	20.50 ± 1.17	26.18 ± 1.76
250				50.01 ± 4.37
350	1.92 ± 0.05	7.38 ± 0.51	40.00 ± 4.74	

Table 4-2; Wall shear stress for different viscosity fluids at varying flow volumes.

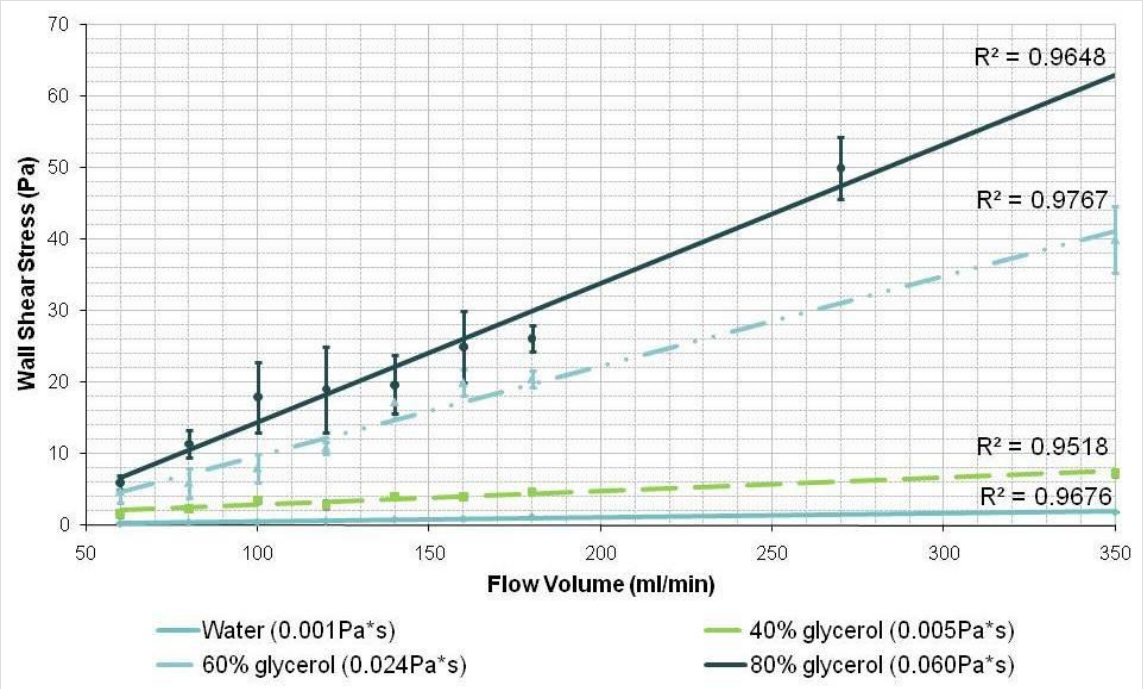

Figure 4-20: WSS produced by different viscosity fluids and their relationship to flow volume.

The results illustrated here show that the flow profiles and peak velocities increase with increasing flow volume as expected ($p<0.0001$) and as a result the WSS increases with

increasing flow volume. In addition it can be seen that the WSS increases with increasing fluid viscosity.

4.6. Computational Fluid Dynamics

Computational fluid dynamics (CFD) has also been used to assess the expected flow profiles within the novel flow chamber. CFD is often used to predict flow velocity patterns within vessels and is largely regarded as reliable estimation of laminar flow (Ku et al. 2002; Quan et al. 2002; Versteeg and Malalasekera 2007). David Hardman (Medical Physics, University of Edinburgh) has used Fluent 6.3.26 (ANSYS, USA) to produce flow profiles through the final flow chamber described in Section 4.3.

The flow chamber dimensions were input into Gambit (Fluent's pre-processor) to produce a computerised model of the flow channel within the chamber. A screen shot of the flow channel can be seen in Figure 4-21.

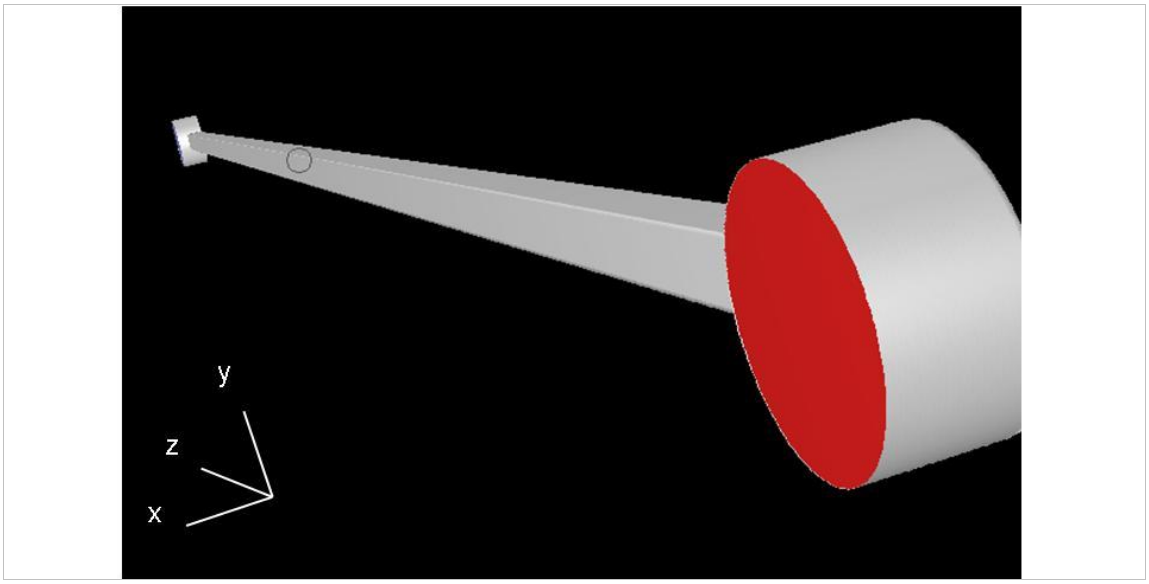

Figure 4-21: Screen shot of flow channel (courtesy of David Hardman).

Following this, flow volumes of 80, 120 and 360ml/min were set to flow through the model and flow profile information was output at 0, 50, 100 and 150mm along the flow channel (from the central point of the flow channel).

4.6.1. Results

Figure 4-22 presents the flow profiles produced by Fluent for the four different viscosity fluids at 80, 120 and 360ml/min flow volumes. It can be seen that the peak flow velocity at the centre of the flow channel can be expected to increase as a function of the flow volume. However the CFD data suggests that the fluid viscosity has little or no effect on the flow velocity as the peak velocities observed for each flow volume do not vary between the different viscosity fluids, with the exception of water which does not have a fully developed flow profile at 350ml/min. This is not the case for the measured LDA data presented in Figure 4-18 reasons for the variations in experimental data are described in Section 4.5. The flow profile for water will not be fully developed at the observation region as the entrance length for water is longer than the channel length. The length of the flow chamber was not increased as a result of this due to the fragility of the flow chamber panels.

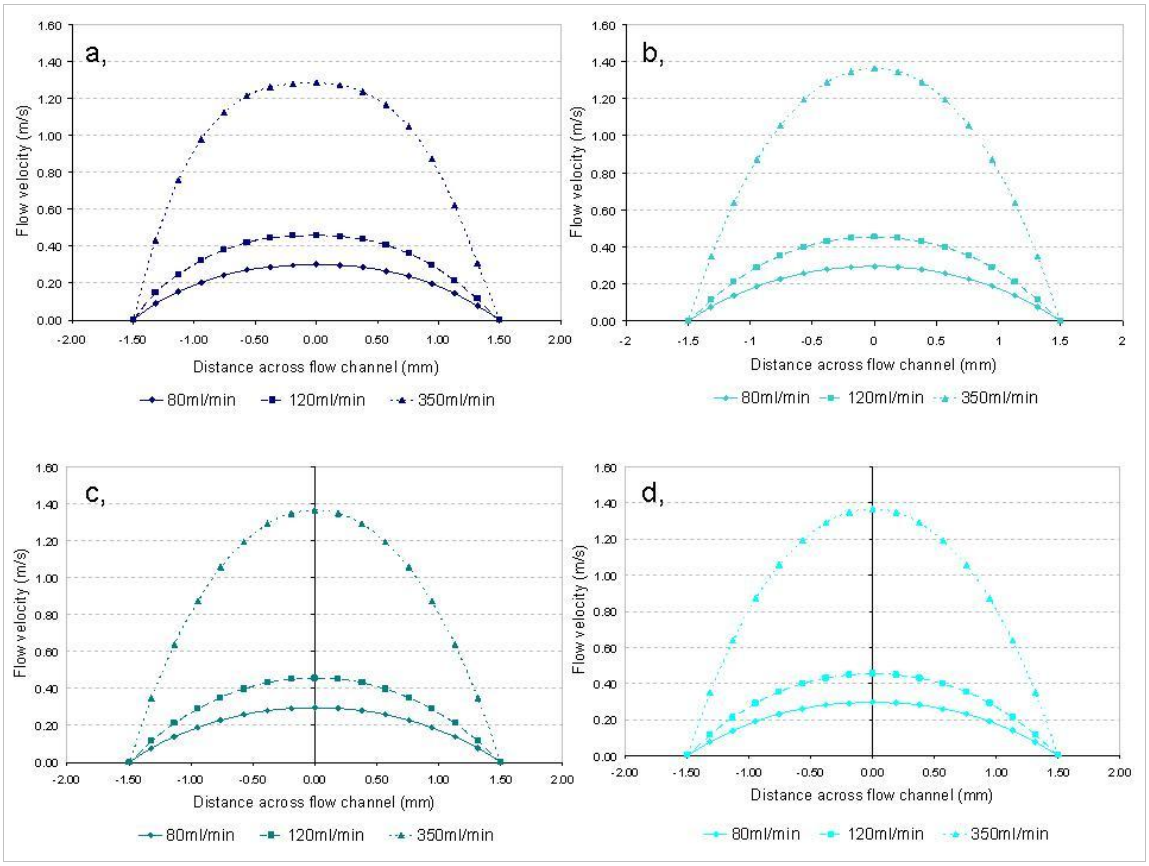

Figure 4-22: CFD flow profiles for different viscosity fluids at differing flow volumes; a, 0% glycerol solution (water); b, 40% glycerol solution; c, 60% glycerol solution and d, 80% glycerol solution.

The expected WSS that will act on the flow chamber walls were calculated from the flow profiles output above, using the first 3 data points of the profiles as in Section 4.5.1, and are presented in Table 4-3 and Figure 4-23 below. Three dimensional flow profiles in the observation region for the three different flow volumes can be seen in Appendix F.

Flow volume (ml/min)	**Wall Shear Stress (Pa)**			
	0% glycerol	**40% glycerol**	**60% glycerol**	**80% glycerol**
80	0.36 ± 0.01	1.61 ± 0.11	8.60 ± 0.60	21.46 ± 1.49
120	0.56 ± 0.02	2.48 ± 0.17	13.23 ± 0.92	33.02 ± 2.29
360	1.68 ± 0.12	7.44 ± 0.52	39.69 ± 2.75	99.05 ± 6.86

Table 4-3: WSS values

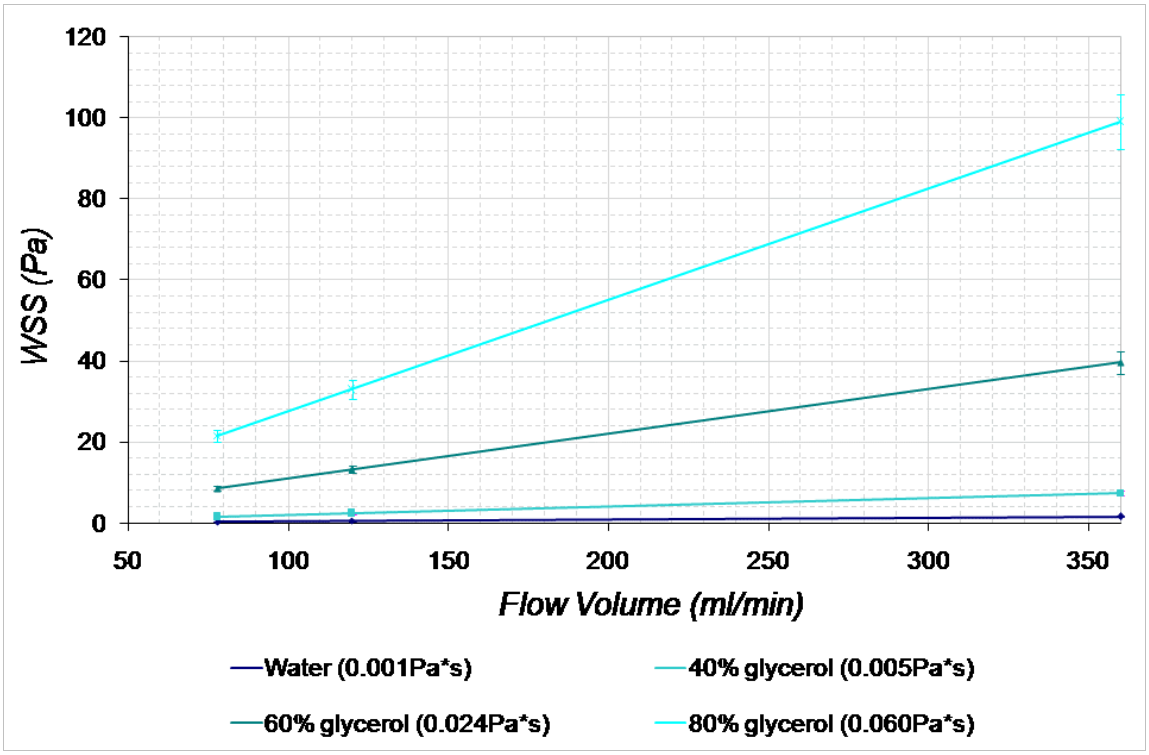

Figure 4-23: WSS at varying flow volumes for different viscosity fluids calculated from CFD results.

4.7. Calculation of the WSS

The WSS (τ) within the flow chamber has also been calculated from the chamber dimensions using Equation 4-7 (Bacabac et al. 2005) for varying flow volumes (Q).

$$\tau = \frac{6\mu Q}{wh^2}$$

Equation 4-7: Shear stress calculation.

Where μ is the fluid viscosity; w and h the channel width and height respectively.

The calculated WSS can be seen in Table 4-4 and Figure 4-24, the errors represented in the table are calculated from the error in the flow channel dimensions. This data shows

a linear relationship between the WSS and flow volume as has been seen previously with experimental and CFD results.

Flow volume (ml/min)	Wall Shear Stress (Pa)			
	0% glycerol	40% glycerol	60% glycerol	80% glycerol
60	0.22 ± 0.01	1.00 ± 0.05	5.33 ± 0.27	13.31 ± 0.67
80	0.30 ± 0.01	1.33 ± 0.07	7.11 ± 0.36	17.75 ± 0.89
100	0.37 ± 0.02	1.67 ± 0.08	8.89 ± 0.44	22.19 ± 1.11
120	0.45 ± 0.02	2.00 ± 0.10	10.67 ± 0.53	26.62 ± 1.33
140	0.52 ± 0.03	2.33 ± 0.12	12.44 ± 0.62	31.06 ± 1.55
160	0.59 ± 0.03	2.67 ± 0.13	14.22 ± 0.71	35.50 ± 1.77
180	0.67 ± 0.03	3.00 ± 0.15	16.00 ± 0.80	39.93 ± 2.00
250	1.00 ± 0.05	4.50 ± 0.23	24.00 ± 1.2	59.90 ± 3.00
350	1.30 ± 0.07	5.83 ± 0.29	31.11 ± 1.6	77.65 ± 3.88

Table 4-4: WSS for varying flow volumes calculated from Equation 4-7.

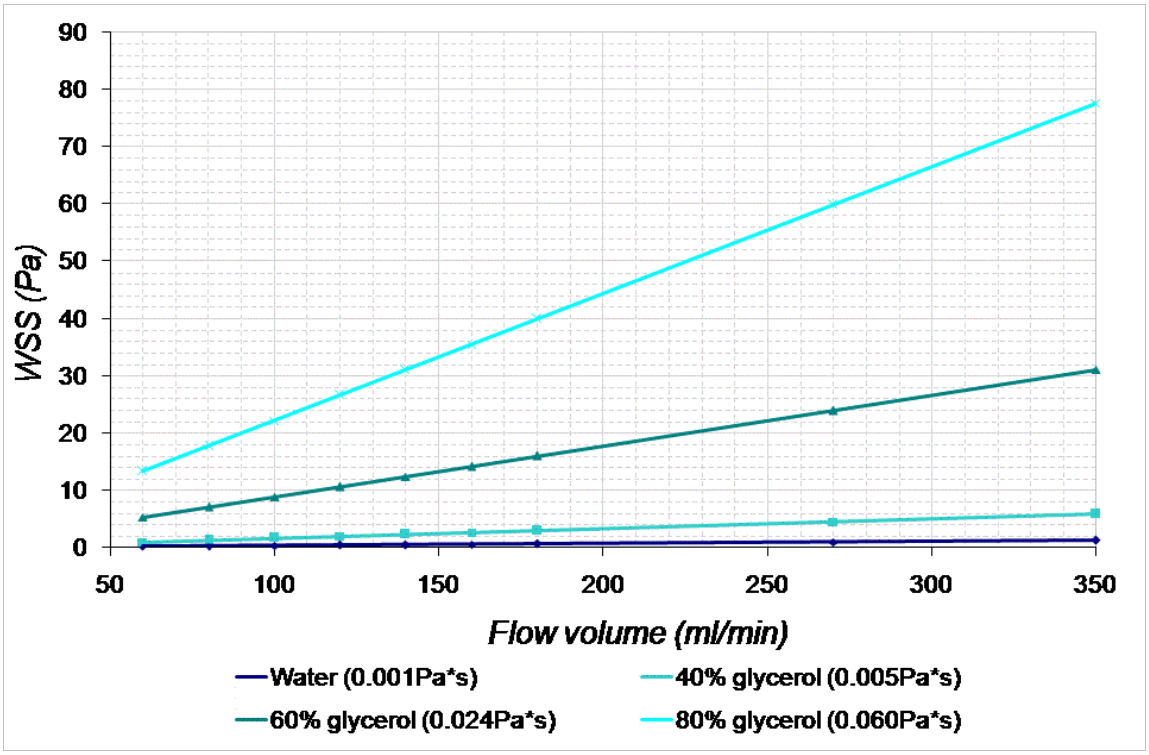

Figure 4-24: Calculated WSS with different viscosity fluids at varying flow volume.

4.8. Comparison of results

The WSS values for the flow chamber described in Section 4.3 have been determined experimentally, through a CFD analysis of the flow chamber and in addition have been calculated using Equation 4-7. These results have been compared and are presented in Figure 4-25. The data suggests that, at low flow volumes, the WSS for each method used are comparable; however the results tend to diverge as the flow volume is increased. In addition, the divergence in results increases with an increase in fluid viscosity, such that with low viscosity fluids, for example water, the divergence is less than 1Pa; however with 80% glycerol solution divergence is greater than 30Pa.

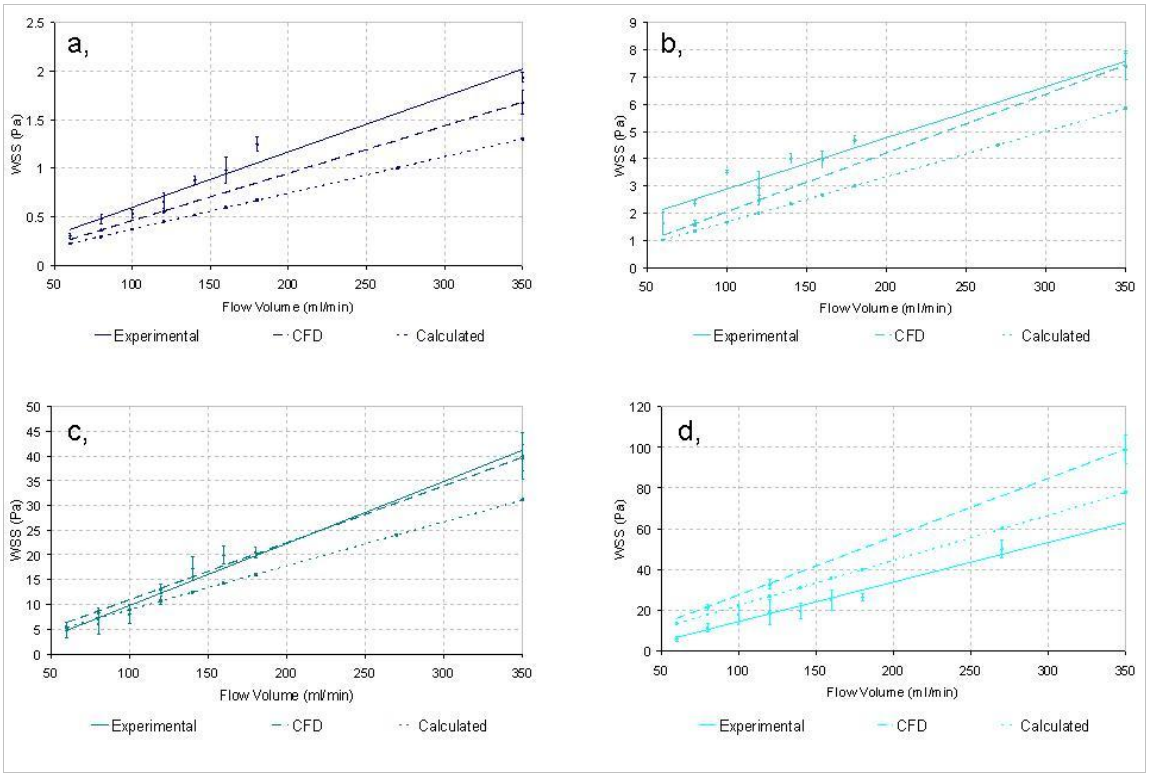

Figure 4-25: WSS at varying flow volumes for different methods of determination; a, for water, b, for 40% glycerol solution, c, for 60% glycerol solution and d, for 80% glycerol solution.

With the lower viscosity fluids, water, 40% glycerol and 60% glycerol solutions (0.001Pa·s, 0.005Pa·s and 0.024Pa·s viscosities) the results presented in Figure 4-25

suggest that CFD provides the best approximation of the results, however for high viscosity fluid, 80% glycerol solution (0.060Pa·s), the calculated values for WSS provide the best approximation to the experimental results.

In light of this comparison the experimentally evaluated WSS will be used as calibration data for the flow chamber as these are the true WSS values achieved. However, if future calculations for the WSS are required at low flow volumes or with low viscosity fluids, a calculation or CFD approximation may be a suitable method of identifying the WSS within the flow chamber.

4.9. Summary

LDA has been used to assess the flow profiles within a specifically designed flow chamber and to calculate the WSS which will be acting upon attached microbubbles within the flow channel. The WSS has been calculated for 4 different viscosity fluids at flow volumes ranging from 60-350ml/min. Physiological flow is pulsatile and occasionally turbulent; however only steady flow in the laminar regime has been investigated here. An accurate and reliable assessment of the WSS against the agar surface is more easily achieved through the use of laminar flow.

Three different methods have been used to determine the WSS within the novel flow chamber, these methods are; experimental determination using LDA, computational determination using CFD and calculated values of WSS using flow chamber dimensions. The comparison of results suggests that at high flow volumes and with high viscosity fluids there is significant variation in the results produced, indicating that the experimental method produces the most accurate WSS. However at lower flow volumes and with low viscosity fluids (0.001-0.005Pa·s) CFD and calculation of the WSS provide acceptable results. However, since all WSS have been determined experimentally for the flow chamber described, this data has been used to calibrate the flow chamber for future investigations.

In conclusion, the WSS values which can be assessed within the flow chamber range from 0.03-50Pa. This makes the flow chamber described in this chapter suitable for investigations into the attachment of microbubbles under human physiological WSS of approximately 3.4Pa in addition to physiological WSS in normal, non-atherosclerotic, mice of up to 40Pa (Cheng et al. 2007a).

The WSS values acquired here can be used to determine the shear stresses at which microbubbles will remain attached to a surface and also under what shear stresses microbubbles in the flow will attach to a surface.

Chapter 5 Intravascular Ultrasound and Characterisation of the IVUS transducer

5.1. Intravascular Ultrasound

Intravascular ultrasound (IVUS) began development in 1971, when the first linear array was invented. It was believed that ultrasound would not be able to penetrate the chest wall sufficiently for study of the heart and so a mechanical array catheter tip was developed for internal study of large blood vessels (Bom et al. 1971). Due to flaws in the catheter tip production this design failed and this approach to studying the heart was discontinued due to the success of non-invasive cardiac imaging, although mechanical array catheters are still available.

It was the mid-eighties before any further development of IVUS was undertaken. This was due to the use of interventional techniques in the coronary arteries and the need for catheter tip visualisation. Because the coronary arteries were smaller than the initial target of IVUS, the large blood vessels, a smaller catheter was required and so the rotating element was developed (Roelandt et al. 1993).

A modern IVUS system comprises an IVUS scanner and compatible rotating, single element IVUS catheter, or a phased array catheter. For the purpose of investigation throughout this thesis a Boston Scientific Clearview IVUS unit has been used in combination with an Atlantis™ SR Pro coronary imaging catheter (Boston Scientific, USA). The scanner and catheter can be seen in Figure 5-1 below. Figure 5-1c shows a diagrammatic view of the catheter with labelled parts.

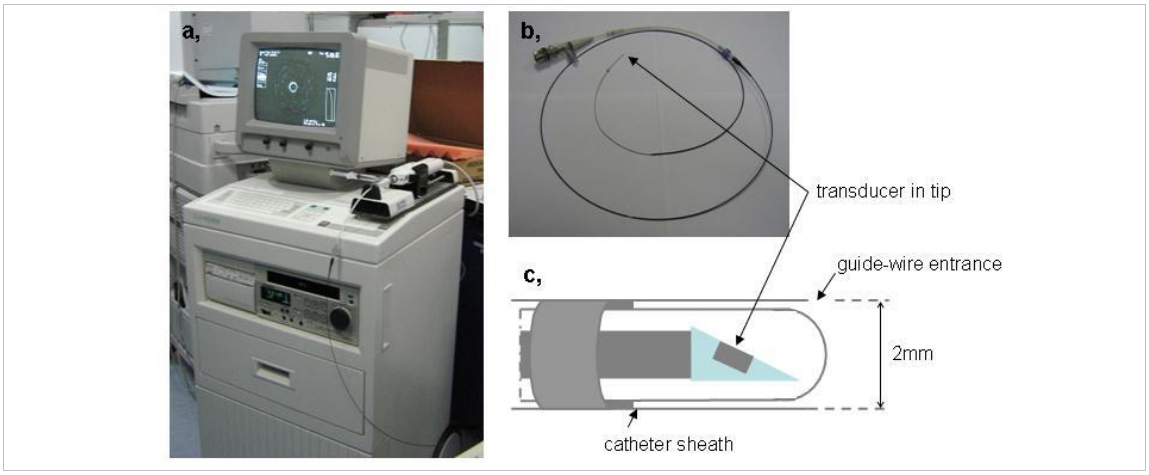

Figure 5-1: IVUS system; (a) Clearview IVUS unit, (b) IVUS catheter , (c) simplified diagram of IVUS catheter (adapted from Lupotti (Lupotti 2002)).

The proximal end of the IVUS catheter is connected to a motor drive which enables controlled and smooth pull-back of the catheter through vessels and also rotates the single element transducer in the tip in order to build up a cross-sectional image of the vessel.

The most common use for IVUS is imaging of the coronary arteries to establish the degree of plaque formation in CHD. The coronary imaging catheter is inserted into the artery, by use of a Doppler guide wire, to the furthest point of study and the IVUS catheter is then pulled-back by the motor drive through the region of study. A typical IVUS image can be seen in Figure 5-2.

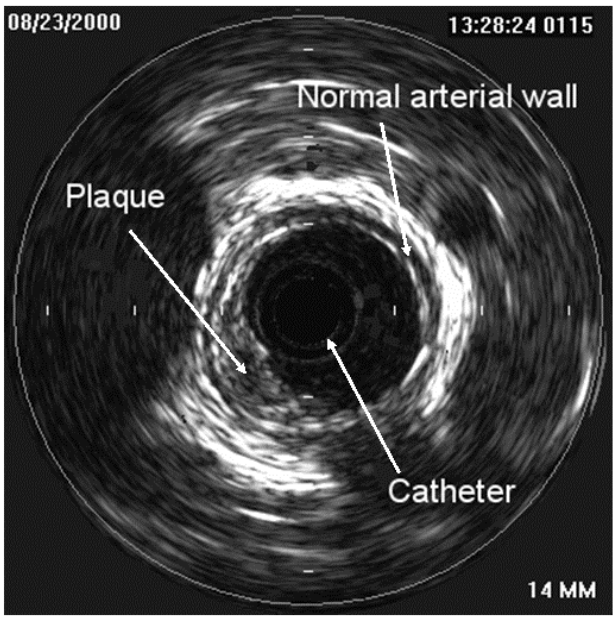

Figure 5-2: IVUS image showing cross section of an atherosclerotic coronary artery and image components (courtesy of Mr. T. Anderson).

5.2. Acoustic Output of IVUS

The acoustic output of an ultrasound transducer is unique to each transducer and scanner combination and is presented as a variety of parameters which quantify the amount of ultrasound emitted by a transducer. The parameters used to describe the ultrasound field include, acoustic pressure, power and acoustic intensity.

The acoustic output of a transducer can be used to assess performance of the system but is predominantly used to measure and assess the safety of ultrasound as discussed briefly in Chapter 2. Since the investigations carried out for the purpose of this thesis do not involve the use of live subjects the safety parameters are not of primary importance. However, when dealing with ultrasound contrast agents, the acoustic pressure is a significant parameter because at lower frequencies, as discussed in Chapter 2, it has been shown that this governs the interaction between the ultrasound and the microbubbles. In

addition by characterising the transducer a measure of the performance of the system can be made.

5.2.1. Acoustic output parameters

The information which can be obtained to assess the acoustic output of a scanner and transducer are detailed in Table 5-1 (Preston 1991).

Parameter	Symbol	Details
Peak pressures	p^+, p^-	Largest positive and negative pressures in the field.
Spatial-peak temporal-average intensity	Ispta	Highest intensity in field.
Power	W	Total acoustic power in the beam
Output beam intensity	Iob	Power divided by radiating area of transducer
Beam width	w	Width of beam at the focus

Table 5-1: Acoustic output information

The important parameter, when considering microbubbles and their interaction with ultrasound, is peak negative pressure which is the parameter measured in this chapter.

5.2.2. Measuring Acoustic Output Parameters

Preston (1991) describes a variety of measurement techniques which can be used to measure the acoustic output of an ultrasound system. Three methods of measuring the acoustic pressure have been outlined, these include, the pulse-echo technique using a small target, optical diffraction techniques and piezoelectric hydrophones.

1. The pulse-echo technique involves detection of an echo from a small spherical target at different positions in the transducer field and measurement of the echo strength as a function of target position to generate a 3-d map of the ultrasound field distribution. This technique is also possible using tungsten wires with a diameter less than the acoustic wavelength (Raum and O'Brien 1997).

2. Compression and rarefaction of an ultrasonic wave causes small changes in the refractive index of the medium through which the wave is propagating. Optical measurement techniques employ this phenomena using optical diffraction to acquire the pressure distribution from an ultrasound field. The advantage of this technique is its non-perturbing and non-invasive nature making it suitable for more hostile environments where a sensitive hydrophone may be destroyed. However, this is a complex technique and therefore other techniques are more commonly employed.

3. The most common method of assessing an ultrasound field is the piezoelectric hydrophone (Huang et al. 2001; IEEE 1990; NEMA 2004; Snook et al. 2000). The hydrophone consists of a thin membrane of piezoelectric elements which convert an incident pressure wave into an electric signal (Figure 5-3 adapted from Preston (Preston 1991)) from which the pressure field can be calculated using Equation 5-1 (Preston 1991).

$$p_{-} = V_{-} / \eta$$

Equation 5-1: Peak negative pressure

Where p_{-} = peak negative pressure, η = hydrophone sensitivity (from calibration of hydrophone) and V_{-} = peak negative voltage.

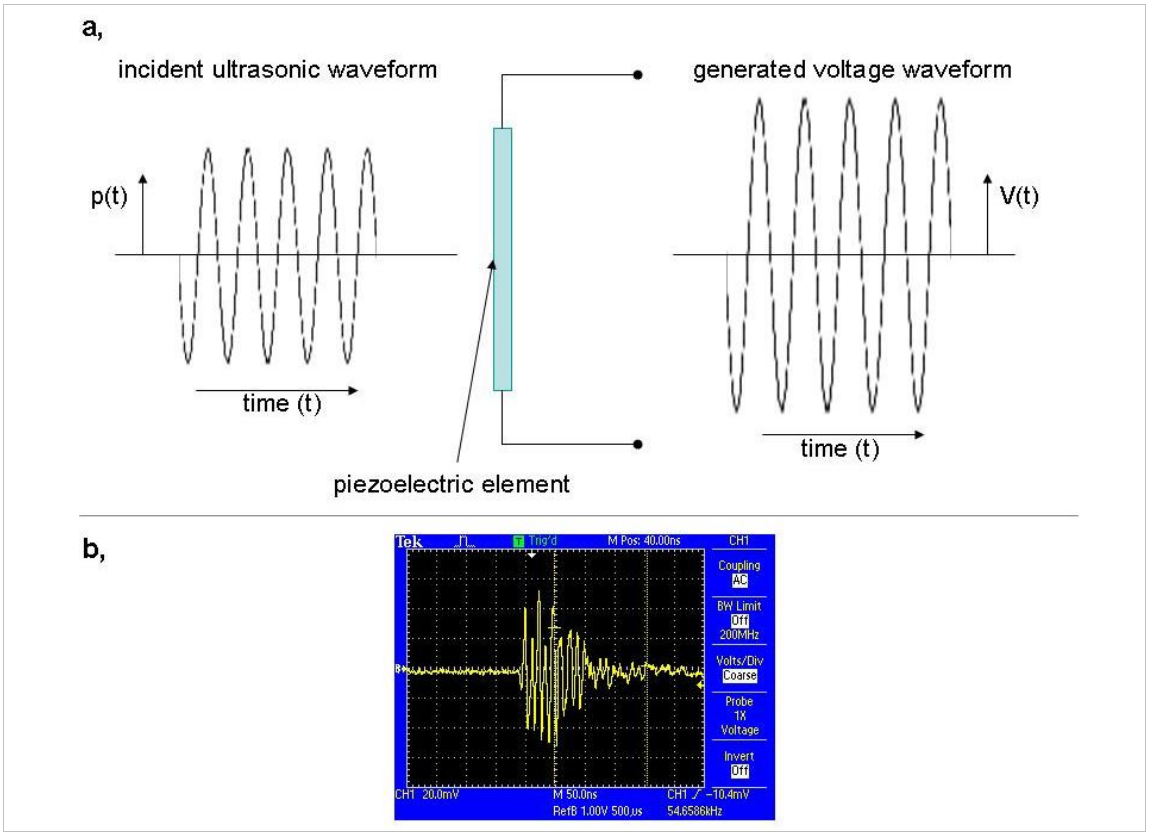

Figure 5-3: (a) Schematic diagram of hydrophone converting an incident acoustic waveform into a voltage waveform and (b) screen shot of measured voltage waveform at 2mm from transducer.

There are a variety of different types of hydrophone including ceramic, needle-probe and membrane, with active elements of the order of 0.5-1mm in diameter, although smaller elements do exist. Sensitivity of the hydrophone increases with the size of the element; however an ideal hydrophone will have a small element comparable to the size of the acoustic wavelength. The advantage of the hydrophone as a measurement tool is its small size and adaptability although this does lead to the hydrophone being very delicate and care must be taken when handling.

For the purpose of this investigation a hydrophone has been used to characterize the IVUS transducer due to its availability within Medical Physics and its reliability. The available hydrophone is a polyvinylidene fluoride (PVDF) membrane hydrophone with a

2mm active element which has been calibrated up to 60MHz (National Physics Laboratory, 19th June 2008).

5.2.3. Method

In order to calibrate the IVUS transducer the equipment was set-up as illustrated in Figure 5-4 and Figure 5-5. The water tank was filled with deionised water 24 hours prior to the investigation and the hydrophone was submersed an hour before the investigation, ensuring visually that there were no air-bubbles trapped beneath the hydrophone. The hydrophone was connected to a digital oscilloscope (Tektronix TDS2000, USA) for data collection. The IVUS catheter was then fed through a customised, fixed tube controlled by a micromanipulator, with the tip of the catheter, housing the transducer, below the hydrophone. The micromanipulator was then used to place the transducer at the optimum angle, approximately 12° to the surface of the water (achieved when the brightest echo could be observed from transducer at minimum gain).

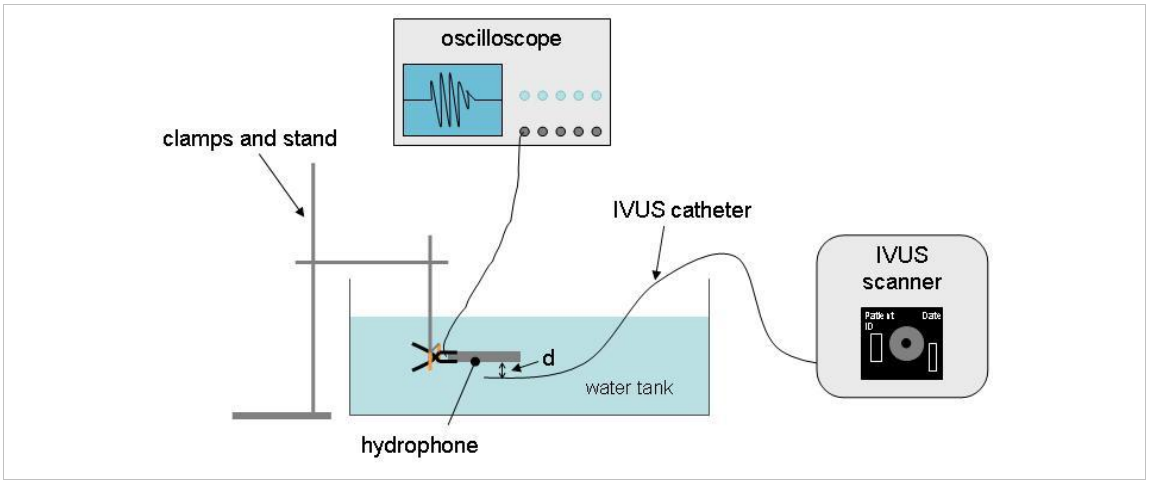

Figure 5-4: Schematic of equipment for characterisation of IVUS catheter.

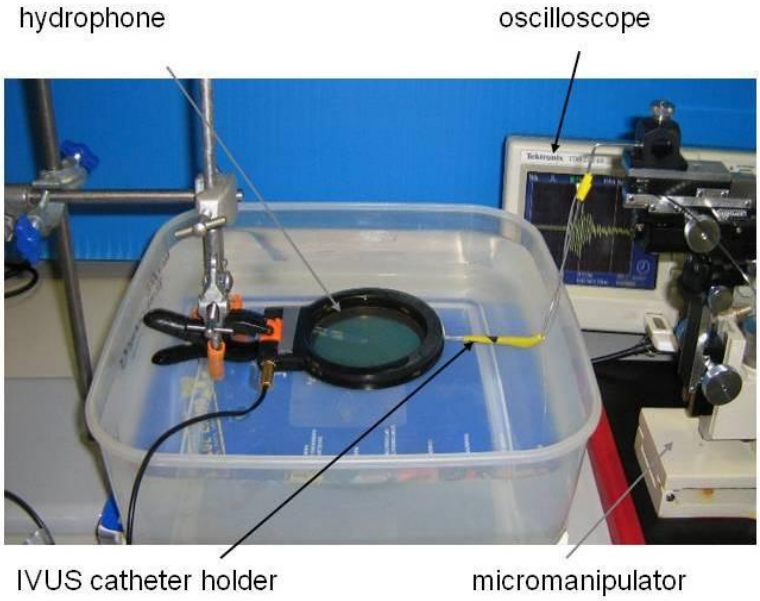

Figure 5-5: Photograph of IVUS characterisation set-up.

The distance of the transducer from the hydrophone was measured using the divisions on the screen of the ultrasound scanner. The transducer position was controlled by the micromanipulator seen in Figure 5-5, and the bright echo from the hydrophone membrane, observed at minimum gain, was lined up with the divisions on the IVUS image at the required distances.

Data from the oscilloscope was captured at 1mm intervals between 1 and 8mm from the transducer. Three sets of data for each distance was collected and an average taken before calculating the peak pressure at set distances from the transducer using the sensitivity information from the hydrophone calibration certificate and Equation 5-1. The sensitivity data from the calibration certificate is presented in Figure 5-6.

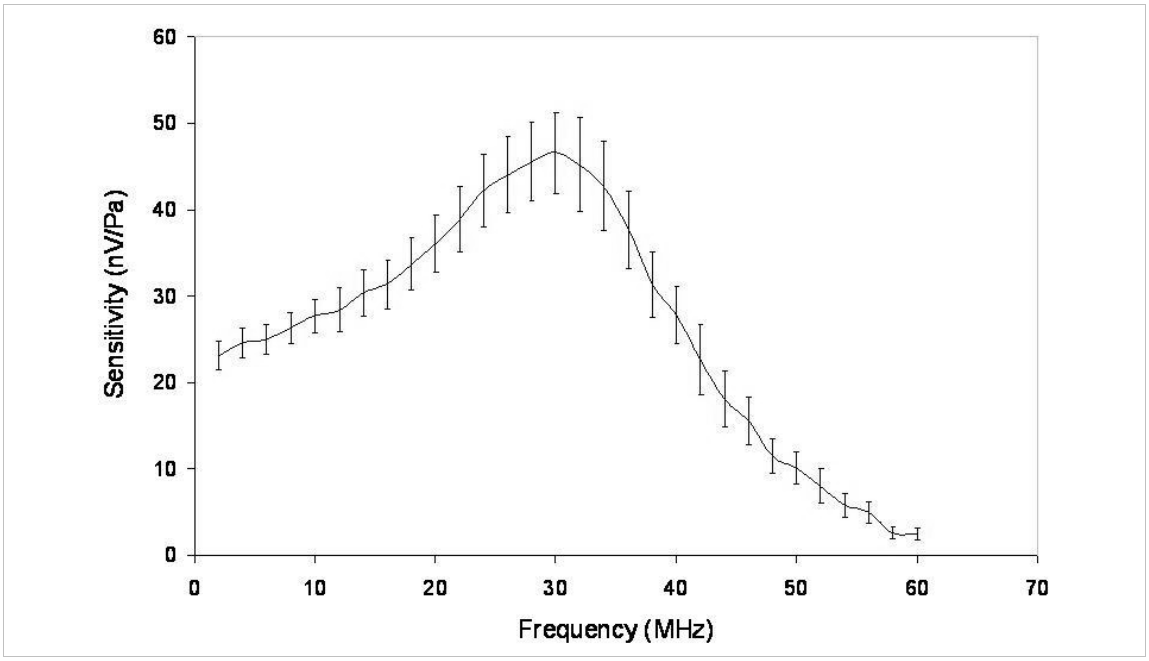

Figure 5-6: Plot of sensitivity against frequency for PVDF membrane hydrophone (calibrated by National Physics Laboratory, UK).

5.2.4. Results

The data, presented in Table 5-2 below, shows that the peak negative pressure decreases as the distance from the transducer increases, as expected. The peak positive pressure also decreases but at a slower rate. The decrease in signal amplitude is due to attenuation of the ultrasound beam as it travels through the medium (de-ionised, de-gassed water). Acoustic pressure data is also represented graphically in Figure 5-7.

Distance from transducer (mm)	Peak pressures (MPa)	
	Negative	**Positive**
1	2.00 ± 0.15	1.94 ± 0.30
2	1.92 ± 0.15	1.97 ± 0.28
3	1.92 ± 0.17	1.92 ± 0.29
4	1.90 ± 0.20	1.89 ± 0.29
5	1.69 ± 0.04	1.87 ± 0.28
6	1.78 ± 0.11	1.94 ± 0.30
7	1.69 ± 0.10	1.84 ± 0.28
8	1.57 ± 0.16	1.82 ± 0.29

Table 5-2: Peak negative and positive pressures as a function of distance from the transducer.

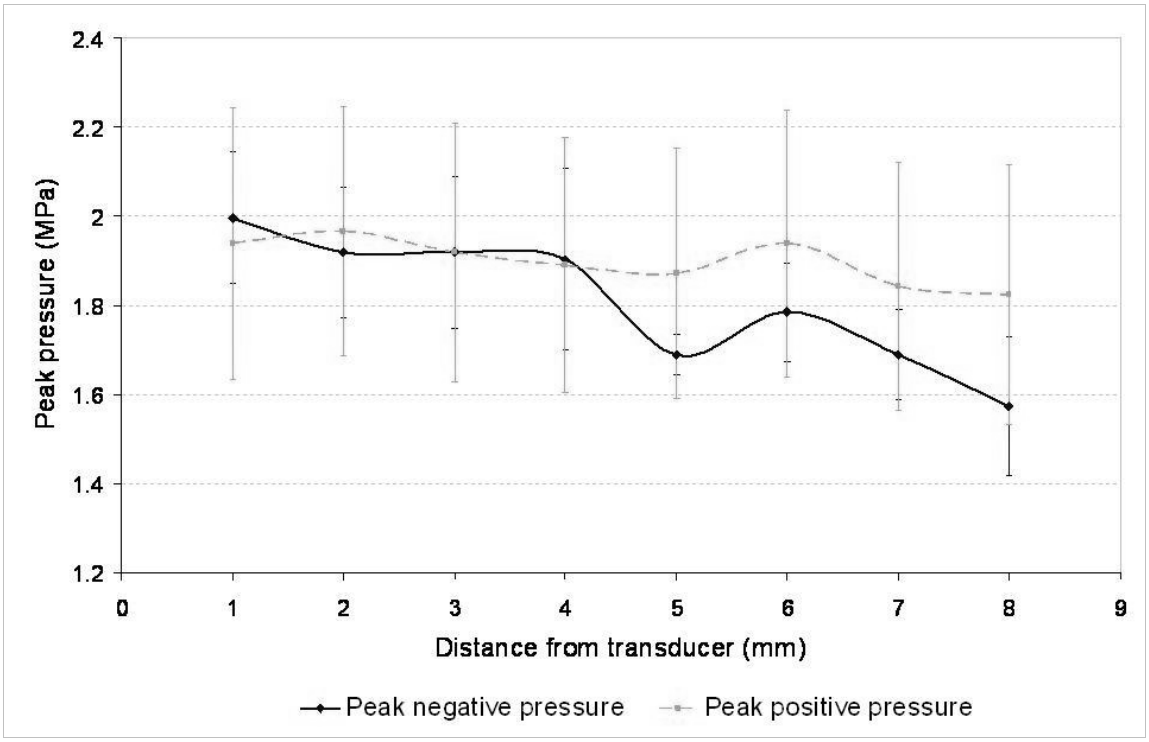

Figure 5-7: Peak positive and negative pressures of IVUS transducer (peak negative pressures have been presented on the positive scale for comparison).

The acoustic pressure data presented in Figure 5-7 shows an increasing difference between the peak negative and peak positive pressures as the distance from the transducer is increased. This is likely to be due to non-linear propagation of the ultrasound wave which may be distorted as it travels through the medium. The unexpectedly low peak negative pressure at 5mm from the transducer could be due to a misalignment of the hydrophone, or environmental factors, such as external noise or vibrations causing a variation in result. In addition these factors may account for the increase in peak positive pressure at 6mm from the transducer.

Previously peak negative pressures for 40MHz IVUS transducers have been reported between 0.6 and 1.45MPa (Butler 2005) and 0.2 and 2.0MPa (Goertz et al. 2006) over a 10mm distance from the transducer. The peak negative pressures collected for this particular transducer lie between 1.6 and 2.0MPa, suggesting that the transducer is performing in a suitable range.

The MI for this transducer and scanner combination has been calculated using Equation 2-7. The central frequency of the transducer was assessed using the RF data collected for analysis and was found to be 40MHz, as illustrated in Figure 5-8. The MI was 0.32 (± 0.10), this is within any safety recommendations on the use of diagnostic ultrasound (ECMUS 2008) and lies within the range of MI where the ultrasound and microbubble interactions produce non-linear responses as described in Chapter 2. Despite this care must be taken as there is no data currently available to confirm this with respect to the in-house UCA.

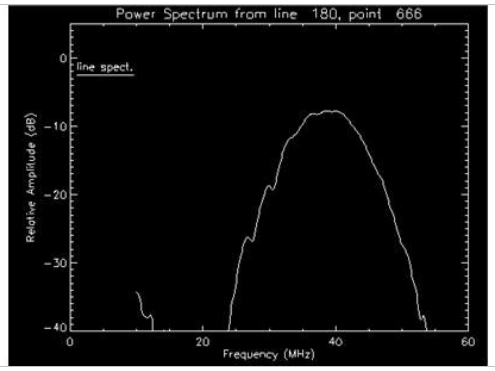

Figure 5-8: Power spectrum from IVUS catheter showing a central frequency of 40MHz.

5.3. Summary

The characteristic information of an ultrasound field is important as an indicator of the safety and performance of an ultrasound transducer.

The peak negative pressures produced by an Atlantis™ SR Pro coronary imaging catheter have been collected for a range of distances from the transducer and have been shown to decrease over distance. The peak positive pressures have also been recorded. The data presented suggests that the catheter being used throughout this thesis is performing well with peak negative pressures between 1.5 and 2.0MPa over 1-8mm distances from the transducer. The MI also suggests that the catheter is operating within suggested safety limits.

Chapter 6 Attachment of antibodies to the in-house microbubbles

In order to attach the in-house microbubbles to a cellular surface it was necessary to incorporate antibodies to the microbubble shell as illustrated and described in Chapter 2. Attachment of antibodies was achieved using a streptavidin-biotin bridge.

A variety of factors were investigated in optimising the attachment of antibodies to the in-house ultrasound contrast agent. These factors are listed below:

- Optimum quantity of streptavidin with respect to microbubble volume.
- Optimum ratio of antibody to microbubbles.
- Attachment techniques.

Initial investigations involved varying the quantity of streptavidin, however, attachment was unsuccessful so a fluorescein isothiocyanate (FITC) conjugated streptavidin was used to assess the optimum amount of streptavidin required for the in-house agent to have all biotin sites filled. Once this had been established different attachment techniques were investigated and the optimum ratio of microbubbles to antibody by

volume was assessed. A final investigation into the optimum quantity of streptavidin for antibody attachment was carried out.

6.1. Streptavidin-Biotin Bridge

Klibanov (1999; Klibanov et al. 1999) and Lindner (2004) have discussed the use of the avidin-biotin link to bind targeting ligands or antibodies to the surface of a microbubble. Other authors (Korpanty et al. 2005; Takalkar et al. 2004) have reported on the use of avidin or streptavidin to bind a biotinylated antibody to an acoustically active microbubble for targeted imaging of specific structures or proteins. The avidin-biotin bond is commonly used due to its strong affinity for binding to biotin. Avidin is a protein made up of four subunits, each of which is capable of binding to biotin. Streptavidin, although not related to avidin, has many of the same properties, including its affinity to bind biotin. The avidin-biotin and streptavidin-biotin bonds are some of the strongest known, natural, non-covalent bonds (Chilkoti and Stayton 2002; Green 1975) and have bond energies of 89.96kJ/mol (Moy et al. 1994; Wilchek and Bayer 1988) and 133.89kJ/mol (Moy et al. 1994; Wong et al. 1999) respectively.. The streptavidin-biotin bond has a lower non-specific binding affinity (does not have a tendency to bind to non-target molecules) (Haugland 2002; Weber et al. 1989), making it more suitable for attaching ligands or antibodies to a microbubble shell. Biotin is also known as vitamin H and is involved in the metabolism of amino acids in addition to being involved in healthy hair and nail growth (Combs 1992).

Figure 6-1 illustrates attachment of an antibody to a lipid-based microbubble via a streptavidin-biotin bridge. In this case the biotin is incorporated into the microbubble shell and a biotinylated antibody is attached by streptavidin.

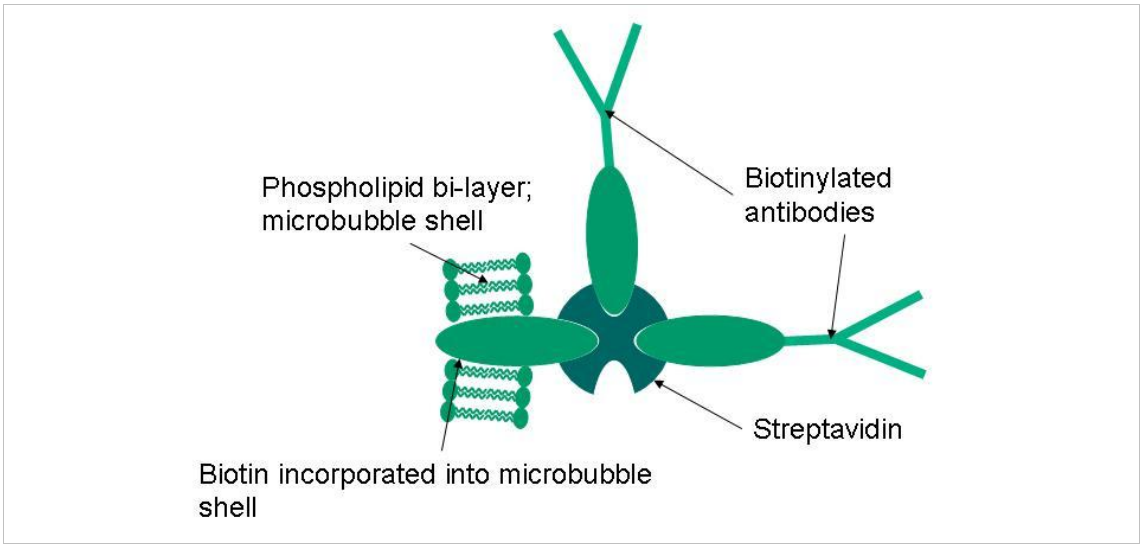

Figure 6-1: The streptavidin-biotin bridge.

6.2. Assessing attachment of the antibodies

Due to the small size of individual antibodies, 7.5-15nm (Ban et al. 1994), it was necessary to find a method which could identify when they had been successfully attached to the microbubble shell as it was not possible to visualise them. In order to identify antibody attachment to the streptavidin, fluorescently tagged antibodies (F2883) can be added to the microbubble conjugated antibodies (CD31) as illustrated in Figure 6-2. When a laser is incident upon a fluorescent marker the fluorophores are excited and then as they relax they emit light of a specific wavelength. As a result it is possible to assess antibody attachment by assessing the amount of fluorescence.

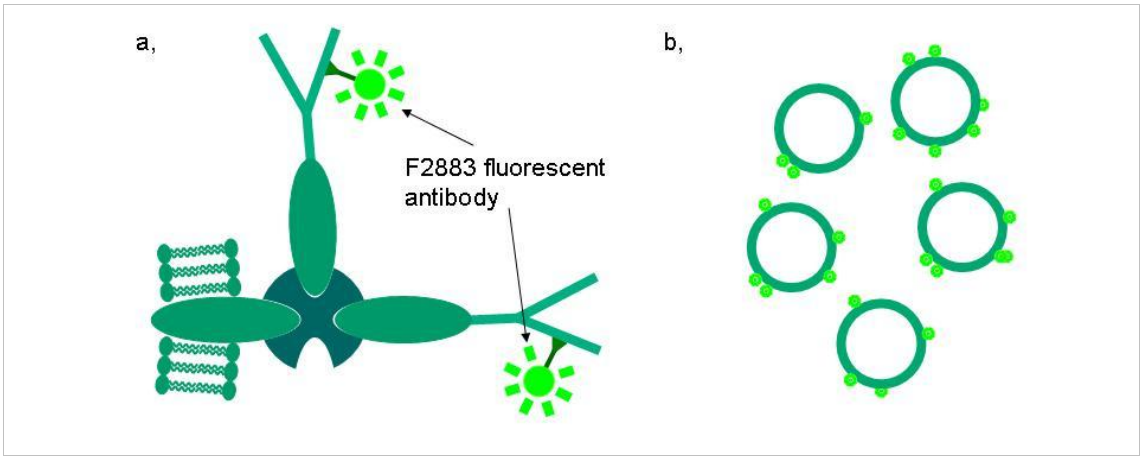

Figure 6-2: Schematic showing; a, antibodies attached to a microbubble shell identified by fluorescently tagged antibodies and b, fluorescently tagged microbubbles.

Techniques which can be used to measure fluorescence include fluorescence microscopy, fluorescence spectroscopy and filter fluorometry (Guilbault 1990; TurnerBiosystems 2009). Fluorescence microscopy can provide a visual indication of fluorescence and with the appropriate software is also capable of quantifying the amount of fluorescence. Fluorescence spectroscopy and filter fluorometry techniques both involve irradiating the sample with a laser and using detectors to determine the fluorescence intensity. Fluorescence spectroscopy returns a fluorescent spectrum from the emitted photons (Lakowicz 1983) and filter fluorometers give a reading of the intensity of fluorescence emitted. Whilst filter fluorometers are a cost effective method of measuring fluorescence they require the use of appropriate filters for the fluorescence being observed, in addition they require regular calibration (TurnerBiosystems 2009). Both types of fluorometer are effected by temperature and humidity and incapable of identifying independent fluorescence events (Guilbault 1990).

Another technique capable of measuring the amount of fluorescence is flow cytometry. This technique is capable of not only quantifying the overall fluorescence but also the percentage of cells with fluorescence. Because of this and the availability of a flow

cytometer, this technique has been used to assess antibody attachment to the in-house microbubbles. A brief description of flow cytometry is given below.

6.2.1. Flow Cytometry

Flow cytometry is an optical technique which is most commonly used to assess cellular structure (Givan 1992; Melamed 1990) and expression of cell surface and internal antigens. The flow cytometer used for data collection in this chapter can be seen in Figure 6-3. Output parameters from flow cytometry include the cell size and complexity (i.e. cells with more structural features, such as granules, provide a greater side scatter signal). In addition the technique is able to identify different cell types and is able to give information regarding the internal structure of a cell through phenotypic characterisation using antibodies.

Figure 6-3: The Tissue Injury and Repair Group's Beckman-Coulter flow cytometer.

The cells in a solution are forced to flow one by one through a laser beam. This single file flow of cells is achieved through the hydrodynamic focusing of the solution containing the cells. Hydrodynamic focusing involves streamlining of the solution by means of a sheath fluid as illustrated in Figure 6-4.

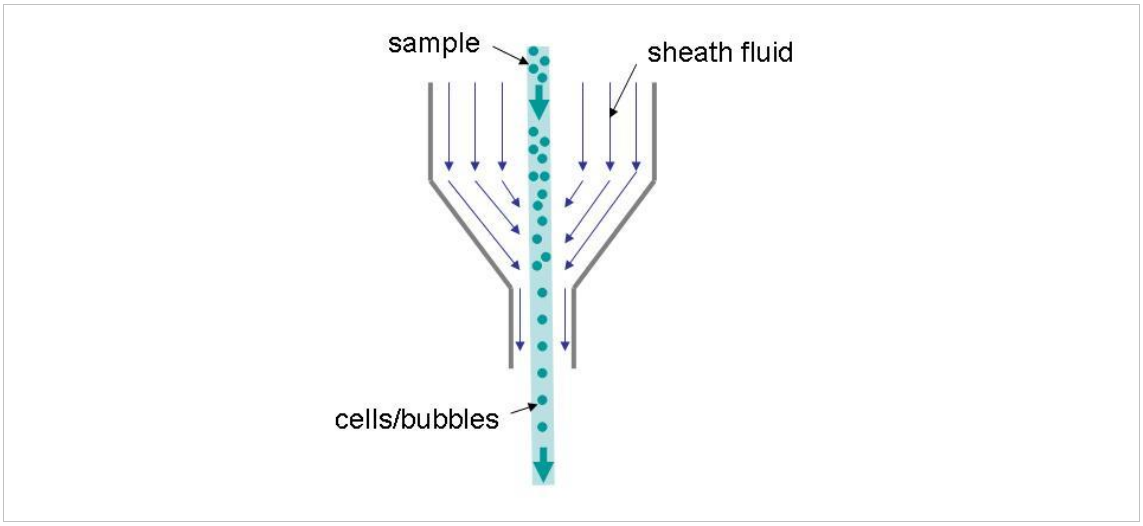

Figure 6-4: Hydrodynamic focusing of a solution containing cells or microbubbles.

Once the cells are flowing in single file they are passed through a laser beam which results in light scattering, this is illustrated in Figure 6-5. As individual cells pass through the laser beam, laser light is scattered forwards and sideways as illustrated in Figure 6-6. Data from the forward scatter can be used to determine the two dimensional size of the particle whilst the sideways scatter can provide further three-dimensional information on complexity.

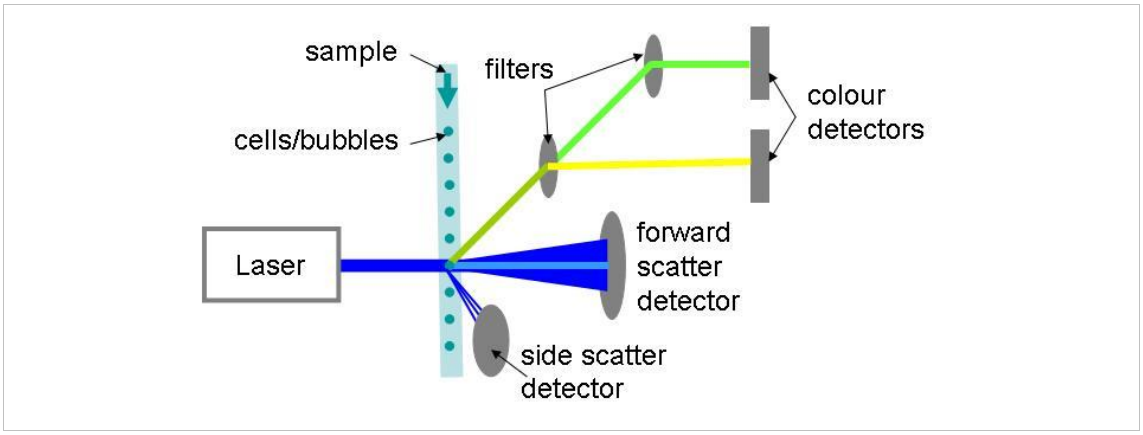

Figure 6-5: Flow cytometry principle.

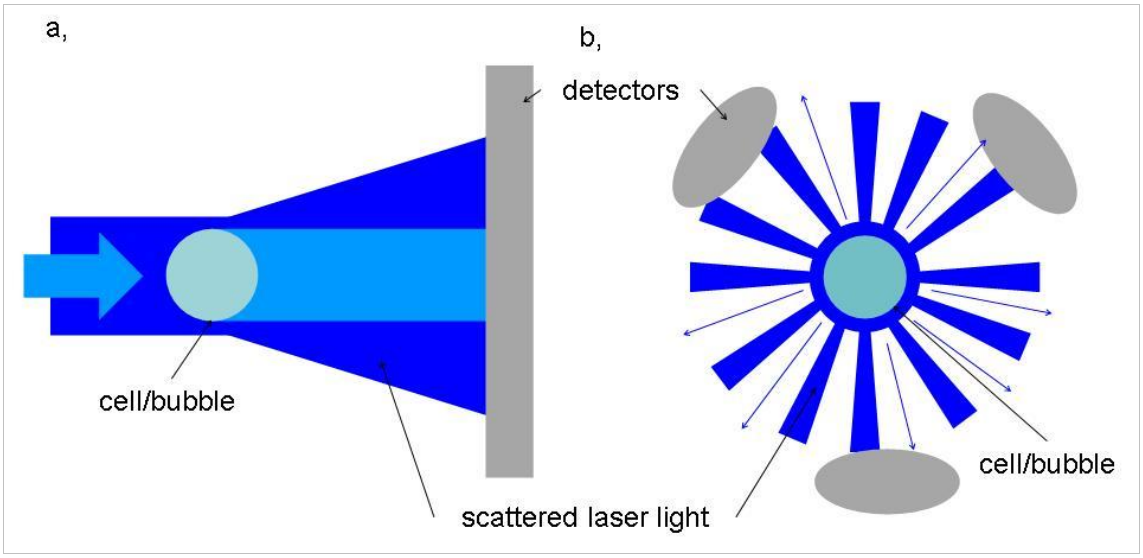

Figure 6-6: Scattering of laser beam by cells or microbubbles; a, forward scatter and b, sideways scatter.

Absorption and fluorescence properties of the biomolecules within the cell can provide the chemical analysis (Sheehan 2000), identifying which biomolecules are present. In addition refractive index measurements can quantify the granularity within the cells. Through this chemical analysis subtle differences between subpopulations of cells can be detected.

In addition to the physical and chemical information, flow cytometry can be used to investigate the fluorescence of a cell or particle. Antibodies with fluorophore tags can be added to the cell. When the laser is incident upon a fluorescent marker the fluorophores are excited and then as they relax they emit light of a specific wavelength. Detectors collecting side scatter can filter the emitted light and identify the fluorophore and intensity of the fluorescence. Fluorescence can therefore provide information about the number of cells with fluorescent markers and the amount of fluorescence per cell.

Due to the comparable sizes between the in-house microbubbles and cells it is possible to use flow cytometry to assess the attachment of antibodies to the microbubbles. The

antibodies on the microbubbles are tagged using a fluorescent antibody as illustrated in Figure 6-2a. When the fluorescently tagged microbubbles are put through the flow cytometer information regarding the number of microbubbles fluorescing, and the amount of fluorescence, can be collected. This identifies the number of microbubbles with antibodies attached.

6.3. Attaching antibodies to the in-house microbubbles

6.3.1. Initial Investigation and Results

Initial investigations into attachment of antibodies to the in-house microbubble involved adding varying amounts of 1mg/ml concentration streptavidin (Sigma-Aldrich, MO, USA) (0, 50, 100 and 150µl) to a millilitre sample of the in-house microbubbles, agitating and incubating at 2-5°C for 20-30 minutes and then incubating with 10µl of CD31 biotinylated antibody (R&D systems, USA) for a further 20-30 minutes. CD31 is an antibody produced by the body to remove aged white blood cells. Also known as platelet endothelial cell adhesion molecule (PECAM-1), the antibody will adhere to endothelial cells and is therefore a suitable targeting antibody for SK-Hep-1 cells used throughout this thesis as described later in Chapter 8.

Figure 6-7 shows only a very small increase in fluorescence with increasing volumes of streptavidin over 50µl. The number of microbubbles fluorescing is less than 10% and therefore the number of microbubbles with antibodies attached is inadequate and would result in only 10% of the microbubbles being able to attach to the cells.

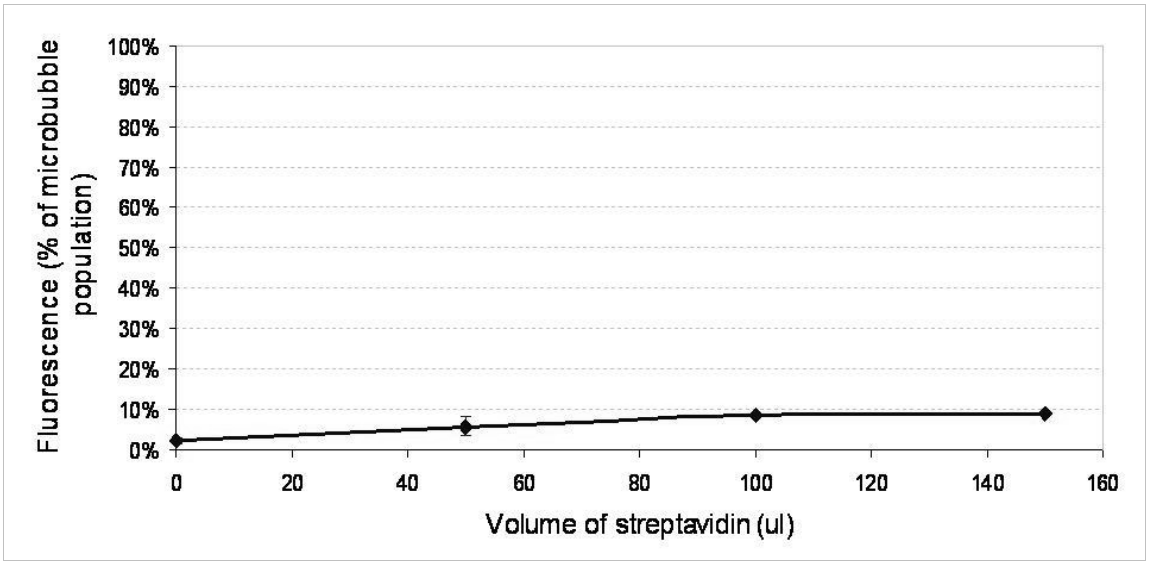

Figure 6-7: Initial results from antibody attachment with varying volumes of streptavidin (error bars represent 1 standard deviation of three data sets).

Due to the low percentage of microbubbles with antibodies attaching an investigation was then carried out into the attachment of streptavidin to the biotinylated microbubbles. In order to assess attachment of streptavidin to the in-house microbubbles using flow cytometry a fluorescent, fluorescein isothiocyanate (FITC) conjugated streptavidin (Sigma-Aldrich, MO, USA) was used so that attachment could be assessed with flow cytometry. FITC conjugated streptavidin was added to the biotinylated microbubbles, agitated for 5s, and then incubated at 2-5°C for 20-30 minutes. Following this the samples were washed twice, diluted 1:10 with phosphate buffered saline (PBS), and assessed using flow cytometry. Figure 6-8 shows the number of microbubbles with streptavidin attached as a percentage of the microbubble population.

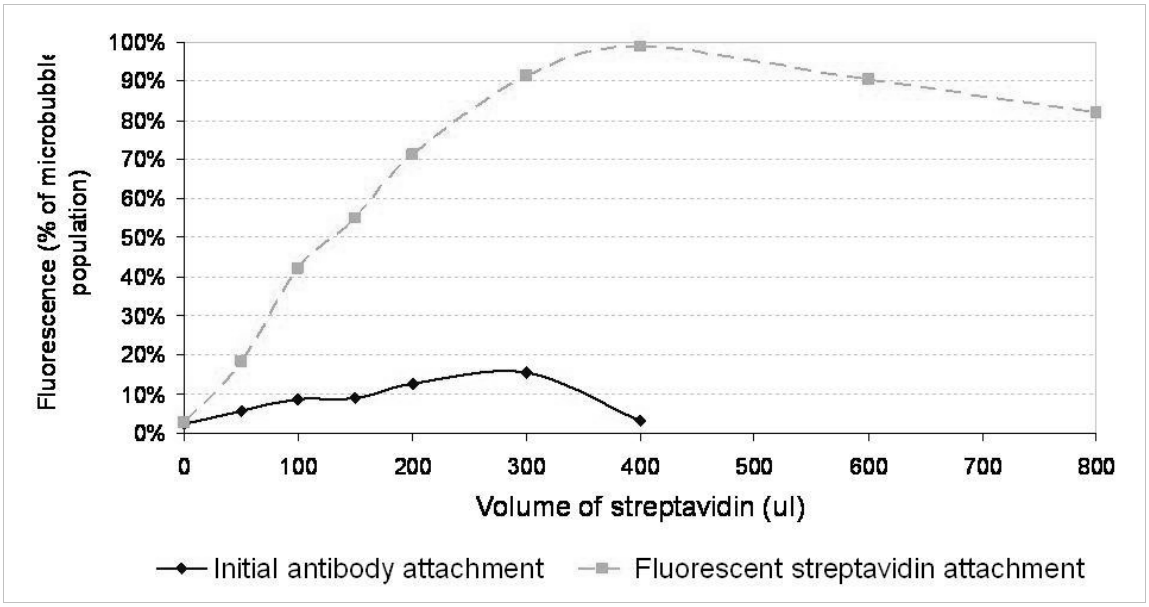

Figure 6-8: Attachment of FITC conjugated streptavidin to microbubbles (error bars represent 1 standard deviation).

As the volume of streptavidin is increased, the percentage of microbubbles with streptavidin attached increases. At 400µl of streptavidin the percentage of the microbubble population with streptavidin attached reaches 97.83 (± 0.02)%. Beyond this there is no further increase in fluorescence, suggesting that 400µl is the optimum volume of streptavidin for attachment to the microbubbles. Microbubble concentrations were found to be approximately $(64.50\pm0.02)\times10^{6}$microbubbles per ml as described in Appendix G. However, the composite image of the microbubbles with streptavidin in Figure 6-9a illustrates clumping of the microbubbles in which the streptavidin attaches microbubbles together.

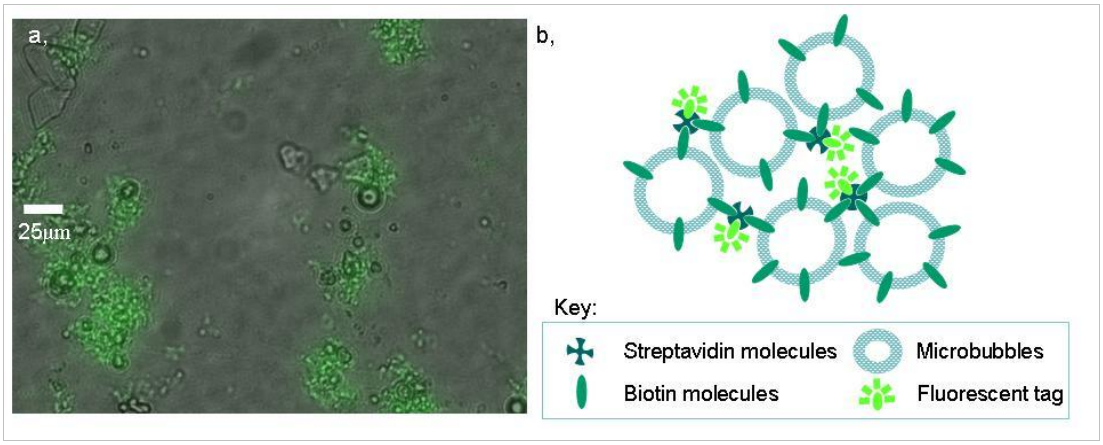

Figure 6-9: Clumping of microbubbles as a result of streptavidin addition; a, composite microscopic image confirming attachment of streptavidin to microbubbles and demonstrating clumping and b, schematic demonstrating clumping.

6.3.2. Secondary Investigation and Results

The results presented in the initial investigation indicate that the streptavidin is attaching to the biotinylated microbubbles. However attachment of the antibodies to the streptavidin coated microbubbles was still not observed. The potential reasons for this are outlined below:

- The biotinylated antibodies were not attaching to the streptavidin on the microbubble surface due to denaturing or faulty product.
- There were insufficient antibodies present to observe attachment to the microbubbles.
- The fluorescent tag was not attaching to the antibodies, therefore not identifying antibodies attached to the microbubbles.
- The streptavidin on the microbubble surfaces were attaching microbubbles together, using up all streptavidin sites or making them inaccessible to biotinylated antibodies.

The author believed this to be due to the clumping of the bubbles and a lack of available streptavidin binding sites, identified in the fourth point above and illustrated in Figure 6-9. In light of this the following variations to the procedure were introduced:

- CD31 was added to the microbubbles before adding streptavidin.
- Samples were agitated whilst adding the streptavidin in an attempt to encourage a greater number of antibodies to attach to the microbubbles.

The next investigation involved reducing the volume of microbubbles used as it was surmised that there may be insufficient antibodies present to compete for the streptavidin binding sites.

Method

The test tubes were set up with 1ml PBS in each. Following this, CD31 biotinylated antibody and the in-house microbubbles were added to the test tubes in volume ratios of 1:10, 1:5, 1:2, 1:1, 5:2, 5:1 and 15:2. The samples were then agitated for 5s each.

A standard quantity of 100µl of streptavidin was then added to each sample whilst agitating and samples were further agitated for 10s. After agitating the samples were incubated at 2-5°C for 20-30 minutes. The samples were then washed twice before adding the fluorescent tag to the antibodies and measuring the number fluorescing with flow cytometry.

Results

At microbubble to antibody ratios, of 0.5 or under by volume, less than 50% of the microbubble population had antibodies attached, whilst as the ratio was increased to one, the percentage of microbubbles with antibodies attached peaked at 70%. Beyond a ratio of 1:1 the fluorescent population decreased rapidly reaching below 10% at a ratio of 7.5. This data is illustrated in Figure 6-10 below. The targeted microbubbles can be seen in

Figure 6-11. These images show that some clumping is observed when targeted (Figure 6-11c and d), although significantly less than observed in initial investigations.

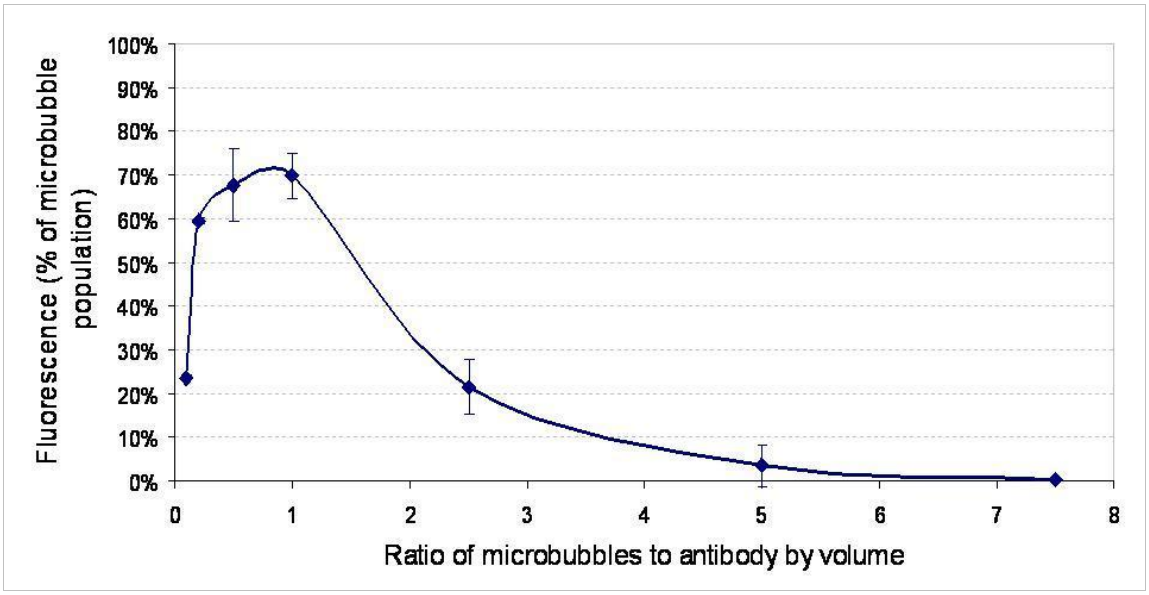

Figure 6-10: Variation in fluorescent population of microbubbles as a function of antibody to microbubble ratio (error bars represent 1 standard deviation).

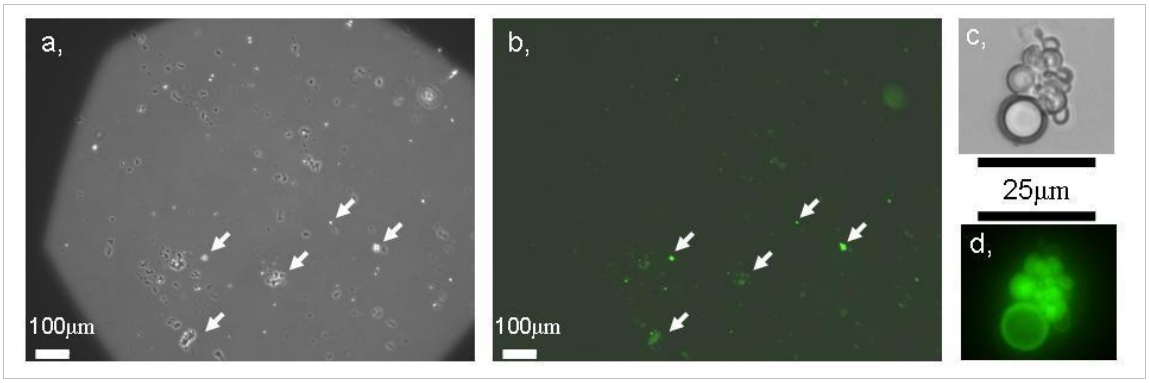

Figure 6-11: Microscopic images of targeted microbubbles at 13×106microbubbles per ml concentration; a, x10 magnification phase contrast image, b, x10 magnification fluorescent image (bright dots showing existence of targeted microbubbles), c, x40 magnification cropped image of a cluster of microbubbles and d, x40 magnification fluorescent image of the same cluster. White arrows indicate some targeted microbubbles.

The data presented in Figure 6-10 shows the optimum ratio of antibodies to microbubbles to be 1:1 as a distinct peak can be seen at this ratio. In light of this, all further investigations into the attachment of antibodies to microbubbles were carried out with equal volumes of antibodies and microbubbles.

6.3.3. Final investigation

Once the optimum ratio of antibodies to microbubbles had been established a further investigation into the optimum volume of streptavidin, for antibody attachment, was carried out.

Method

Test tubes were set up with 1ml PBS, following this 10µl of microbubbles and 10µl of biotinylated CD31 were added and the solutions were agitated (an equal number of test tubes were set up containing 10µl of microbubbles and 50µl of a negative antibody as a control set).

Streptavidin was then added to all the samples whilst agitating and samples were agitated for a further 10s after addition. Initially streptavidin in aliquots of 10, 15, 20, 25, 30, 40, 50, 60, 100 and 150µl were added to the negative and positive samples. This was followed by an investigation into smaller volumes of streptavidin and aliquots of 2, 4, 6, 8, 10 and 15µl were added to negative and positive samples.

All samples were then incubated at 2-5°C for 20-30 minutes and then washed twice. Following this the fluorescent tag was added to the antibodies for assessment with flow cytometry.

Results

The data collected from the investigation involving larger volumes of streptavidin is presented in Figure 6-12. From this data it can be seen that there is a minimum in

antibody attachment between 20 and 30µl and that optimum attachment occurs at 10 and 50µl.

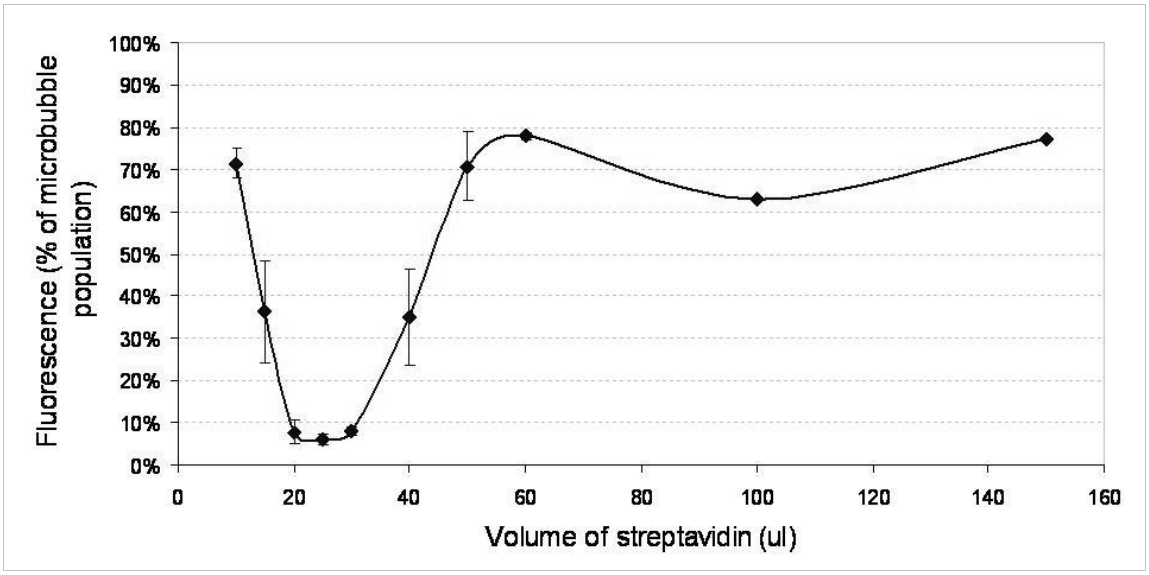

Figure 6-12: Fluorescence as a percentage of the microbubble population for large volumes of streptavidin (error bars represent 1 standard deviation).

Due to the peak observed at 10µl an investigation into smaller volumes of streptavidin was carried out and the data from this investigation is illustrated in Figure 6-13 below. This data shows a peak of 91.20(±0.03)% at 8µl of streptavidin suggesting that this is the optimum amount of streptavidin to be used in antibody attachment.

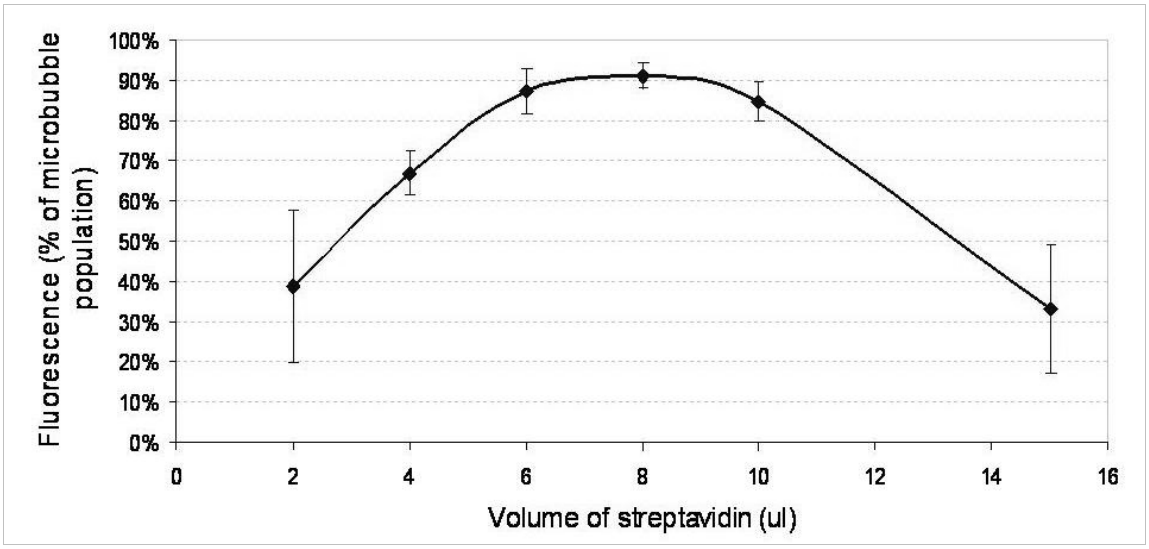

Figure 6-13: Fluorescence as a percentage of the microbubble population for small volumes of streptavidin (error bars represent 1 standard deviation).

6.4. Discussion

Initial investigations carried out were to determine the optimum volume of streptavidin to facilitate antibody attachment. The results from this investigation, which are presented in Figure 6-7, suggest that little antibody attachment had been achieved with the original attachment method. When observed under the microscope it was evident that clumping of the microbubbles was occurring. To confirm that this clumping was a result of the streptavidin attaching the microbubble biotin sites together an investigation into the attachment of a FITC conjugated streptavidin was carried out. This investigation confirmed that streptavidin was binding to the microbubble biotin sites and is illustrated in Figure 6-8 and Figure 6-9. In addition Figure 6-9 confirms that the streptavidin is the cause of the microbubble clumping.

Once streptavidin attachment had been confirmed changes to the attachment procedure for the antibodies were introduced. The primary change was the addition of the antibodies to the microbubbles prior to the addition of streptavidin. In addition it was

hypothesised that the low antibody attachment may be due to an uneven number of antibodies to microbubbles and therefore an investigation into the effect of varying the antibody to microbubble ratio by volume was carried out.

The results presented in Figure 6-10 demonstrate that the hypothesis was correct and suggests that optimum attachment occurs at 1:1 volume ratio of antibodies to microbubbles. At this ratio antibody attachment was at 80% of the microbubble population.

Once attachment of antibodies was established a second investigation into varying volumes of streptavidin was carried out. The first investigation, results of which are presented in Figure 6-12, involved volumes from 10µl to 150µl. This data suggested that there was a significant drop in the percentage of microbubbles with antibodies attached at 20-40µl. With peaks in the number of microbubbles with antibodies attached at 10 and 60µl. The author believes that the initial peak in antibody attachment is due to there being sufficient streptavidin to bind the biotinylated antibodies to the microbubbles. As the volume of streptavidin increases this results in many unbound streptavidin sites causing the microbubbles to clump together, preventing antibodies from being fluorescently tagged as they are trapped inside clumps of microbubbles. Above 60µl of streptavidin it is believed that the microbubble biotin sites are swamped therefore preventing clumping of microbubbles resulting in a high percentage of microbubbles with antibodies attached.

Due to the economics of the project it was decided to do a further investigation into smaller volumes of streptavidin, from 2-15µl. This was carried out to establish if 10µl of streptavidin was optimum. The results presented in Figure 6-13 suggest that peak antibody attachment occurs at 8µl of streptavidin per 10µl of microbubbles.

As a result of these investigations, it was shown that the optimum ratio of antibodies to microbubbles to streptavidin is 5:5:4 by volume.

6.5. Summary

Antibodies have been shown to attach to the in-house microbubbles via a streptavidin-biotin bridge. The optimum ratio of antibodies to microbubbles to streptavidin is 5:5:4. This composition produces a microbubble population with 91.2% antibody attachment, nine times greater than the initial attachment achieved.

In conclusion, using the streptavidin-biotin bridge, we have successfully shown that biotinylated antibodies can be attached to the in-house microbubble. In Chapter 7 the strength of attachment of the streptavidin-biotin bond will be measured in the flow chamber previously described and in Chapter 9 attachment of the targeted microbubbles developed in this chapter will be assessed under flow.

Chapter 7 Attachment and Detachment of the UCA under Increasing WSS: Streptavidin-Biotin Bond.

The strength of attachment of the microbubble UCA was investigated by assessment of the detachment of the agent under increasing WSS. Previously Butler et al. (2005) determined that the agent attached to an agar surface via a streptavidin-biotin bond can withstand WSS of up to 3.4Pa. As described in Chapter 4, a novel parallel-plate flow chamber was designed and calibrated to 50Pa WSS. In this chapter the strength of the streptavidin-biotin bond has been tested up to 50Pa; over an order of magnitude greater than previously tested and comparable to shear stresses found in non-diseased coronary arteries and in small animal vessels (Cheng et al. 2007a), the purpose of this investigation was to determine the feasibility of using the UCA for future small animal studies. WSS values found in mouse aortas and human coronary arteries are presented in Table 7-1.

Animal	Vessel	Average WSS	Peak WSS	Methods	Reference
Mouse	Aorta	22Pa	60Pa	Computational	(Suo et al. 2007)
Human	Coronary arteries	NA	8.06Pa	Measured in vivo	(Wentzel et al. 2006)
Human	Coronary arteries	0.68Pa	NA	Measured in vivo	(Doriot et al. 2000)

Table 7-1: Values of WSS found in healthy vessels of mice and humans.

In addition attachment of the in-house UCA via a streptavidin-biotin bond has been investigated under flow. For this investigation the biotinylated in-house UCA was introduced to water flowing over a streptavidin coated agar surface at very low WSS.

Microbubbles containing 5% biotin were used throughout this investigation. Biotinylated in-house microbubbles were produced in accordance with Appendix D.

7.1. Detachment Investigation

For the detachment investigation, biotinylated microbubbles were attached to streptavidin-coated agar and placed inside the flow chamber. The flow chamber incorporated an agar well to facilitate the attachment of the agent under flow conditions. Agar was produced using the protocol outlined in Appendix H and manufactured to fit into the agar well of the flow chamber. The processes involved in attachment of the agent to the agar are outlined below.

7.1.1. Methods and Materials

Coating agar strips with streptavidin

Streptavidin (Sigma-Aldrich, MO, USA) was dissolved in a coating buffer (1 capsule bicarbonate to 100ml de-ionised water) in a 1:12 (streptavidin to buffer) ratio by volume. The agar was then coated with 1ml of the streptavidin buffer solution covered and left for a minimum of 18 hours to ensure optimum adsorption of the streptavidin.

Excess coating buffer and streptavidin was rinsed off the agar after 18 hours using saline.

Attaching microbubbles

The biotinylated in-house microbubbles were then added to the streptavidin coated agar surface. Microbubbles were transferred to the agar surface in 1ml aliquots, the coated agar was then covered and left for two hours. After two hours the agar surface was rinsed with saline again to remove excess microbubbles.

Assessment of attachment

Once microbubbles had been attached, the 200×7×2mm agar strips were placed inside the flow chamber. The flow chamber was then clamped shut and connected to the pump, as illustrated in Figure 4-7 with the LDA set-up. The flow chamber is shown in Figure 7-1.

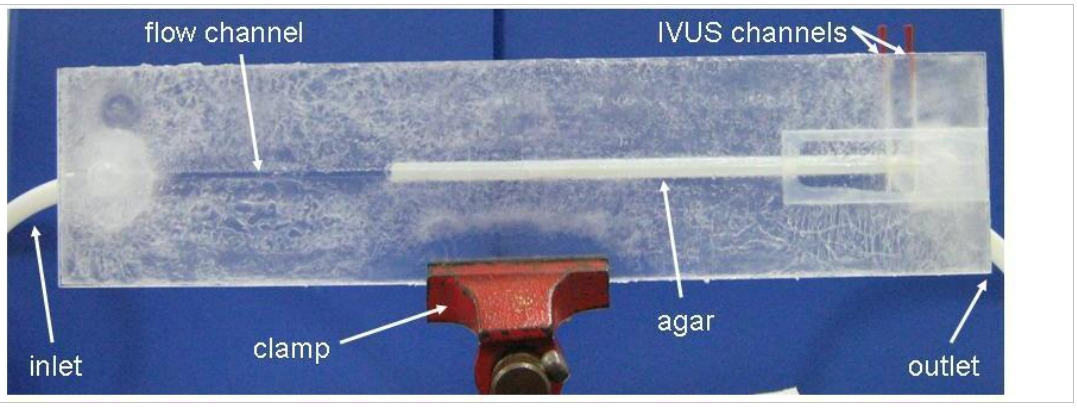

Figure 7-1: Photograph of flow chamber sealed with silicon grease (which can be seen as the texture on the plastic) and showing agar well. (A greater number of clamps were used, when passing flow through chamber, than pictured.)

WSS was varied by increasing the flow volume through the flow chamber at 20ml·min^{-1} intervals from 60-180ml·min^{-1}. An additional result was collected at 350ml·min^{-1}.

At each interval IVUS images of the reflection from attached microbubbles was collected. In addition the RF data from the IVUS images was collected and analysed in IDL to determine the mean backscatter from the microbubbles, as described in Chapter 3.

A control investigation was also carried out in which microbubbles were transferred onto a non-streptavidin-coated agar strip, which was then left for two hours, rinsed and subjected to the same shear stresses as the attached microbubbles.

Each experiment was repeated three times and the mean backscatter compared. An IVUS image and mean backscatter measurement were also collected from a plain agar surface and a streptavidin-coated agar surface, with no microbubbles attached, as a baseline.

7.1.2. Results

Control Investigation

The IVUS images collected from the control investigation are shown in Figure 7-2. The baseline image, agar with no microbubbles attached, can be seen in Figure 7-2f. In static conditions (at 0Pa WSS) the mean backscatter from the non-streptavidin-coated surface, which was exposed to microbubbles, is brighter, suggesting that microbubbles are attached to this surface. As described previously the RF data from the IVUS image was analysed in order to quantify the mean backscatter from the microbubbles on the agar surface. A region of interest was centered over the surface echo of the agar and analysed. Figure 7-3 shows the decrease in mean backscatter as the WSS is increased to relatively low WSS values. The mean backscatter from the non-streptavidin-coated surface which was exposed to microbubbles is more than 10dB greater than the mean backscatter from a plain agar surface in static conditions ($p<0.05$). As the WSS is increased to 0.88Pa (a relatively low WSS) the mean backscatter decreases to -33.5(±0.9)dB suggesting that the microbubbles have detached from the surface as, at this

WSS the mean backscatter value is the same as that from the plain agar surface (p=0.39). This is confirmed by the echo in Figure 7-2e.

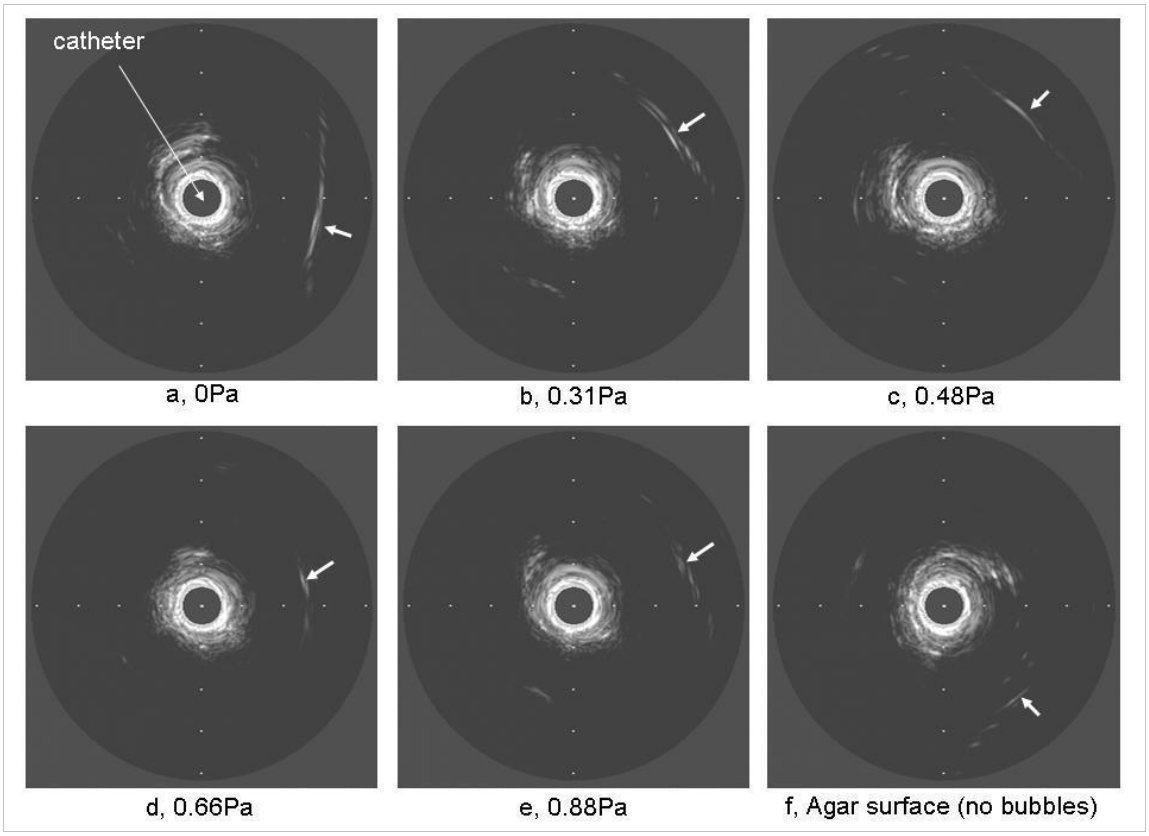

Figure 7-2: IVUS images from control investigation showing mean backscatter from microbubbles attached to an uncoated agar surface at a, 0Pa; b, 0.30Pa; c, 0.44Pa; d, 0.66Pa; e, 0.88Pa and f, a plain agar surface. Agar surfaces identified by white arrows.

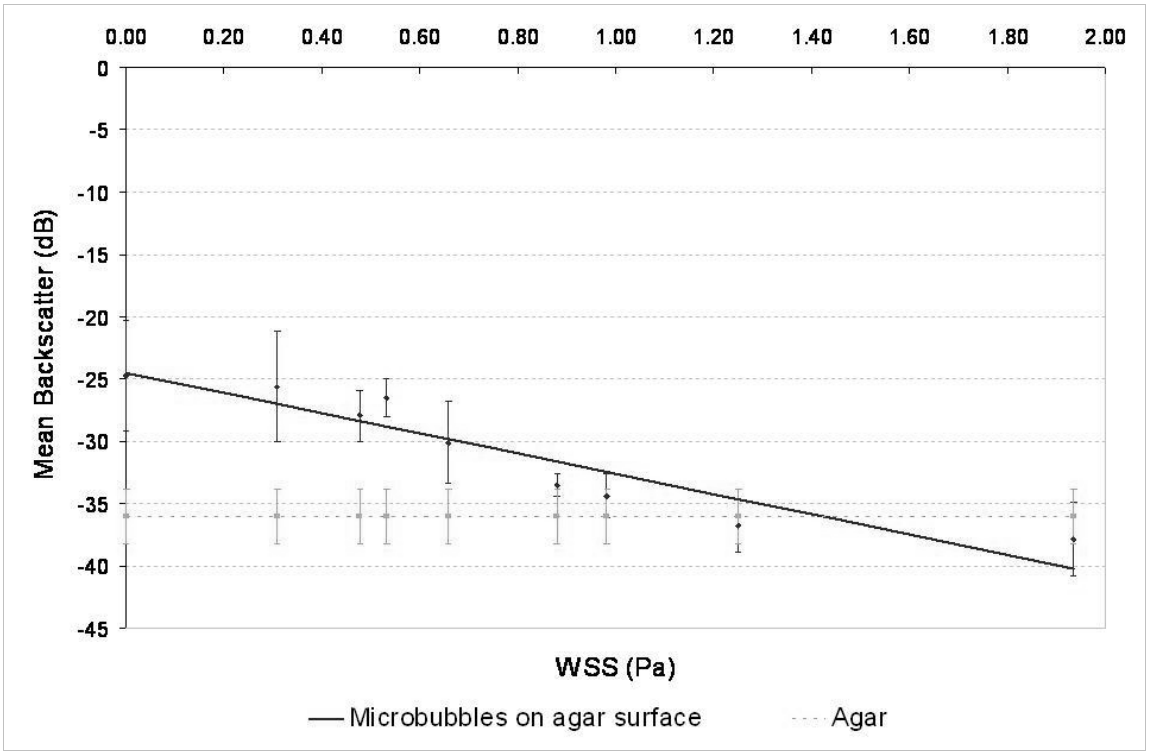

Figure 7-3: Control investigation showing mean backscatter from non-streptavidin-coated agar surface exposed to microbubbles in addition to mean backscatter from an agar surface. (Error bars represent 1 standard deviation.)

Streptavidin-Biotin Attachment

Under a streptavidin-biotin attachment mechanism the in-house UCA was found to remain attached up to 50Pa WSS. Figure 7-4 shows the echoes received from the microbubbles attached to the agar via a streptavidin-biotin bond at 0 and 50Pa WSS compared to the echo from a plain agar surface and a streptavidin coated agar surface. These IVUS images show that the echo from the agar surface with microbubbles attached is brighter than that from the plain and streptavidin coated agar surfaces at both 0 and 50Pa. This indicates that microbubbles have remained attached to the streptavidin coated surfaces at 50Pa WSS.

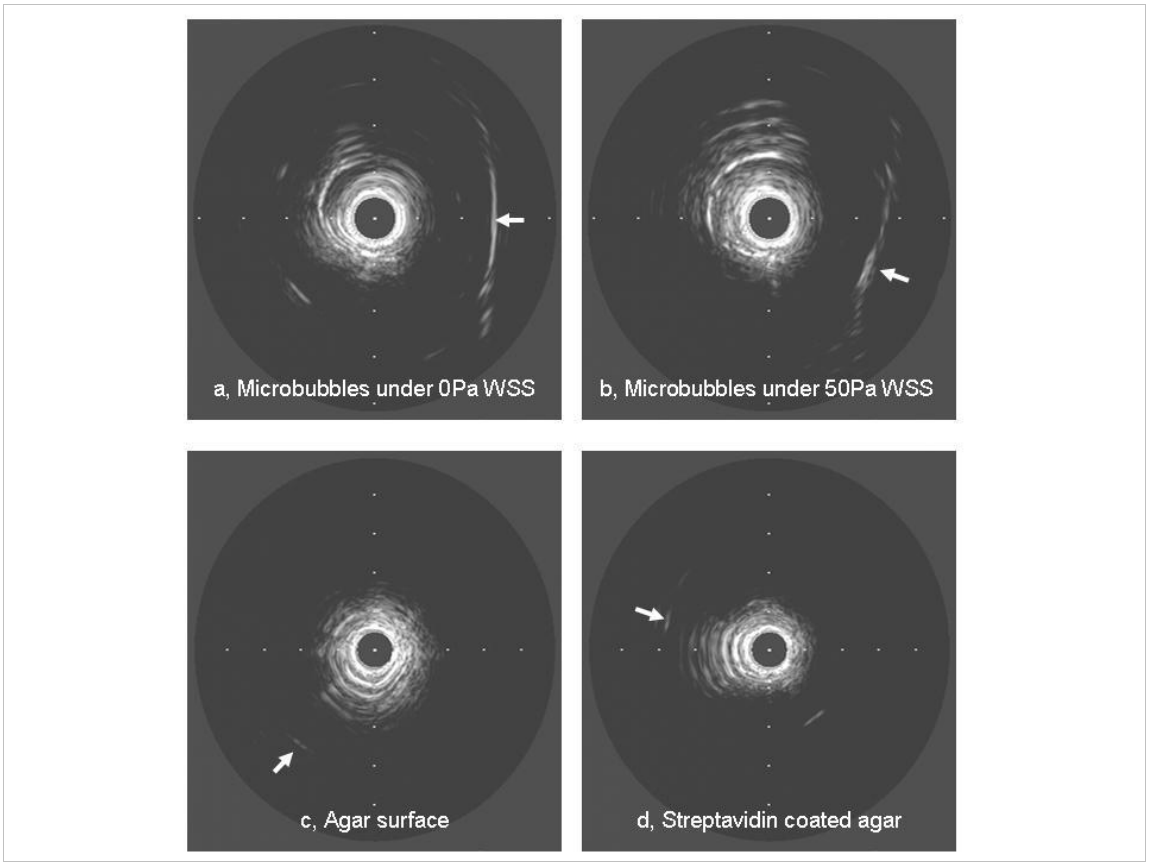

Figure 7-4: Echoes from agar surface with microbubbles attached at a, 0Pa and b, 50Pa WSS compared to echo from c, a plain agar surface and d, a streptavidin coated agar surface. White arrows indicate agar surface.

The mean backscatter analysis, which can be seen in Figure 7-5, confirms that the echo received from the surface with microbubbles attached is greater than the mean backscatter from plain agar. Under static conditions the mean backscatter from the attached microbubbles is -21.5(±1.6)dB which is 15.0(±2.4)dB greater than the mean backscatter from a streptavidin coated agar surface ($p<0.01$). As the WSS is increased the mean backscatter decreases slightly but at 50Pa WSS it is -34.9(±5.5)dB, still 1.5dB greater ($p=0.65$) than that from the control surface indicating that, although potentially a proportion of the microbubbles remain attached even at very high WSS, this is not a statistically significant difference.

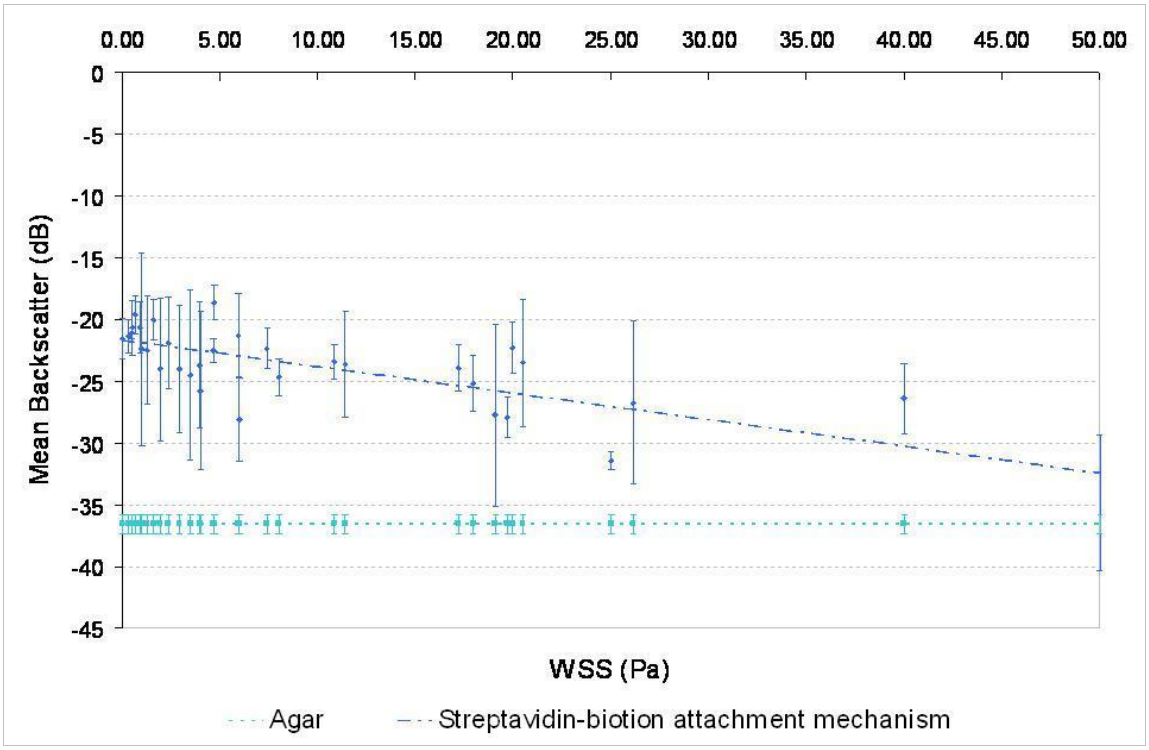

Figure 7-5: Mean backscatter from microbubbles attached to a streptavidin coated agar surface at increasing WSS compared to the mean backscatter from a streptavidin coated agar surface without microbubbles attached. (Error bars represent one standard deviation.)

The results from the control investigation and the streptavidin attachment investigation can be seen together in Figure 7-6. The strength of attachment to the agar via a streptavidin-biotin bond was 75 times greater than attachment without this bond.

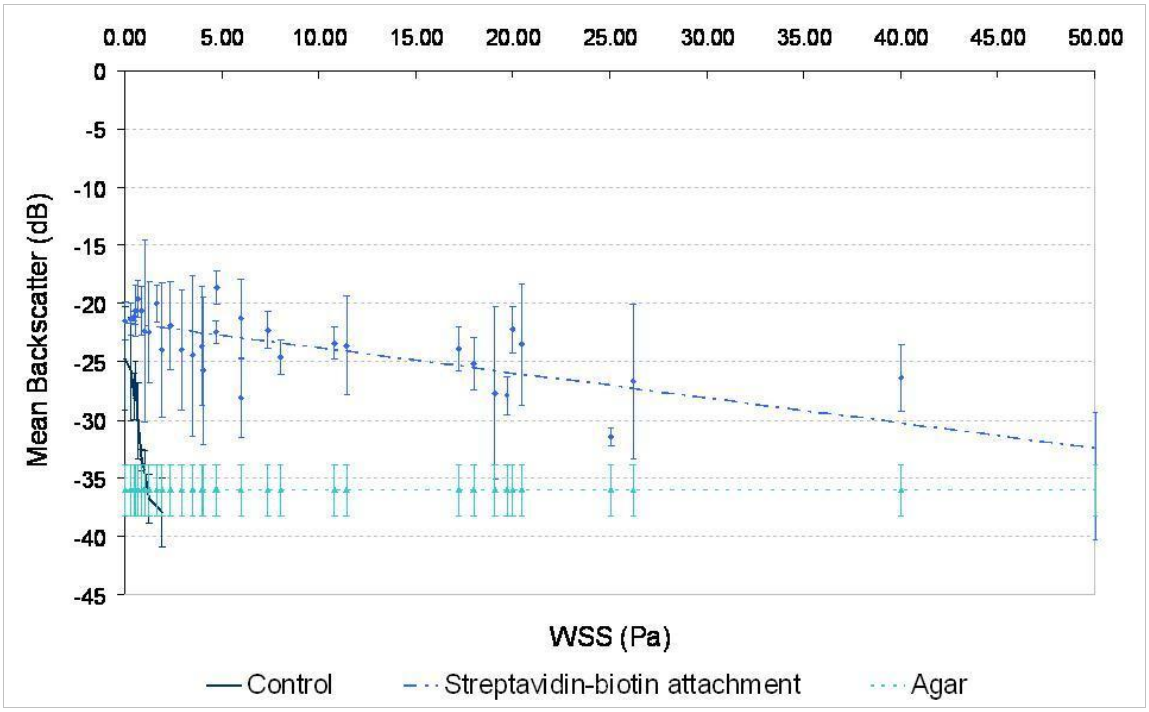

Figure 7-6: Comparison of the mean backscatter at increasing WSS for the streptavidin –biotin attachment and the control investigation. (Error bars represent one standard deviation.)

7.2. Detachment over time

An investigation into the length of time the in-house microbubbles remain attached to the agar surface was carried out, under low WSS. The purpose of this investigation was to determine if the streptavidin-biotin bond would remain stable for the duration of an ultrasound examination.

7.2.1. Materials and Methods

Microbubbles were attached to the agar strips as described in Section 7.1.1. The microbubble coated agar strips were then placed in the flow chamber and the attached microbubbles were subjected to a WSS of 0.48Pa for 150 minutes. IVUS images and RF data were collected every 15 minutes.

In addition a control investigation was carried out. Microbubbles were attached to the agar strips and placed inside the flow chamber. The flow chamber was filled with water but the microbubbles were not subjected to shear stress for the duration of the investigation. IVUS images and RF data of the attached microbubbles were collected every 15 minutes for 150 minutes.

Data from a plain agar strip was collected at the same time for comparison.

7.2.2. Results

The IVUS images in Figure 7-7 show the reflections from microbubbles attached to an agar surface under 0 and 0.48Pa WSS at 0 and 150 minutes and compare this echo to the reflection from agar in Figure 7-7f.

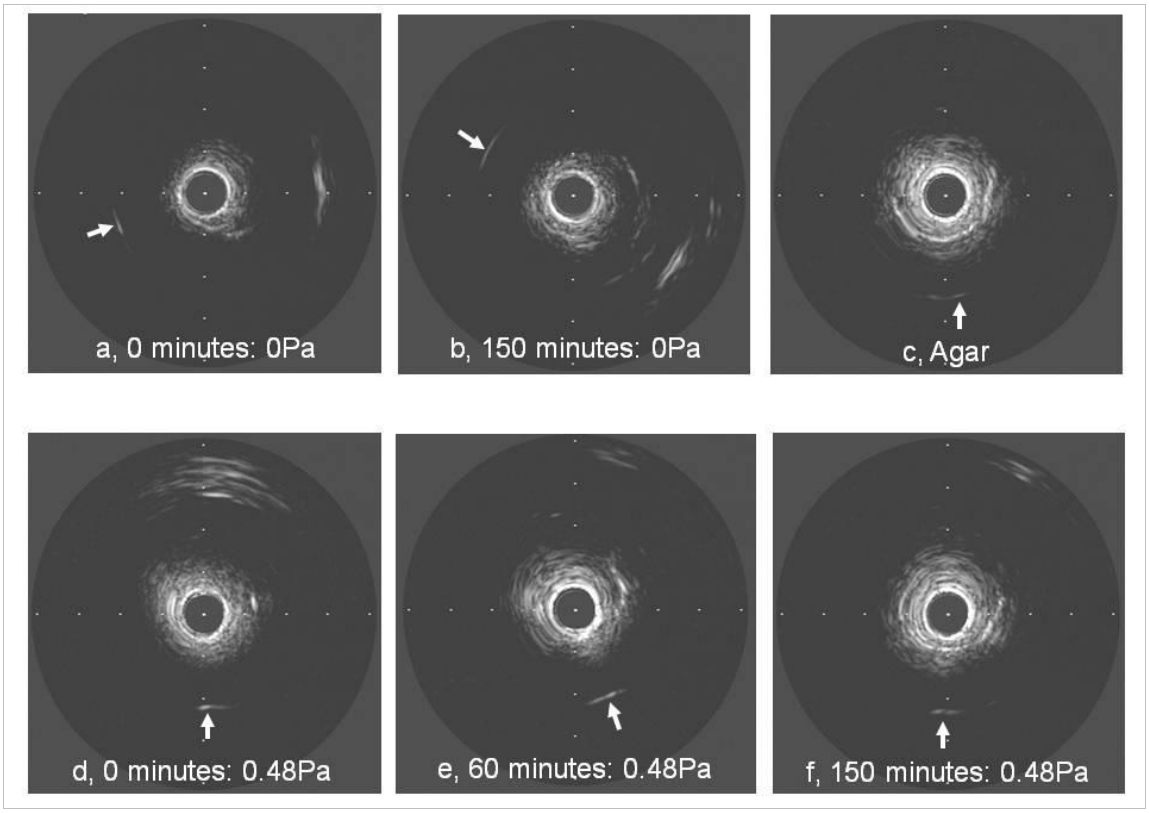

Figure 7-7: IVUS images collected at different time intervals for a-b microbubbles subjected to 0Pa WSS and d-f, microbubbles subjected to 0.48Pa WSS compared to c, the reflection from agar.

The reflection from the attached microbubbles under 0Pa WSS does not vary significantly over the 150 minute period whilst the reflection from the microbubbles subjected to 0.48Pa WSS decreases over 150 minutes. However, despite a decrease in the reflection the echo after 150 minutes is still enhanced compared with that from plain agar ($p<0.01$).

Analysis of the RF data confirms that the mean backscatter from the attached agent decreases by 5dB under 0.48Pa WSS over 150 minutes, whilst the mean backscatter from the agent attached under 0Pa WSS varies by only 1dB. This data is presented in Figure 7-8.

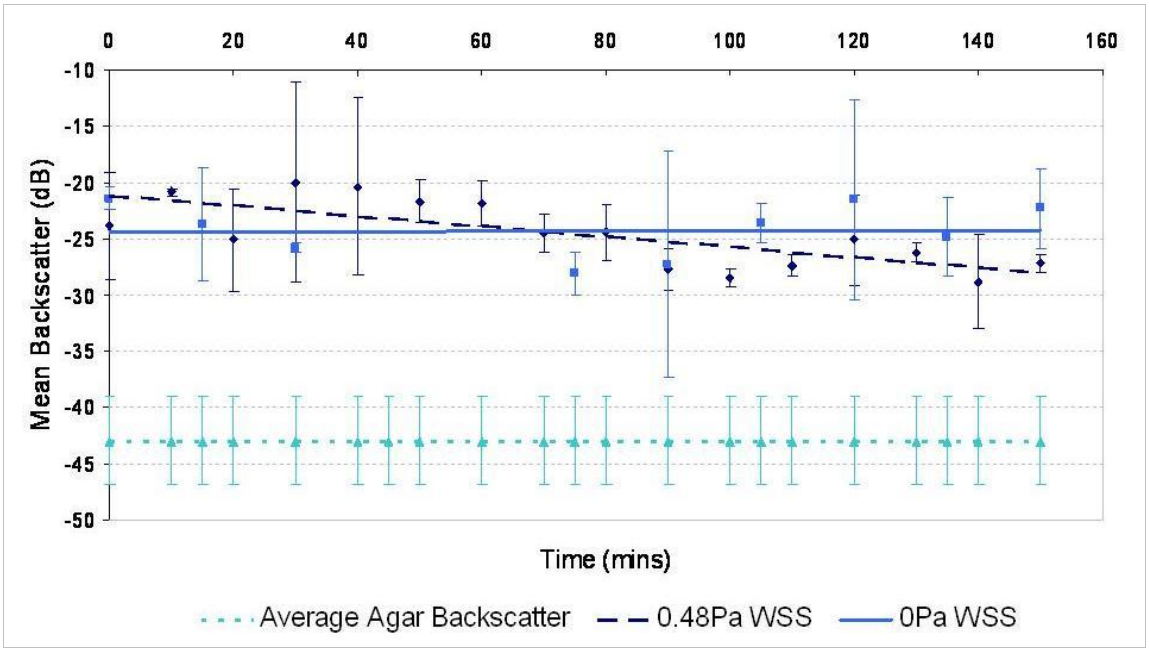

Figure 7-8: Mean backscatter from microbubbles subjected to 0Pa and 0.48Pa WSS over time. (Error bars represent one standard deviation.)

7.3. Attachment Investigation

Attachment of the agent to agar under low WSS was investigated. This was achieved by introducing microbubbles to the flow across agar. Agar strips were coated in

streptavidin, as described in Section 7.1, then placed inside the flow chamber and subjected to a WSS of 0.31Pa, the lowest achievable in the novel flow chamber. Biotinylated contrast agent was then injected directly into the flow channel and allowed to circulate in the flow for 10 minutes following which an IVUS image and RF data from the agar surface were collected and compared to IVUS data collected before introducing contrast agent to the flow. This investigation was repeated three times.

7.3.1. Initial Results

Figure 7-9b shows the echo received from the streptavidin coated agar surface after 10 minutes of circulating the in-house UCA under 0.31Pa WSS. The echo is not enhanced compared to that received from the plain agar surface suggesting that microbubbles are not attaching under flow conditions. The mean backscatter from the coated surface after being subjected to flow and biotinylated contrast agent was -33.8(±3.0)dB and the mean backscatter from the agar surface was -34.4(±1.9)dB. This illustrates that the variation in echogenicity is minimal at less than 1dB suggesting that there is no attachment under 0.31Pa WSS.

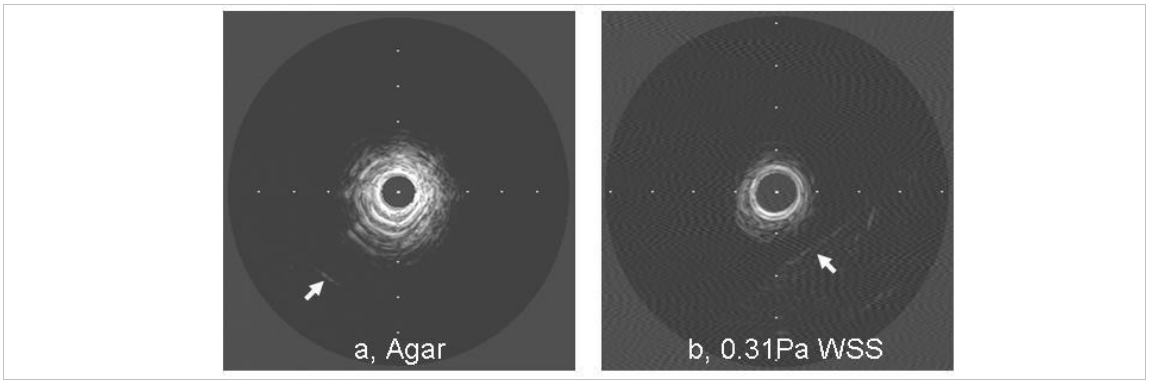

Figure 7-9: IVUS images a, of agar surface before introducing contrast agent to the flow and b, of a streptavidin coated agar surface after being subjected to contrast under 0.31Pa WSS

7.3.2. Further attachment investigations

Since the results presented above suggested that no microbubbles were attaching, under even low wall shear stresses, visual observations of attachment, with a microscope were investigated. Microscopic visualisation of the agar surface was attempted, however this proved to be inconclusive as the agar is opaque and the methods used to section very fine samples of the agar surface may have caused any attached agent to detach. Therefore the adapted rear panel of the flow chamber designed for cellular adhesion (described in depth in Chapter 8) was used and attachment to microscope slides was attempted.

Microscope slides were coated in streptavidin using the same method used to coat the agar strips previously. The slides were then placed inside the flow chamber and subjected to 0.31Pa WSS. A 2.4ml volume of the in-house contrast agent was then injected directly into the flow channel and circulated for 5 minutes.

Figure 7-10 shows microscopic images of slides after being subjected to biotinylated contrast agent at 0.31Pa WSS. Figure 7-10b shows that there are a very small number of microbubbles attaching under low WSS, less than $8mm^{-2}$.

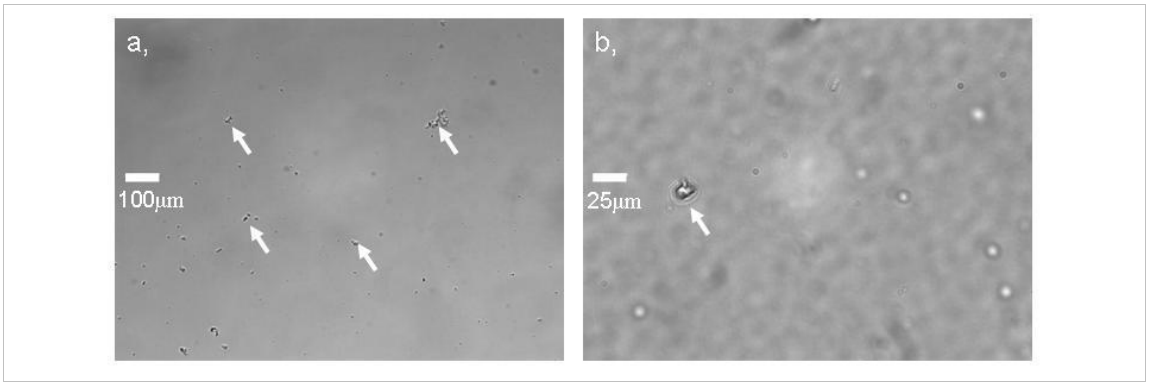

Figure 7-10: Microscopic images of slides after being subjected to contrast agent at 0.31Pa WSS a, x10 magnification and b, x40 magnification.

7.4. Discussion

The biotinylated in-house UCA has been shown to remain attached to a streptavidin coated agar surface up to 50Pa WSS, showing that the streptavidin-biotin bond can withstand the shear stresses experienced in the coronary arteries of small animals. This investigation has shown that the streptavidin-biotin bridge is a suitable method for attaching antibodies to the shells of the in-house microbubbles as it is capable of withstanding high WSS. In addition the streptavidin-biotin bond has high specificity meaning that the streptavidin is unlikely to bond to other proteins, therefore optimizing the antibody attachment. Antibody attachment and the streptavidin-biotin bond are discussed further in Chapter 6.

In this Thesis I have demonstrated that microbubbles attached to agar via a streptavidin bond are able to withstand 75 times the shear stress that microbubbles with no specific attachment mechanism are able to withstand. However, despite this the in-house UCA was shown to remain attached to a non-streptavidin coated agar surface up to 0.66Pa WSS. The mechanisms behind this attachment could be either an electrostatic or chemical mechanism, as described in Section 2.3. The author believes this limited attachment to be the result of electrostatic forces between the microbubbles and the agar surface.

Investigations into the detachment of the agent over time have shown that the streptavidin-biotin bond is capable of withstanding a WSS of 0.48Pa for up to 2.5 hours. The effect of higher WSS over time on the attached agent was not assessed due to the leak from the flow chamber which occurred at higher WSS after a limited running time. The results from this investigation do however indicate that the streptavidin-biotin bond is capable of retaining attachment for the duration of a diagnostic ultrasound scan. Minimal detachment may have occurred during this time as RF analysis suggests that the mean backscatter from the attached microbubbles decreases very slightly over time, it is possible that the detachment of the agent under increasing WSS as observed in Section

7.1.2 may be due in part to time as the duration of the investigation was approximately 30 minutes.

Initial attachment investigations under flow proved to be inconclusive and were therefore repeated using microscope slides for a visual assessment of attachment. The results from this investigation showed that there was minimal attachment of the in-house agent to a streptavidin coated surface under flow conditions with a WSS of 0.31Pa, the lowest measurable WSS in the developed flow chamber. These results suggest that attachment is occurring but that it is minimal and therefore not detectable using IVUS. In order to use the agent in-vivo it will be necessary to optimize the attachment under flow conditions to produce a measurable difference in mean backscatter from the target surface.

7.5. Summary

When attached to a streptavidin-coated agar surface prior to being subjected to flow conditions the in-house UCA has been shown to remain attached under a WSS of 50Pa, although a decrease in the echogenicity of the agent and therefore the quantity of the agent attached is observed. In addition the in-house agent was shown to remain attached via a streptavidin-biotin bond under a low WSS of 0.48Pa for over 2 hours. This work suggests that a streptavidin-biotin bridge is a suitable mechanism for attaching antibodies to the microbubble shell.

However, although investigations into attachment of the in-house agent under flow conditions have shown some microbubble attachment the attachment is limited and does not produce a detectable signal when used in conjunction with IVUS.

Chapter 8 Cellular Adhesion

In order to assess attachment of the in-house UCA to a cellular surface under varying shear stress it was necessary to develop a flow chamber which would enable the growth of a cellular monolayer. In addition it was necessary for the cells to remain adhered to the surface under shear stress.

Initial investigations involved developing the optimum surface for growing cells within the flow chamber described in Chapter 4. A variety of materials which were compatible with IVUS were investigated for cell growth as described in Section 8.2 below. Following this cells were grown on microscope slides and the flow chamber adapted to incorporate the slides for a visual assessment of cellular adhesion under flow.

Finally cells were grown within μ-slides from Ibidi (Munchen, Germany), described in Section 8.4. These cells were subjected to low WSS and observed under a microscope to assess cellular adhesion.

8.1. SK-Hep-1 Cells

The cell lines used throughout this thesis for cellular adhesion studies and microbubble attachment under flow were SK-Hep-1 cells and human umbilical vein endothelial cells (HUVEC). SK-Hep-1 cells are reported to be from human hepatocellular carcinomas (Heffelfinger et al. 1992; Lin et al. 1998) however, studies have shown that the cells exhibit endothelial characteristics (Heffelfinger et al. 1992; Lirdprapamongkol 2006). A microscopic image of the SK-Hep-1 cells is shown in Figure 8-1. This cell line was chosen due to the robust nature and endothelial characteristics of the cells.

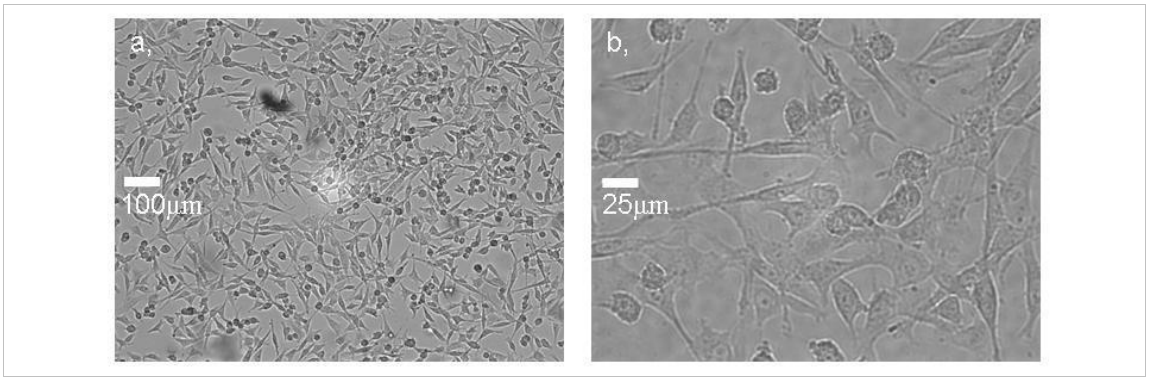

Figure 8-1: Microscopic images of SK-Hep-1 cells; a, ×10 magnification and b, ×40 magnification.

Sk-Hep-1 cells were grown in Dulbecco's Modified Eagle Medium (DMEM) by Linda Norrie (Medical Physics, The University of Edinburgh).

8.2. Cell growth surfaces compatible with the parallel plate flow chamber

Due to intended usage of the microbubble UCAs it was desirable to be able to assess the attachment of the UCA to cells using IVUS. To this end, cell growth was attempted on a variety of materials which would be compatible with the flow chamber designed in Chapter 4.

Initial investigations into different cell growth materials involved using agar and gelatin. Agar was produced using the protocol described in Appendix H and has already been shown to be acoustically transparent in Chapter 7. In order to assess cellular adhesion to agar, 1mm thin discs of agar were placed in two wells of a Corning® Costar® cell culture 6-well plate (Sigma-Aldrich, MO, USA). Cells were then seeded in both wells containing agar and two control wells. The resulting cell growth caused the agar to dissolve and proved unsuccessful.

Gelatin was also investigated as this could be manufactured and moulded to fit in the agar well of the flow chamber. A 10% gelatin solution was mixed and allowed to set in a Petri dish. Following this the gelatin was assessed with IVUS to determine the feasibility of using gelatin for IVUS assessment of microbubbles attached to cells under flow. The IVUS image of a gelatin surface can be seen in Figure 8-2 showing the bright reflection from the surface. Although every care was taken to remove bubbles from the solution, it is believed that the bright reflection was due to bubbles forming within the gelatin as it set. Due to this reflection from the gelatin it proved unsuitable for use with IVUS; in addition, when attempting to grow cells on the gelatin, it was dissolved by the growing cells.

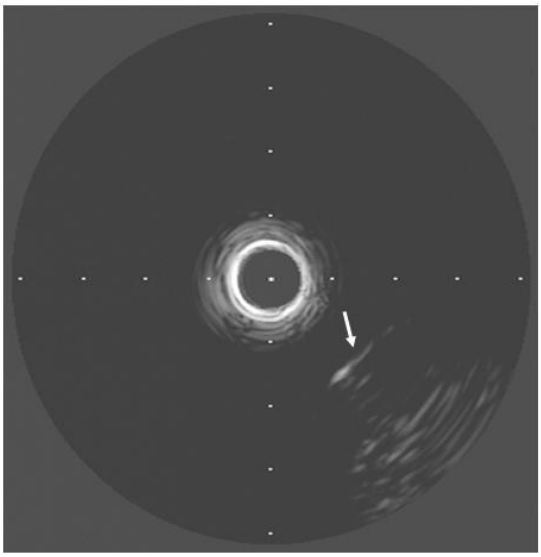

Figure 8-2: IVUS image showing reflection from a gelatin surface, as identified by the white arrow.

Further attempts to grow cells inside the flow chamber involved the use of a Mylar® (DuPont Teijin Films, Stevenage, UK) polyester film. In order to assess the echogenicity of the film it was cut to fit over the agar well and sealed within the flow chamber. The surface of the Mylar® was then assessed with IVUS. Figure 8-3 below shows the reflection from the Mylar® film in the flow chamber with water flowing through the channel compared to the reflection from an agar surface.

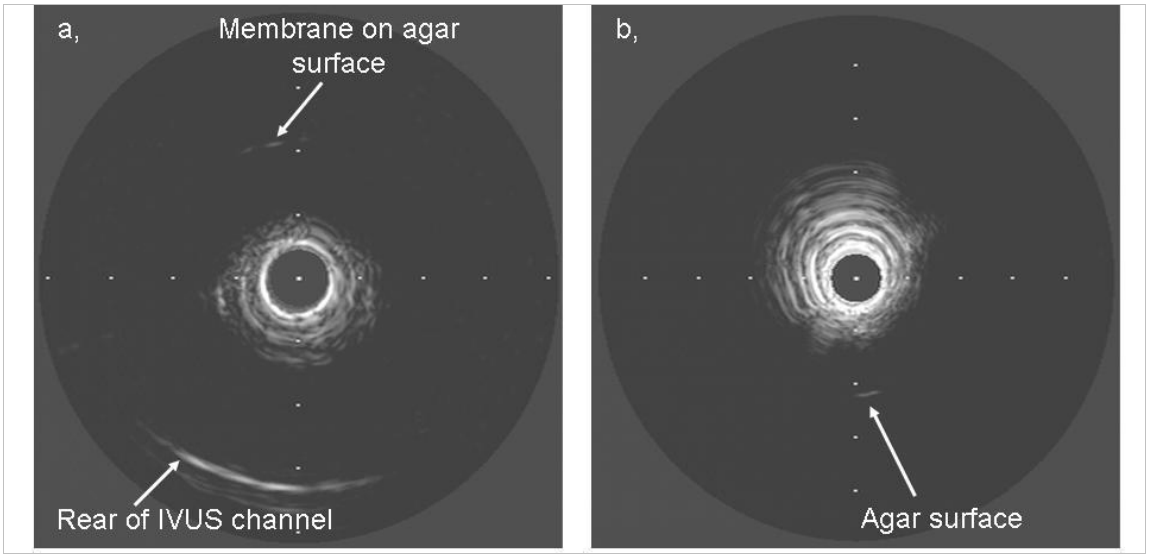

Figure 8-3: IVUS reflections from a, mylar film over agar and b, agar.

Although the echo from the film is slightly brighter than that from agar the echogenicity is -32.80(±0.26)dB, compared to the average mean backscatter from microbubbles attached to an agar surface which is -23.21(±1.43)dB. This made Mylar® film a feasible, low backscatter option for growing cells within the flow chamber.

8.2.1. Growing cells on Mylar film

The next stage in the investigation was to investigate cell growth on the film. Cell growth was assessed through determining the cellular confluence (percentage of area with cells adhered) as described in Appendix I. Initially cells were grown without a cell growth substrate. Small pieces of film were cut to fit flat within a Petri dish and cells were seeded directly onto the surface. Microscopic images of cells grown on the film can be seen in Figure 8-4. The cells did not grow to confluence and so different cell substrates were investigated to encourage cell growth.

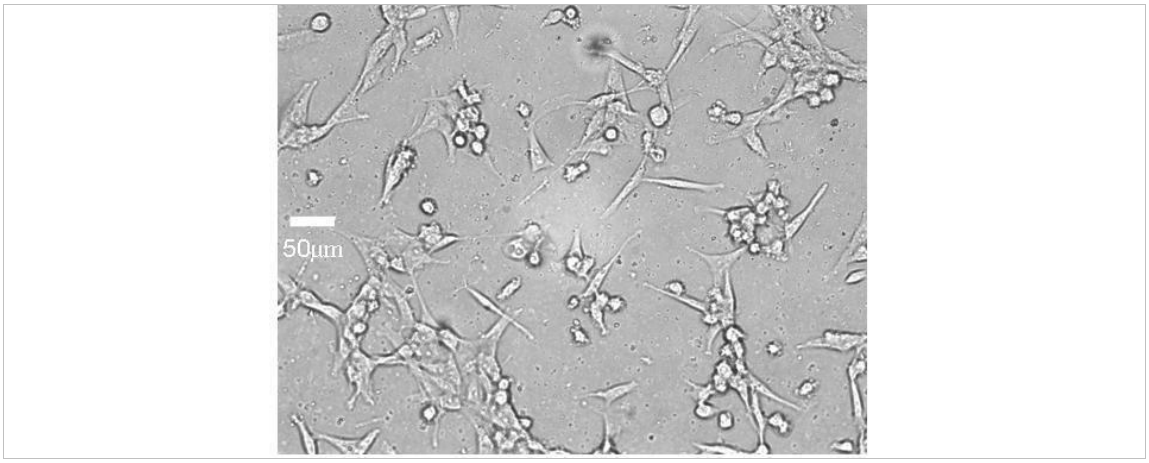

Figure 8-4: Cells grown on uncoated Mylar film (×200 magnification).

Collagen, a common cell substrate which can be produced easily and economically in the laboratory, was used; in addition BD Cell-Tak™ (BD biosciences, USA), a cell and tissue adhesive, was investigated. Figure 8-5 shows the microscopic images of cells grown on film using these substrates. The cells grown using Cell-Tak™ have a confluence of 5.4 (±0.7)%, this was less than the cells grown using collagen as a substrate, which has a confluence of 50.3 (±13.6)%. In addition cellular adhesion was not improved through the use of Cell-Tak™, as demonstrated in Figure 8-6.

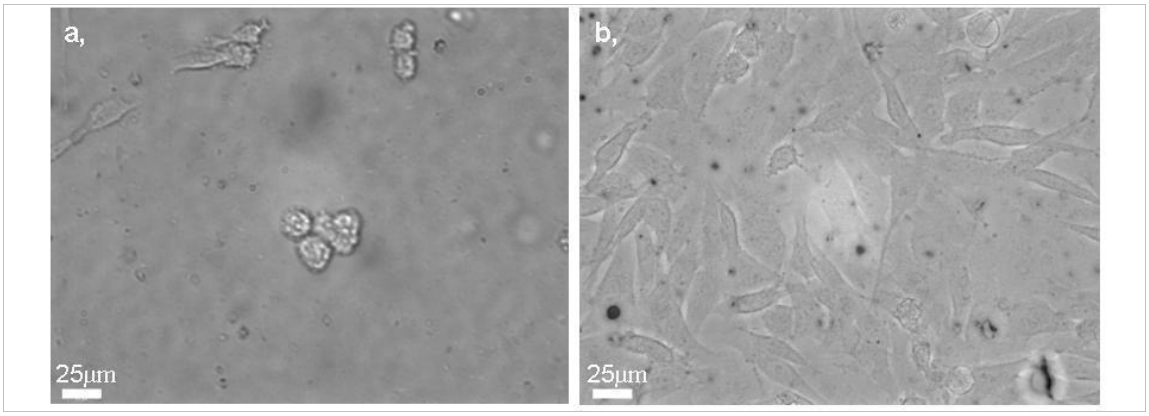

Figure 8-5: Microscopic images of cells grown with a, Cell-Tak™ and b, collagen.

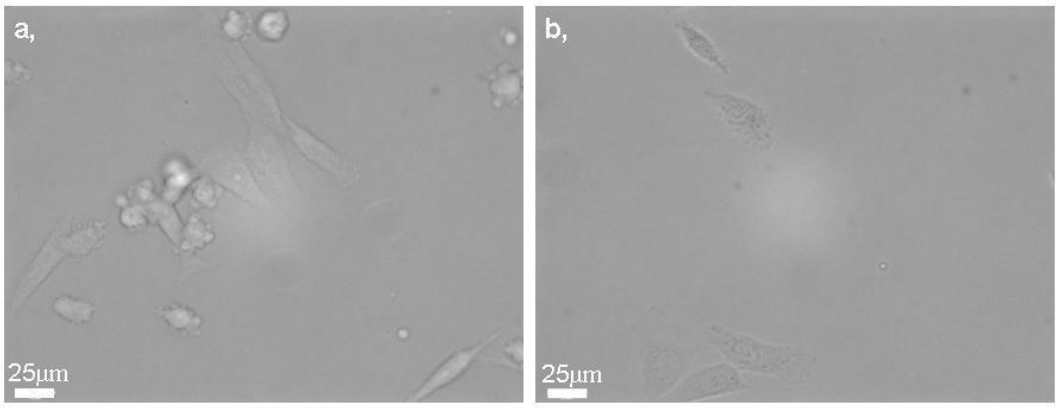

Figure 8-6: Microscopic images of cells grown with Cell-Tak™; a before being subjected to warmed PBS and b, after being subjected to warm PBS.

8.2.2. Scratched film

As collagen produced the higher cellular confluences, further investigations were carried out to attempt to improve cellular adhesion. It was hypothesized that the membrane was too smooth for the cells to remain attached in the event of shear stresses, in light of this the film surface was scratched using fine sandpaper.

The roughened film resulted in an improvement in cellular confluence, as can been seen in Figure 8-7. Scratching the membrane improved the confluence of the uncoated films by 37.02(±19.44)%, whilst the collagen coated film had a confluence increase of 37.57(±16.32)%. These results suggested that scratching the film significantly improved cellular confluence.

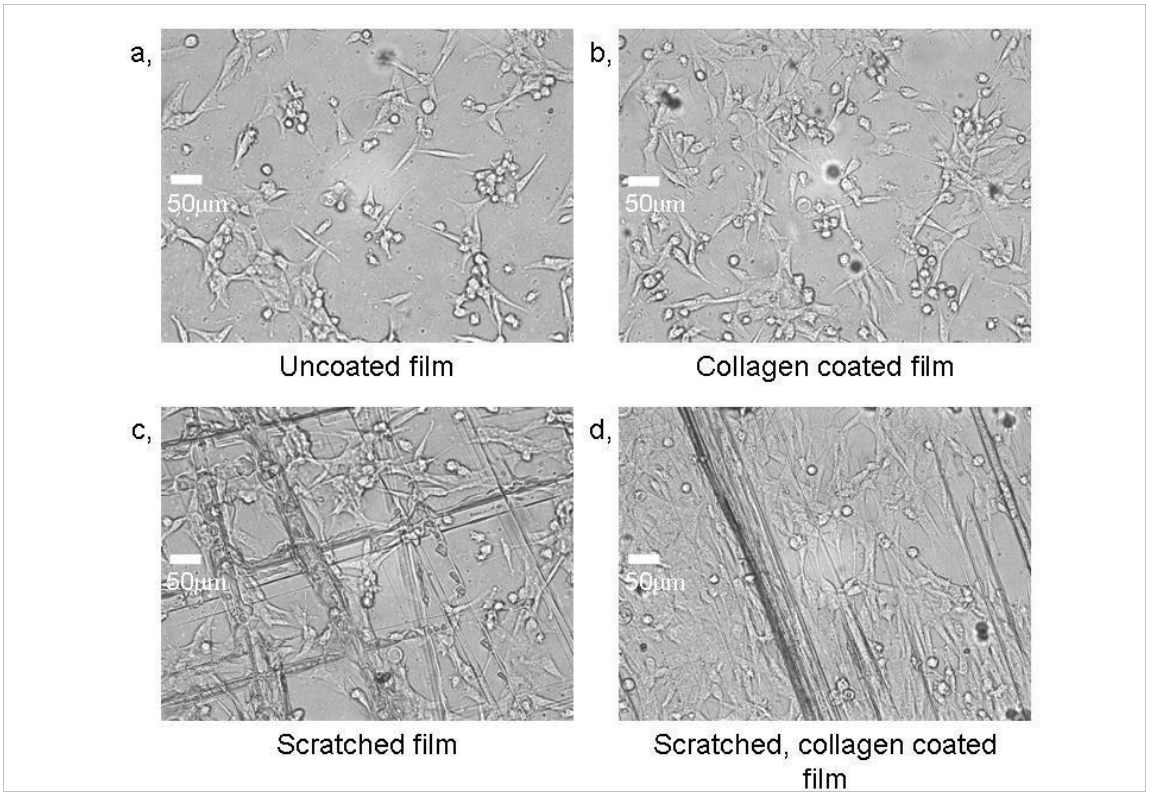

Figure 8-7: Microscopic images of cells grown on; a, uncoated film, b, scratched uncoated film, c, collagen coated film and d, scratched, collagen coated film.

In order to be able to assess microbubble attachment to the cells under flow it was necessary to be able to subject the film to flow and retain cellular confluence, therefore initial investigations involved dipping the cell coated membranes into warmed phosphate buffered saline (PBS).

8.2.3. Method

Cells were grown to over 60% confluence on squares of scratched film in a Petri dish. The PBS was then warmed to 37°C as cells do not survive for long in colder temperatures. Cells were then imaged using the Leica microscope described in Chapter 3. Following this the cell coated films were gently dipped into the warm PBS and

slowly removed, before being returned to the Petri dish. The cells were then imaged a second time and the confluences compared.

8.2.4. Results

After being subjected to warm PBS and a change of environment, the cells grown on membranes were found to detach very rapidly. This is shown in Figure 8-8. Loss of confluence on the collagen coated films was 67.5%, whilst loss of confluence on the scratched, collagen coated film was 40.5%, resulting in the confluence reducing to less than 2%. The author and colleagues believe that the significant loss in confluence is due to tension changes in the film. Due to the unreliability of growing cells on the film an alternative method of growing cells within the flow chamber was required.

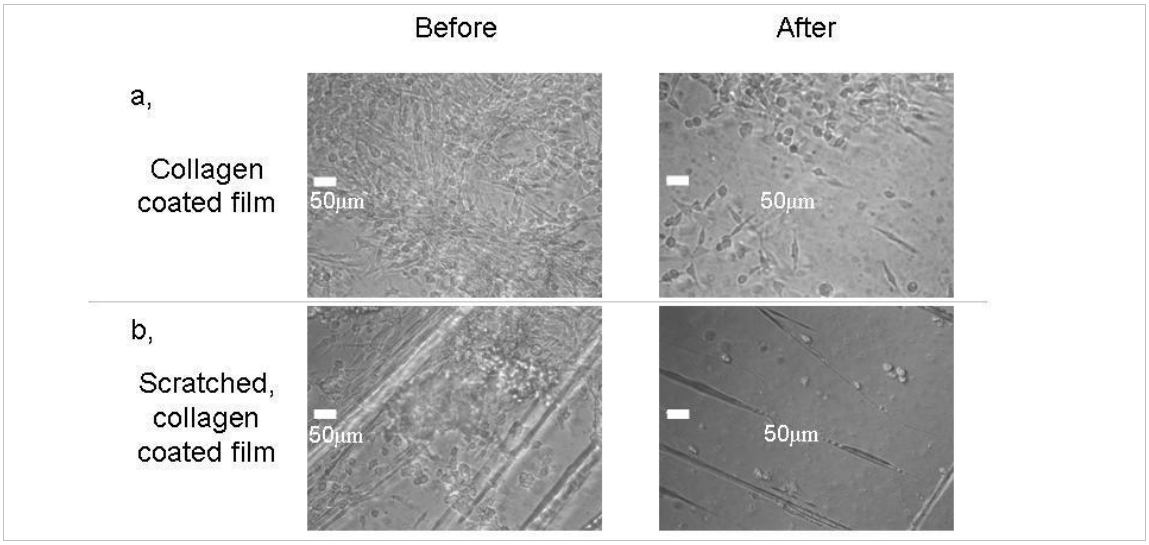

Figure 8-8: Microscopic images of slides (x200mag) before and after being subjected to warm PBS; a, a collagen coated film and b, a scratched, collagen coated film.

8.3. Flow chamber adaptations and microscope slides

During the previous investigations, cells were also grown on uncoated and collagen coated glass microscope slides successfully as illustrated in Figure 8-9. The average

confluence on cells grown on the uncoated slides and collagen coated slides was 81.5(±2.0)% and 90.8(±4.1)% respectively. Due to the reproducibility of these confluences the collagen coated slides were chosen for further investigation.

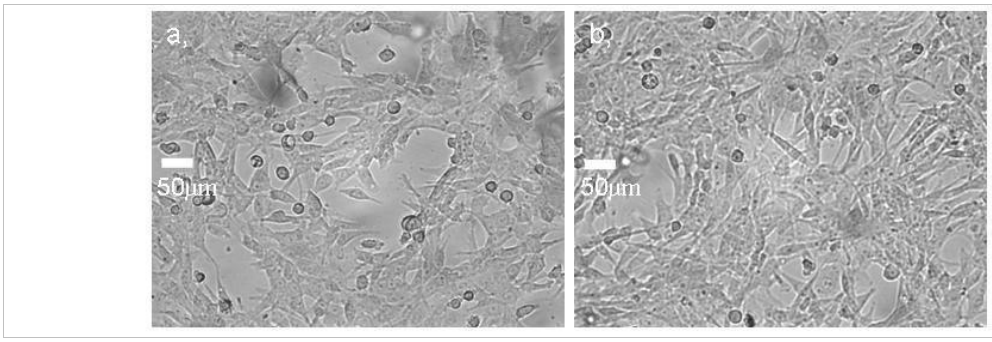

Figure 8-9: Cells grown on; a, an uncoated microscope slide and b, a collagen coated microscope slide.

In order to assess the effect of flow on cellular confluence the flow chamber was adapted to allow for the incorporation of a microscope slide. This allowed a visual assessment of the cellular adhesion and microbubble attachment; however, due to the acoustic properties of glass it was not possible to assess the microbubble attachment with IVUS. The adapted rear panel of the flow chamber is shown in Figure 8-10.

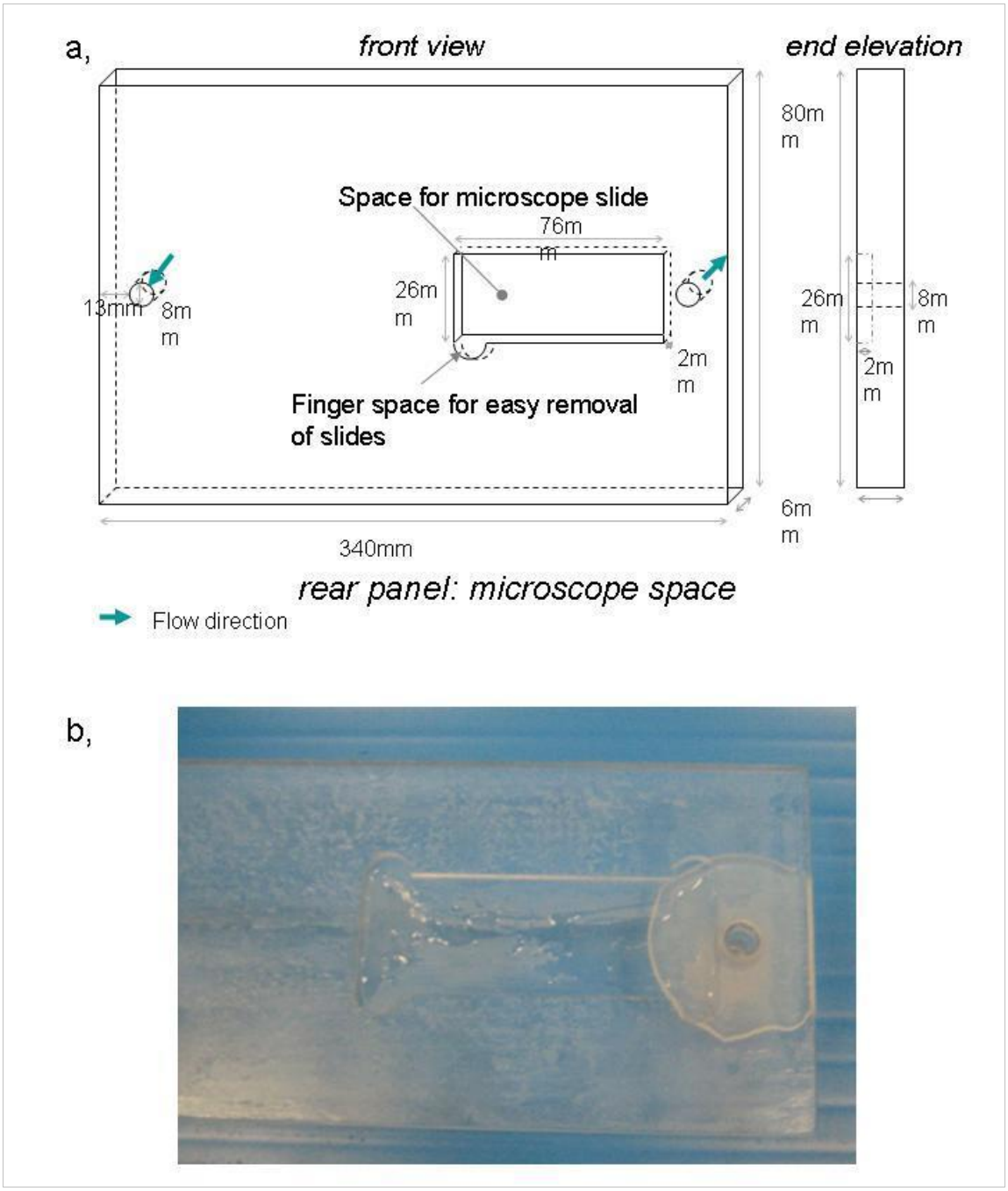

Figure 8-10: Adaptations to rear panel of flow chamber; a, schematic and b, photograph of space for microscope slide.

8.3.1. Method

Cells were seeded onto collagen coated microscope slides and imaged with the Leica microscope, the slides were then placed into the flow chamber and the chamber was sealed with grease, care was taken to avoid getting grease close to the flow channel in the observation region as this would cause cell death.

The cells within the flow chamber were then subjected to a flow of warmed medium at 37°C with a flow volume of 60ml/min, corresponding to WSS of 0.31. A water bath was used to maintain medium temperature at 37°C.

The cells were subjected to flow for 5 minutes after which the slides were carefully removed and imaged again under the microscope. The confluence before and after being subjected to WSS was compared.

The investigation was then carried out a further two times before repeating at 80 and 100ml/min flow volumes (corresponding to WSS of 0.48 and 0.53Pa).

In addition a control was carried out at 0Pa WSS, in which the cells were subjected to static warmed medium for 5 minutes.

8.3.2. Results

It was found that even at low WSS (0-0.53Pa), the cellular confluence decreased rapidly during the investigations. At 0Pa WSS, the decrease in confluence was 34.5(±6.9)%, showing that even with no flow a loss in confluence is observed. At 0.53Pa the decrease in confluence was 74.7(±6.8)%. Figure 8-11 shows the confluence loss at increasing WSS. The data suggests that due to the large decrease in confluence, under no flow and relatively low WSS, this method would not be suitable for assessing attachment of microbubbles to cells under WSS.

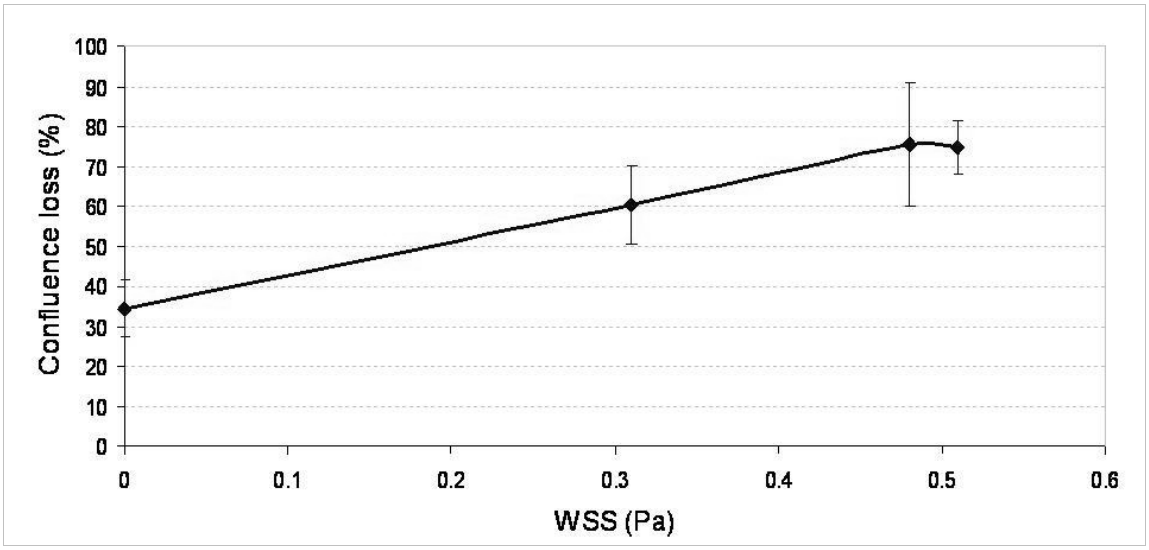

Figure 8-11: Confluence loss at increasing WSS.

The significant loss of confluence at low WSS is believed to be due to environmental conditions. The optimum temperature for cells is 37°C and although the medium was warmed to this temperature the surrounding temperature was approximately 22°C. In addition, the flow chamber, although sealed to prevent leaks in the flow was not a sterile environment, this meant that the cells were subject to contaminants such as bacteria, although this should not have had an effect throughout the short timescale of the experiment. The last factor to consider was the use of grease with which to seal the flow chamber, if the grease came into contact with the cells this could have been the cause of cell death, resulting in cells 'curling up' or shearing off the slides, in addition the grease was not sterile and may also carry contaminants.

The resultant decrease in confluence may be due to the WSS being too high for the cells to withstand. Although Kooten et al. (1994) has shown HUVECs and human adult saphenous vein cells (HASVC) to remain adhered to a surface up to approximately 18Pa no results could be found to indicate the cellular retention of SK-Hep-1 cells.

8.4. *Ibidi flow cells*

Following these investigations into utilizing the existing flow chamber, an alternative flow system was required. Ibidi (Ibidi, Germany) µ-slide $I^{0.8}$ were used, the Ibidi flow slides are presented in Figure 8-12. The flow channel of the slides measure 50×5×0.8mm and have a volume of 200µl.

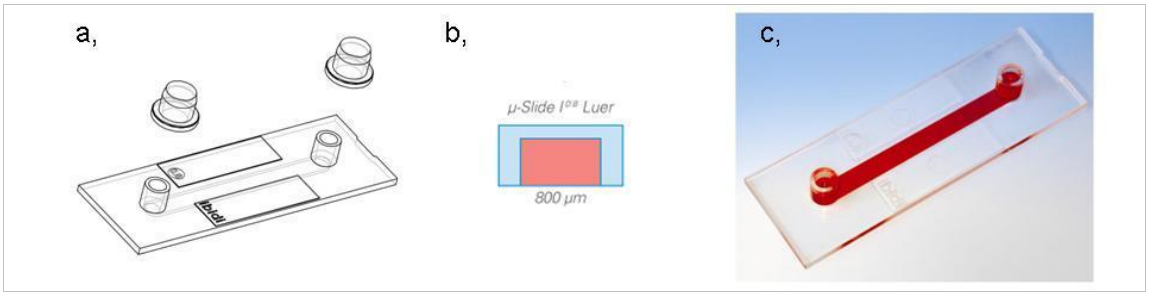

Figure 8-12: Ibidi flow slides; a, schematic, b, side-view of slides and c, photograph of slide (reprinted with permission from Kahl at Ibidi (2009)).

8.4.1. Shear stress

The shear stress in the flow channel was determined from numerical calculations for varying flow volumes (Horn 2008) provided by the manufacturer. A graph showing the calibration of WSS as relating to flow volume can be seen in Figure 8-13. These results were calculated for DMEM which has a viscosity of 8.4×10^{-4} Pa·s (Gosgnach et al. 2000).

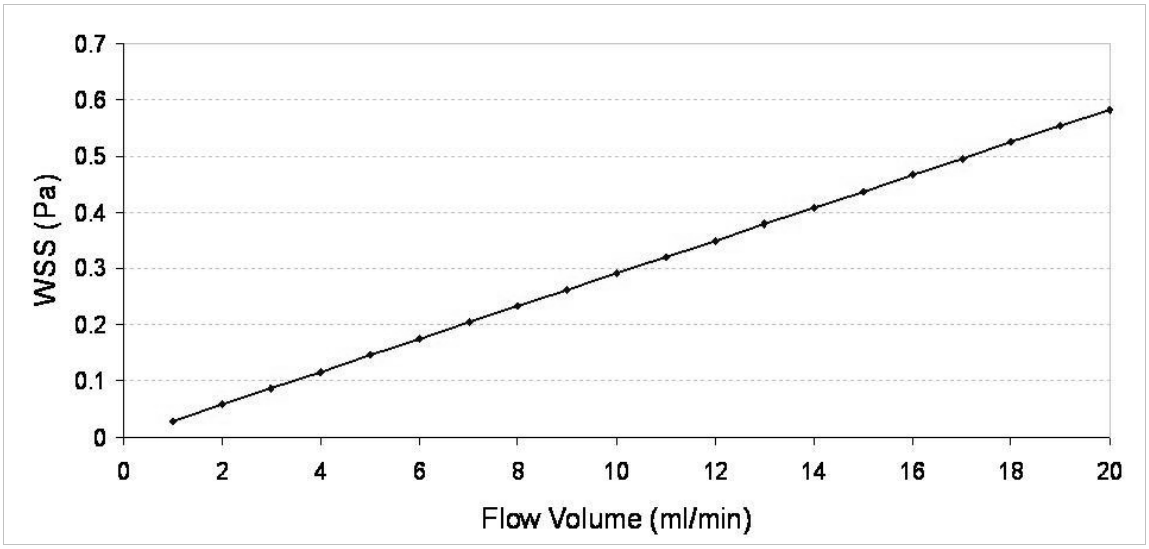

Figure 8-13: WSS as a function of flow volume for DMEM.

The EP1 Econo pump (Bio-Rad, Hemel Hempstead, UK) had previously been calibrated for varying flow volumes and calibration was confirmed prior to beginning each experiment and necessary adjustments made. The maximum flow volume achievable with the pump was 6.4ml/min corresponding to a WSS of 0.19Pa, although 6.0ml/min was the maximum flow volume used to minimize stress on the equipment.

Reynolds numbers for the Ibidi µ-slides for flow volumes from 1-6ml/min were between 0.24×10^{-6} and 1.49×10^{-6} confirming that laminar flow will occur at these flow volumes.

8.4.2. Growing cells in Ibidi µ-slides

A volume of 200µl of cells, in a $3.5\times10^{5}\,ml^{-1}$ concentration were injected into the flow channel following the manufacturer's recommendations, as outlined in Appendix J. The slides were then placed in an incubator for 24 hours after which the cells reached approximately 50% confluence.

8.4.3. Method

Tubing with an internal diameter of 1.6mm was connected to the flow slide using Luer connectors. The tubing connected the slide to a pump and a reservoir of warm medium at 37°C. The slide was placed on a warm plate on the microscope platform in order to record images of the cells after being subjected to varying WSS. The equipment set up can be seen in Figure 8-14.

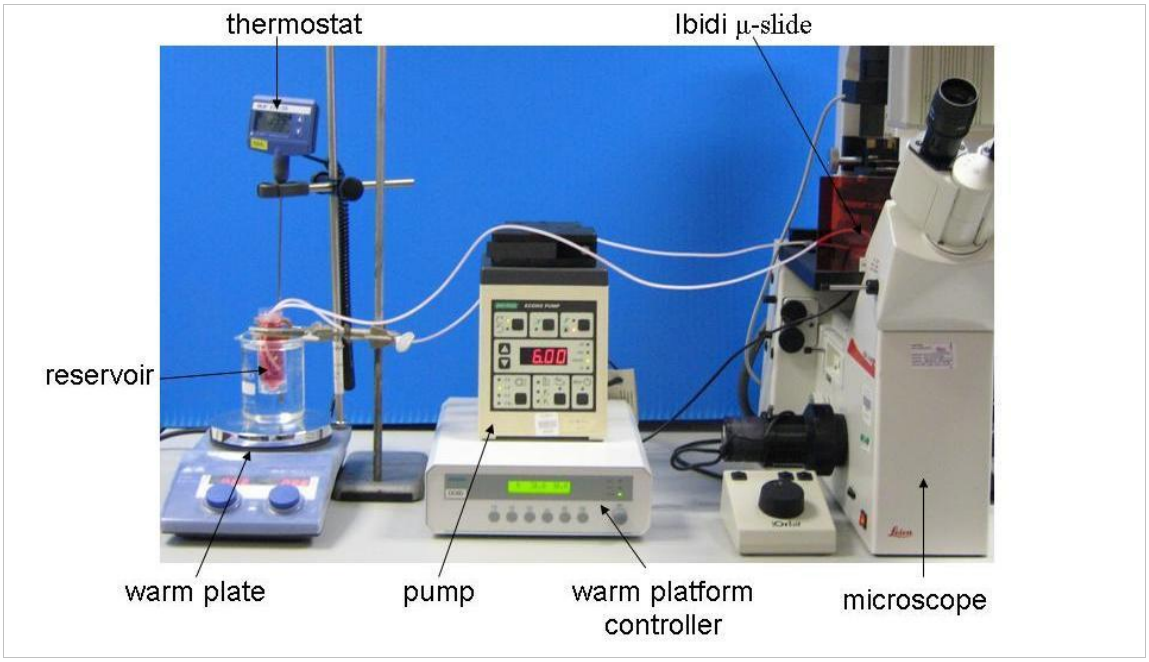

Figure 8-14: Flow slide experimental set up.

Once set up an image of the cells was collected with the 40× and 10× objective lenses. A flow volume of 1ml/min was set and allowed to run for 2 minutes. More images were collected and then the flow volume was increased to 2ml/min for two minutes. Flow volume was increased every two minutes at 1ml/min increments up to 6ml/min, corresponding to WSS of 0.03, 0.06, 0.09, 0.12, 0.15 and 0.17Pa. Images were collected after cells were subjected to each increase in WSS for two minutes.

In addition a control, in which the cells were subjected to 0Pa WSS was carried out. These investigations were repeated three times.

8.4.4. Results

The Ibidi μ-slides provided excellent cellular adhesion under flow. Figure 8-15 illustrates the loss in confluence as the WSS is increased from 0.00 to 0.17Pa. At 0.17Pa the decrease in confluence is less than 1% suggesting excellent adhesion under very low WSS. In addition, when compared to the control investigation the decrease is comparable to the confluence decrease with no WSS suggesting that confluence loss is a result of time and not WSS.

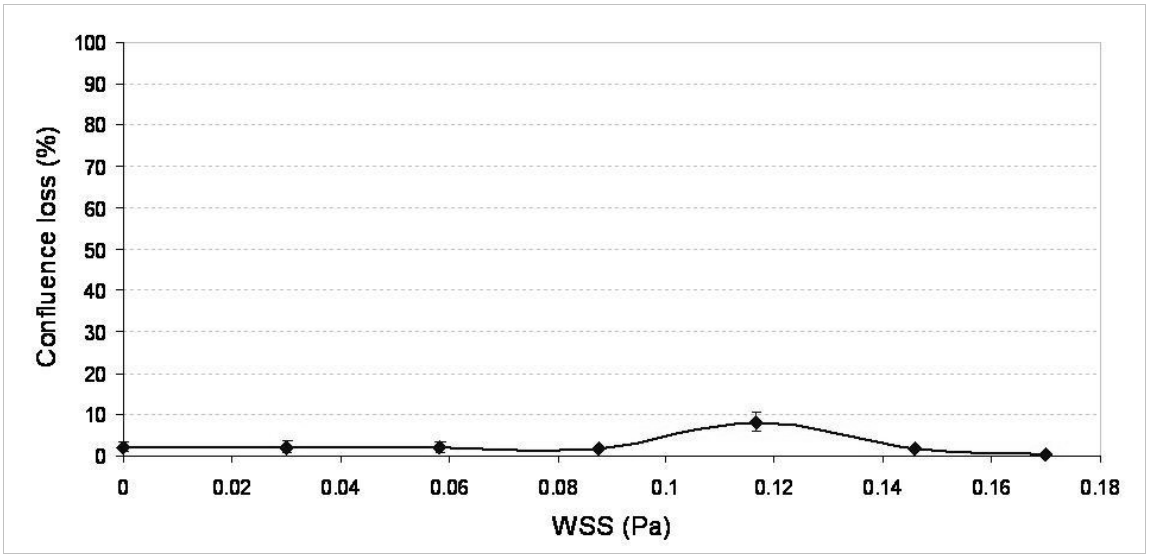

Figure 8-15: Loss of confluence as a function of WSS.

The loss of confluence over time is due to the cells retracting (shrinking) as can be seen in Figure 8-16. These images were taken from the third control investigation. The retraction of cells is believed to be due to the lack of optimal conditions, for example; temperature and CO_2 levels.

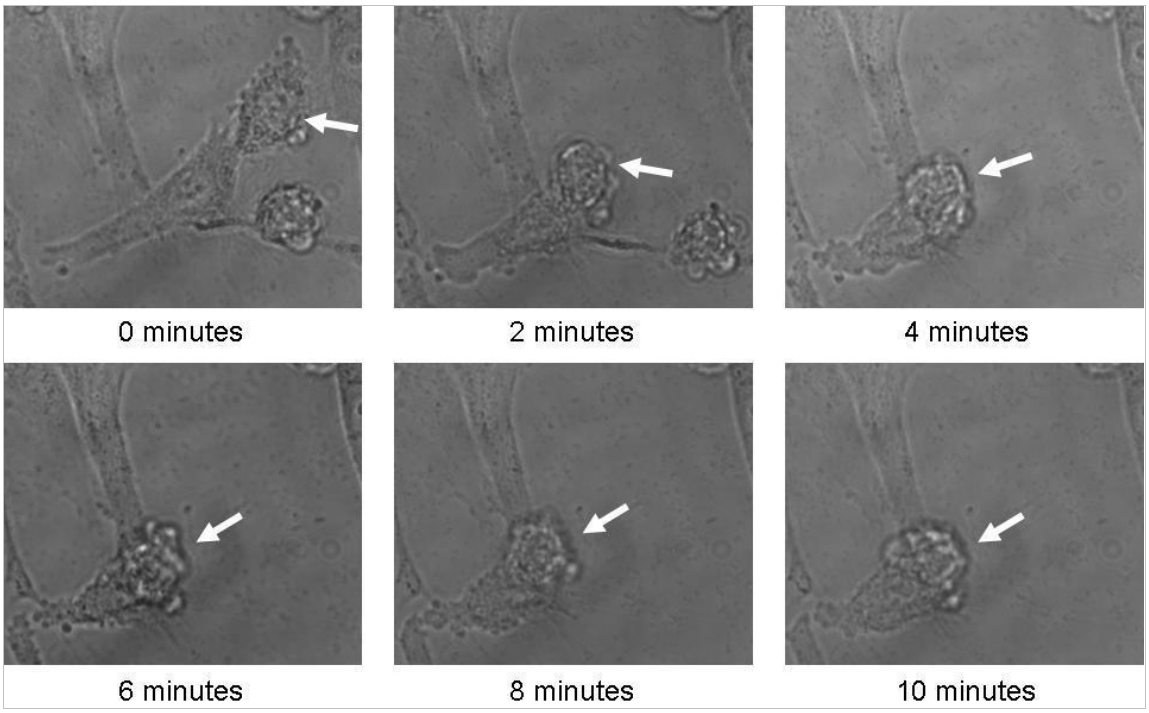

Figure 8-16: Timelapse showing a cell retracting over 10 minutes, white arrow indicates cell in question.

8.5. Summary

Initial investigations involved an investigation into different acoustically suitable materials for cell growth and assessment with IVUS. The first material investigated was agar which was already found to be acoustically suitable for use with IVUS in Chapter 7. Unfortunately attempts to grow a cellular monolayer on the agar were unsuccessful. Gelatin was then investigated but found to be unsuitable for use with IVUS due to the bubbles which would form on setting, in addition it was found to be unsuitable for cell growth.

The next investigation carried out was into the use of a Mylar® polyester film which could be placed over the agar and assessed with IVUS. The film was found to be acoustically translucent and as such cell growth on the film was investigated. Collagen

and Cell-Tal™ were investigated as cell substrates and although cells initially appeared to grow well on the film it was found that they sheared off with minimal changes in tension, making the film unsuitable for cell growth.

Due to the lack of acoustically suitable materials for cell growth the flow chamber was adapted to allow for incorporation of a microscope slide. Cells were shown to grow to confluence on collagen coated microscope slides and were therefore used in the flow chamber to assess cellular adhesion under shear stress. At WSS of 0.31-0.53Pa the cells were found to shear off rapidly with a confluence loss of more than 60% at the lowest WSS achievable. In addition the control investigation, with no WSS, demonstrated a confluence loss of more than 30% suggesting that the flow chamber environment was not ideal for cellular adhesion.

Following attempts to use the flow chamber described in Chapter 4 for cellular adhesion investigations it was determined that a flow system allowing for investigations at very low WSS (<0.2Pa) was required. For this reason Ibidi µ-slides were purchased and SK-Hep-1 cells grown in them. Cellular adhesion in the Ibidi µ-slides was excellent with only a 2% confluence loss at the highest shear stress achievable (0.17Pa).

The Ibidi µ-slides were found to be the optimal method of investigating attachment of the microbubbles to a cellular monolayer under WSS and further investigations were carried out using these slides as described in the following chapter.

Chapter 9 Attachment of microbubbles to cells under low WSS

The objective of this work was to actively target the UCA to a cellular surface under flow to determine the feasibility of using the agent in-vivo for targeting applications. The following chapter describes the methods used to achieve this objective.

In Chapter 6 it was shown that the UCA has been successfully targeted to SK-Hep-1 cells by optimising the attachment of CD31 antibody to the microbubble shell by way of a streptavidin-biotin bridge as described in Chapter 6. Microbubble attachment to cells under static conditions was investigated first. This was followed by an investigation into the attachment of microbubbles under very low WSS.

9.1. Introduction

In order to undertake future clinical trials of the agent being developed at Edinburgh University it is necessary to successfully target the agent under flow conditions. To this end a flow system has been developed in Chapter 8 to enable assessment of attachment of microbubbles to cells under very low, controlled WSS.

Previously Villanueva et al. (1998) has visually demonstrated attachment of a lipid microbubble to cells expressing a surface protein which is seen in early atherosclerosis at a shear rate of $25s^{-1}$. Other authors (Ferrante et al. 2009; Klibanov et al. 2006; Rychak et al. 2006b; Takalkar et al. 2004) have demonstrated the attachment of targeted microbubbles to P-selectin, a cell adhesion molecule found on the surface of endothelial cells.

Rychak et al. (2006a) has demonstrated attachment of P-selectin targeted microbubbles in mouse cremaster muscles using ultrasound mediated microbubble attachment which is discussed later in this chapter. Attachment of targeted microbubbles to P-selectin has been demonstrated by Takalkar et al. (2004) for WSS from 0.03Pa to 0.17Pa and Klibanov et al. (2006) has investigated the attachment of microbubbles, targeted with a fast binding ligand to P-selectin up to 0.5Pa WSS.

9.2. Static attachment

Static attachment investigations were carried out in Multiwell plates and Petri dishes with no flow. Initial investigations involved assessment of attachment to seeded cells which was followed by an investigation into attachment to cells in solution. Finally ultrasound was used to mediate microbubble attachment to cells under static conditions.

9.2.1. Initial investigations

Cells were seeded in 6-well plates as described in Chapter 8. Targeted microbubbles were then added to two wells in $12.9\times10^{6}ml^{-1}$ concentration, a non-targeted control microbubble was added to two wells and the final two wells had no microbubbles. These latter two wells were used as baseline data.

The microbubbles were incubated with the cells for one hour after which the medium was replaced twice to remove excess microbubbles. A FITC conjugated Anti-Mouse IgG, F2883 (Sigma-Aldrich, UK) was added to the wells in 50µl aliquots ($0.02mg\cdot ml^{-1}$) to identify the presence of microbubbles and cells were incubated for a further 30

minutes. Medium was replaced once to remove any excess F2883 and the cells observed with fluorescence microscopy.

Initial Results

Microscopic images of the wells can be seen in Figure 9-1. This figure shows a comparison of the wells observed for targeted and non-targeted microbubble addition. Under these conditions, no microbubbles were observed attached to the cells. Although a single microbubble appeared to be attached to the cells in Figure 9-1a, the lack of this in the fluorescent image suggested that this microbubble was not targeted

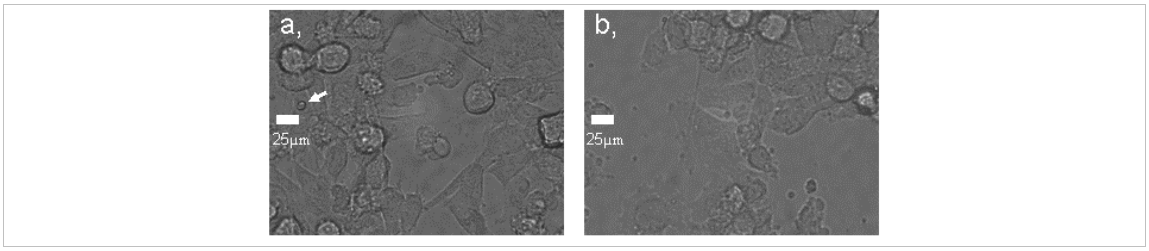

Figure 9-1: Microscopic image of; a, well to which targeted microbubbles were added and b, well to which non-targeted microbubbles were added, white arrow shows location of suspected microbubble.

9.2.2. Attachment of microbubbles to cells in solution

It was hypothesised that the lack of attachment observed in the initial investigation (Section 9.2.1) was due to the buoyancy of the microbubbles resulting in the microbubbles not coming into direct contact with the cellular surface. In order to determine if this were the case microbubbles were then added to cells in solution.

Cells were added to the wells of a 6-well plate in 3ml aliquots with a concentration of $7.7\times10^{5}ml^{-1}$. Microbubbles (previously incubated at 37°C) were then added in 100µl aliquots with a concentration of $12.9\times10^{6}ml^{-1}$. Targeted microbubbles were added to two wells, Non-targeted microbubbles to two wells and the final two wells were left as a baseline with no microbubbles added. The cells were then incubated over night to allow

them to seed. After 24 hours the medium was gently replaced twice to remove any excess, unattached microbubbles. A 50µl aliquot ($0.02 mg \cdot ml^{-1}$) F2883 was added to all the wells, as in Section 9.2.1, and cells were incubated for a further 30 minutes. Finally the medium was gently replaced to remove excess F2883 and the cells observed with fluorescence microscopy.

Results

Microbubbles added to cells in solution were found to adhere with a very high number of microbubbles per unit area.

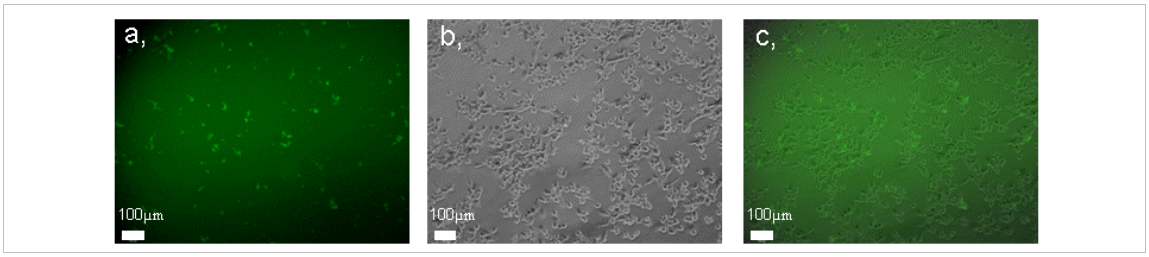

Figure 9-2: Microscopic images with 10x objective showing; a, contrast enhanced fluorescent image and b, bright-field image and c, merged image of microbubbles attached to cells in solution.

When added to cells in solution, the mean number of microbubbles was $83.3(\pm 63.2) mm^{-2}$, the high standard deviation in the result suggests that there is a very uneven distribution of microbubbles, this may be due to the solution of microbubbles not being agitated sufficiently, however, once added to the well it was not possible to agitate thoroughly as this may have caused detachment of cells. In addition the uneven distribution of microbubbles may be due to an uneven distribution of cells. Despite the large variation, the average microbubble count of targeted microbubbles was significantly greater ($p<0.0001$), five times the average microbubble count from non-targeted microbubbles indicating that the attachment was from active targeting of the microbubbles. A comparison of the data is shown in Figure 9-3.

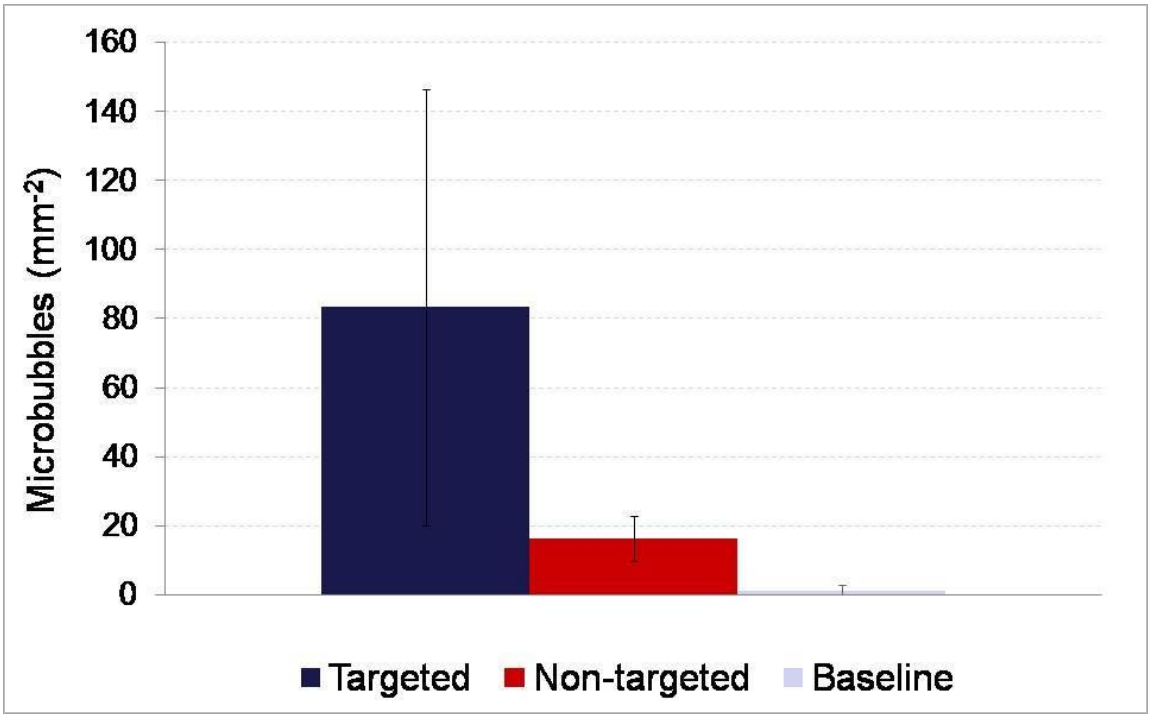

Figure 9-3: Microbubbles observed per square millimetre for targeted, non-targeted and baseline microbubble samples when attached to cells in solution.

9.2.3. Ultrasound Mediated Microbubble Attachment

The intended clinical application of the UCA makes the previous attachment method of the microbubbles unsuitable since it would not be possible to suspend the target cells within the body; therefore a method of forcing the microbubbles onto the cellular surface was required. Ultrasound has been well documented as a means to enhance delivery of microbubble UCAs (Dayton et al. 1999a; Dayton et al. 1999b; Lum et al. 2006; Rychak et al. 2004; Rychak et al. 2006a; Zhao et al. 2004) by way of the acoustic radiation force. Dayton et al (Dayton et al. 1997) has derived an equation for the acoustic radiation force, this has been adapted by Rychak et al (Rychak et al. 2005) and can be seen in Equation 9-1, the parameters are identified in Table 9-1.

$$F_p = \frac{2\pi P^2 R}{\delta \omega \rho c}\left[\frac{D}{T}\right]$$

Equation 9-1: Primary acoustic radiation force.

Equation 9-1 is subject to the following assumptions as identified by Rychak *et al.* (Rychak et al. 2005):

- The magnitude of the pressure is constant with each ultrasound pulse
- There is a unidirectional pressure gradient

Symbol	Parameter	Value	Source and notes
c	Speed of sound (ms^{-1})	1500	(Rychak et al. 2005)
P	Peak pressure (Pa)	0.064 (±0.017)	Measured (Appendix K)
R	Microbubble radius (μm)	5.64 (±0.36)	Measured (Chapter 3)
δ	Total damping coefficient	1.27	(Chatterjee and Sarkar 2003; Rychak et al. 2005)
ω	Microbubble resonant frequency (MHz)	40	Microbubbles optimised for 40MHz US (Chapter 3)
ρ	Density ($kg \cdot m^{-3}$)	1005.5 (±6.1)	Measured
D	Pulse duration (μs)	0.24 (±7.6)	Measured (Appendix K)
1/T	Pulse repetition frequency (μs^{-1})	28.6 (±1.3)	Measured (Appendix K)

Table 9-1: Parameters and values used for determination of the primary acoustic radiation force.

Assuming the values outlined in Table 9-1 above and using Equation 9-1 the primary radiation force acting on the microbubbles is approximately 15.7(±3.2)nN. However many of the values used, with the exception of those measured directly, are estimates, making the value subject to possible errors which cannot be calculated.

Additional forces which may be acting on the microbubbles include the secondary acoustic radiation force, between microbubbles, resulting in an attractive force (Dayton et al. 1997; Dayton et al. 1999b; Rychak et al. 2005; Schmidt et al. 2008; Zhao et al. 2004) and the buoyancy force due to the gas content of the microbubbles (Rychak et al. 2005). The secondary radiation force for the low concentrations used in these investigations is considered negligible as there is an inverse square relationship between the force and the distance between the microbubbles.

However the buoyancy force is in the opposite direction from the primary acoustic radiation force. The buoyancy force can be calculated from Equation 9-2 (Rychak et al. 2005).

$$F_B = \frac{4}{3}\pi R^3 g\left(\rho - \rho_{MB}\right)$$

Equation 9-2: Buoyancy force acting on microbubble.

Where R is the microbubble radius, g, is the gravitation acceleration, ρ and ρ_{MB} are density of medium and microbubble respectively.

The buoyancy force, assuming negligible microbubble density, has been estimated of the order of 0.1nN for a lipid microbubble (Rychak et al. 2005). Assuming that secondary radiation forces are negligible and have no effect on the vertical direction of the microbubbles the resultant downward force on the microbubbles due to insonation with 10-22MHz ultrasound is 15.6(±3.3)nN.

Method

Cells were seeded in 90mm diameter Petri dishes overnight. A single millilitre of pre-warmed positively targeted microbubbles at $12.9\times10^{6}ml^{-1}$ concentration and 37°C were added to the cell medium (9ml). The microbubbles were then insonated for two minutes with the Diasus scanner (Dynamic Imaging, Livingston, Scotland). The parameters for the scanner and transducer were set at maximum and can be found in Table 9-2. The transducer was kept at a focal distance of 2mm, as measured on the scanner screen, and gently moved across the central area of the Petri dish and back as illustrated in Figure 9-4.

The cells and microbubbles were then gently washed through replacement of medium twice before the addition of F2883 in the same manner as for Section 9.2.2. This was repeated with non-targeted fluorescent microbubbles.

In addition the investigation was repeated in an identical manner without insonation as a control. The entire process was repeated three times on three different days.

Parameter	**Value**
Mechanical Index (MI)	0.19
Transmit Power (%)	97-99%
Frequency	L 10-22MHz

Table 9-2: Parameters of Diasus scanner.

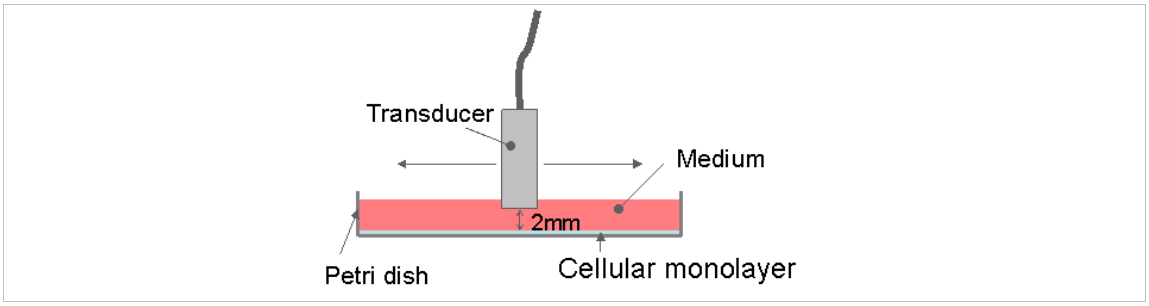

Figure 9-4: Ultrasound mediated microbubble attachment to SK-Hep-1 cells, schematic diagram.

Results

The primary acoustic radiation force is a viable method of directing microbubbles towards a target surface to facilitate attachment. The targeted microbubbles, which were insonated with ultrasound (L10-22MHz) demonstrated greater attachment than a control investigation in which ultrasound was not used. In addition, non-targeted microbubbles did not exhibit significant attachment relative to the positively targeted microbubble samples. A microscopic image of a microbubble attached using ultrasound can be seen in Figure 9-5.

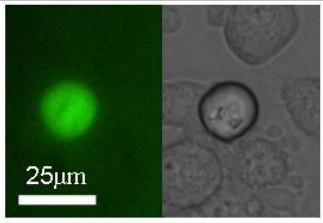

Figure 9-5: Microscopic image of a microbubble attached to cells using ultrasound (×400 magnification)

Ultrasound mediated microbubble attachment increased attachment of microbubbles by 11mm^{-2}. In addition, attachment of targeted microbubbles was 26mm^{-2} greater than attachment of non-targeted microbubbles, a statistically significant difference ($p<0.001$). This data can be seen in Figure 9-6.

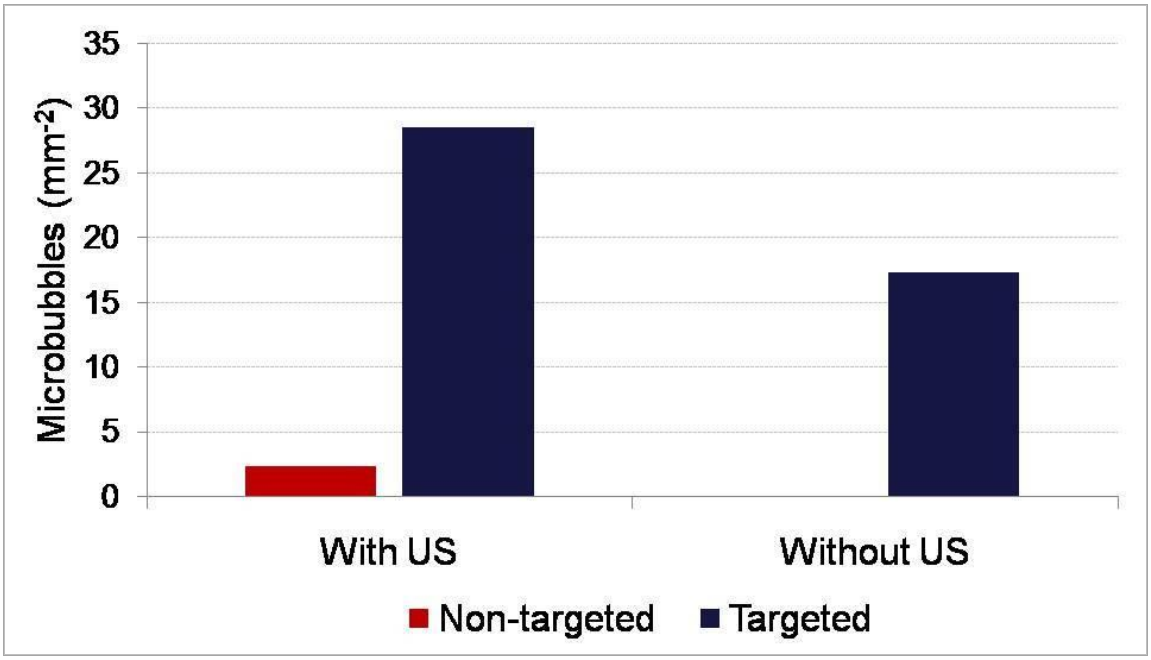

Figure 9-6: Ultrasound mediated microbubble attachment.

9.3. Attachment to cells in Ibidi μ-slides

Previously in Chapter 8 cellular adhesion has been assessed in Ibidi μ-slides. In order to determine the feasibility of attaching the contrast agent under flow conditions attachment was assessed under very low WSS within the μ-slides.

9.3.1. Method

Cells were seeded in the Ibidi μ-slides over night by Linda Norrie (Medical Physics, University of Edinburgh). The seeding procedure is outlined in Appendix J. Once the cells had reached approximately 60% confluence fluorescent microbubbles were added. Due to the unpredictable nature of cells on some occasions it was necessary to feed the cells and allow longer for them to reach confluence, this procedure is also outlined in Appendix J. It was decided that above a confluence of 60% there would be enough cellular matter for microbubble attachment.

Static attachment in flow slides

The first investigation carried out was regarding static attachment of microbubbles within the flow slides. This was achieved by adding fluorescent, positively targeted (CD31-conjugated) microbubbles to pre-warmed medium in a $2.6\times10^{6}ml^{-1}$ concentration and adding the medium to the slides as described for medium replacement in Appendix J. The slides were then incubated for 30minutes at 37°C. After incubation any excess unattached microbubbles were removed by very gently replacing the medium twice. The slides were then imaged with the fluorescence microscope.

The static attachment investigation was also repeated with a negatively targeted microbubble and a non-targeted microbubble. The negatively targeted microbubble was produced in the same way as the positively targeted microbubble as described in Chapter 6, however the CD31 antibody was replaced with the same volume and concentration of biotinylated Mouse IgG1 Negative isotype control (AbD Serotec, Martinsried, Germany).

The entire investigation was then repeated with a $5.2\times10^{6}ml^{-1}$ concentration of microbubbles.

Attachment under very low WSS in flow slides

Following static attachment investigations in the flow slides a study of attachment under flow with very low WSS was undertaken. The flow system described in Chapter 8, Section 8.4 and illustrated in Figure 8-14 was used. Positively targeted microbubbles were added to the reservoir in a $1.3\times10^{6}ml^{-1}$ concentration and warmed to 37°C before use. During flow the temperature of the medium was maintained through immersion in a water bath at 37°C.

The flow system was set-up and the cells in the slides subjected to microbubbles at 0.03Pa WSS for 10 minutes. Following this the reservoir was replaced for one

containing medium with no microbubbles and the cells washed for a further 10 minutes at 0.03Pa WSS as illustrated in Figure 9-7.

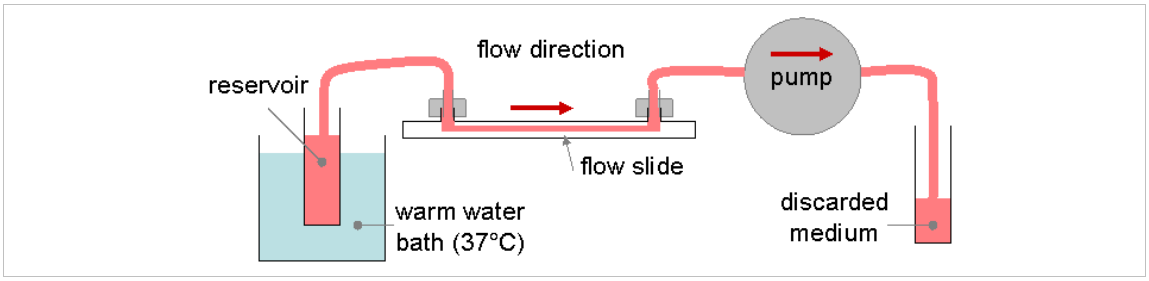

Figure 9-7: Removal of excess microbubbles.

Following washing the slides were then immediately observed under the fluorescence microscope to assess attachment of microbubbles.

Ultrasound Mediated attachment under flow

In order to determine if ultrasound can facilitate and improve attachment of the microbubbles under flow the microbubbles were subjected to 10-22MHz ultrasound.

The flow system was set up as illustrated in Figure 8-14. The flow slide, with tubing securely attached, was immersed in a warm water bath (37°C) above a block of acoustic absorber. The L10-22MHz transducer was set up at a distance of 2mm from the surface of the slide as shown in Figure 9-8. The distance between the transducer and slide was measured using the calipers on the Diasus scanner screen as illustrated in Figure 9-9. The focal distance of the scanner was set to lie at the centre of the flow channel.

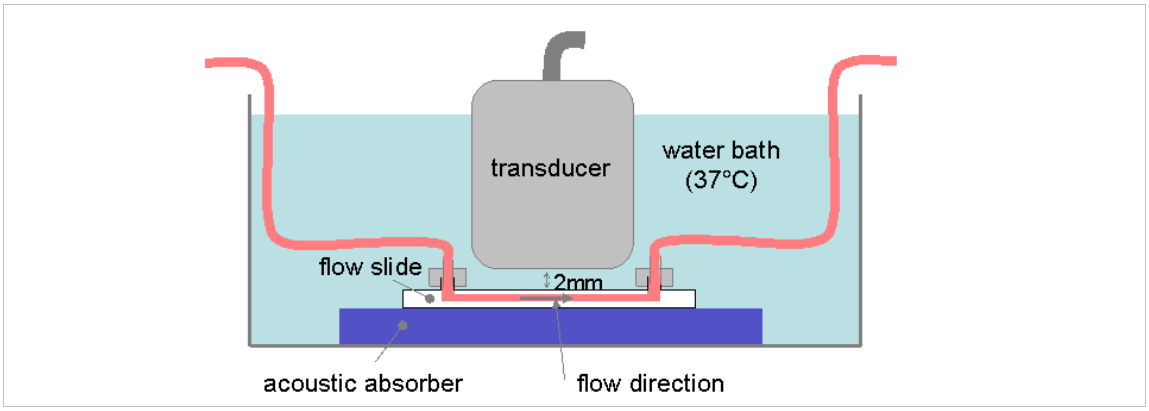

Figure 9-8: Ultrasound mediated attachment of microbubbles within µ-slides.

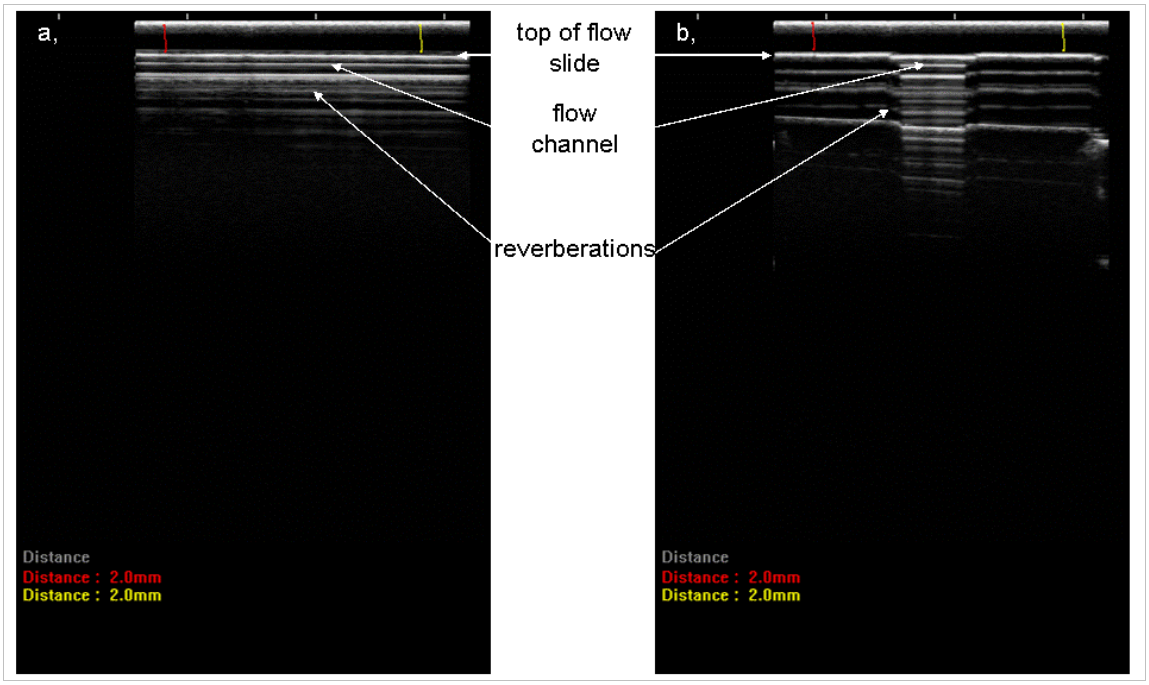

Figure 9-9: Diasus image showing measurement of distance between transducer and slide and identifying slide structures; a, along the length of flow channel and b, cross section of flow channel.

Fluorescent microbubbles were added to the reservoir in the same concentration as described in Section 9.3.1 above. Cells were then subjected to microbubbles in flow with a WSS of 0.03Pa for 10 minutes. The slides were insonated for the duration of the

investigation, parameters of the ultrasound scanner and transducer are defined in Table 9-2.

Following the investigation the slides were washed as described previously and observed using fluorescence microscopy.

9.3.2. Results and Discussion

Static attachment in flow slides

Targeted microbubbles have been successfully attached to a cellular monolayer in the Ibidi flow slides under static conditions. Positive targeting of the microbubbles increased microbubble attachment by $15mm^{-2}$ ($p<0.05$) at a microbubble concentration of $2.58\times10^{6}ml^{-1}$ and by $10mm^{-2}$ ($p<0.01$) for microbubble concentrations of $5.16\times10^{6}ml^{-1}$. An increase in microbubble concentration did not cause an increase in microbubble adherence for the positively targeted microbubbles, however there was an increase of $5mm^{-2}$ in microbubble adherence for the negatively targeted microbubbles. This increase in adherence of the non-targeted microbubbles suggests that only a portion of adherence of positively targeted microbubbles is a result of active targeting. The data from this investigation can be seen in Figure 9-10.

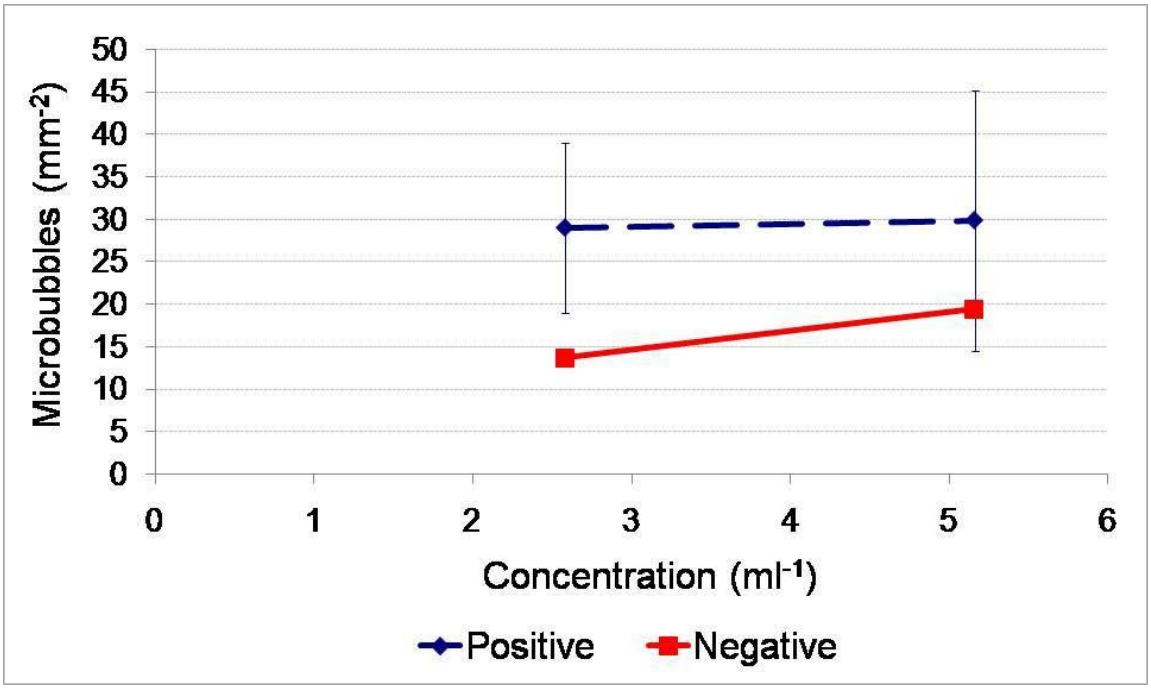

Figure 9-10: Microbubble adherence as a function of concentration for positively and negatively targeted microbubbles.

Images of microbubbles attached to the cells can be seen in Figure 9-11. This confirms that adherence does occur for negatively targeted microbubbles, however, there is an observable increase in adherence of positively targeted microbubbles.

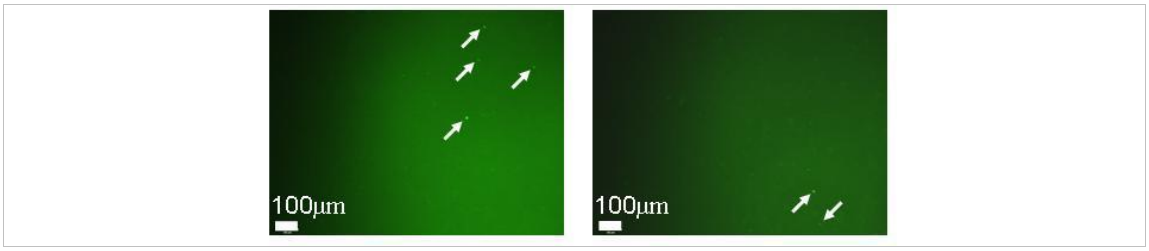

Figure 9-11: Microscopic images (10× objective) of microbubbles adhered to cells in the Ibidi flow slides; a, positively targeted microbubbles and b, negatively targeted microbubbles (white arrows indicate some of the microbubbles present in the image).

Attachment under very low WSS in flow slides

Attachment of microbubbles under 0.03Pa WSS was investigated. Figure 9-12 shows the average number of microbubbles attached per square millimetre at 0 and 0.03Pa WSS. At 0.03Pa the average microbubble count for positively targeted microbubbles was 4.0(±2.4)mm^{-2}, whilst at 0Pa this value was 29.1(±10.0)mm^{-2}. Suggesting that under flow conditions fewer microbubbles attach to the cellular surface. This could be a result of the antibody-cell interaction being too slow to form attachment in flow, or due to attached microbubbles washing off during the removal of excess microbubbles. Alternatively the lack of attachment may have been due to microbubbles not coming into contact with the cellular surface as a result of microbubble migration towards the vessel axis (Rychak et al. 2006a). Hence ultrasound was investigated as a means to facilitate microbubble attachment.

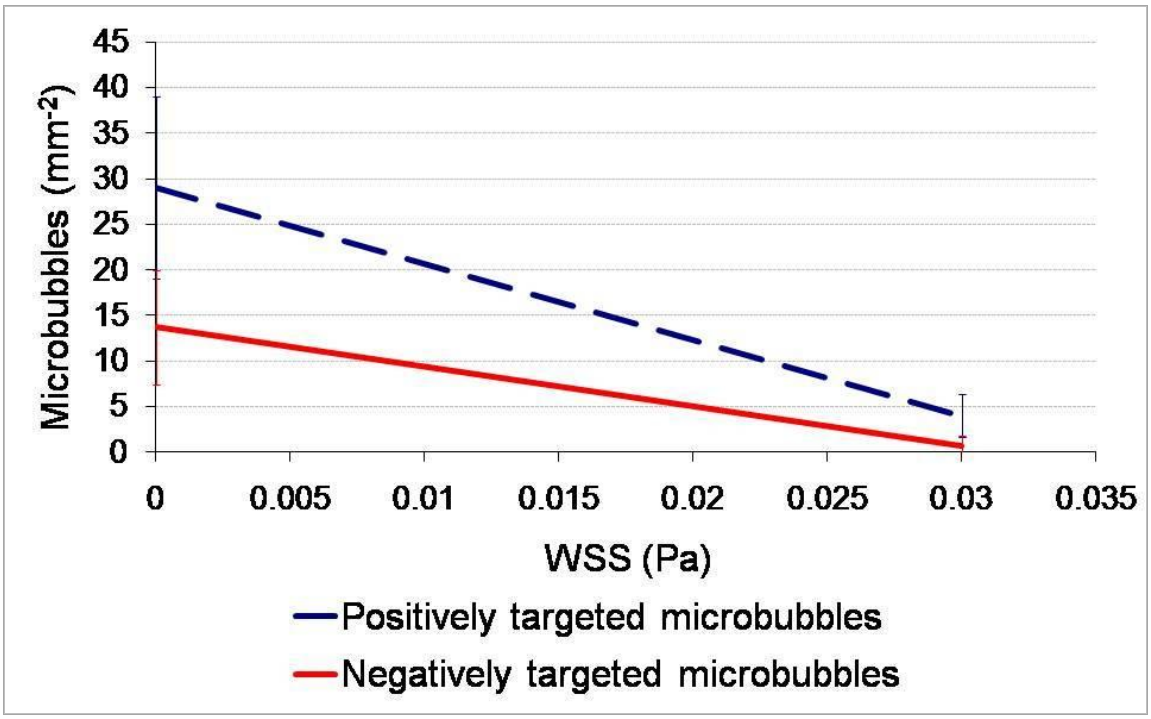

Figure 9-12: Microbubble adherence as a function of WSS for positively and negatively targeted microbubbles.

Figure 9-13 shows microscopic images of microbubbles attaching to a cellular surface under 0.03Pa WSS. The microbubbles demonstrate grouping which is likely to be due to microbubble manufacture, however, this may also be a result of the secondary radiation force as described previously. Further investigations would need to be carried out to determine the reason for this grouping of microbubbles.

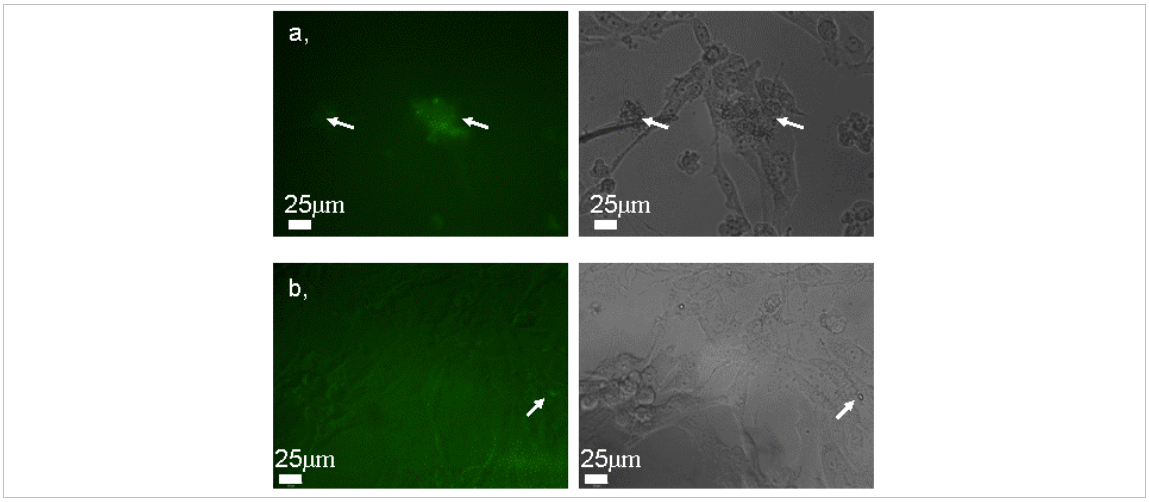

Figure 9-13: Microscopic images of; a, positively targeted microbubbles attached to cells and b, cells subjected to negatively targeted microbubbles, under 0.03Pa flow (×400 magnification).

Overall positively targeted microbubble attachment under 0.03Pa WSS was 3.2mm^{-2} greater than that of negatively targeted microbubbles suggesting that the attachment observed is a result of active microbubble targeting. However this demonstrates very limited attachment.

Ultrasound Mediated attachment under flow

Ultrasound mediated microbubble attachment has been demonstrated under 0.03Pa WSS. An increase in microbubble adherence of 15.5(±7.9)mm^{-2} has been observed for ultrasound mediated attachment ($p<0.01$). Figure 9-14 illustrates the increase in attachment as a result of the primary acoustic radiation force.

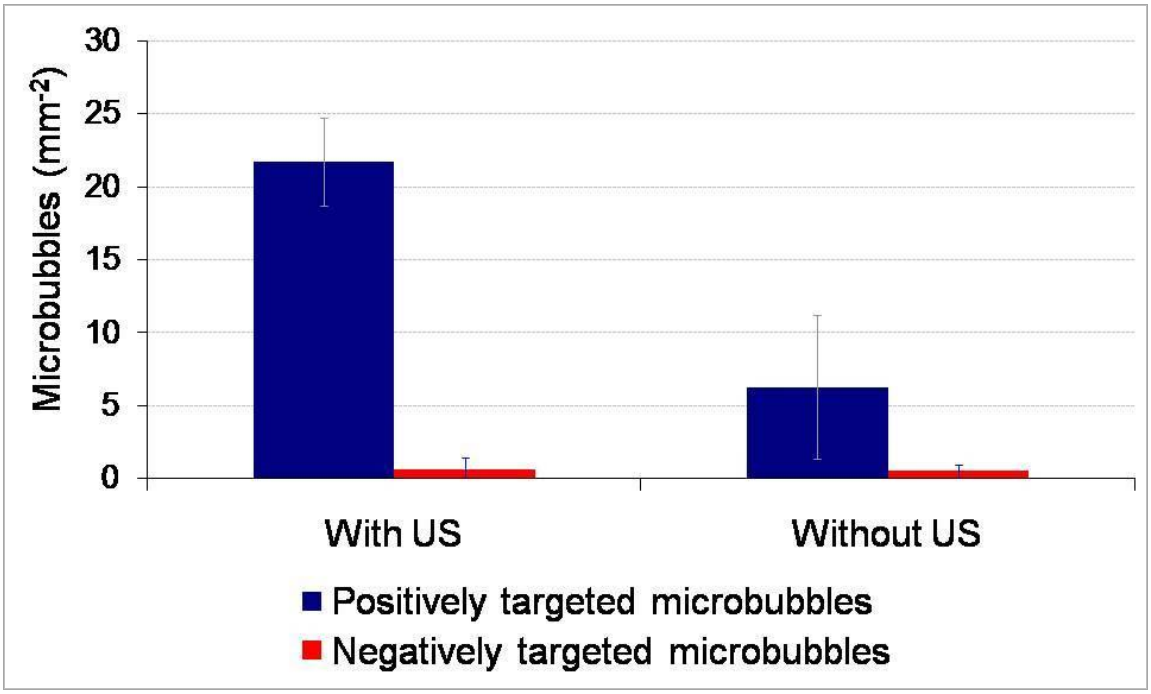

Figure 9-14: Microbubble adherence for positively and negatively targeted microbubbles with and without ultrasound.

Images of microbubbles attaching with and without ultrasound can be seen in Figure 9-15. This confirms that increased attachment occurs under flow conditions as a result of the acoustic radiation force. However, attachment is still limited and it is therefore necessary to investigate attachment of microbubbles under flow in order to optimise such attachment.

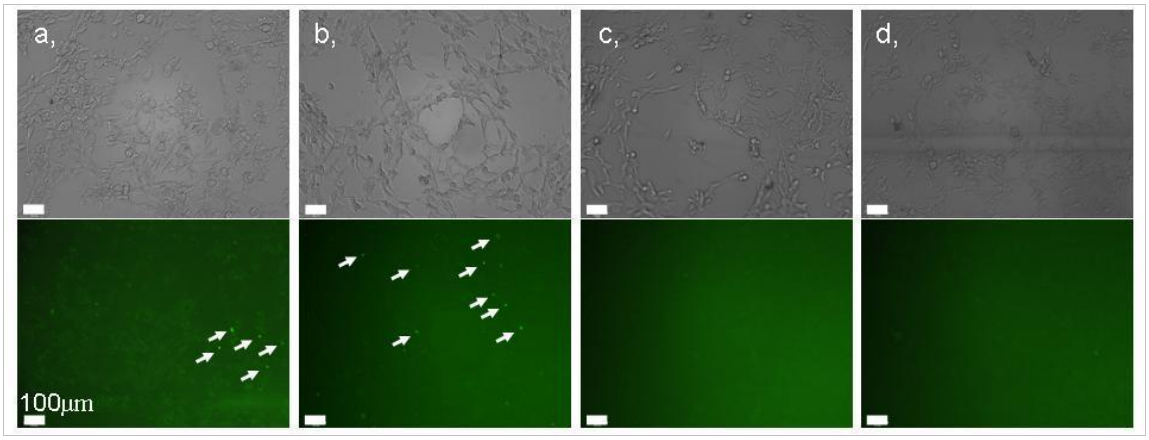

Figure 9-15: Microscopic images of microbubble attachment (x100 magnification); a, positively targeted microbubbles without ultrasound, b, positively targeted microbubbles with ultrasound, c, negatively targeted microbubbles without ultrasound and d, negatively targeted microbubbles with ultrasound. Microbubbles on a and b identified by white arrows, no microbubbles were observed on c and d.

Although attachment of microbubbles using acoustic radiation force has been successful it is possible that the technique is limited due to the plastic slides used for the attachment investigations. Since plastic reflects much of the ultrasound, as demonstrated in Figure 9-9, it is probable that the primary acoustic radiation force is significantly reduced and that with an alternative flow model, with an acoustic window, greater attachment may be observed when insonated with ultrasound. Unfortunately such an investigation was not possible within the time scales of this PhD.

9.4. Summary

Positively targeted microbubbles have been shown to actively target SK-Hep-1 cells when added to cells in solution and using acoustic radiation force to facilitate attachment. In addition the acoustic radiation force acting on the microbubbles has been calculated and found to be 15.6(±3.3)nN.

Attachment of microbubbles to cells under flow has been investigated in Ibidi µ-slides under very low WSS of 0.03Pa. This is at the same WSS investigated by Klibanov (2006) and Rychak (2006a). Limited microbubble attachment was observed under 0.03Pa WSS and relative to the negatively targeted microbubbles there is a 3.2mm^{-2} increase suggesting that active attachment has been observed. However some attachment may not be due to active targeting but as a result of other targeting mechanisms, for example chemical or electrostatic interactions, indicated by very limited attachment of the negatively targeted microbubbles.

Ultrasound has been used to facilitate the attachment of microbubbles under flow. The acoustic radiation force has increased attachment of microbubbles under 0.03Pa WSS by 15.5(±7.9)mm^{-2}. These results suggest that ultrasound is a viable method of facilitating attachment of the microbubbles under flow by using acoustic radiation force to drive the microbubbles towards the target surface.

Prior to pre-clinical trials of the UCA it is necessary to demonstrate significant active targeting of the microbubbles. In addition it would be advantageous to be able to investigate the echogenicity of the microbubbles attached to a cellular surface in order to determine the feasibility of IVUS investigations. As a result, further investigations regarding microbubble targeting under higher WSS are necessary prior to future animal investigations. Possibilities for further investigations and alternative targeting strategies are discussed in Chapter 10.

Chapter 10 Conclusions and Evaluation

A lipid-based microbubble UCA has been developed which upon further development will be targeted to vulnerable plaques observed in coronary heart disease. Vulnerable plaques have been identified as the leading cause of mortality in people suffering from heart disease (Kurzweil and Grossman 2004) and currently there are limited methods capable of distinguishing vulnerable plaques from stable plaques. The in-house contrast agent, which will be targeted to inflammation markers exhibited by vulnerable plaques, (Lindner 2002a) has been developed for use with high-frequency (40MHz) IVUS. The investigations presented in this thesis represent the initial development stages of the UCA in optimisation of the echogenicity of the agent and demonstrating targeting feasibility under varying shear stress.

10.1. Optimization of the UCA

10.1.1. Conclusion

Optimisation of the UCA for 40MHz IVUS has been achieved through investigating the effect of various methods on the echogenicity of the agent. Methods investigated included agitation, high-shear mixing, sonication and diffusion. In addition the effect of

temperature on production was investigated. It was found that the optimum manufacture method was use of the high-shear mixer before heating of the lipids and use of the CapMix™ for rapid agitation after heating of the lipids. The optimum production temperature was determined to be 78ºC and optimum length of agitation was 45s.

Various compositions were also investigated and the most echogenic composition was found to be the 30% cholesterol composition. This was in a comparison with two alternative compositions.

In addition to optimisation of the agent, stability of the agent over three months was also investigated. The agent was found to remain stable for three months when stored in the refrigerator at 2-5ºC as demonstrated in Section 3.4.2.

10.1.2. Statistical Analysis

An ANOVA test was carried out on the comparison of techniques data in order to determine if the differences between the data were statistically significant. The F test value was found to be 7.093 and p value <0.001 suggesting a significant difference between the results. Further analysis shows that there was a 95% confidence interval of -33.71dB to -27.46dB for agitation which was similar to the confidence interval of the sample involving high shear mixing after. (-33.82dB to -27.58dB). These were both greater than the confidence intervals for alternative techniques, this further supports the decision to use both techniques in production of the agent.

10.1.3. Evaluation and possible sources of error

The microbubble production techniques described in Chapter 3 were investigated as they have previously been used by other authors to produce UCAs (Fry et al. 1995; Klibanov et al. 2004; Schneider et al. 2004; Schneider et al. 2006; Talu et al. 2006). For the sonication method it was necessary to position the tip of the sonicator in the centre of the vessel containing the microbubble sample visually. Although every care was taken to ensure that the sonicator tip was central visual assessment of its location is subjective

which may have lead to variations in the result. However, an average of three samples was collected in order to eliminate such variations.

Analysis of the RF data was carried out in order to quantify the mean backscatter produced by each sample. The software used to determine the mean backscatter of each sample calculated the mean backscatter relative to a perfect reflector. The perfect reflector used throughout this thesis was the reflection from an air-water interface. A perfect reflector signal was collected each time a sample was analysed in order to take into account any changes in signal from the IVUS transducer. The reflector data was subject to a degree of variation as it was assessed visually, as demonstrated in Appendix C. However the variation in three data sets collected was 1dB suggesting that the method used to acquire the reflector data was highly reproducible.

Errors in the RF analysis of the mean backscatter were not possible to calculate due to the complexity of the software program, however, since all the results were analysed using the same program and compared against each other any errors will be consistent between samples.

All backscatter results from the different compositions are the mean of a minimum of three sets of experiments, with the exception of the stability investigation. Three regions of interest (ROI) were analysed for each microbubble sample and the average of the three ROIs determined in order to take into account any variation in the sample. This value was then averaged over the three data sets collected. All data was presented with the standard deviation from the three data sets as an error. It was not possible to collect more than one data set for the three month stability trial due to the consumption of resources required for this trial and the time scale of the trial.

During the stability trials it was also noted that some samples presented with mould, despite the sustained echogenicity of the samples the contaminated samples were not considered suitable for use in further investigations and were discarded. Currently the agent is manufactured in a non-sterile environment due to the in-vitro nature of the early

development stages; however, further development of the agent for in-vivo use will be carried out in sterilised surroundings.

10.2. Calibration of a novel flow chamber

Laser Doppler anemometry was used to calibrate a novel flow chamber designed to investigate attachment of the UCA to an agar surface using IVUS. The flow chamber was successfully calibrated up to 50Pa WSS. Higher WSS was achieved through use of higher viscosity fluids produced from glycerol solutions. In addition to the LDA investigation, CFD and calculations were also used to determine the WSS within the flow chamber. A comparison of the different methods suggests that there is good correlation between the calculations, CFD and experimental values for low flow volumes. However at higher flow volumes the WSS values differ by as much as 20Pa. In conclusion, at low flow volumes, calculated WSS values are suitable for estimating expected WSS within a vessel.

10.2.1. Evaluation and Sources of Error

Glycerol solutions of 40, 60 and 80%, used to produce high viscosity fluids, were calculated by mass. Required volumes were calculated and measured using a measuring cylinder, resulting in an accurate solution. However, the glycerol was found to settle out of solution after time and if there was any variation in the solution this would have resulted in an inaccurate viscosity estimate. This was avoided through stirring of the solution at regular intervals and the solution was covered when stored to ensure that evaporation was minimised. In addition, viscosity values were determined through interpolation of data from Kaye and Laby (Kaye and Laby 2004). Since interpolation involves determination of a value from an observed trend it may not be a truly accurate value, this would result in an inaccurate calculation of the WSS. However, the tables presented by Kaye and Laby are very comprehensive and so the values determined are assumed to be accurate.

The resolution of LDA is dependent upon the direction of the measurements. The measurement volume, as illustrated in Figure 4-3 measures 200×45×45μm; this results in resolutions of 200μm in the z (forward) direction, 45μm in the x-direction and 45μm in the y-direction. The resolution of the measurements of flow velocity presented in this thesis was 200μm. Ideally the flow velocities would have been measured in the planes with the optimal resolutions; however, in order to be able to investigate the attachment of microbubbles to agar with an IVUS catheter it was necessary to be able to introduce the catheter behind the agar. In order to investigate agar in the y-direction using IVUS the catheter would have needed to be introduced to the flow which would have resulted in a disruption to the flow. Alternatively the depth of the central panel could have been increased to allow for an IVUS inlet, the 3×3mm cross-section was used as this is the closest approximation to a 3mm diameter coronary artery possible with a parallel plate flow chamber.

When determining the shear rate within the flow chamber from the flow profiles as described in Section 4.5 three data points adjacent to the wall were used. Three data points were selected to reduce any shear rate errors resulting from an anomalous result as illustrated in Figure 10-1a. Due to the parabolic shape of the flow profile it was decided that the use of four points was more likely to result in an inaccurate increase in the measurement of shear rate as demonstrated in Figure 10-1b.

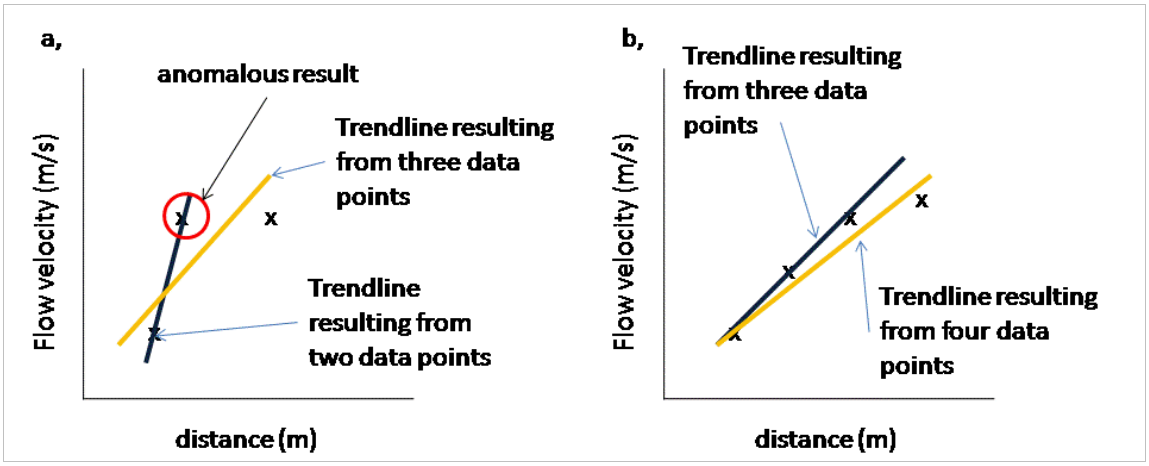

Figure 10-1: Errors resulting from a, the use of two data points and b, the use of four data points.

Any extreme outliers observed in the flow profile were assumed to be anomalous resulting from reflections of the laser from discontinuities in the flow chamber, or scattering from the agar surface or Perspex. However, it is possible that outliers were a result of turbulent flow. Since the flow chamber has been designed such that laminar flow should be observed at low flow volumes it was assumed that these results were anomalous.

Statistical analysis of the flow profiles was carried out using the R-squared value as determined by the parabolic trendline produced using the available function within the Microsoft Excel software. An R-squared value greater than 90% was accepted as significant correlation and above 80% was assumed to be good correlation. All R-squared values were greater than 80% with the majority greater than 90% suggesting good correlation of the data. In addition correlation p values were calculated for all trendlines presented.

The maximum WSS observed using 80% glycerol solution, with a viscosity of 0.06Pa·s, at 270ml·min^{-1} flow volume was 50Pa. Although higher WSS has been observed in stenosed vessels (Li et al. 2007) and mice (Table 7-1) it was not possible to reach higher WSS within the flow chamber described. The maximum flow volume that could be

passed through the flow chamber with the 80% glycerol solution was 270 $ml \cdot min^{-1}$ and although it was attempted to pass higher glycerol solutions through the system, this caused the pump to seize and was therefore not possible. In order to investigate attachment or detachment of the agent at higher WSS it would be necessary to design a different flow system.

Other sources of error in the flow system include discontinuities in the flow channel resulting from the agar well and microscope slide. In addition, discontinuities or scatter may be observed if the silicone grease, used to seal the flow chamber, projects into the flow channel. The former issue was addressed by visual and tactile assessment of the points where the agar meets the Perspex, or microscope slide meets the Perspex. Every effort was made to ensure that the discontinuity was minimal. The latter issue was addressed through regular cleaning of the flow channel and visual observations to ensure that no grease could be seen in the channel.

The flow system has been designed to assess attachment and detachment of UCAs under varying, controlled WSS and calibrated to 50Pa. Calibration of the flow chamber can be considered accurate, assuming that laminar, non-turbulent flow is observed at all times.

10.3. IVUS Characterisation

The IVUS scanner and transducer described in Chapter 5 was characterised in order to determine the acoustic pressure output of the scanner. The maximum acoustic peak negative pressure was found to be -2.0 ± 0.15MPa, at 1mm from the transducer, as determined from the peak negative voltages measured using a membrane hydrophone. The MI was then calculated and found to be 0.32 ± 0.10, suggesting that the insonated microbubbles could behave non-linearly, but that microbubble destruction is unlikely at this pressure.

10.3.1. Statistical Errors

The error presented for the peak negative pressure was the standard deviation of the data sets collected ($n = 3$). The error presented for the MI was calculated using the standard deviation of the data sets averaged and the uncertainty in the sensitivity measurements, provided by the calibration certificate (National Physics Laboratory).

10.3.2. Evaluation and sources of experimental errors

The distance of the hydrophone from the transducer was measured using the distance divisions on the IVUS scanner screen as shown in Figure 5-2. The axial resolution of an IVUS system lies between 80μm (Rosales and Radeva 2005) and 190μm (Elliott and Thrush 1996) for frequencies of 20-50MHz, suggesting that for 40MHz IVUS the resolution enables an accurate measurement of the distance between the transducer and hydrophone, to within 20%.

Positioning of the hydrophone was achieved through visual observation of the brightest echo on the IVUS scanner screen achieved at minimum gain, as described for reflector data collection in Appendix C. Although this method is highly subjective the error was minimised through lowering the gain on the screen, making the contrast on the screen more obvious.

Another source of error was the potential presence of bubbles in the water bath and in particular, underneath the hydrophone. The former issue was addressed through the use of de-ionised water which was allowed to sit for 24 hours prior to running experiments. The latter was assessed through careful placement of the hydrophone in the water bath and allowing the hydrophone to be completely submerged before clamping in place. The hydrophone was then left for an hour to allow any bubbles formed in placing it to disperse or dissolve.

10.4. Attachment of Antibodies to Microbubbles

10.4.1. Conclusion

Targeting of the microbubbles was achieved through the attachment of antibodies to the microbubble shell by means of a streptavidin-biotin bridge as illustrated in Figure 6-1. CD31 antibodies have been successfully attached to the microbubbles with over 90% of the microbubble population being targeted. As a result the microbubbles have been successfully targeted to SK-Hep-1 cells.

10.4.2. Evaluation and sources of error

Antibody attachment was optimised for small volumes of microbubbles in order to minimise project expenses; however when attaching antibodies to larger volumes of microbubbles a 20% drop in the population of targeted microbubbles was observed with only 70% of microbubbles having antibodies attached. This could be due to a number of reasons; the number of microbubbles with biotin in the shell being less, the solution of antibodies and microbubbles being unevenly distributed or there being insufficient antibodies or streptavidin to fill all the biotin sites. Distribution of the antibodies and microbubbles was achieved through use of the Rotamix and the samples were agitated for 5s before addition of streptavidin which would ensure an even distribution. In order to investigate the effect of biotin and the number of biotin sites per microbubble further investigations would have been advantageous but were not conducted due to time restrictions.

Fluorescence measurements of antibody attachment were achieved through the addition of a fluorescent antibody (F2883) to the CD31 attached to the microbubbles. It is possible that there were CD31 antibodies attached to the microbubbles which did not get tagged by the F2883, giving a falsely low value of antibody attachment, alternatively unattached F2883 may have remained in solution, unattached to the CD31 which would have given a false high value. In order to minimise errors from the latter the samples

were washed after the addition of F2883. The former was addressed through a brief investigation into different concentrations of F2883 being added to the microbubbles, no variation greater than that observed between samples was seen.

10.5. Attachment and Detachment via a streptavidin-biotin mechanism

10.5.1. Conclusions

The streptavidin-biotin bond has been assessed under flow conditions up to 50Pa WSS. The bond was found to be capable of withstanding 50Pa WSS making it over 75 times stronger than a suspected electrostatic bond. This is of an order with the difference in rupture forces between a streptavidin-biotin bond (160pN) and a weak non-covalent (electrostatic) bond (4pN) making the rupture force of the streptavidin-biotin bond 40 times greater than that required for the electrostatic bond (Picotwist 2009). In conclusion, the streptavidin-biotin bond is strong enough to withstand the shear stresses it might experience in healthy human coronary arteries and of an order with the shear stress observed in mice, as described in Table 7-1. However, the maximum WSS under which the streptavidin-biotin bond will remain attached has not been investigated due to flow chamber limitations as described in Section 10.2. In order to determine if the bond is able to withstand the higher WSS expected in diseased mouse coronary arteries further investigation would be required. Use of the streptavidin-biotin bond however is itself under question as it may cause an unwanted immune response (Anderson et al. 2009) due to its being a foreign protein, it is therefore necessary to investigate more biocompatible targeting techniques.

Attachment of the microbubbles under flow was observed at low WSS, however the attachment was minimal. In order to be able to assess attachment using IVUS it will be necessary to improve the number of microbubbles attaching under flow. In addition the attachment could not be confirmed since the microbubbles were not observed using

fluorescence microscopy, it is possible that the bubbles observed were a result of the water flow and not in fact targeted microbubbles.

10.5.2. Statistical Analysis

Correlation P-values and Pearsons correlation coefficients have been calculated and presented where possible. A $p<0.01$ is considered a significant correlation and correlation coefficients greater than 80% (0.8) are considered significant. Errors are presented as one standard deviation ($n \geq 3$) unless identified otherwise.

In addition t-tests were carried out and p-values calculated for comparisons of the average data points to controls. These are presented alongside the data.

10.5.3. Sources of Error and Evaluation

Potential sources of error from the investigation in Chapter 7 come from the WSS estimate, discontinuities in the flow chamber will cause a large error in the measurement of WSS and turbulent flow may occur within the flow chamber. This was avoided through regular cleaning of the flow chamber and visual observations of the flow channel as described in Section 10.2.1.

Mean backscatter analysis of detachment of the microbubbles was carried out at two locations along the flow channel and averaged. It was not possible to observe the attachment of microbubbles to agar visually and it is possible that distribution of the microbubbles was not even across the agar surface. In addition, it was not possible to observe the exact same position of the agar with the IVUS at each increase in WSS therefore resulting in some variation of the mean backscatter in each position.

Placement of the transducer during the detachment investigations was done carefully due to very bright echoes observed from the edges of the flow channel. Positioning was carried out through identifying these very bright echoes and ensuring that the transducer

was as central to the flow channel as possible as illustrated in Figure 10-2. The flow channel was identified from other echoes by the occasional bubble observed in the flow.

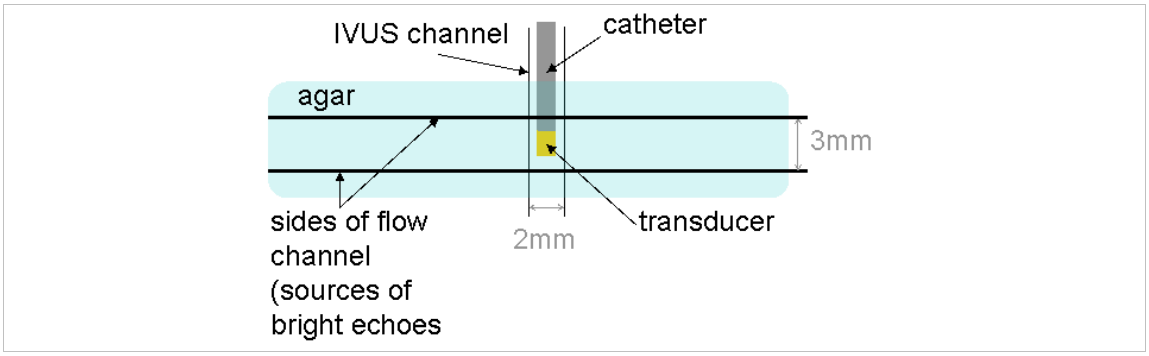

Figure 10-2: Positioning of transducer behind agar.

10.6. Cellular Adhesion

10.6.1. Conclusions

Cellular adhesion under varying WSS has been investigated. The flow chamber developed in Chapter 4 was adapted to allow for cell growth within the flow channel. However due to environmental situations, such as temperature and toxins it was found that cells rapidly detached under low WSS. An alternative flow system was developed with the use of Ibidi μ-slides to allow for assessment of cellular adhesion under very low WSS. Cellular retention under WSS up to 0.17Pa was found to be greater than 90% making the Ibidi flow cells suitable for assessment of microbubble attachment to cells under very low WSS.

10.6.2. Sources of Error and Evaluation

Cellular adhesion was assessed through an investigation into the confluence of cells before and after being subjected to increasing WSS. The confluence of the cells was determined through the use of a confluence grid as described in Appendix I. This technique was accurate to within 1%. Accuracy could have been improved by

increasing the number of squares in the grid used; however this would have increased the time required to determine the confluence of each image and was therefore limited by time constraints and image resolution.

In addition to the confluence calculations it was also not always possible to compare the confluence in the same region as the slides were moved to and from the microscope platform. In order to rectify this, the final investigation was carried out in the Ibidi slides with the slides stationary on the microscope platform. This however resulted in only one data set being available per investigation and did not take into account the possibility of uneven cellular distribution.

Finally the use of live cells resulted in some limiting factors in the experimental procedures. It was necessary to ensure that the environment was kept as close to 37°C as possible throughout the investigations, this was achieved through the use of warm water baths and a specially designed warm plate for the microscope. In addition cells were subjected to toxins and bacteria in the air which may have resulted in greater confluence loss than expected; this was remedied through the use of the Ibidi flow cells which were enclosed and sterile.

10.7. Attachment of microbubbles to cells

10.7.1. Conclusions

The microbubbles have been successfully attached to SK-Hep-1 cells under very low (0.03Pa) WSS through the use of the primary acoustic radiation force. This was achieved through targeting of the agent by attachment of CD31 antibodies as described in Chapter 6. Attachment of the agent under flow conditions is a significant step in the development of a targeted UCA; however, in order to be able to observe the attached microbubbles with IVUS it is necessary to optimize the number of microbubbles adhered to the cells. Potential further investigations to optimize this attachment are discussed in Section 10.9.

10.7.2. Statistical Analysis

ANOVA tests have been used to identify the statistical significance for the data presented in Chapter 9 and p values have been presented. A p value less than 0.05 has been considered statistically significant.

10.7.3. Sources of Error and Evaluation

Observation of the attached microbubbles was achieved through the use of fluorescence microscopy. The fluorescent microbubbles were assessed with flow cytometry to determine the number of microbubbles containing the fluorescent lipid. Since only 50% of the microbubbles in a sample contained the fluorescent lipid it is possible that there were microbubbles present which weren't observed under the microscope. In order to try to eliminate this problem the attached microbubbles were observed with fluorescence and bright-field microscopy and an average of the microbubbles counted in each image was calculated (errors represent the standard deviation).

In addition to the problem described above the fluorescent lipid is also known to wear off if subjected to bright lights for any length of time, the microbubbles were therefore kept in the dark as long as possible, however, for health and safety reasons it was not always possible to carry things out in the dark.

The distribution of microbubbles attached to cells was not even, suggesting that there were either areas of lower WSS or that some cells were not able to adhere to the antibodies attached to the microbubbles. For the purpose of this investigation the slides were studied to find areas of highest microbubble attachment and images collected from these areas. Since visual observation is subjective it is possible that this technique may have resulted in manual errors.

Ultrasound was investigated as a means to facilitate the attachment of microbubbles to the cellular surface due to the tendency of microbubbles to float, or under flow, migrate to the centre of the flow channel. The force acting on the microbubbles was calculated

(Section 9.2.3) using an equation described by Rychak et al. (Rychak et al. 2006a). The force calculated does not take into account the secondary radiation forces and assumes that the buoyancy force is of the order of 0.1nN. Since these forces do exist, determination of the force acting on the microbubble could be subject to error. In addition, Equation 9-1 assumes that the microbubbles are insonated at their resonant frequency, since the microbubbles have been optimized for resonance at 40MHz US and the scanner used for this investigation operates at 10-22MHz this may also be a source of error in the calculation.

In Section 9.2.3 the microbubbles are being attached to cells in Petrie dishes, when studying the ultrasound to which the microbubbles and cells were subjected to, as described in Appendix K, a significant increase in acoustic pressure was observed at 4mm from the transducer, this is believed to be due to generation of standing waves. It is possible therefore that the microbubbles were subjected to greater pressures and forces than estimated.

When using the ultrasound with the Ibidi flow slides it is probable that ultrasound wave is reflected by the top surface of the slides since the slides are produced from plastic. Despite this an increase in microbubble attachment was observed when using the acoustic radiation force.

10.8. Overall

The field of ultrasound contrast agents is continually expanding. Researchers around the world are developing new UCAs and investigating the properties and potential diagnostic and therapeutic uses of different agents. Medical Physics at Edinburgh University is playing a significant role in the development of new agents for specific targeting purposes. The agent being developed is intended for use in the diagnosis of coronary heart disease.

The work presented in this Thesis, in addition to demonstrating the development of the agent described, also provides a description of the different methods used to this end. The novel flow chamber described in Chapter 4, designed specifically for the assessment of detachment and attachment of the agent under very high WSS, could easily be adapted or used for the assessment of alternative targeting mechanisms. In addition the flow set-up described in Chapter 9 has been shown to be suitable for assessment of microbubble targeting to a cellular monolayer.

Antibody attachment to the microbubbles, as described in Chapter 6, demonstrates the potential problems arising from this technique. A major step in the development of the agent, the techniques investigated and described, both for attachment and assessment of attachment, will prove useful for the development of alternative targeting strategies both in future development of the agent produced at Edinburgh University and for other researchers investigating antibody attachment.

Ultrasound mediated delivery of microbubble UCAs using acoustic radiation force has been investigated by a variety of authors (Dayton et al. 1999a; Fowlkes et al. 1993; Lum et al. 2006; Rychak et al. 2004; Rychak et al. 2005; Rychak et al. 2006a). This technique has been demonstrated in Chapter 9. The acoustic radiation force has been shown to improve attachment of the agent to a cellular surface both in static conditions and under very low WSS.

Although other research is being carried out into UCAs targeted to inflammation and atherosclerotic plaques (Klibanov et al. 2006; Lindner 2002a; Lindner et al. 2001; Villanueva et al. 1998), to the author's knowledge, Edinburgh University is the only group investigating the targeting applications of a UCA designed specifically for use with high-frequency ultrasound. This will allow for higher resolution imaging of the vulnerable plaques to which the agent will be targeted.

10.8.1. Conclusion

The microbubble being developed at Edinburgh University has been shown to successfully attach to a cellular monolayer under very low WSS confirming the feasibility of the agent for targeting applications. The agent will be targeted to atherosclerotic plaque and initial *in-vivo* investigations will be carried out in small animals. The streptavidin-biotin bond has been shown to be able to withstand flow with a WSS up to and over 50Pa which is of an order with WSS observed in healthy mice (Table 7-1), however as described in Section 10.5 this may not be an ideal attachment mechanism for *in-vivo* applications.

In addition the UCA has been successfully optimized for use with high-frequency 40MHz IVUS.

10.9. Future Investigations

Preclinical investigations with the agent will involve the assessment of contrast agent targeting in small animals, notably mice. Small animal imaging is a continually developing field of study and the Medical Physics department recently purchased a Vivo770, high frequency, high resolution *in-vivo* ultrasound imaging system (Visualsonics B.V, Amsterdam, The Netherlands) for pre-clinical imaging purposes. Prior to preclinical investigations in small animals further development of the UCA will be required.

Future development of the agent will involve further optimization of antibody attachment, demonstrated in Chapter 6, to enable attachment of a greater number of microbubbles to the cells. The greater number of microbubbles which can adhere to cells under flow would result in a greater contrast to tissue ratio which is highly desirable.

Suggested future investigations include an assessment of detachment of the agent from cells under controlled shear stress in addition to investigating the maximum WSS under

which the agent will attach. Attachment of the agent under very low WSS, as demonstrated in Chapter 9, is limited, in order to be able to investigate attachment using IVUS a greater number of adhered microbubbles is required. This could be achieved through further development of the flow chamber presented in Chapter 4. Schmidt *et al* (2008) have developed a flow cell with an acoustically transparent plastic, Rexolite (C-Lec Plastics, Inc., Beverly, NJ, USA). This flow cell could potentially allow for the development of an optically and acoustically suitable flow chamber for future attachment investigations.

Currently attachment of the targeted agent to excised ovine and swine aortas is being investigated in the Department. This involves the use of alternative antibodies targeted to the endothelial cells of the vessels. Increasing the attachment of antibodies to large volumes of microbubbles will help to improve the attachment. However in order to investigate the attachment *in-vivo* it is suggested that alternative antibody attachment methods be developed to eliminate potential auto-immune reactions from the streptavidin.

Development of the UCA here at Edinburgh University is still in its early stages; however, the work presented throughout this thesis has shown significant advances. The next steps in development of the agent have been outlined above. The field of ultrasound contrast imaging is still continuing to expand and shows significant promise in both diagnostic and therapeutic applications. The work described throughout this thesis has focused on development of the UCA for diagnosis purposes through targeting of vulnerable plaques in CHD; however the agent also has therapeutic potential as a drug or gene delivery vehicle which could also be investigated. In addition the agent could be used to target alternative structures as a diagnostic tool for diseases other than CHD.

Appendices

Appendix A Resonance Frequency of Microbubbles

Optimisation of the microbubble agent being produced at Edinburgh University has been achieved through assessment of the maximum echogenicity achievable using different production methods. However, an estimate of the optimum microbubble size for resonance at 40MHz has been carried out using Equation 2-6.

Symbol	Description	Value	Reference
f_0	Resonance frequency	Variable	n/a
r	Radius of encapsulated microbubble	Variable	n/a
γ	Polytropic exponent for encapsulated gas	1.4	(MacDonald 2004)
χ	Shell elasticity parameter	$8Nm^{-1}$	(MacDonald 2004)
ρ_0	Liquid density	$998.2kgm^{-3}$	(Kaye and Laby 2008)
σ_{st}	Surface tension	$0.072Nm^{-1}$	(MacDonald 2004)
P_0	Ambient static pressure	100kPa	(MacDonald 2004)

Table A-1: Resonance frequency data

Using the data provided in Table A-1 the graph in Figure A-1 has been produced in order to provide an estimate of the microbubble size which will resonate at 40MHz. The

blue line on the graph represents the estimated optimum radius size of 0.7µm. This suggests that a microbubble of diameter 1.4µm would resonate with 40MHz ultrasound.

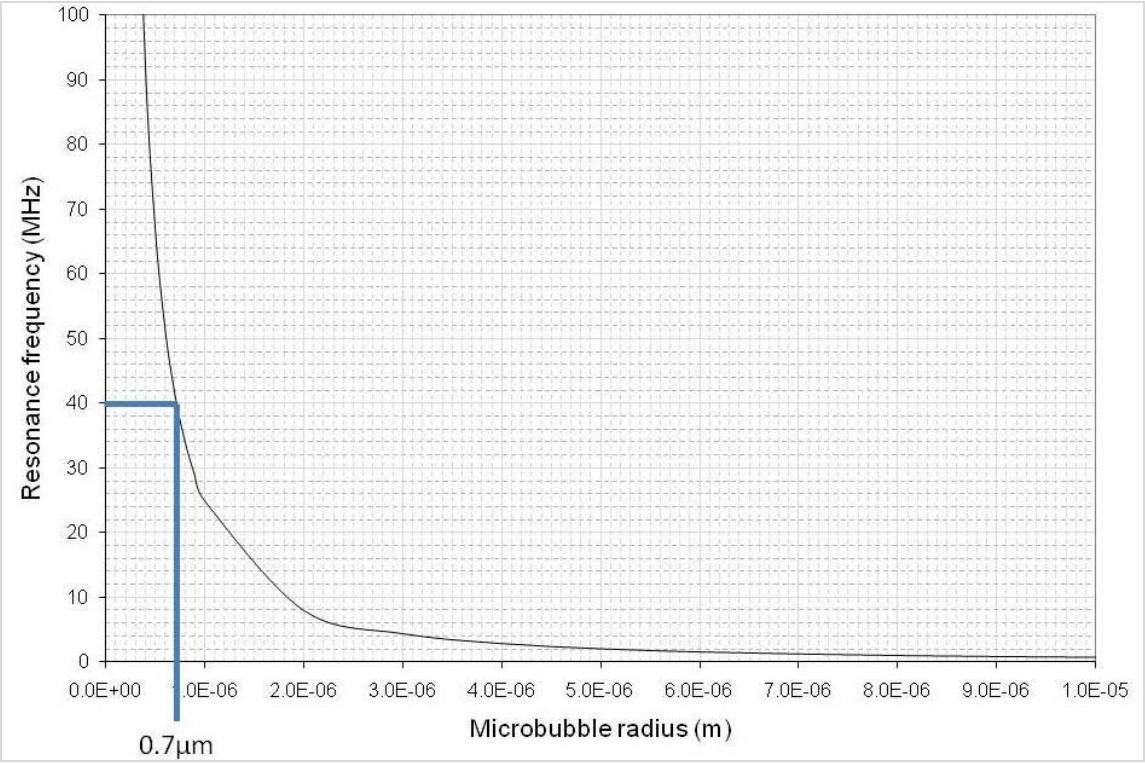

Figure A-1: Resonance against frequency.

Appendix B Radio Frequency Data Analysis

Radio frequency data was collected using a program developed in LabView (National Instruments, USA). A screen shot of the program user interface is shown in Figure B-1. This allows the various controls of the digitizing card (Gage Applied CS8500, Gage Applied Technologies, Lachine, Canada) to be adjusted to the optimum settings for use with the IVUS scanner. The data captured by the card is stored as unformatted raw binary data as a '.sig' file.

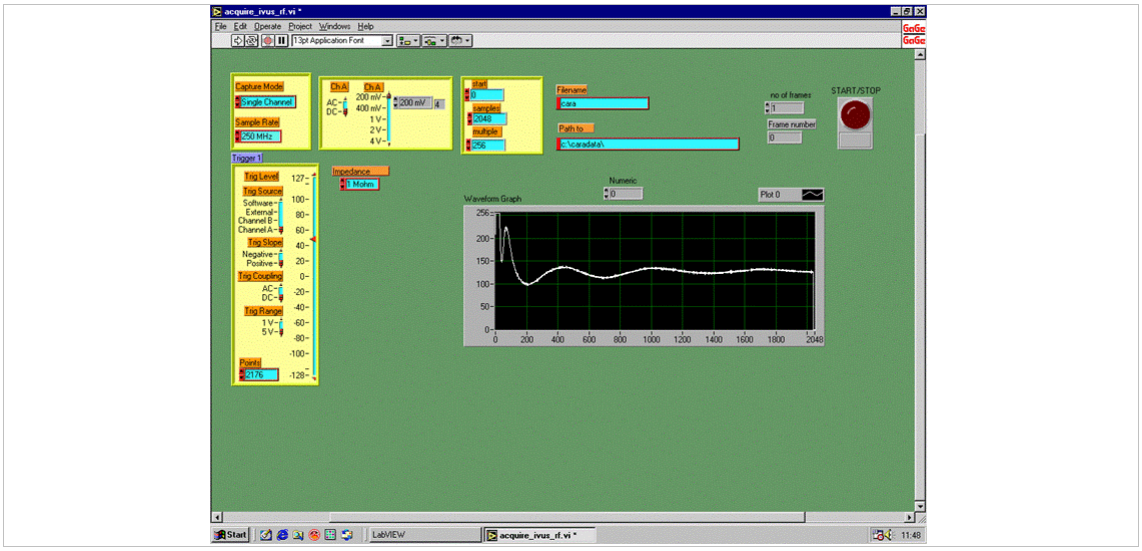

Figure B-1: Screen Shot of LabView software.

Once RF data has been collected in LabView for all microbubble samples the RF signal from a standard reflector is collected. Collection of reflector data is outlined in Appendix C. The raw data is then scan converted using a program written in IDL as explained in Chapter 3. This program outputs a bitmap image of the raw data as illustrated in Figure B-2 and a scan converted image as illustrated in Figure B-3.

Figure B-2: Bitmap image of raw RF data.

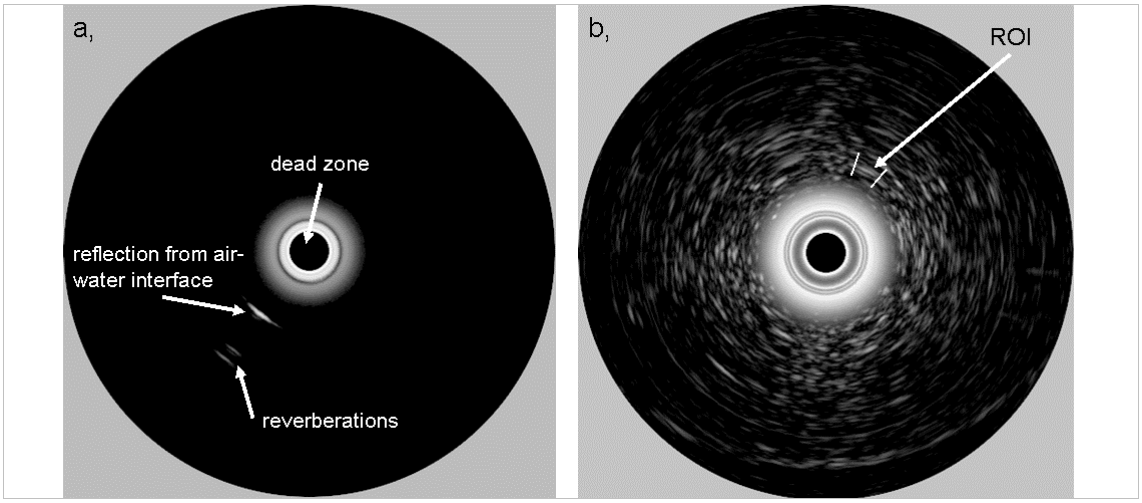

Figure B-3: Scan converted images a, of a perfect reflector showing bright reflection and reverberations and b, of a contrast sample showing a selected region of interest.

After the RF data has been scan converted the 'reflector' program is run. This allows the user to select the reflection from the air-water interface (identified on Figure B-3a) using a cursor; the program then determines the peak signal within that region and fast Fourier transforms (FFT) the raw data, saving it to a data file for comparison with sample data, in addition the power spectrum is shown on screen.

Analysis is carried out using a further IDL program called 'Analyse_ROI.pro' program. This allows the user to select which reflector data the file should be compared to and to select a region of interest (ROI) within the sample scan converted image using either the cursor or co-ordinates, as illustrated in Figure B-3b. When collecting data from contrast samples co-ordinates were used to select the ROI in order to maintain continuity. Once

the program has run, a text file is output with a number of computed values including the mean, maximum and minimum backscatter power for the ROI.

The mean backscatter power was used throughout this thesis to compare the echogenicity of microbubble samples.

Appendix C Collection of Perfect Reflector Data

The reflector data used in the analysis of mean backscatter was collected from an air-water interface. In order to accurately analyse sample data it was necessary to achieve the brightest reflection from the interface. The optimum reflection was observed when the ultrasound beam was perpendicular to the surface. Due to the angle of the transducer within the catheter it was necessary to maintain a 12° angle between the catheter and the air-water interface. The optimum angle was determined from a visual study of the brightness of the echo at varying angles in addition to maximising the number of multiple reflections from the air-water interface. The accuracy of this could have been further improved through use of a hydrophone, however one was not available initially and in order to maintain continuity it was decided that a visual assessment was to be used throughout.

C.1 Method:

A micromanipulator (Narishige, Japan) was used to position the transducer at the optimum angle and 2mm depth from the air-water interface. This set up can be seen in Figure C-1.

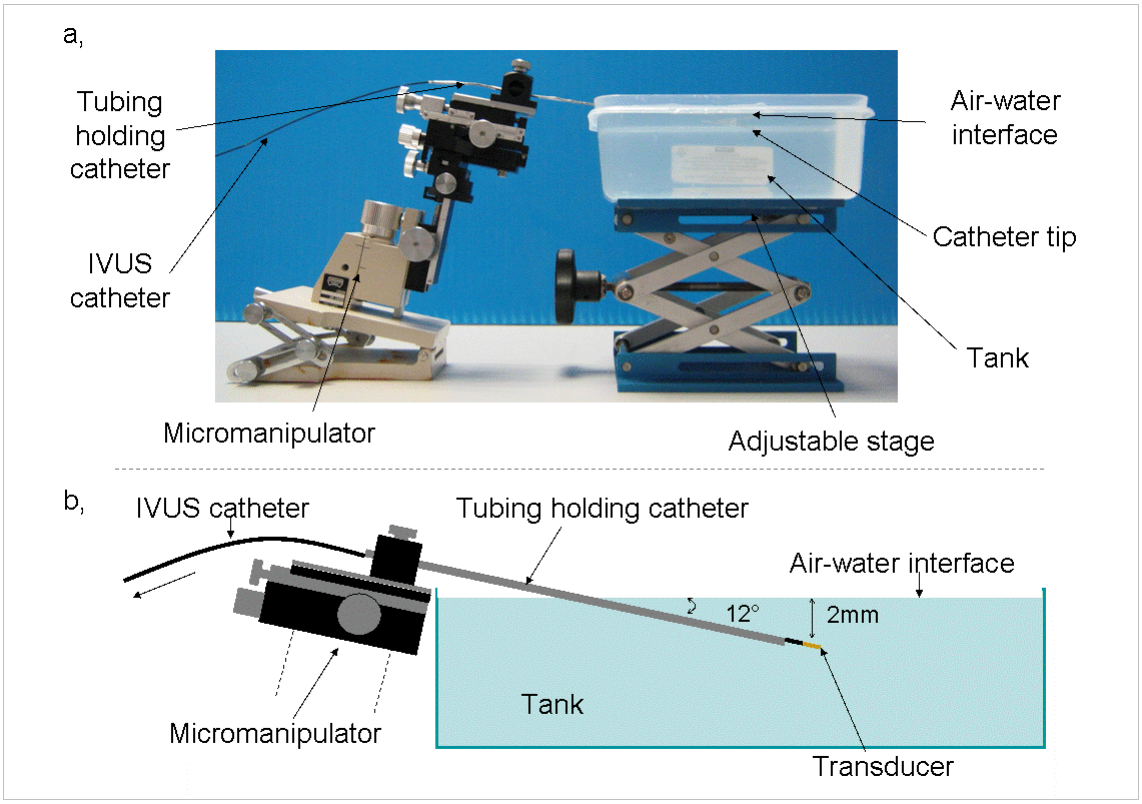

Figure C-1: Reflector data collection a, photograph of set-up detailing equipment and b, schematic of set-up illustrating angle and depth of transducer (not to scale).

Perfect reflector calibration data was collected after each set of contrast evaluation scans to take into account any variations in transducer performance. In order to determine reproducibility of the reflector data three sets of RF data were collected in one day with the equipment being taken apart and reconstructed for each data collection. The RF data was then collected for a random sample. The same co-ordinate of the microbubble sample was then analysed against each perfect reflector data to evaluate any variations in the perfect reflector data. This was repeated with a different sample of microbubbles to produce two sets of data.

C.2 Results:

The mean backscatter from the sample collected for each reflector can be seen in Figure C-2. The first data set collected had an average backscatter of -44.09(±0.88)dB with a range of 1.63dB, the second data set had an average backscatter of -41.13(±0.65)dB with a range of 1.28dB. The small range of the data collected confirms the reproducibility of the perfect reflector data.

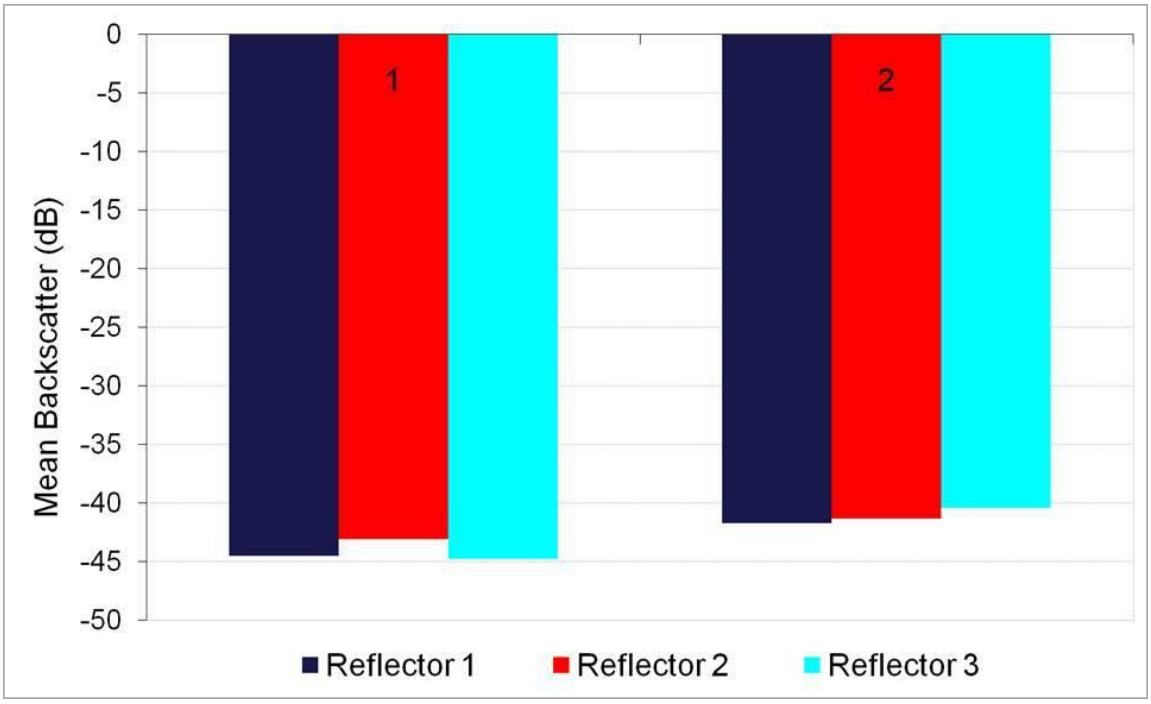

Figure C-2: Mean backscatter comparison for two sets of reflector data.

In conclusion, visual assessment of the perfect reflector data is reproducible to within a deviation of approximately 1dB. Visual determination of the brightest reflection is a suitable method of collecting reflector data and was used throughout this thesis in order to determine the echogenicity of microbubble samples.

Appendix D In-house microbubble protocol

Production of the in-house microbubble UCA was optimised in Chapter 3. A variety of techniques were investigated. These techniques included; agitation, sonication, high shear mixing, varying production temperatures and altering the lipid composition of the microbubble shell. The optimised production procedure involved high shear mixing of the initial lipid solution and agitation of the microbubble suspension. This procedure is outlined below.

D.1 Lipids:

The optimal lipid composition determined in Chapter 3 was the 30% cholesterol composition. Therefore the ratio of lipids used throughout this thesis was 56:30:11:3 (PC:Chol:PE:PG). Each 100mg of lipids is dissolved in 4ml saline.

When incorporating biotin into the microbubble shell for antibody attachment the following composition was used: 56:30:6:3:5 (PC:Chol:PE:PG:Biotinylated PE).

D.2 Procedure:

1. Prepare a hot water bath set to 78°C.
2. Weigh out dry lipids and dissolve in saline.
3. Homogenize lipids in solution using a hand held high-shear mixer for one minute.
4. Place flask containing lipid solution into hot water bath and set up stirrer to 1000rpm and attach condenser. Leave lipids to heat for one hour.
5. Remove microbubbles from water bath and agitate vigorously for 45s.
6. Store microbubbles for up to 3 months in glass container at 2-5°C.

Appendix E Flow volume calibration

Flow through the flow chamber was controlled by a pump (Micropumps Ltd, UK) which in turn is controlled by a power supply (Eagle Power Ltd, UK). In order to accurately assess the flow volumes through the flow chamber it was necessary to calibrate the power supply. This was achieved by measuring the flow volumes over a one minute period at varying voltage settings.

E.1 Method

Flow chamber was clamped together and tubing attached. Following this, the voltage of the power supply was increased in 5V intervals and flow volume measured at each interval. This was repeated four times for each voltage interval and for the four different viscosity fluids identified in Chapter 4.

E.2 Measurement of flow volumes

Flow volumes at each voltage interval were measured using a measuring cylinder. Flow through the flow chamber was collected in a measuring cylinder for one minute. This was repeated three times. In addition repeat measurements of the flow volume were collected on different days due to environmental effects upon this parameter such as temperature and pressure. The average was calculated from all data sets.

E.3 Results

The calibration graph can be seen in Figure E-1. Flow volume increases linearly with the pump voltage, the Microsoft Excel (Microsoft®, USA) linear trend line has been used to determine correlation of the data.

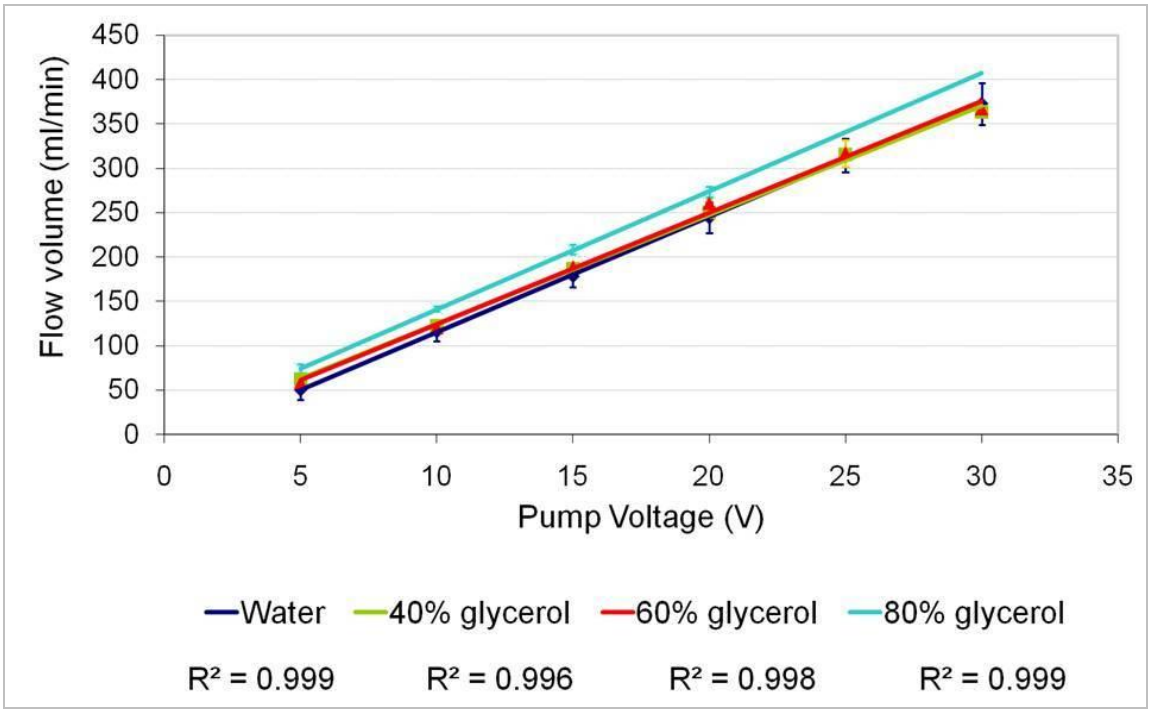

Figure E-1: Flow volumes produced at varying voltages. Error bars represent one standard deviation.

A calibration table was produced by interpolation of the above data using the Microsoft Excel trend line function. Table E-1 suggests the necessary voltages needed to produce required flow volumes. Since flow volumes can vary dependant upon environmental conditions a calibration check was carried out at the beginning of each investigation to confirm the flow volumes achieved and necessary adjustments carried out.

Flow volume (ml/min)	Voltage required to achieve flow volume (V)			
	Water	40% glycerol	60% glycerol	80% glycerol
60	5.8 ± 0.38	4.8 ± 0.41	4.9 ± 0.40	3.9 ± 0.38
80	7.3 ± 0.38	6.4 ± 0.41	6.5 ± 0.40	5.4 ± 0.38
100	8.8 ± 0.38	8.0 ± 0.41	8.1 ± 0.40	6.9 ± 0.38
120	10.4 ± 0.38	9.7 ± 0.41	9.7 ± 0.40	8.4 ± 0.38
140	11.9 ± 0.38	11.3 ± 0.41	11.3 ± 0.40	9.9 ± 0.38
160	13.4 ± 0.38	12.9 ± 0.41	12.9 ± 0.40	11.4 ± 0.38
180	15.0 ± 0.38	14.5 ± 0.41	14.5 ± 0.40	12.9 ± 0.38
350	28.1 ± 0.38	28.4 ± 0.41	28.0 ± 0.40	25.7 ± 0.38

Table E-1: Calibration table for pump.

Appendix F Flow Profiles

Figure F-1 shows some flow profiles collected in the z-plane in order to determine the location of the centre of the flow channel, determined as the location of the peak velocity. This technique was used to set up the LDA rig to measure the flow profile adjacent to the agar surface. The variations observed at the sides of the chamber are due to reflections from the edges of the flow channel. These flow profiles suggest a central co-ordinate of 5mm.

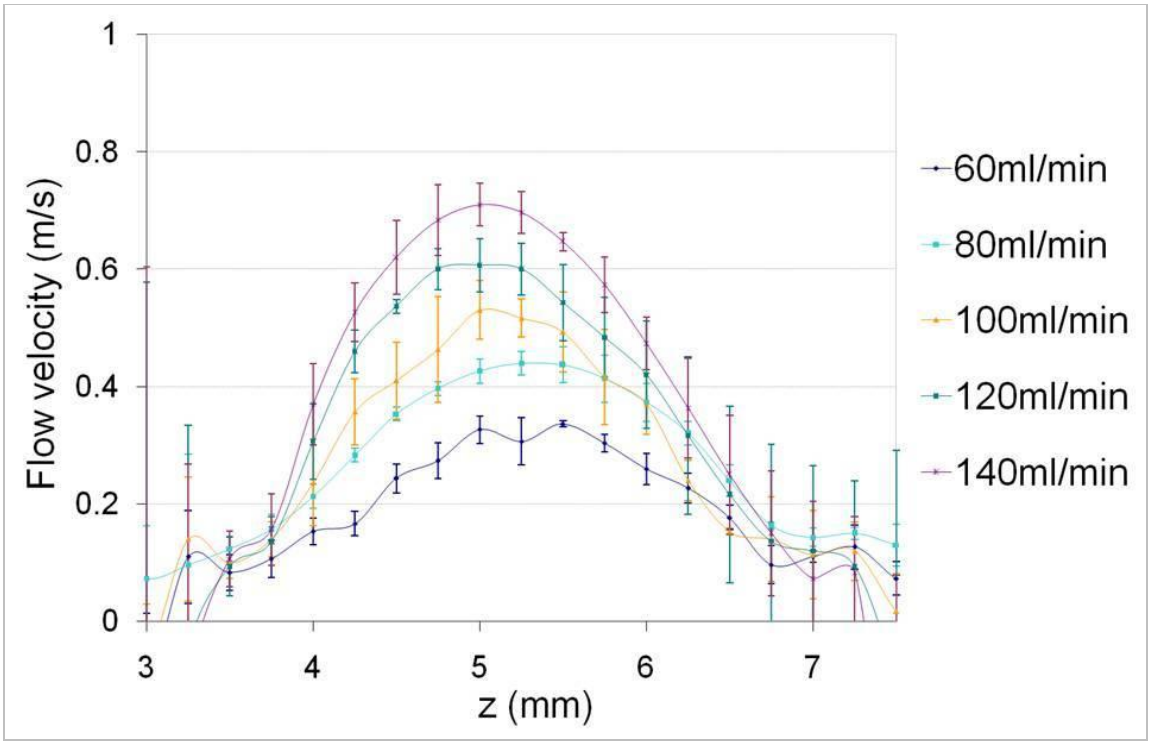

Figure F-1: Flow profiles used to set up central location of LDA.

Figure F-2 shows the three dimensional flow profiles produced by CFD analysis of the flow chamber described in Chapter 4.

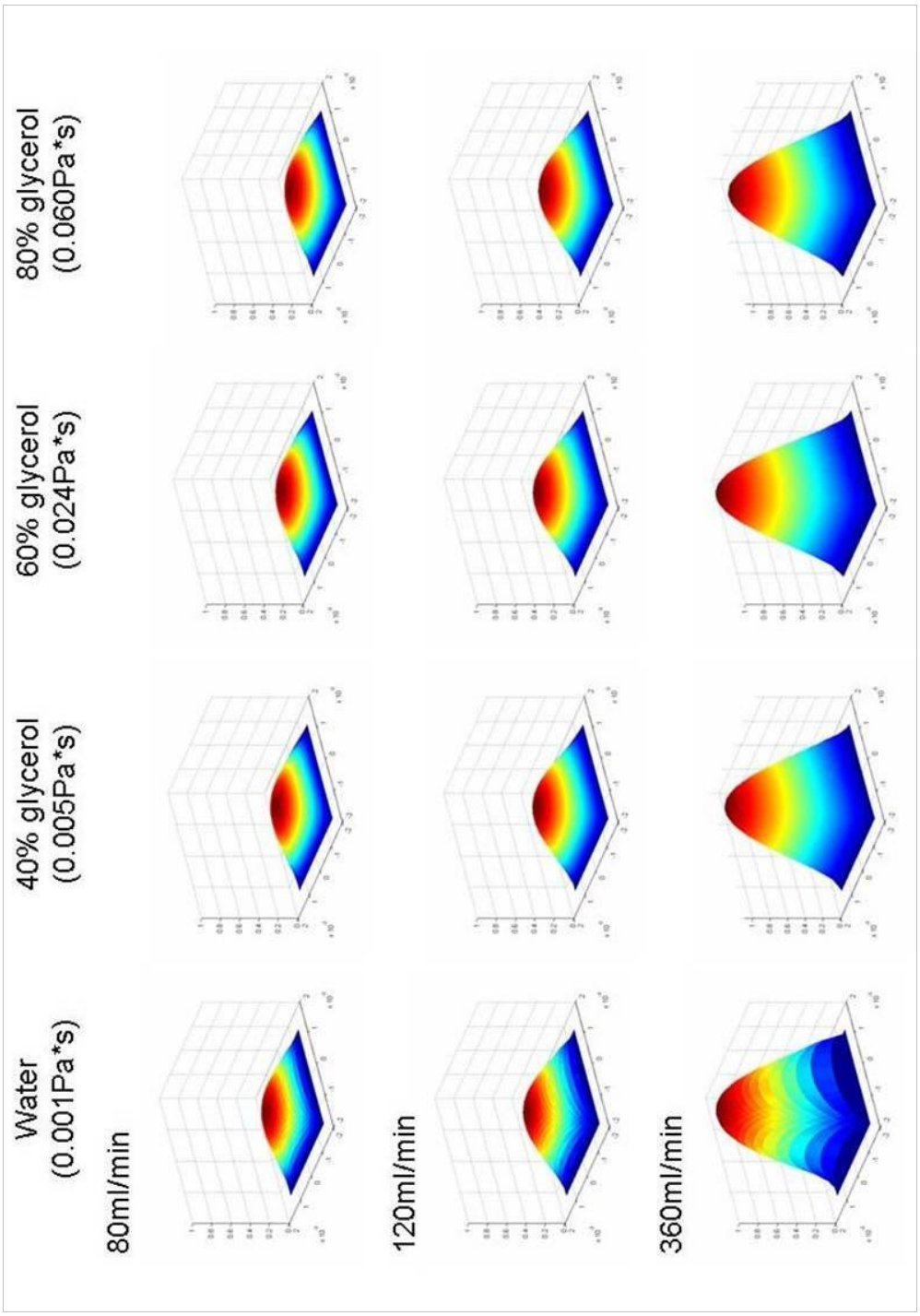

Figure F-2: Three dimensional CFD flow profiles at observation region for flow chamber.

Appendix G Calculation of Microbubble Concentration

A cell counting technique has been used in order to determine the microbubble concentration. The microbubbles were diluted, with a dilution factor of 100, and introduced to a Neubauer chamber as illustrated in Figure G-1.

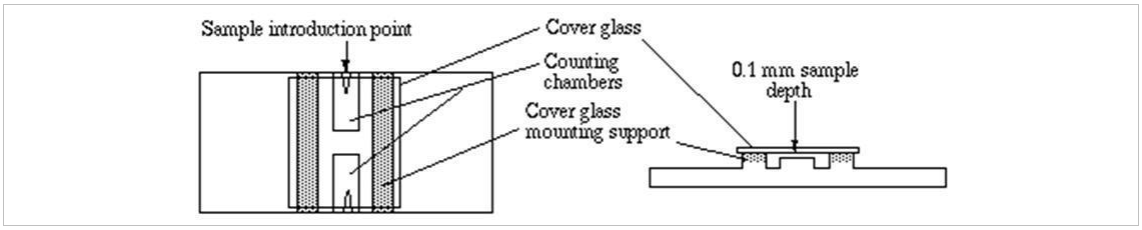

Figure G-1: Neubauer chamber (reprinted with permission from David Caprette (Caprette 2000)).

The microbubbles within the large central grid, illustrated in Figure G-2, were counted for each side of the chamber and the average determined.

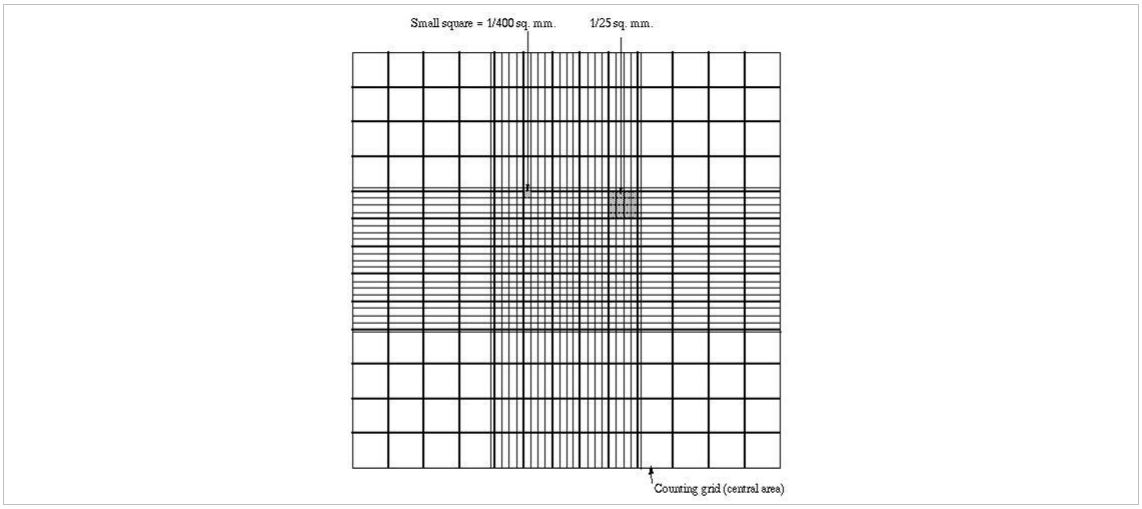

Figure G-2: Counting grid of Neubauer chamber as observed under microscope (reprinted with permission from David Caprette (Caprette 2000)).

Equation G-1 was then used to calculate the concentration of microbubbles.

$$[microbubble] = Mb_{total} \times D \times 10^4$$

Equation G-1: Microbubble concentration calculation (Perez 2006).

Where [*microbubble*] is the microbubble concentration, MB_{total} is the total average microbubble count and *D* is the dilution factor.

Appendix H Agar Production

The following protocol was used for production of agar throughout this thesis. Agar was poured into a suitable mould and then cut to size for the flow chamber in Chapter 4.

H.1 Ingredients (% by mass)

- De-mineralised water (82.40)
- Glycerol (99% solution) (11.32)
- Benzalkonium Chloride (50% solution) (0.92)
- Agar (3.00)

H.2 Method

1. Combine all ingredients in a fume hood.
2. De-gas the solution to remove any air bubbles.
3. Heat to 96℃ for one hour in a water bath. Stir throughout.
4. Cool to 42℃ and pour into mould or container.

Appendix I Calculation of Cellular Confluence

Cellular confluence is the area of a surface to which cells are seeded, presented as a percentage. In order to accurately and repeatedly quantify the confluence of cells seeded to a variety of surfaces, bright-field microscopic images were collected and overlaid with a grid as illustrated in Figure I-1. The confluence was then calculated from Equation I-1 below.

$$Confluence\,(\%) = \frac{N_x}{N_{total}} \times 100$$

Equation I-1: Calculation of cellular confluence.

Where N_x is the number of grid squares with cell matter in and N_{total} is the total number of grid squares.

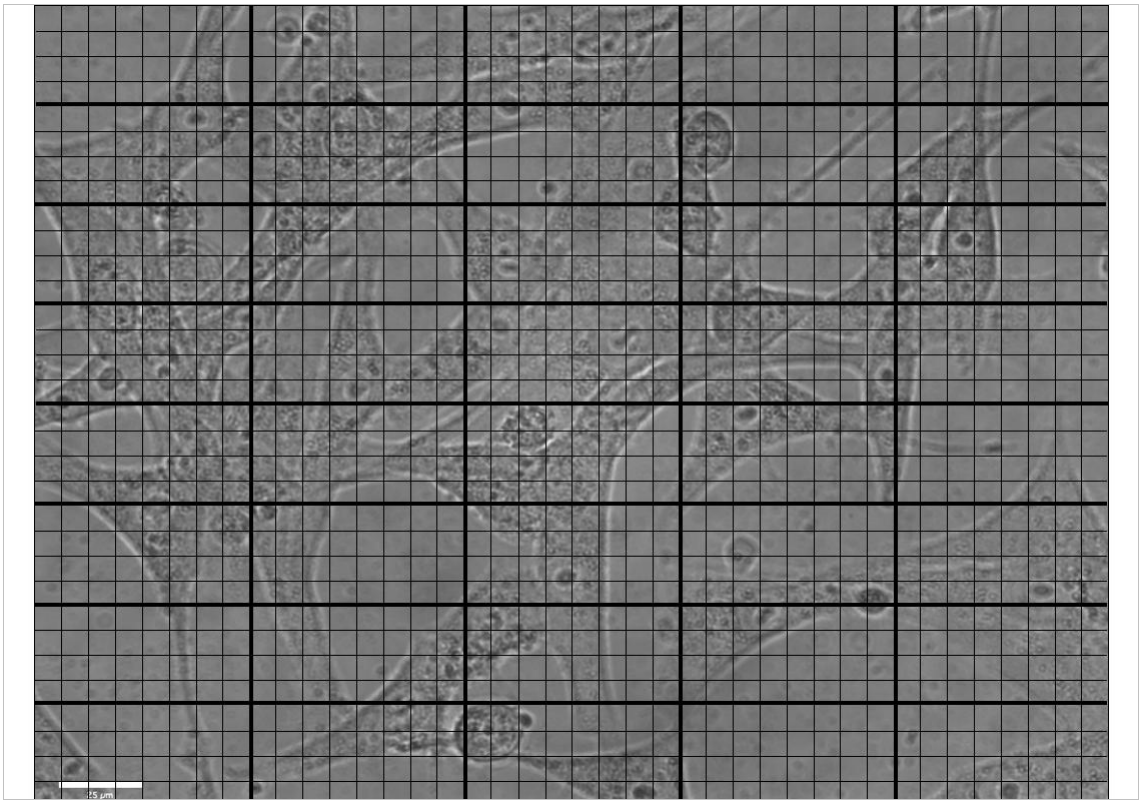

Figure I-1: Microscopic image (×400 magnification) overlaid with confluence grid.

Appendix J Preparation of Ibidi µ-slides

J.1 Seeding cells within µ-slides

Cell concentration was determined using the cell counting procedure outlined in Appendix G for calculation of microbubble concentrations. Once the cell concentration had been calculated they were added to warmed medium (37°C) to produce a $3\times10^{5}ml^{-1}$ concentration as per manufacturer's recommendations.

The cell containing medium was then injected into the flow channel of the µ-slides with 1ml syringes as illustrated in Figure J-1. The slides used for the experiments in this thesis are described and illustrated in Chapter 8, Section 8.4.

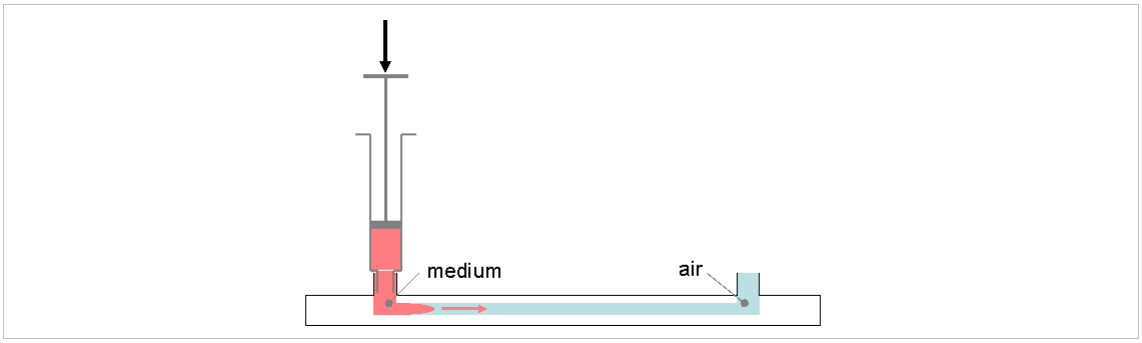

Figure J-1: Injecting cellular medium into Ibidi µ-slides.

J.2 Replacing medium

If the cells did not reach 50% confluence after 24 hours it was necessary to replace the medium to allow the cells longer to reach a suitable confluence for the experiments. This was achieved by adding 5% fetal calf serum to the medium, by volume, and replacing the medium as illustrated in Figure J-2.

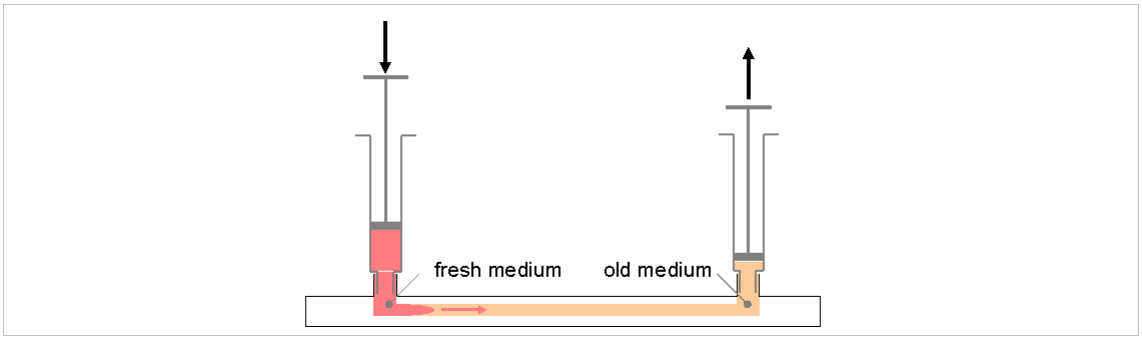

Figure J-2: Replacing medium in flow slides.

Care had to be taken when injecting medium into the flow slides to prevent the accumulation of bubbles. If bubbles did form when adding medium it was possible to remove them by gently tapping the bottom of the slide, however this technique was not ideal to use when cells had already been seeded within the slides as this could cause cells to detach from the surface.

Appendix K Diasus Characterisation and Determination of Acoustic Radiation Force Parameters

It was necessary to characterise the Diasus scanner used to facilitate microbubble attachment to cells in Chapter 9 to determine the force and other factors which the microbubbles were subjected to. The Diasus scanner was characterised using the same equipment described in Chapter 5 for IVUS characterisation.

K.1 Method

The hydrophone was anchored in place, level, using a specially designed holder on top of a piece of acoustic absorber. The transducer used in Chapter 9 was clamped above the hydrophone and could be moved up and down. The set-up is illustrated in Figure K-1.

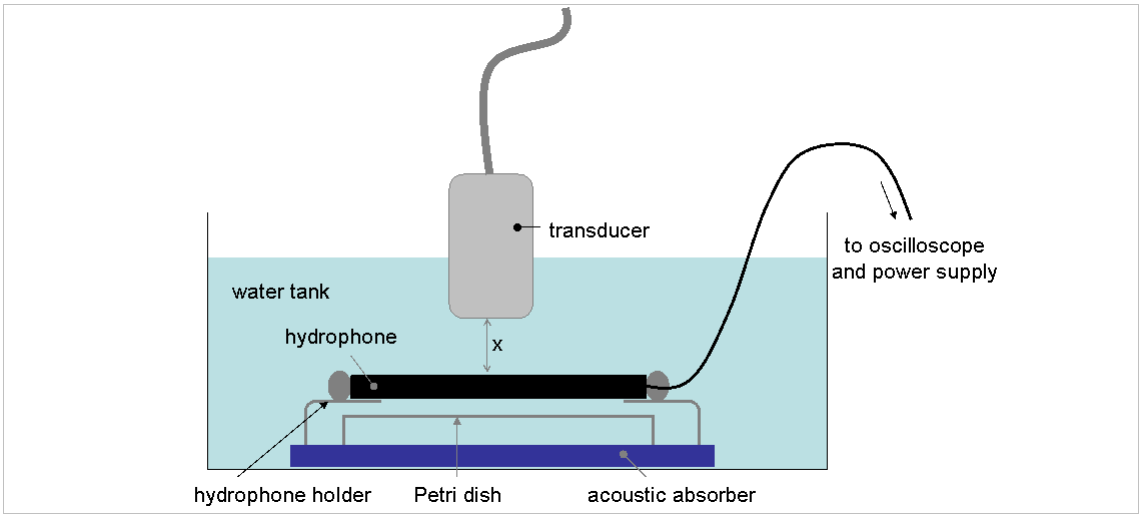

Figure K-1: Diasus characterisation, experimental set-up.

The hydrophone was levelled using a spirit level and transducer was levelled using the callipers on the scanner and making sure that there was an equal distance between the

transducer and hydrophone face at either end of the transducer. This is illustrated in Figure K-2.

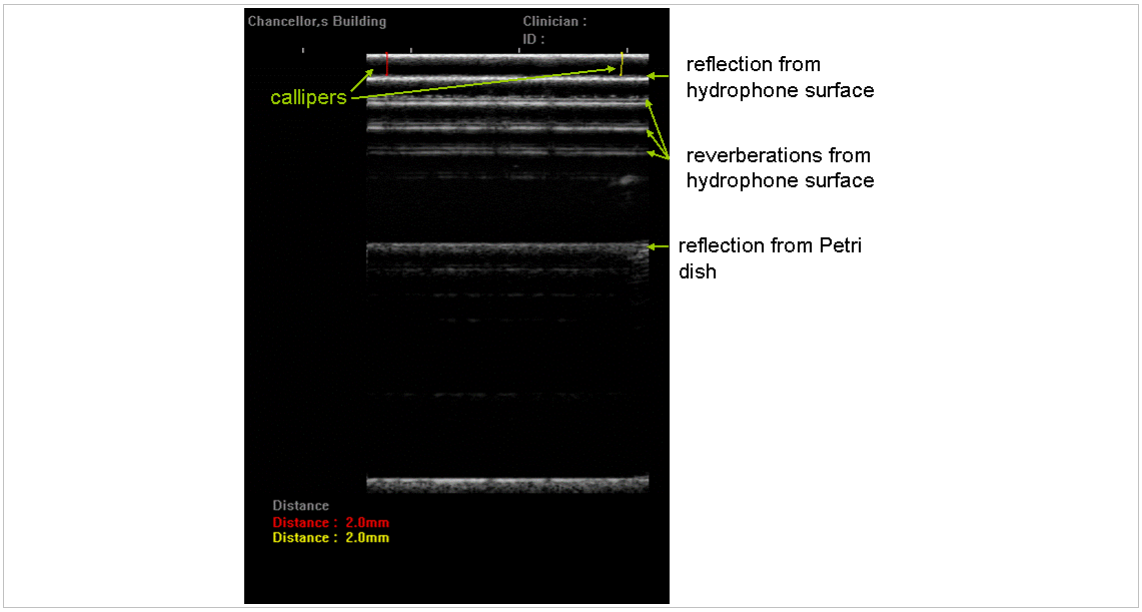

Figure K-2: Using callipers on Diasus scanner to ensure that transducer was parallel to the hydrophone.

The signals produced by the hydrophone were collected using the oscilloscope for distances of 2, 4, 6, 8 and 10mm from the transducer face. Distances were measured using the callipers on the scanner. It was not possible to collect data for smaller distances than 2mm due to the risk of damage to the fragile hydrophone membrane. The investigation was then repeated placing a Petri dish base-up 16mm from the bottom of the hydrophone to investigate the effects of the plastic surface on the waveform. This was the closest it was possible to get the Petri-dish to the hydrophone.

The entire investigation was repeated four times over the course of two weeks.

In addition to peak negative pressures, calculated using Equation 5-1, waveforms over a greater time scale were collected in order to determine the pulse repetition frequency (PRF) and pulse duration.

K.2 Results

The variation in Peak negative pressure can be seen in Figure K-3. The peak negative pressure decreases as the distance between the hydrophone and transducer increases, with the exception of a large increase in pressure at 4mm when the Petri dish was placed beneath the hydrophone. The author and colleagues believe that this change in pressure is the result of standing waves being formed on reflection of the ultrasound from the Petri dish plastic. Since this occurred at 4mm from the transducer face it was assumed that the suspected presence of standing waves had no effect on the forces acting on the microbubbles as calculated in Chapter 9 due to the distance between transducer and plastic surface being 2mm.

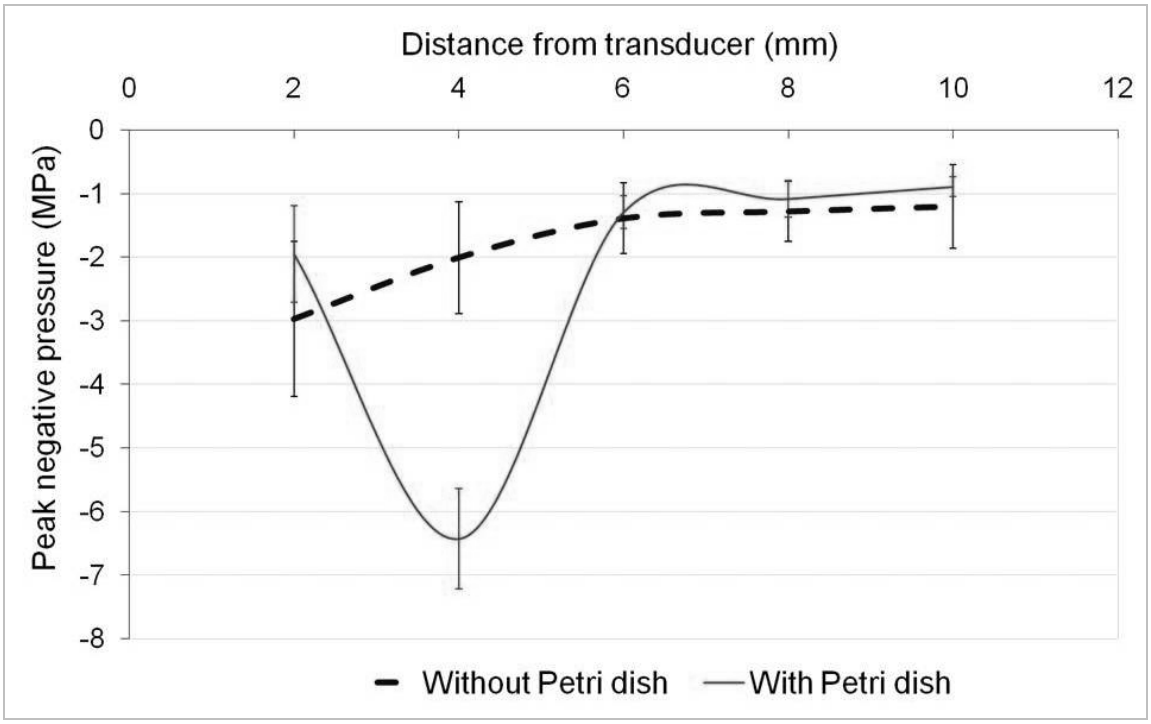

Figure K-3: Peak negative pressure as a function of distance from transducer face.

The PRF was calculated from Equation K-1, where *T* was the time between the start of each pulse. Measurement of T is shown in Figure K-4. The PRF was found to be $3.5(\pm 0.2)\times 10^{-4} s^{-1}$ (n=3).

$$PRF = \frac{1}{T}$$

Equation K-1: PRF

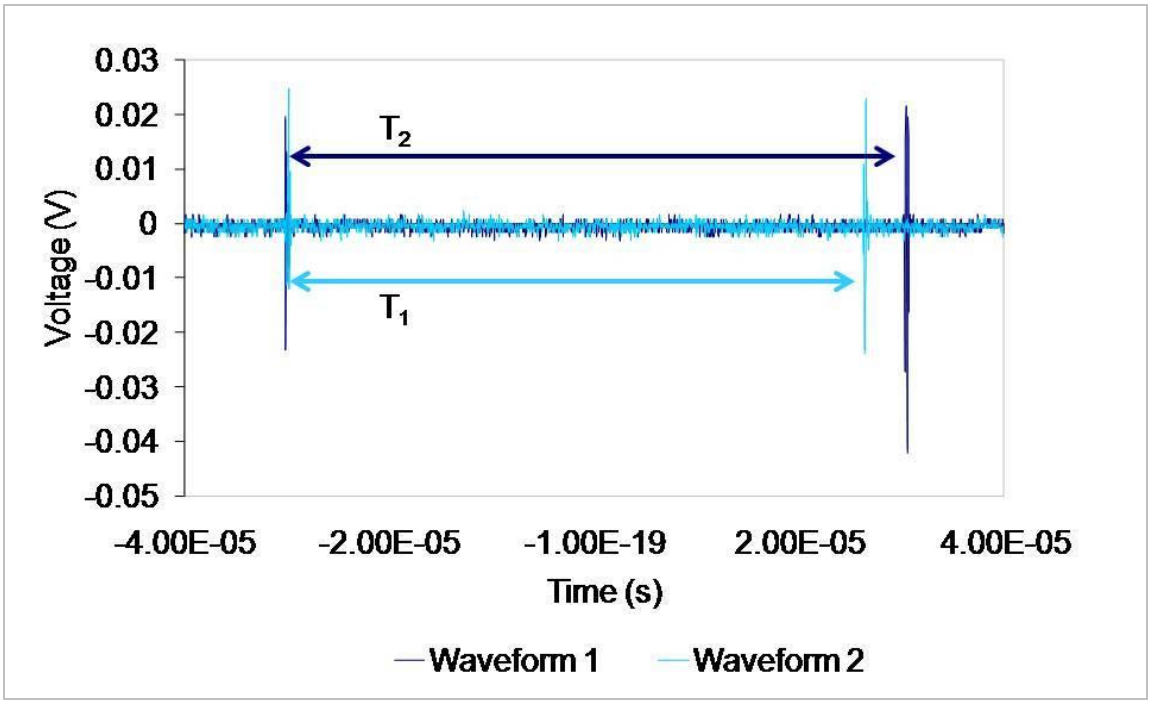

Figure K-4: Determination of T.

Finally the pulse duration (D) was determined from the waveforms as illustrated in Figure K-5. The pulse duration was determined to be 0.24(±0.08)µs (n=9).

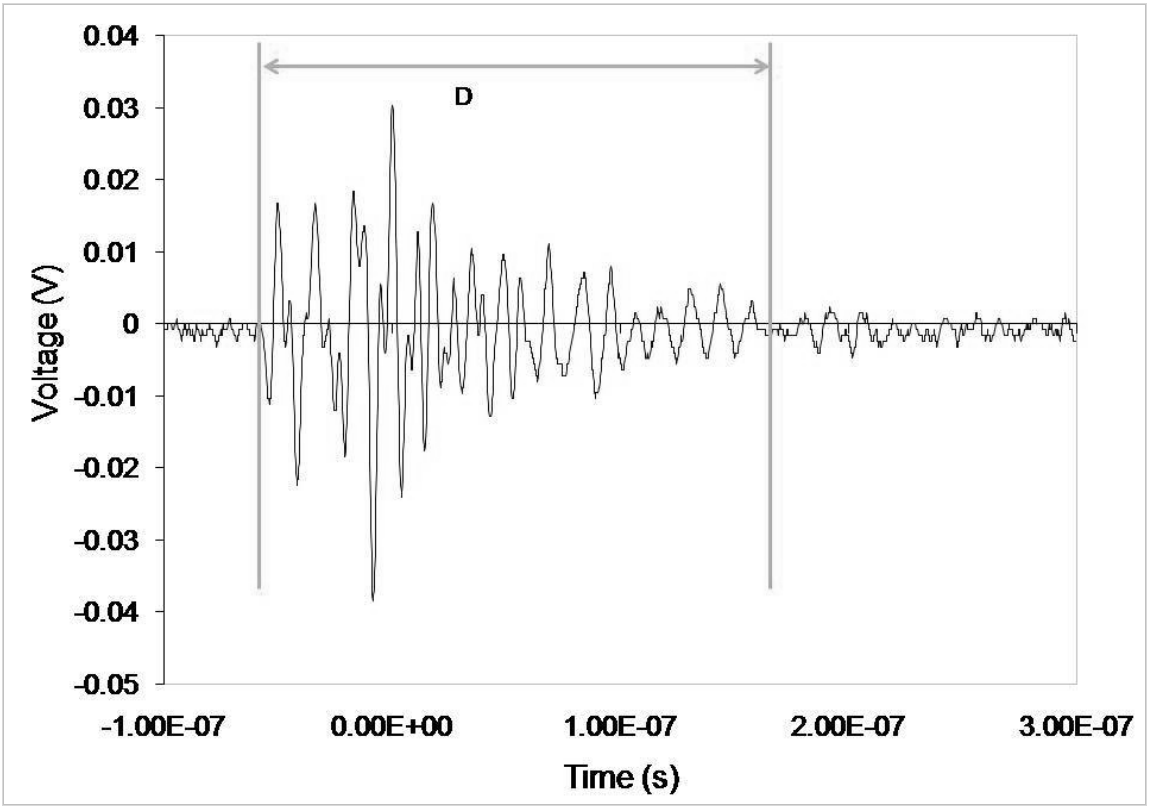

Figure K-5: Determination of D.

Conferences and Publications

Abstracts accepted for presentation at national and international conferences:

'*Characterization of a High Frequency In-house Ultrasound Contrast Agent*', Adele Edgeworth, Carmel Moran, Jim Ross, Mairead Butler, Tom Anderson and Norman McDicken, Scottish Society for Experimental Medicine Annual Meeting 2007, Glasgow. Poster presentation.

'*Laser Doppler Anemometry, a Method to Assess the Targeting Strength of an In-house, Targeted, Microbubble, Ultrasound Contrast Agent*' AL Edgeworth, JA Ross, T Anderson, MB Butler, WJ Easson, WN McDicken and CM Moran, British Medical Ultrasound Society Annual Scientific Meeting 2008, Liverpool. Poster presentation.

'*A method for assessing the strength of an avidin-biotin attachment mechanism of a targeted, high-frequency, in-house microbubble ultrasound contrast agent*.' Adele Edgeworth, Mairead Butler, Jim Ross, Tom Anderson, Linda Norrie, Norman McDicken and Carmel Moran. Fourteenth European Symposium on Ultrasound Contrast Imaging 2009, Rotterdam, The Netherlands. Oral presentation.

Conference papers:

'*Strength of Attachment of an in-house Ultrasound Contrast Agent*', A.L. Edgeworth, T. Anderson, J.A. Ross, I.F. Ansell, M. Butler, L. Norrie, W.N. McDicken, C.M. Moran. IEEE International Ultrasonics Symposium 2009, Rome, Italy. Defended in a poster presentation.

Papers accepted for publication to BMUS Ultrasound Journal

'Novel Flow Chamber to Investigate Binding Strength of a Lipid-Based, High-Frequency, Ultrasonic Contrast Agent', A.L. Edgeworth, T. Anderson, J.A. Ross, M. Butler, W.N. McDicken, C.M. Moran. Awaiting publication .

References

4-Antibody. 'Antibodies Overview.' (http://www.4-antibody.com/index.htm) November 2009.

Ali M, Magee D and Dasgupta U. Signal Processing Overview of Ultrasound Systems for Medical Imaging. (2008) Retrieved May 2010, 2010.

Alvarez Sanchez MV, Varadarajulu S and Napoleon B. EUS contrast agents: what is available, how do they work, and are they effective? Gastrointestinal Endoscopy (2009); 69(2, Supplement 1): S71-S77.

Anderson CR, Rychak JJ, Backer JM, Backer MV, Ley K and Klibanov AL (2009). Covalent Coupling of Targeting Ligands to the Microbubble Surface: Design Logic for scVEGF-Microbubbles. Fourteenth European Symposium on Ultrasound Contrast Imaging, Rotterdam, The Netherlands, Erasmus MC.

Arronson P, Ward J and Wiener C. The Cardiovacular System at a Glance. Oxford: Blackwell Publishing, 2004.

Avanti Polar Lipids Inc. 'Avanti Catalogue 2008.' (http://www.avantilipids.com) December 2008.

Bacabac RG, Smit TH, Cowin SC, Van Loon JJWA, Nieuwstadt FTM, Heethaar R and Klein-Nulend J. Dynamic shear stress in parallel-plate flow chambers. Journal of Biomechanics (2005); 38(1): 159-67.

Ban N, Escobar C, Garcia R, Hasel K, Day J, Greenwood A and McPherson A. Crystal structure of an idiotype-anti-idiotype Fab complex. Proc. Nati. Acad. Sci. USA (1994); 91: 1604-08.

Barnett SB and Kossoff G. Safety of Diagnostic Ultrasound (Progress in Obstetric & Gynecological Sonography). London: Taylor & Francis, 1997.

Baun J. Interaction with Soft Tissue. Physical principles of General and Vascular Ultrasonography. San Francisco, ProSono. (2009): 230.

Bekeredjian R, Chen S, Grayburn PA and Shohet RV. Augmentation of cardiac protein delivery using ultrasound targeted microbubble destruction. Ultrasound in Medicine & Biology (2005a); 31(5): 687-91.

Bekeredjian R, Grayburn PA and Shohet RV. Use of ultrasound contrast agents for gene or drug delivery in cardiovascular medicine. Journal of the American College of Cardiology (2005b); 45(3): 329-35.

British Heart Foundation Health Promotion Research Group. 'Coronary Heart Disease Statistics.' 25th March 2007.

Bierig SM and Jones A. Accuracy and Cost Comparison of Ultrasound Versus Alternative Imaging Modalities, Including CT, MR, PET, and Angiography. Journal of Diagnostic Medical Sonography (2009): 8756479309336240.

Biondi-Zoccai G. www.metcardio.org/ppts/2007/vulnerable-coronary-plaque.ppt. www.metcardio.org.(2006).

Blasi C. The autoimmune origin of atherosclerosis. Atherosclerosis (2008); In Press, Corrected Proof.

British Medical Ultrasound Society; Safety Group. 'BMUS Guidelines for the Safe Use of Diagnostic Ultrasound Equipment.' (http://www.bmus.org/policies-guides/pg-safety03.asp) October 2008.

Bom N, Lancée C, Honkoop J and Hugenholtz P. Ultrasonic viewer for cross-sectional analyses of moving cardiac structures. Biomedical Engineering (1971); 6(11): 500-3.

Borsboom JMG, Chin CT and de Jong N. Nonlinear coded excitation method for ultrasound contrast imaging. Ultrasound in Medicine & Biology (2003); 29(2): 277-84.

Brown BH, Smallwood RH, Barber DC, Lawford PV and Hose DR. Medical Physics and Biomedical Engineering. Bristol: Institute of Physics, 1999.

Browne JE, Watson AJ, Gibson NM, Dudley NJ and Elliott AT. Objective measurements of image quality. Ultrasound in Medicine & Biology (2004); 30(2): 229-37.

Butler M. High Frequency Ultrasonic Imaging of Targeted Microbubble Contrast Agents Under Controlled Shear Stress. Medical Physics: The University of Edinburgh, Edinburgh. (2005), Doctor of Philosophy: (189).

Butler MB, Moran CM, Anderson T, Cunningham C, Ross JA, Easson WJ, Fox KAA and McDicken WN. Laser Doppler anemometry measurements of the shear stresses on ultrasonic contrast agent microbubbles attached to agar. Ultrasound in Medicine & Biology (2005); 31(4): 545-52.

Calliada F, Campani R, Bottinelli O, Bozzini A and Sommaruga MG. Ultrasound contrast agents: Basic principles. European Journal of Radiology (1998); 27(Supplement 2): S157-S60.

Cantrell GL. Novel Ultrasound Contrast Agents.(2000) US, Mallinckrodt Inc.

Caprette D. Experimental Sciences. Using a Counting Chamber.(2000), Rice University.

Chatterjee D and Sarkar K. A Newtonian rheological model for the interface of microbubble contrast agents. Ultrasound in Medicine & Biology (2003); 29(12): 1749-57.

Cheng C, Helderman F, Tempel D, Segers D, Hierck B, Poelmann R, van Tol A, Duncker DJ, Robbers-Visser D, Ursem NTC, van Haperen R, Wentzel JJ, Gijsen F, van der Steen AFW, de Crom R and Krams R. Large variations in absolute wall shear stress levels within one species and between species. Atherosclerosis (2007a); 195(2): 225-35.

Cheng YC, Shen CC and Li PC. Nonlinear pulse compression in pulse-inversion fundamental imaging. Ultrasonic Imaging (2007b); 29(2): 73-86.

Chilkoti A and Stayton PS. Molecular Origins of the Slow Streptavidin-Biotin Dissociation Kinetics. Journal of the American Chemical Society (2002); 117(43): 10622-28.

Chun Yuan WSK. MRI of atherosclerosis. Journal of Magnetic Resonance Imaging (2004); 19(6): 710-19.

Church CC. The effects of an elastic solid surface layer on the radial pulsations of gas bubbles. The Journal of the Acoustical Society of America (1995); 97(3): 1510-21.

Church CC. Spontaneous homogeneous nucleation, inertial cavitation and the safety of diagnostic ultrasound. Ultrasound in Medicine & Biology (2002); 28(10): 1349-64.

Clinical Safety Statement for Diagnostic Ultrasound. ECoMUS (ECMUS).(2006).

Combs GF. The Vitamins: Fundamental Aspects in Nutrition and Health. San Diego: Academic Press, 1992.

Texas Heart Institute. 'Heart Information Centre.' (http://www.texasheart.org/AboutUs/index.cfm) October 2008.

Correas J-M, Bridal L, Lesavre A, MØjean A, Claudon M and HØlØnon O. Ultrasound contrast agents: properties, principles of action, tolerance, and artifacts. European Radiology (2001); 11: 1316-28.

Cosgrove D. Echo enhancers and ultrasound imaging. European Journal of Radiology (1997); 26(1): 64-76.

Cosgrove D. Ultrasound contrast agents: An overview. European Journal of Radiology (2006); 60(3): 324-30.

Crouse JR, Goldbourt U, Evans G, Pinsky J, Sharrett AR, Sorlie P, Riley W and Heiss G. Arterial enlargement in the atherosclerosis risk in communities (ARIC) cohort. In vivo quantification of carotid arterial enlargement. The ARIC Investigators. Stroke (1994); 25(7): 1354-59.

Culp WC, Porter TR, McCowan TC, Roberson PK, James CA, Matchett WJ and Moursi M. Microbubble-augmented Ultrasound Declotting of Thrombosed Arteriovenous Dialysis Grafts in Dogs. Journal of Vascular and Interventional Radiology (2003); 14(3): 343-47.

Cunningham KS and Gotlieb AI. The role of shear stress in the pathogenesis of atherosclerosis. Lab Invest (2004); 85(1): 9-23.

Dai Q, Jiang Y, Liu Z, Yang J and Leng J. 2036: Value of contrast-enhanced ultrasound in the differentiation of benign from malignant adnexal masses. Ultrasound in Medicine & Biology (2006); 32(5, Supplement 1): P91.

Dalecki D. WFUMB safety symposium on echo-contrast agents: Bioeffects of ultrasound contrast agents in vivo. Ultrasound in Medicine & Biology (2007); 33(2): 205-13.

Dalecki D, Raeman CH, Child SZ, Cox C, Francis CW, Meltzer RS and Carstensen EL. Hemolysis in vivo from exposure to pulsed ultrasound. Ultrasound in Medicine & Biology (1997); 23(2): 307-13.

Dalecki D, Rota C, Raeman CH and Child SZ. Premature cardiac contractions produced by ultrasound and microbubble contrast agents in mice. Acoustics Research Letters Online (2005); 6(3): 221-26.

DantecDynamics. Laser Optical Measurement Systems and Sensors. (2007) Retrieved August 2008, 2008, from http://www.dantecdynamics.com/Default.aspx?ID=653.

Dayton P, Klibanov A, Brandenburger G and Ferrara K. Acoustic radiation force in vivo: a mechanism to assist targeting of microbubbles. Ultrasound in Medicine & Biology (1999a); 25(8): 1195-201.

Dayton PA, Morgan KE, Klibanov AL, Brandenburger G, Nightingale KR and Ferrara KW. A preliminary evaluation of the effects of primary and secondary radiation forces on acoustic contrast agents. Ultrasonics, Ferroelectrics and Frequency Control, IEEE Transactions on (1997); 44(6): 1264-77.

Dayton PA, Morgan KE, Klibanov AL, Brandenburger GH and Ferrara KW. Optical and acoustical observations of the effects of ultrasound on contrast agents. Ultrasonics, Ferroelectrics and Frequency Control, IEEE Transactions on (1999b); 46(1): 220-32.

De Backer TLM, De Buyzere M, Segers P, Carlier S, De Sutter J, Van de Wiele C and De Backer G. The role of whole blood viscosity in premature coronary artery disease in women. Atherosclerosis (2002); 165(2): 367-73.

de Jong N, Frinking PJA, Bouakaz A, Goorden M, Schourmans T, Jingping X and Mastik F. Optical imaging of contrast agent microbubbles in an ultrasound field with a 100-MHz camera. Ultrasound in Medicine & Biology (2000a); 26(3): 487-92.

de Jong N, Frinking PJA, Bouakaz A and Ten Cate FJ. Detection procedures of ultrasound contrast agents. Ultrasonics (2000b); 38(1-8): 87-92.

Della Martina A, Allemann E, Bettinger T, Bussat P, Lassus A, Pochon S and Schneider M. Grafting of abciximab to a microbubble-based ultrasound contrast agent for targeting to platelets expressing GP IIb/IIIa - Characterization and in vitro testing. European Journal of Pharmaceutics and Biopharmaceutics (2007); In Press, Corrected Proof: 1388.

DeMaria AN, Narula J, Mahmud E and Tsimikas S. Imaging Vulnerable Plaque by Ultrasound. Journal of the American College of Cardiology (2006); 47(8, Supplement 1): C32-C39.

Deng CX and Lizzi FL. A review of physical phenomena associated with ultrasonic contrast agents and illustrative clinical applications. Ultrasound in Medicine & Biology (2002); 28(3): 277-86.

Department of Health. 'Hospital Activity Statistics.' (http://www.performance.doh.gov.uk/hospitalactivity/data_requests/imaging_and_radiodiagnostics.htm) May 2010.

Dickson BC and Gotlieb AI. Towards understanding acute destabilization of vulnerable atherosclerotic plaques. Cardiovascular Pathology (2003); 12(5): 237-48.

Dijkmans PA, Juffermans LJM, Musters RJP, van Wamel A, ten Cate FJ, van Gilst W, Visser CA, de Jong N and Kamp O. Microbubbles and ultrasound: from diagnosis to therapy. European Journal of Echocardiography (2004); 5(4): 245-56.

Dijkmans PA, Visser CA and Kamp O. Adverse reactions to ultrasound contrast agents: Is the risk worth the benefit? European Journal of Echocardiography (2005); 6(5): 363-66.

Dolan MS, Gala SS, Dodla S, Abdelmoneim SS, Xie F, Cloutier D, Bierig M, Mulvagh SL, Porter TR and Labovitz AJ. Safety and Efficacy of Commercially Available Ultrasound Contrast Agents for Rest and Stress Echocardiography: A Multicenter Experience. Journal of the American College of Cardiology (2009); 53(1): 32-38.

Dollet B, van der Meer SM, Garbin V, de Jong N, Lohse D and Versluis M. Nonspherical Oscillations of Ultrasound Contrast Agent Microbubbles. Ultrasound in Medicine & Biology (2008); In Press, Corrected Proof.

Doriot PA, Dorsaz PA, Dorsaz L, De Benedetti E, Chatelain P and Delafontaine P. In-vivo measurements of wall shear stress in human coronary arteries. Coron Artery Dis. (2000); 11(6): 495-502.

Duck FA. Hazards, risks and safety of diagnostic ultrasound. Medical Engineering & Physics (2008); In Press, Corrected Proof.

Durst F, Melling A and Whitelaw JH. Principles and Practice of Laser-Doppler Anemometry: Academic Press, 1976.

Eckersley RJ, Chin CT and Burns PN. Optimising phase and amplitude modulation schemes for imaging microbubble contrast agents at low acoustic power. Ultrasound in Medicine & Biology (2005); 31(2): 213-19.

EFSUMB. 'Clinical Safety Statement for Diagnostic Ultrasound ' (http://www.efsumb.org/guidelines/2008safstat.pdf)

Elliott MR and Thrush AJ. Measurement of resolution in intravascular ultrasound images. Physiological Measurement (1996); 17: 259-65.

Falk E, Shah PK and Fuster V. Coronary Plaque Disruption. Circulation (1995); 92(3): 657-71.

Fatemi M and Greenleaf JF. Vibro-acoustography: An imaging modality based on ultrasound-stimulated acoustic emission. Proceedings of the National Academy of Sciences of the United States of America (1999); 96(12): 6603-08.

Federal Food, Drug, and Cosmetic Act (FD&C Act).(2005).

Ferrante EA, Pickard JE, Rychak J, Klibanov A and Ley K. Dual targeting improves microbubble contrast agent adhesion to VCAM-1 and P-selectin under flow. Journal of Controlled Release (2009); In Press, Accepted Manuscript.

Fichtlscherer S, Heeschen C and Zeiher AM. Inflammatory markers and coronary artery disease. Current Opinion in Pharmacology (2004); 4(2): 124-31.

Fields S and Dunn F. Correlation of echographic visualizability of tissue with biological composition and physiological state. The Journal of the Acoustical Society of America (1973); 54(3): 809-12.

Forsberg F, Shi WT and Goldberg BB. Subharmonic imaging of contrast agents. Ultrasonics (2000); 38(1-8): 93-98.

Fowlkes JB, Gardner EA, Ivey JA and Carson PL. The role of acoustic radiation force in contrast enhancement techniques using bubble-based ultrasound contrast agents. The Journal of the Acoustical Society of America (1993); 93(4): 2348-48.

Frías JC, Lipinski MJ, Albelda MT, Ibáñez B, Soriano C, García-España E, Jesús L, Jiménez-Borreguero and Badimon3 JJ. Nanoparticles as contrast agents for MRI of atherosclerotic lesions. Clinical Medicine: Cardiology (2008); 2: 173-79.

Frinking PJA, Bouakaz A, Kirkhorn J, Ten Cate FJ and de Jong N. Ultrasound contrast imaging: current and new potential methods. Ultrasound in Medicine & Biology (2000); 26(6): 965-75.

Fry FJ, Sanghvi NT, Foster RS, Bihrle R and Hennige C. Ultrasound and microbubbles: Their generation, detection and potential utilization in tissue and organ therapy--Experimental. Ultrasound in Medicine & Biology (1995); 21(9): 1227-37.

Galonska M, Ducke F, Kertesz-Zborilova T, Meyer R, Guski H and Knollmann FD. Characterization of Atherosclerotic Plaques in Human Coronary Arteries With 16-Slice Multidetector Row Computed Tomography by Analysis of Attenuation Profiles. Academic Radiology (2008); 15(2): 222-30.

Givan AL. Flow Cytometry: First Principles. New York: Wiley-Liss, 1992.

Glagov S, Weisenberg E, Zarins CK, Stankunavicius R and Kolettis GJ. Compensatory enlargement of human atherosclerotic coronary arteries. N Engl J Med (1987); 316(22): 1371-75.

Goertz DE, Frijlink ME, de Jong N and van der Steen AFW. Nonlinear intravascular ultrasound contrast imaging. Ultrasound in Medicine & Biology (2006); 32(4): 491-502.

Goertz DE, Frijlink ME, Tempel D, Bhagwandas V, Gisolf A, Krams R, de Jong N and van der Steen AFW. Subharmonic Contrast Intravascular Ultrasound for Vasa Vasorum Imaging. Ultrasound in Medicine & Biology (2007); 33(12): 1859-72.

Goldberg BB, Liu J-B and Forsberg F. Ultrasound contrast agents: A review. Ultrasound in Medicine & Biology (1994); 20(4): 319-33.

Gorski KA and Watson S. Functional Assessment of Coronary Artery Disease. Invasive Cardiology: a Manual for Cath Lab PersonneI. Watson and Gorski. Sudbury, MA, Physician's Press. (2005), 19: 398.

Gosgnach W, Messika-Zeitoun D, Gonzalez W, Philipe M and Michel J-B. Shear stress induces iNOS expression in cultured smooth muscle cells: role of oxidative stress. Am J Physiol Cell Physiol (2000); 279(6): C1880-88.

Gramiak R and Shah PM. Echocardiography of the Aortic Root. Investigative Radiology (1968).

Green NM. Avidin. Advances in Protein Chemistry (1975); 29: 85-133.

Guilbault GG. Practical Fluorescence. New York: Marcel Dekker, Inc., 1990.

Hart D and Wall BF. Radiation exposure of the UK population from medical and dental x-ray examinations.(2002), National Radiological Protection Board.

Harvey CJ, Blomley MKJ, Eckersley RJ and Cosgrove DO. Developments in ultrasound contrast media. European Journal of Radiology (2000); 11: 675-89.

Harvey CJ, Pilcher JM, Eckersley RJ, Blomley MJK and Cosgrove DO. Advances in Ultrasound. Clinical Radiology (2002); 57(3): 157-77.

Haugland RP. Handbook of Fluorescent Probes and Research Products. 9th edition. (2002), from http://www.mobitec-us.com/probes/.

Heffelfinger S, Hawkins H, Barrish J, Taylor L and Darlington G. SK HEP-1: A human cell line of endothelial origin. In Vitro Cellular & Developmental Biology - Animal (1992); 28(2): 136-42.

Hilgenfeldt S, Lohse D and Zomack M. Sound scattering and localized heat deposition of pulse-driven microbubbles. The Journal of the Acoustical Society of America (2000); 107(6): 3530-39.

Horn E. Application Note 11. Shear stress and shear rates for µ-Slides I Luer and µ-Slide VI, based on numerical calculations.(2008), Ibidi Integrated Biodiagnostics: 11.

Hoskins P, Thrush A, Martin K and Whittingam T. Diagnostic Ultrasound: Physics and Equipment. Cambridge: Greenwich Medical Media, 2002.

Huang B, Snook K and Shung KK (2001). Characterization of high-frequency transducers with small aperture hydrophones. Ultrasonics Symposium, 2001 IEEE.

Hyafil F and Fayad ZA. Evaluating Vulnerable Atherosclerotic Plaque with MRI. Cardiac PET and PET/CT Imaging. (2007): 360-72.

IEEE. IEEE Guide for Medical Ultrasound Field Parameter Measurements. (1990) Retrieved 17/04/09, 2009.

Jackson BA, Schwane JA and Starcher BC. Effect of ultrasound therapy on the repair of Achilles tendon injuries in rats. Medicine & Science in Sports & Exercise (1991); 23(2): 171-76.

Jansen MA, Nederhoff MGJ and van Echteld CJA. Intracellular sodium MRI in acute regional myocardial ischemia and reperfusion. Journal of Molecular and Cellular Cardiology (2006); 40(6): 968-69.

Kahl V. Ibidi images.(2009), Ibidi.

Kaufmann BA and Lindner JR. Molecular imaging with targeted contrast ultrasound. Current Opinion in Biotechnology (2007); 18(1): 11-16.

National Physical Laboratory (online). 'Kaye and Laby Tables of Physical and Chemical Constants.' (http://www.kayelaby.npl.co.uk/) 9th May 2008.

Kips JG, Segers P and Van Bortel LM. Identifying the vulnerable plaque: A review of invasive and non-invasive imaging modalities. Artery Research (2008); 2(1): 21-34.

Klabunde RE. Cardiovascular Physiology Concepts: Lippincott Williams & Wilkins, 2005.

Klibanov A, Rychak JJ and Ley KF. Microbubble Compositions and Method of Preparing and Using the Same.(2004), Targeson LLC EP1551459, US 20050260189.

Klibanov AL. Targeted delivery of gas-filled microspheres, contrast agents for ultrasound imaging. Advanced Drug Delivery Reviews (1999); 37(1-3): 139-57.

Klibanov AL, Hughes MS, Villanueva FS, Jankowski RJ, Wagner WR, Wojdyla JK, Wible JH and Brandenburger GH. Targeting and ultrasound imaging of microbubble-based contrast agents. Magnetic Resonance Materials in Biology, Physics, and Medicine (1999); 8(3): 177-84.

Klibanov AL, Rychak JJ, Yang WC, Alikhani S, Li B, Acton S, Lindner JR, Ley K and Kaul S. Targeted ultrasound contrast agent for molecular imaging of inflammation in high-shear flow. Contrast Media Mol Imaging (2006); 1: 259–66.

Kooten TGv, Schakenraad JM, Mei HCvd, A. Dekker, Kirkpatrick CJ and Busscher HJ. Fluid shear induced endothelial cell detachment from glass - influence of adhesion time and shear stress. Med Eng Phys (1994); 15: 506-12.

Korosoglou G, Behrens S, Bekeredjian R, Hardt S, Hagenmueller M, Dinjus E, Bohm KJ, Unger E, Katus HA and Kuecherer H. The potential of a new stable ultrasound contrast agent for site-specific targeting. An in vitro experiment. Ultrasound in Medicine & Biology (2006); 32(10): 1473-78.

Korpanty G, Grayburn PA, Shohet RV and Brekken RA. Targeting vascular endothelium with avidin microbubbles. Ultrasound in Medicine & Biology (2005); 31(9): 1279-83.

Ku JP, Draney MT, Arko FR, Lee WA, Chan FP, Pelc NJ, Zarins CK and Taylor CA. In Vivo Validation of Numerical Prediction of Blood Flow in Arterial Bypass Grafts. Annals of Biomedical Engineering (2002); 30(6): 743-52.

Kunitomo M. Oxidative Stress and Atherosclerosis. YAKUGAKU ZASSHI (2007); 127(12): 1997-2014.

Kurzweil R and Grossman T. The New Understanding: Most Heart Attacks Are Caused By Vulnerable Plaque and Inflammation. Fantastic Voyage: Live Long Enough to Live Forever New York, Rodale Books. (2004): 400.

Lakowicz JR. Principles of Fluorescence Spectroscopy. New York: Plenum Press, 1983.

Lanza GM and Wickline SA. Targeted ultrasonic contrast agents for molecular imaging and therapy. Progress in Cardiovascular Diseases (2001); 44(1): 13-31.

Brian Larson. 'NDT Resource Centre.' (www.ndt-ed.org) May 2010.

Lathia JD, Leodore L and Wheatley MA. Polymeric contrast agent with targeting potential. Ultrasonics (2004); 42(1-9): 763-68.

Leber A, von Ziegler F, Becker A, Becker C, Reiser M, Steinbeck G, Knez A and Boekstegers P. Characteristics of coronary plaques before angiographic progression determined by Multi-Slice CT. The International Journal of Cardiovascular Imaging (formerly Cardiac Imaging) (2008); 24(4): 423-28.

Levick JR. An Introduction to Cardiovascular Physiology: Arnold Publishers, 2003.

Li MX, Beech-Brandt JJ, John LR, Hoskins PR and Easson WJ. Numerical analysis of pulsatile blood flow and vessel wall mechanics in different degrees of stenoses. Journal of Biomechanics (2007); 40: 3715–24.

Lin LI, Ke YF, Ko YC and Lin JK. Curcumin Inhibits SK-Hep-1 Hepatocellular Carcinoma Cell Invasion in vitro and Suppresses Matrix Metalloproteinase-9 Secretion. Oncology (1998); 55(4): 349-53.

Lind L. Circulating markers of inflammation and atherosclerosis. Atherosclerosis (2003); 169(2): 203-14.

Lindner JR. Assessment of inflammation with contrast ultrasound. Progress in Cardiovascular Diseases (2001); 44(2): 111-20.

Lindner JR. Detection of inflamed plaques with contrast ultrasound. The American Journal of Cardiology (2002a); 90(10, Supplement 3): L32-L35.

Lindner JR. Evolving applications for contrast ultrasound. The American Journal of Cardiology (2002b); 90(10, Supplement 1): 72-80.

Lindner JR. Molecular imaging with contrast ultrasound and targeted microbubbles. Journal of Nuclear Cardiology (2004); 11(2): 215-21.

Lindner JR, Ismail S, Spotnitz WD, Skyba DM, Jayaweera AR and Kaul S. Albumin Microbubble Persistence During Myocardial Contrast Echocardiography Is Associated With Microvascular Endothelial Glycocalyx Damage. Circulation (1998); 98(20): 2187-94.

Lindner JR, Song J, Christiansen J, Klibanov AL, Xu F and Ley K. Ultrasound Assessment of Inflammation and Renal Tissue Injury With Microbubbles Targeted to P-Selectin. Circulation (2001); 104(17): 2107-12.

Lirdprapamongkol K (2006). Endothelial characteristic of a cell line "SK-Hep-1", Unknown.

Liu Y, Miyoshi H and Nakamura M. Encapsulated ultrasound microbubbles: Therapeutic application in drug/gene delivery. Journal of Controlled Release (2006); 114(1): 89-99.

Lodge MA, Braess H, Mahmoud F, Suh J, Englar N, Geyser-Stoops S, Jenkins J, Bacharach SL and Dilsizian V. Developments in Nuclear Cardiology: Transition from Single Photon Emission Computed Tomography to Positron Emission Tomography/Computed Tomography. Journal of Invasive Cardiology (2005); 17(9): 491-96.

Lum AFH, Borden MA, Dayton P, Kruse DE, Simon SI and Ferrara KW. Ultrasound radiation force enables targeted deposition of model drug carriers loaded on microbubbles. Journal of Controlled Release (2006); 111: 128 – 34.

Lupotti FA. Quantitative Blood Flow as Assessed by Intravascular Ultrasound. Faculty of Medicine: Erasmus University, Rotterdam. (2002), PhD: (188).

MacDonald CA, Sboros V, Gomatam J, Pye SD, Moran CM and Norman McDicken W. A numerical investigation of the resonance of gas-filled microbubbles: resonance dependence on acoustic pressure amplitude. Ultrasonics (2004); 43(2): 113-22.

Main ML, Goldman JH and Grayburn PA. Ultrasound contrast agents: balancing safety versus efficacy. Expert Opinion on Drug Safety (2009); 8(1): 49-56.

Maseri A and Fuster V. Is There a Vulnerable Plaque? Circulation (2003); 107(16): 2068-71.

McDonald DA. Blood Flow in Arteries. London: Edward Arnold (Publishers) Ltd., 1960.

Melamed MR. Flow Cytometry and Sorting. New York: Wiley-Liss, 1990.

MHRA. Medicines and Medical Devices Regulation: What You Need to Know. (2008), from www.mhra.gov.uk.

Migaleddu V, Scanu AM, Quaia E, Rocca PC, Dore MP, Scanu D, Azzali L and Virgilio G. Contrast-Enhanced Ultrasonographic Evaluation of Inflammatory Activity in Crohn's Disease. Gastroenterology (2009); 137(1): 43-52.

Millar HD. Doppler tip wire guide.(1988) US, Jaworski, Francis J.

Miller AP and Nanda NC. Contrast echocardiography: new agents. Ultrasound in Medicine & Biology (2004); 30(4): 425-34.

Miller DL and Dou C. Membrane damage thresholds for pulsed or continuous ultrasound in phagocytic cells loaded with contrast agent gas bodies. Ultrasound in Medicine & Biology (2004); 30(3): 405-11.

Miller DL and Gies RA. Gas-body-based contrast agent enhances vascular bioeffects of 1.09 MHz ultrasound on mouse intestine. Ultrasound in Medicine & Biology (1998); 24(8): 1201-08.

Moran C, Butler M and Ross J. Private communication.(2007).

Moran C, Ross J and Oliver C. Ultrasonic characterization of a newly developed targeted ultrasonic contrast agent. European Journal of Echocardiography (2003b); 4(S19).

Moran CM, Ross JA, Cunningham C, Butler M, Anderson T, Newby D, Fox KAA and McDicken WN. Manufacture and acoustical characterisation of a high-frequency contrast agent for targeting applications. Ultrasound in Medicine & Biology (2006); 32(3): 421-28.

Moy VT, Florin E-L, Rief M, Ludwig M and Gaub HE. Forced Unbinding of the Avidin-biotin Complex. (1994) Retrieved 2nd October 2009, 2009, from http://edoc.hu-berlin.de/conferences/conf1/moy-v-t/PDF/Moy.pdf.

NEMA. Acoustic Output Measurement Standard For Diagnostic Ultrasound Equipment, Revision 3. (2004) Retrieved 15th April, 2009.

National Health Service. 'National Electronic Library for Medicines.' (http://www.nelm.nhs.uk/en/) November 2009.

Nichols WW and O'Rourke MF. McDonald's Blood Flow in Arteries. London: Edward Arnold, 1990.

Oelze ML. Bandwidth and resolution enhancement through pulse compression. Ultrasonics, Ferroelectrics and Frequency Control, IEEE Transactions on (2007); 54(4): 768-81.

Ophir J and Parker KJ. Contrast agents in diagnostic ultrasound. Ultrasound in Medicine & Biology (1989); 15(4): 319-33.

Parham P. Immune System. Oxford: Garland Science, 2004.

Pawelski L. The Effect of Multislice CT on Examination Time and Patient ThroughputThis is a featured page Radiography: University of South Australia, (2005), Masters:

Pedro R. Moreno JEM. Detection of High-Risk Atherosclerotic Coronary Plaques by Intravascular Spectroscopy. Journal of Interventional Cardiology (2003); 16(3): 243-52.

Perez S. Cell counts using Improved Neubauer haemocytometer.(2006).

Picano E. Economic and biological costs of cardiac imaging. Cardiovascular Ultrasound (2005); 3(1): 13.

Picotwist. Forces involved at the biological level. (2009) Retrieved 23rd December 2009, 2009, from www.picotwist.com.

Postema M, Bouakaz A, Chin CT and Jong Nd (2002). Optically Observed Microbubble Coalescence and Collapse. IEEE Ultrasonics Symposium.

Postema M, Marmottant P, Lancee CT, Hilgenfeldt S and Jong Nd. Ultrasound-induced microbubble coalescence. Ultrasound in Medicine & Biology (2004a); 30(10): 1337-44.

Postema M, van Wamel A, Lancee CT and de Jong N. Ultrasound-induced encapsulated microbubble phenomena. Ultrasound in Medicine & Biology (2004b); 30(6): 827-40.

Preston RC. Output Measurements for Medical Ultrasound. Berlin: Springer-Verlag, 1991.

Quan L, Xu XY, Uwe K, Malcolm BR, Ian M and Peter H. Quantitative comparison of CFD predicted and MRI measured velocity fields in a carotid bifurcation phantom. Biorheology (2002); 39(3): 467-74.

Raum K and O'Brien WD, Jr. Pulse-echo field distribution measurement technique for high-frequency ultrasound sources. Ultrasonics, Ferroelectrics and Frequency Control, IEEE Transactions on (1997); 44(4): 810-15.

Reynolds O. An experimental investigation of the circumstances which determine whether the motion of water shall be direct or sinuous, and of the law of resistance in parallel channels. Philosophical Transactions of the Royal Society (1883); 174: 935-82.

Richards SC. Fluid Mechanics. Washington: Taylor & Francis Inc, 1989.

Roelandt T, Bom N, Roelandt J and Roelandt J. Intravascular Ultrasound (Developments in Cardiovascular Medicine): Kluwer Academic Publishers 1993.

Rosales M and Radeva P. A Basic Model for IVUS Image Simulation. Handbook of Biomedical Image Analysis. (2005): 1-55.

Ross J and Moran C. Improved Microbubble Composition and method for making the same.(2006).

Ross J and Moran C. Private communication.(2007).

Rott N. A Note on the History of the Reynolds Number. Annual Review Fluid Mechanics (1990);(22): 1-11.

Rudd JHF, Davies JR and Weissberg PL. Imaging of Atherosclerosis -- Can We Predict Plaque Rupture? Trends in Cardiovascular Medicine (2005); 15(1): 17-24.

Rychak JJ, Klibanov AL and Hossack J (2004). Acoustic radiation force enhances adhesion of microbubbles targeted to P-selectin. Ultrasonics Symposium, 2004 IEEE.

Rychak JJ, Klibanov AL and Hossack JA. Acoustic radiation force enhances targeted delivery of ultrasound contrast microbubbles: in vitro verification. Ultrasonics, Ferroelectrics and Frequency Control, IEEE Transactions on (2005); 52(3): 421-33.

Rychak JJ, Klibanov AL, Ley KF and Hossack JA. Enhanced Targeting of Ultrasound Contrast Agents Using Acoustic Radiation Force. Ultrasound in Medicine & Biology (2006a); In Press, Corrected Proof.

Rychak JJ, Lindner JR, Ley K and Klibanov AL. Deformable gas-filled microbubbles targeted to P-selectin. Journal of Controlled Release (2006b); 114(3): 288-99.

Samuel S, Miller DL and Fowlkes JB. The relationship of acoustic emission and pulse-repetition frequency in the detection of gas body stability and cell death. Ultrasound in Medicine & Biology (2006); 32(3): 439-47.

Schaar JA, van der Steen AFW, Mastik F, Baldewsing RA and Serruys PW. Intravascular Palpography for Vulnerable Plaque Assessment. Journal of the American College of Cardiology (2006); 47(8, Supplement 1): C86-C91.

Schmidt BJ, Sousa I, van Beek AA and Böhmer MR. Adhesion and ultrasound-induced delivery from monodisperse microbubbles in a parallel plate flow cell. Journal of Controlled Release (2008); 131(1): 19-26.

Schneider M, Bussat P, Yan F and Guillot C. Ultrasound Contrast Agents and Process for the Preparation Thereof Patent number: WO/2004/069284.(2004), Bracco Res SA WO/2004/069284.

Schneider M, Yan F, Puginier J, Barrau M-B, Bussat P, Hybl E and Bichon D. Ultrasound Contrast Agents and Methods of Making and Using Them.(2006), Bracco International B.V.

Schroeder AP and Falk E. Vulnerable and dangerous coronary plaques. Atherosclerosis (1995); 118: S141-S49.

Sheehan D. Physical Biochemistry: Principles and Applications Chichester, UK: WileyBlackwell, 2000.

Shen C-C, Cheng Y-C and Li P-C (2007). P3B-4 Coded Excitation and Nonlinear Pulse Compression in Pulse-Inversion Fundamental Imaging. Ultrasonics Symposium, 2007. IEEE.

Shi WT, Forsberg F, Raichlen JS, Needleman L and Goldberg BB. Pressure dependence of subharmonic signals from contrast microbubbles. Ultrasound in Medicine & Biology (1999); 25(2): 275-83.

Singh V. Safety Standards for Medical Ultrasound Systems. World Congress on Medical Physics and Biomedical Engineering 2006. (2007): 2764-66.

Smith DAB, Porter TM, Martinez J, Huang S, MacDonald RC, McPherson DD and Holland CK. Destruction Thresholds of Echogenic Liposomes with Clinical Diagnostic Ultrasound. Ultrasound in Medicine & Biology (2007); 33(5): 797-809.

Snook KA, Bin H, Smith NB and Shung KK (2000). An exposimetry system for characterization of acoustic fields above 20 MHz. Ultrasonics Symposium, 2000 IEEE.

Streeter VL. Fluid Mechanics. New York: McGraw-Hill, 1962.

Stride E and Saffari N. Microbubble ultrasound contrast agents: a review. Proc. Instn Mech. Engrs (2003a); 217.

Stride E and Saffari N. On the Destruction of Microbubble Ultrasound Contrast Agents. Ultrasound in Med. & Biol. (2003b); 29(4): 563–73.

Stride E and Saffari N. The potential for thermal damage posed by microbubble ultrasound contrast agents. Ultrasonics (2004); 42: 907–13.

Suo J, Ferrara DE, Sorescu D, Guldberg RE, Taylor WR and Giddens DP. Hemodynamic Shear Stresses in Mouse Aortas: Implications for Atherogenesis. Arterioscler Thromb Vasc Biol (2007); 27(2): 346-51.

Tachibana K. Ultrasound therapy for stroke and regenerative medicine. International Congress Series (2004); 1274: 153-58.

Tachibana K and Tachibana S. Application of Ultrasound as a New Drug Delivery System. Japanese Journal of Applied Physics (1999); 38(1): 3014-19.

Takalkar AM, Klibanov AL, Rychak JJ, Lindner JR and Ley K. Binding and detachment dynamics of microbubbles targeted to P-selectin under controlled shear flow. Journal of Controlled Release (2004); 96(3): 473-82.

Talu E, Hettiarachchi K, Nguyen H, Lee AP, Powell RL, Longo ML and Dayton PA. Lipid-stabilized Monodisperse Microbubbles Produced by Flow Focusing for Use as Ultrasound Contrast Agents. IEEE Ultrasonics Symposium (2006).

ter Haar G. Therapeutic applications of ultrasound. Progress in Biophysics and Molecular Biology (2007); 93(1-3): 111-29.

Thieme T, Wernecke KD, Meyer R, Brandenstein E, Habedank D, Hinz A, Felix SB, Baumann G and Kleber FX. Angioscopic evaluation of atherosclerotic plaques: validation by histomorphologic analysis and association with stable and unstable coronary syndromes. J Am Coll Cardiol (1996); 28(1): 1-6.

Tsutsui JM, Xie F and Porter RT. The use of microbubbles to target drug delivery. Cardiovascular Ultrasound (2004); 2(23).

Turner Biosystems Inc. 'An Introduction to Fluorescence Measurements.' (http://www.turnerbiosystems.com/doc/appnotes/998_0050/0050_c2.php) 7th October 2009.

Ueda Y, Hirayama A and Kodama K. Plaque Characterization and Atherosclerosis Evaluation by Coronary Angioscopy. Herz (2003); 28(6): 501-04.

Unger EC, Hersh E, Vannan M, Matsunaga TO and McCreery T. Local drug and gene delivery through microbubbles. Progress in Cardiovascular Diseases (2001a); 44(1): 45-54.

Unger EC, Matsunaga TO, McCreery TP, Sweitzer R, Schumann P, Quigley R and Zutshi R. Therapeutic applications of microbubbles. The Journal of the Acoustical Society of America (2001b); 110(5): 2669-69.

Unger EC, Porter T, Culp W, Labell R, Matsunaga T and Zutshi R. Therapeutic applications of lipid-coated microbubbles. Advanced Drug Delivery Reviews (2004); 56(9): 1291-314.

Versteeg HK and Malalasekera W. An Introduction to Computational Fluid Dynamics: The Finite Volume Method. Harlow, England: Prentice Hall, 2007.

Villanueva FS, Jankowski RJ, Klibanov S, Pina ML, Alber SM, Watkins SC, Brandenburger GH and Wagner WR. Microbubbles Targeted to Intercellular Adhesion Molecule-1 Bind to Activated Coronary Artery Endothelial Cells. Circulation (1998); 98(1): 1-5.

Virmani R, Kolodgie FD, Burke AP, Farb A and Schwartz SM. Lessons From Sudden Coronary Death : A Comprehensive Morphological Classification Scheme for Atherosclerotic Lesions. Arterioscler Thromb Vasc Biol (2000); 20(5): 1262-75.

Wald NJ and Law MR. A strategy to reduce cardiovascular disease by more than 80%. BMJ (2003); 326(7404): 1419-.

Wang J, Geng Y-J, Guo B, Klima T, Lal BN, Willerson JT and Casscells W. Near-infrared spectroscopic characterization of human advanced atherosclerotic plaques. J Am Coll Cardiol (2002); 39(8): 1305-13.

Watrasiewicz BM and Rudd M. Laser Doppler Measurements. London: Butterworths, 1976.

Weber PC, Ohlendorf DH, Wendoloski JJ and Salemme FR. Structural origins of high-affinity biotin binding to streptavidin. Science (1989); 243(4887): 85-88.

Weller GER, Villanueva FS, Klibanov AL and Wagner WR. Modulating Targeted Adhesion of an Ultrasound Contrast Agent to Dysfunctional Endothelium. Annals of Biomedical Engineering (2002); 30(8): 1012-19.

Wentzel J, Gijsen FJH, Schuurbiers JCH, Garcia-Garcia HM, van der Steen AFW and Serruys PW. Study on the relationship between plaque composition and shear stress in human coronary arteries in vivo. Journal of Biomechanics (2006); 39(Supplement 1): S280-S80.

Wilchek M and Bayer EA. The avidin-biotin complex in bioanalytical applications. Analytical Biochemistry (1988); 171(1): 1-32.

Williams AR, Wiggins RC, Wharram BL, Goyal M, Dou C, Johnson KJ and Miller DL. Nephron Injury Induced by Diagnostic Ultrasound Imaging at High Mechanical Index with Gas Body Contrast Agent. Ultrasound in Medicine & Biology (2007); 33(8): 1336-44.

Wong J, Chilkoti A and Moy VT. Direct force measurements of the streptavidin-biotin interaction. Biomolecular Engineering (1999); 16(1-4): 45-55.

Yabushita H, Bouma BE, Houser SL, Aretz HT, Jang I-K, Schlendorf KH, Kauffman CR, Shishkov M, Kang D-H, Halpern EF and Tearney GJ. Characterization of Human Atherosclerosis by Optical Coherence Tomography. Circulation (2002); 106(13): 1640-45.

Yea Y and Cummins HZ. Localised fluid flow measurement with an He-Ne laser spectrometer. Applied Physics Letters (1964); 4(10): 176-78.

Yonemoto Y, Yanagisawa H, Kawara Z and Kunugi T. Coalescence of Microbubble. Journal of the Japanese Society for Experimental Mechanics (2008); 8(1): 38-44.

Zhao S, Borden M, Bloch SH, Kruse D, Ferrara KW and Dayton PA. Radiation-Force Assisted Targeting Facilitates Ultrasonic Molecular Imaging. Mol Imaging (2004); 3(3): 135–48.

Zimarino M, Prati F, Stabile E, Pizzicannella J, Fouad T, Filippini A, Rabozzi R, Trubiani O, Pizzicannella G and De Caterina R. Optical coherence tomography accurately identifies intermediate atherosclerotic lesions--An in vivo evaluation in the rabbit carotid artery. Atherosclerosis (2007); 193(1): 94-101.